

The properties of post-novae

IRMA FUENTES MORALES

Instituto de Física y Astronomía
Facultad de Ciencias



Universidad de Valparaíso
Doctorado en Astrofísica

Marzo 2022
Valparaíso. Chile.

This thesis is solely my own composition,

except where specifically indicated in the text.

Total or partial reproduction, for scientific or academic purposes,
is authorised including a bibliographic reference to this document.

Irma Fuentes Morales

Marzo 2022.

Valparaíso. Chile.

*“Cuando creíamos que teníamos todas las respuestas,
de pronto, cambiaron todas las preguntas”*

Mario Benedetti

Acknowledgements

Quisiera comenzar mis agradecimientos a ese Ser que a pesar de que me aleje de Él por tiempos sin duración definida, siempre está presente y guía mis pasos. En una noche despejada, mirando el pedacito de cielo visible desde mi ventana en el cerro Playa Ancha, o en un atardecer con el horizonte en llamas, siento su infinita presencia.

En el transcurso del doctorado emergió en mi una poderosa fuerza que me desvió parcialmente de la astronomía. Así, de forma paralela a esta tesis, emerge Ruta Sustentable, que nació sin un objetivo claro, y que ahora me ha impulsado de vuelta a la ruta de la ciencia con una visión más amplia de la contribución con la que puedo aportar en el camino que prosiga después del doctorado. Agradezco a Dios por cruzar mi vida con la vida de mujeres maravillosas, con las que hemos ido construyendo el sueño colectivo de dejar una huella positiva en este planeta. Agradezco el apoyo incondicional de Mariana, Paula, Rosa, a todo el equipo que se ha unido en el camino, a mi familia, en especial a mi mami, por comprender mis largas ausencias en la vida familiar en pos de construir estos sueños.

Este trabajo no habría podido finalizarlo sin la infinita paciencia y consejo de Claus, gracias por estar ahí, a pesar de las muchas veces que me alejé y quise abandonar este camino, estuviste ahí para volverme a encaminar, gracias.

El final de esta tesis es mucho más que el término de una etapa académica. En el proceso de escritura aparecieron obstáculos impensados, personas importantes se fueron de mi vida, pero también desafíos que mi yo del 2015, cuando comenzó esta etapa del doctorado, no hubiera sido capaz de sobrellevar. Es así que el llegar a esta etapa de término no tan solo el doctorado finaliza, sino el fin de una etapa profunda de crecimiento personal. Al final de esta travesía agradezco a todos los que han aparecido para potenciar mi propósito de vida y por creer que esta astrónoma puede aportar no tan solo al campo de las estrellas variables cataclísmicas y novas sino que también a trabajar por una sociedad más justa.

Por último agradezco a la Comisión Nacional de Investigación Científica y Tecnológica, Programa Formación de Capital Humano Avanzado (CONICYT-PFCHA) Doctorado Nacional 2017-21171099 por financiamiento de la beca doctoral.

Contents

Acknowledgements	ii
Abstract	viii
1 Introduction	1
1.1 Motivation	1
1.2 Geometry of interacting binary stars	2
1.3 The Cataclysmic Variable stars' world	2
1.3.1 Mass transfer mechanism	4
1.3.2 Accretion discs	6
1.3.3 Type of outbursts on CVs	6
1.4 CV classification	8
1.5 CV evolution	10
1.5.1 Angular-momentum loss mechanisms in CVs	10
1.5.2 Other AML mechanisms	12
1.5.3 The orbital period distribution of CVs	12
1.5.4 The hibernation model	14
1.6 Optical properties of Novae	15
1.6.1 The nova eruption: The Thermonuclear Runaway	15
1.6.2 The nova shell and the evolution of the spectrum after the eruption	16
1.6.3 The recurrence scale of nova eruptions	18
1.6.4 Recurrent novae	19
1.6.5 Spectral classification of novae	20
1.6.6 Classification by light curve properties	20
1.6.7 The colours of novae	24
1.6.8 Relationship for Maximum Magnitude vs Rate of Decline, t_3 and amplitude of eruption	25
1.7 The properties of post-novae	28
1.8 Life after eruption project	30

1.9	Thesis outline	31
2	Recovery of old Novae	34
2.1	Introduction	34
2.2	Photometric data	35
2.3	Spectroscopic data	37
2.4	Analysis and Results	42
2.4.1	Searching for post-novae in colour-colour diagrams	42
2.4.2	Recovered post-novae	42
2.4.2.1	EL Aql (1927)	45
2.4.2.2	EY Aql (1926)	45
2.4.2.3	V606 Aql (1899)	48
2.4.2.4	V908 Oph (1954)	48
2.4.2.5	KT Mon (1942)	49
2.4.2.6	KY Sgr (1926)	50
2.4.2.7	V726 Sgr (1936b)	51
2.4.2.8	V1149 Sgr (1945)	52
2.4.2.9	V1583 Sgr (1928)	53
2.4.2.10	V3964 Sgr (1975)	53
2.4.2.11	V4049 Sgr (1978)	53
2.4.2.12	V825 Sco (1964)	55
2.4.3	New spectra for known post-novae	56
2.4.3.1	V1370 Aql (1982)	56
2.4.3.2	V693 CrA (1981)	58
2.4.3.3	LW Ser (1978)	60
2.4.3.4	V4077 Sgr (1982)	61
2.4.4	Discarded post-nova candidates	62
2.5	Discussion and conclusions	64
2.5.1	Remarks about spectroscopic characteristics of individual post-novae	64
2.5.2	About the strategies to recover post-novae	68
2.5.3	An updated perspective of the post-nova population	69
2.5.3.1	Behavior of emission lines for post-novae	69
2.5.3.2	Relationship between amplitude and speed class of post-novae	71
2.6	Summary	75
2.7	Appendix	84

3	The orbital period distribution of novae	86
3.1	Introduction	87
3.2	Observations and data reduction	88
3.2.1	Photometric data	88
3.2.2	Spectroscopic data	89
3.2.3	Periodicity search	90
3.3	Results	92
3.3.1	RS Car (1895)	92
3.3.2	V365 Car (1948)	94
3.3.3	X Cir (1927)	94
3.3.4	IL Nor (1893)	96
3.3.5	DY Pup (1902)	97
3.3.6	V363 Sgr (1927)	99
3.3.7	V2572 Sgr (1969)	100
3.3.8	XX Tau (1927)	102
3.3.9	CQ Vel (1940)	106
3.3.10	RW UMi (1956)	108
3.3.11	Improved ephemerides of eclipsing novae with previously known orbital periods	111
3.4	The Orbital period distribution of novae	111
3.4.1	Observed period distribution	112
3.4.2	Simulation	112
3.4.3	Comparison	115
3.5	Summary and conclusions	118
3.6	Appendix	120
4	Concluding summary and future prospects	133
	Publication list of Irma Fuentes-Morales	137
	Bibliography	153

List of Tables

1.1	Classification of nova light curves	21
2.1	Proposals related to the project	35
2.2	Log of observations.	38
2.3	Fields with colour-colour diagrams in order to detect possible post-nova candidates.	41
2.4	Equivalent width (top) and FWHM (bottom) of the emission lines present in the spectra of the old novae studied in this chapter	57
2.5	RA DEC coordinates, colours and date of the observation for those targets who are not the old nova counterpart.	63
2.6	Selected photometric data for old novae.	78
2.7	Equivalent width and FWHM data for old novae.	81
3.1	Log of observations	91
3.2	Epochs of humps observed in the time-resolved data for V2572 Sgr	104
3.3	Values of the possible orbital frequencies and its respective orbital period for XX Tau	105
3.4	Epochs for the eclipsing systems.	109
3.5	Ephemerides for the eclipsing systems whose orbital periods could be confirmed by the CTIO observations	111
3.6	Novae with uncertain published P_{orb}	113
3.7	Eclipse epochs of the eclipsing novae WY Sge, V728 Sco, OY Ara and V849 Oph	126
3.8	Spectroscopic measurements for V2572 Sgr, XX Tau, RW UMI and CQ Vel	128
3.9	The orbital periods of novae	129

List of Figures

1.1	Binary classification in terms of the Roche Lobe	3
1.2	Scheme of a Cataclysmic binary system	4
1.3	Representation of a Keplerian disc and its velocity profile of emission lines	7
1.4	Schematic representation of the S curve	9
1.5	Schematic representation of the CV types.	10
1.6	CV evolution in terms of the orbital period	11
1.7	Orbital period distribution of non-magnetic CVs	11
1.8	Light curve of V5591 Sgr (Nova Sgr 2012c) observed at the moment of the eruption	16
1.9	$H\alpha$ image for the nova shell surrounding to DQ Her as was seen in 1997 and 2018 .	17
1.10	$H\alpha$ profile variations taken about one week after the nova eruption reported in 2013 for the nova V339 Del	19
1.11	General structure of a nova light curve and its relation with the main spectroscopic phases	22
1.12	Classification system for nova light curves defined by Strope et al. (2010)	24
1.13	The distribution of novae in the HR-diagram derived from GAIA DR2	25
1.14	Amplitude of the eruption versus t_2 for novae	27
1.15	Distances derived from GAIA DR2 vs MMRD distances. Figure from Della Valle & Izzo (2020)	28
1.16	Equivalent width and FWHM	29
1.17	V-band light curves of post-novae	32
1.18	Transmission curves for Johnson-Cousins, Sloan <i>griz</i> broad-band filters and narrow- band filters from SOAR telescope	33
1.19	Sample of post-novae erupted before 1986 at the start of the project	33
2.1	$rH\alpha SII$ colour-colour diagram	42
2.2	$UBVR$ colour-colour diagram	43
2.3	$VH\alpha SII$ colour-colour diagram	44
2.4	Spectra of recovered post-novae published in Tappert et al. (2016)	46
2.5	Spectra of recovered post-novae in this work	47

2.6	Spectrum of the likely recurrent nova KY Sgr	51
2.7	H α profiles for individual spectra of EL Aql, V606 Aql V1583 Sgr and V3964 Sgr	54
2.8	Close-up on selected wavelength ranges in the spectrum of the eclipsing V825 Sco	56
2.9	Spectra of the previously known post-novae	59
2.10	Close-up on the H α emission line for those novae seen apparently at high inclination: V726 Sgr and LW Ser	60
2.11	Equivalent width of the main emission lines seen in old novae versus time since the eruption.	72
2.12	FWHM for H α and H β emission lines versus time since the eruption for old novae and amplitude	73
2.13	Equivalent width of the main emission lines seen in old novae versus the amplitude of the eruption.	74
2.14	Amplitude versus t_3	76
2.15	Spectra for those candidates found via colour-colour diagram which turned out to not be the post-novae	84
2.16	Spectra for selected candidates considered as the old nova counterpat by Mróz et al. (2015) which turned out not to be the post-novae	85
3.1	Phased light curves for RS Car and V365 Car	93
3.2	X Cir light curves from the du Pont telescope	96
3.3	Phased light curve for IL Nor and Periodogram of the photometric data	98
3.4	Phased light curve for DY Pup	100
3.5	Phased light curve for V363 Sgr and its periodogram	101
3.6	Phase light curves of V2572 Sgr and its periodogram	103
3.7	Photometric phased light curve and radial velocity for XX Tau	107
3.8	Phased light curve and radial velocity for CQ Vel	108
3.9	Phase-folded radial velocities of RW UMi and its periodogram	110
3.10	The current orbital period distribution of the novae on logarithmic scale	114
3.11	Orbital period distribution of the observed post-nova systems compared with the simulation assuming the empirical consequential AML model and the classical con- sequential AML model	116
3.12	Normalised average spectrum for V2572 Sgr, RW UMi, CQ Vel and XX Tau	120
3.13	The CTIO light curve of X Cir	121
3.14	The CTIO light curves of V2572 Sgr	121
3.15	V-band light curves of IL Nor taken in 2015 at du Pont telescope.	122
3.16	V-band Light curves of V2572 Sgr taken with EFOSC2/NTT in May 2012 and with du Pont telescope in May-July 2015	123

3.17	Light curves of XX Tau taken at du Pont telescope	124
3.18	V-band Light curves of CQ Vel taken at du Pont telescope.	125
4.1	Sample of post-novae erupted before 1986 at the beginning of this thesis in 2015 compared to 2021	134

Abstract

The impact of nova eruptions on the long-term evolution of Cataclysmic Variables (CVs) is one of the least understood and intensively discussed topics in the field. A decisive ingredient to improve this would be to establish a large sample of post-novae with known properties. Novae are objects that are well studied in the maximum stage, but after the eruption a significant amount of time on large telescopes is needed to study them, due to them mostly turning into very faint objects.

In order to obtain a significant sample of post-novae, Tappert et al. started a project to enlarge the sample since 2009, called “Life after eruption”. This thesis is the direct continuation of their project, which is based on observations both photometric and spectroscopically using a variety of telescopes located in Chile. The steps to recover post-novae consist of (i) identifying post-nova candidates in the field through color-color diagrams (ii) confirming them through their spectral characteristics and (iii) if possible, obtaining the orbital period through time-series data either photometrically or spectroscopically, with the ultimate goal to obtain a significant and reliable sample in order to update some general aspects of the post-nova population, such as the orbital period distribution and their spectral characteristics.

In this work, we present the spectroscopic confirmation for eleven post-novae. Collecting spectroscopic parameters from the literature including these new data, we present an updated spectral study of the post-novae. With all data from the “Life after eruption” project the observational lack of objects that erupted more than 60 years ago is significant filled. The main result points to there being no correlation between the mass transfer rate and the time since eruption, in good agreement with previous studies. The interpretation that strong equivalent widths would be indicators of low-mass transfer rate is not entirely correct (e.g. [Patterson 1984](#)), because they appear to be indicators of inclination rather than of the mass transfer rate. A more conclusive result for the behavior of the mass transfer can only be obtained with a larger sample of novae erupted especially more than 100 years ago.

We also present an updated orbital period distribution of novae using the new orbital periods found here, identifying the false-claims ones in the literature and stated reasons why they are not reliable. We compare the observational data with a theoretical period distribution calculated using both an empirical and the classical recipe for angular momentum loss. We find that neither model reproduces the observed peak in the 3 – 4 h range, suggesting that the prescription for magnetic braking usually used in CV evolution above the period gap is not totally understood.

Chapter 1

Introduction

1.1 Motivation

All stars experience variations during their life. Although in most stars those variations are barely perceptible, there are several types of stars with strong and continuous variations with relatively short time-scales, which makes it possible to observe complete cycles of that change on human time-scales.

One type of these stars are the Cataclysmic Variables stars (CVs). They are constantly showing brightness variations over a wide range of time-scales, from seconds to decades, irregularly changing their brightness by several magnitudes, declining to quiescence states and repeating cycles of brightness variations. The main reason for these variations is the presence of an accretion disc. The discs are a common configuration in the universe, because they appear both on stellar scales and on extragalactic scales, either in binary stars or in stellar and planet formation or in the active nucleus of galaxies. The study of CVs is very important, because the disc is developing on relatively short-time scales, allowing to study its dynamics in more detail than in any other object.

An event that is observed in these objects, when the pressure of the accreted material from the secondary triggers a thermonuclear explosion on the surface layer of the WD, is known as a nova eruption. Currently, the models propose that all CVs experience a nova eruption at least once in their life. Nevertheless, the impact of nova eruptions on CVs is not well understood. For this purpose, population studies of post-novae would provide observational information on the importance of certain properties.

Several questions still remain open. Do all CVs experience nova eruptions? What happens next? Do high-mass transfer rate CVs become novae or post-nova CVs become high mass transfer systems? Do post-novae decline into a hibernation state? To answer these questions a systematic study of the post-novae is required. However, this needs samples of statistically significant size, and the number of identified and studied post-novae is still too small. The goal of this thesis is

to increase the number of post-novae from data based on optical spectroscopy and photometry to perform statistical studies and to try to address these questions.

1.2 Geometry of interacting binary stars

Stars are found as multiple systems, the most common ones being those composed by two stars, called binary stars. In these, the more massive star is called primary and its companion is called secondary. The distance between the components in relation with their sizes and their masses defines the interaction of the system, where concepts like Lagrange points, Roche Lobe and mass transfer are important to understand the physics governing the system. Although we will not delve deeply into these topics, because they are beyond the scope of this thesis, a brief description of these concepts will be made.

Lagrange points are zones where the forces equilibrium is achieved. In these points, denoted by L_1 , L_2 , L_3 , L_4 y L_5 (Fig. 1.1 left), a small object could remain in a stationary state without the need for further corrections (e.g. as is the case of the recently launched space telescope James Webb to the Sun-Earth L_2 , Gardner et al. 2006). The equipotential surface enveloping both stars and crossing the L_1 point is the Roche lobe for these stars. The size of the lobe depends directly on the masses. Its characteristic eight shape is due to the gravitational forces of both components and the Coriolis acceleration caused by the rotation around the center of mass. Based on the relation of both components with the Roche lobe, binary stars are classified in three groups: (i) Detached binaries: Each component is inside its Roche lobe, thus they are affected mainly by the influence of their own gravity, so that each star evolves independently. (ii) Contact binaries: Each star has filled its Roche lobe and their stellar atmospheres form a common envelope around them. (iii) Semidetached binaries: One star fills its Roche lobe to such an extent that the material in its atmosphere can escape through L_1 point, transferring mass towards the primary star, and possibly forming an accretion disc around the primary in non-magnetic binaries.

Novae are events that occur in Cataclysmic variable stars, which are semidetached binaries. The following briefly details the main characteristics of these systems.

1.3 The Cataclysmic Variable stars' world

In most stars, large-scale changes occur so slowly that it is not possible to perceive significant changes in a human lifetime. However, there are stars which have relatively short dynamical time-scales, making it possible to observe continuous and unpredictable variations within a short period of time. Among such stars are the cataclysmic variables (CVs). They can change their brightness on all time scales, from seconds up to decades, increasing irregularly in brightness by a large factor, then drop back down to a quiescent state.

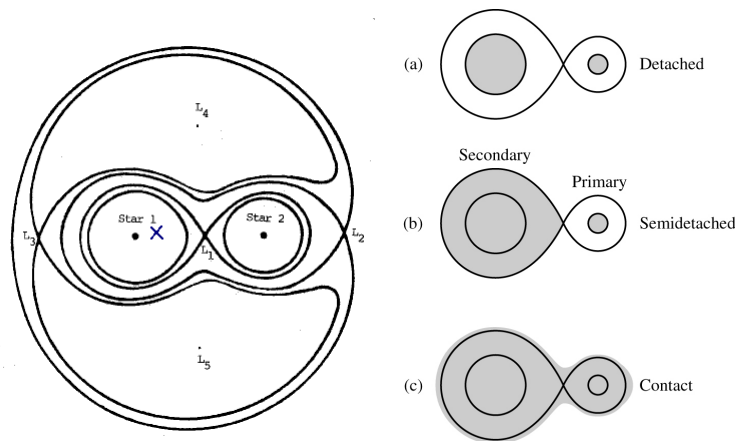


Figure 1.1: Left: Equipotential surfaces in a binary system. *star 1* represents the primary star, *star 2* the secondary and \times is the center of mass of the system. L_x are the Lagrange points where the forces are cancelled out. Right: Binary stars classification (a) Detached system: Stars do not fill their Roche lobe, evolving independently. (b) Semidetached system: The secondary star fills its Roche lobe, reaching the point L_1 , generating mass transfer to primary. (c) Contact binaries. Both components have filled their lobes and their stellar atmospheres form a common envelope around them (figures taken from [Carroll & Ostlie 2006](#)).

In the nineteen-sixties, [Kraft \(1962\)](#) was the first to establish that CVs are pairs of stars, orbiting so closely that stellar material flows between them. Currently, we know that it is a system of two stellar components; a white dwarf primary (WD) and a mass transferring secondary, generally a red dwarf rather like our Sun, but redder and less massive. The stars are so close to each other that the combination of all the forces that form the Roche potential, among them, the gravity of the white dwarf, distort the secondary, and the white dwarf accretes matter from the companion. Therefore, the secondary is often referred to as the donor star. The infalling matter, which is usually rich in hydrogen, forms an accretion disc around the white dwarf as long as its magnetic field is weak ($B < 10$ MG). In CVs with stronger magnetic WDs, the flow of material is confined to follow the lines of its magnetic field ([Warner 1995](#)).

The primary is a white dwarf, the depleted core of a star of low to intermediate mass (initial mass below $9 M_{\odot}$) on the MS in the final stage of its life. They are very compact objects with the mass of the Sun in the volume of the Earth. Given the high density, in the Fermi gas, the electrons are confined to small regions, however, the Pauli exclusion principle prevents electrons to have the same quantic number, generating a force by the degenerate electron pressure which is in opposition to the gravitational force. These compact objects can not be more massive than $M \approx 1.44 M_{\odot}$ ([Chandrasekhar 1931](#)), which is the mass limit to keep the hydrostatic equilibrium between the degenerate electron pressure force and the gravitational force. Contrary to main-sequence stars, more massive WDs are smaller than less massive ones.

The range of observed WD masses of CVs is $0.6 - 1.2 M_{\odot}$ with a calculated average $M_{\text{wd}} = 0.83 \pm 0.23 M_{\odot}$ which is larger than the mean mass of single WDs ([Zorotovic et al. 2011](#)). Depending on the initial mass of the WD in the binary system, two paths can be expected:

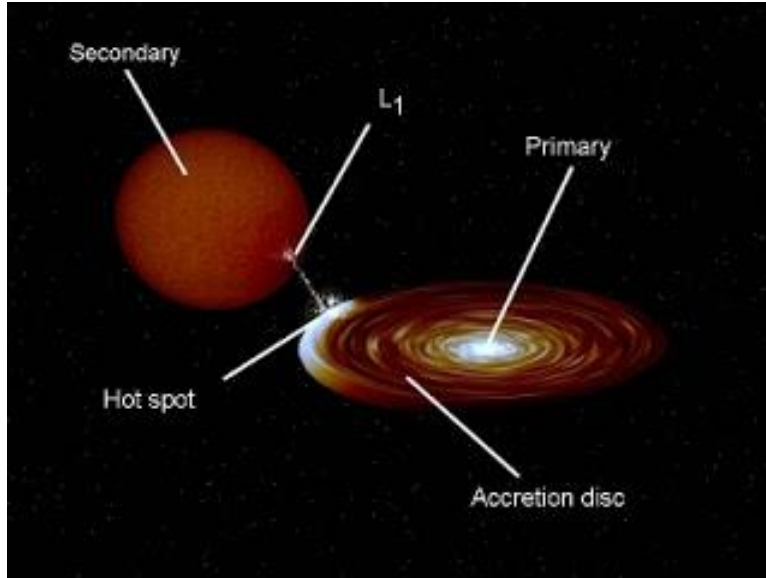


Figure 1.2: Artistic representation of a CV. The secondary fills its Roche lobe, transferring material through the L_1 point to the primary, via an accretion disc. The impact point of the material on the disc is known as the bright spot (Hellier 2001).

If the WD mass is close to Chandrasekhar’s limit, the accreted material triggers an ignition in a degenerated medium, causing a Supernova Ia explosion.

If the mass of the WD is well below the critical limit, the accumulated gas on the WD increases its surface temperature. Because the degenerated gas is not ruled by the ideal gas laws, the temperature rises triggering a thermonuclear runaway in the surface layers of the WD, causing a nova eruption. This event is described in more detail in section 1.6.

1.3.1 Mass transfer mechanism

In the course of the evolution of the binary system, one of the stars may increase its radius, allowing it to have contact with the Roche lobe. When the surface of the star reaches the L_1 point, its material is affected by the gravitational force of the other star, expanding its atmosphere toward the companion’s Roche lobe, inducing mass transfer. In a binary system, the relation between the masses M_1 and M_2 and the distance r between them is given by Kepler’s third law,

$$P^2 = \frac{4\pi^2}{G(M_1 + M_2)} r^3, \quad (1.1)$$

where P is the orbital period and G the gravitational constant. Then, the mass transfer (\dot{M}) is regulated by the separation between the components, the orbital period and the mass ratio q :

$$q = \frac{M_2}{M_1} \quad (1.2)$$

where M_1 is the mass of the primary and M_2 is the mass of the secondary. For stable and continuous mass transfer, the donor must be in constant contact with its Roche lobe. This condition is maintained through angular momentum (J) loss. For CVs, the orbital J is expressed as:

$$J = M_1 a_1 \frac{2\pi a_1}{P_{orb}} + M_2 a_2 \frac{2\pi a_2}{P_{orb}}. \quad (1.3)$$

Establishing $M = M_1 + M_2$ as the total mass of the binary system and $a = a_1 + a_2$ as the separation between the components, Eq. 1.3 becomes:

$$J = M_1 M_2 \sqrt{\frac{Ga}{M}}. \quad (1.4)$$

A logarithmic differentiation of Eq. 1.4 gives the relationship that conducts the mass-transfer mechanism on CVs:

$$\frac{\dot{J}}{J} = \frac{\dot{M}_1}{M_1} + \frac{\dot{M}_2}{M_2} + \frac{\dot{a}}{2a} - \frac{\dot{M}}{2M}. \quad (1.5)$$

Assuming that the mass lost by the secondary is accreted on the primary, i.e., $-\dot{M}_2 = \dot{M}_1$, then the total mass is conserved ($\dot{M} = 0$). Rearranging and substituting these terms in Eq. 1.5 yields:

$$\frac{\dot{a}}{a} = 2\frac{\dot{J}}{J} - 2\frac{\dot{M}_2}{M_2}(1 - q). \quad (1.6)$$

When the angular momentum is conserved, i.e., $\dot{J} = 0$, and because $\dot{M}_2 < 0$, this equation reveals that the mass transferred from the less massive star to the more massive one generates an increase of the binary separation (a), when $M_2 < M_1$.

The response of the Roche lobe radius to the mass transfer is given by the equation:

$$\frac{\dot{R}_L}{R_L} = 2\frac{\dot{J}}{J} - 2\frac{\dot{M}_2}{M_2} \left(\frac{5}{6} - q \right). \quad (1.7)$$

In consequence, Eq. 1.7 indicates that the variation of the Roche lobe size is a function of the mass ratio q . In the case of the angular momentum being conserved ($\dot{J} = 0$), the Roche lobe radius increases if $q < 5/6$ (based on Knigge et al. 2011a).

In systems with a low-mass secondary, the characteristic \dot{M} average is $\sim 10^{-9}$ - $10^{-10} M_\odot$ / yr, for systems with $P_{orb} < 2$ hr is $\sim 10^{-10} M_\odot$ / yr, for $P_{orb} > 3$ hr is about 10^{-8} to $10^{-9} M_\odot$ /yr (Warner 1995; Frank et al. 1992).

1.3.2 Accretion discs

The flow of matter out of L_1 must reduce its angular momentum to the value that the material has in orbits closer to the WD. The gas follows a trajectory determined by the gravitational influence of the primary, passing close to the WD, spiraling around it. The material is turbulent until it manages to settle into the type of orbit that requires the lowest energy: a circular orbit. From Kepler's laws, gas orbiting near the WD has a large kinetic energy, which generates friction with gas farther away. Turbulence and friction heat the gas, so that energy is extracted in the form of outward radiation, but, by the conservation of angular momentum, the gas must also move into farther orbits. Thus, the ring expands to form a thin disc, called an accretion disc. The disc continues to expand-out and inwards, ultimately allowing the WD to accrete the material. Angular momentum is transported outward from the disc, allowing gas to flow into the disc, releasing energy. At the outer edge of the disc the tidal forces of the secondary interact with the disc, absorbing the angular momentum and returning it to the orbit of the donor. This is the disc boundary.

The Keplerian rotation law implies differential rotation. Thus, the accretion disc can be represented as a set of concentric gas rings moving with different angular velocity expressed as:

$$\Omega_{Kep}(r) = \left(\frac{GM}{r^3} \right)^{1/2} \quad (1.8)$$

where r is the distance from each ring to the WD. Since the gas near the primary rotates faster than gas in outermost orbits, the viscous characteristic of the disc plasma will represent a tendency to decrease the velocity difference between two adjacent gas rings, i.e., ultimately try to force them into corotation. Thus, the viscosity causes angular momentum to flow to the outer parts of the disc. The differential rotation of a Keplerian disc is seen as a double-peaked emission line profile in the spectrum with the peaks being displaced from the central wavelength λ by the value of the radial velocity of the last zone emitting to that value and the separation between the double peaks reduced due to the inclination of the system (see Fig. 1.3). The core of the line originates in the zone along the line of sight which has a large area around zero radial velocity and the line wings come from the innermost regions of the disc where the velocities are higher than the outer ones but the area is smaller, contributing less flux than the outer regions (Horne & Marsh 1986).

1.3.3 Type of outbursts on CVs

Although viscosity is fundamental to understand the behavior of the disc, knowledge of its physics is still incomplete. Shakura & Sunyaev (1973) proposed that turbulent gas must generate eddies smaller than the vertical height of the disc, so viscosity would be a function of height, the speed of sound in the gas, and a parameter that is associated with the degree of viscosity.

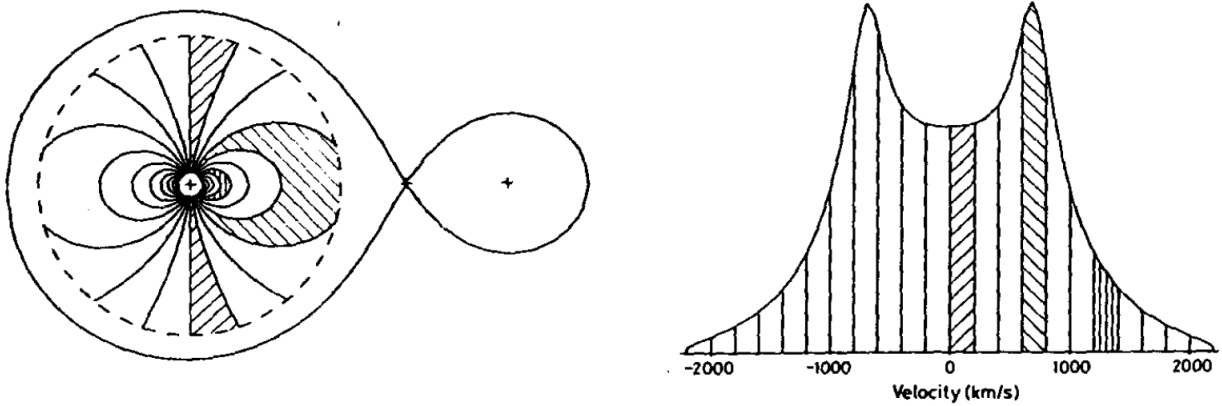


Figure 1.3: Representation of a Keplerian disc and its velocity profile of emission lines. The line of sight of the observer is below the left plot. The disc is seen edge-on for a system with $q=0.15$. The different shadings in the velocity bins match the shading areas in the left diagram. Figure from [Horne & Marsh \(1986\)](#).

[Osaki \(1974\)](#) suggested that if the mass transferred from the secondary is constant, and if this rate is higher than what can be transported by viscosity in the disc, the disc becomes unstable. Subsequently, [Hoshi \(1979\)](#) and [Meyer & Meyer-Hofmeister \(1981\)](#) discovered the physical mechanism governing the stability of the disc, showing that viscosity controls temperature levels, causing the disc to become thermally unstable when hydrogen is partially ionized. To understand the mechanism we must consider the following: The material flowing through the disc is the product of viscosity and surface density Σ (mass per unit area). The mass flow also determines the energy released in the form of radiation, further establishing the surface temperature of the disc.

If the viscosity is high in any area of the disc, the radiated energy is also high, implying a rise in surface temperature. If this rise is small, this could increase the turbulence of the gas, increasing the viscosity, which causes the material to flow inward, emptying that region. The low density of that region decreases the viscous heating, so the disc temperature drops to its normal value, allowing the region to fill again. This is the scenario in a steady state situation. Now, if the accretion rate is very high in a region of the disc, the viscous heating will be very large as the density in that region increases. As a consequence, the temperature rises enormously, producing a high rate of released radiation. When the hydrogen in the disc is heated to more than ~ 7000 K the gas is partially ionized, which leads to the charged H^- particles absorbing the released radiation (the increase in H^- particles increases the opacity, i.e. the ability to obstruct the passage of radiation), which generates a further increase in temperature, and as a consequence an increase in the ionization of the gas, causing a large opacity. This again yields an increase of the viscosity, causing the material to flow inward, emptying that region. The low density reduces the heating due to viscosity, however, this reduction is compensated by the opacity that absorbs the radiation. Thus, the temperature continues to increase until the hydrogen is completely ionized. At this

stage the opacity is not temperature sensitive; the disc is in an equilibrium state but at very high temperature compared to the quiescent state.

However, in this high-viscosity state, the gas flowing inward exceeds that flowing in from the mass stream transferred from the secondary. The disc cannot sustain this state, so it must return to an equilibrium state, returning to its initial condition. This whole cycle corresponds to the model of thermal instability in the disc (Osaki 1974; Cannizzo & Kaitchuck 1992; Lasota 2001). This cycle can be visualized in a graph that relates the density of the surface disc with its surface temperature. This curve is called the “S-curve” (Figure 1.4) and shows the thermal equilibrium states of the disc. The mass transfer rate from the secondary and the orbital period are the most determining factors in the disc behavior. The former because it is related to the viscosity and the latter because of its connection with the size of the Roche lobe and thus, the space disc the disc has to spread out. Osaki (1996) suggested a critical mass value of \dot{M} that divides discs into stable and unstable ones.

$$\dot{M}_{\text{crit}} \simeq 2.7 \times 10^{17} \text{ g s}^{-1} (P_{\text{orb}}/4 \text{ hr})^{1.7} \quad (1.9)$$

Above this value the discs are stable and hot. This type of CV is called nova-like. Below this value, discs are thermally unstable, and produce **outbursts** in dwarf novae. An outburst is a rise in brightness due to the disc instability.

If the mass transfer rate is high and the separation between the components is small, the disc during a **superoutburst** becomes large enough to reach the resonance point where it is affected by the tidal force of the secondary, deforming it to an eccentric shape. The increase in brightness due to the elongated disc is known as a **superoutburst** (based on chapter 5, Hellier 2001).

A totally different type of outburst is produced when the material accreted on the WD surface triggers a thermonuclear eruption on its surface layer, called a **nova eruption**. Magnetic or non-magnetic systems that underwent a nova eruption are called **classical novae** (CNe). Because this thesis is focused on these objects, an extensive review of them is found in section 1.6.

1.4 CV classification

CVs are classified based on the WD’s magnetic field strength. Two big groups are distinguished: magnetic and non-magnetic CVs.

Magnetic CVs. The magnetic field of the WDs prevents the formation of an accretion disc either partially or fully. In this group polars and intermediate polars are found.

- **Intermediate Polars (IPs)** or DQ Her type stars. They have primaries with medium-low magnetic fields, where the magnetosphere truncates the accretion disc in its inner part. In these systems it is also possible to detect the WD’s spin period (P_{spin}) which is asynchronous

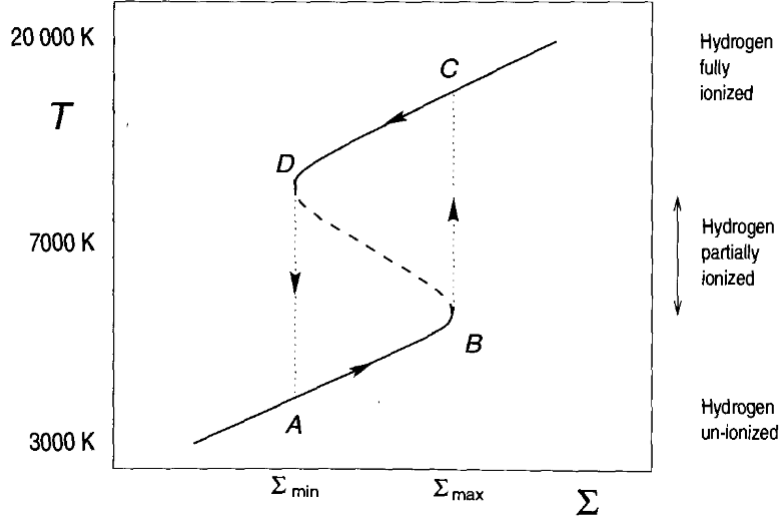


Figure 1.4: Schematic representation of the S curve, which shows the thermal equilibrium states of the disc. The x-axis corresponds to the surface mass density (mass per unit disc). The y-axis corresponds to the surface temperature of the disc. In the upper part of the curve, the disc consists of fully ionized hydrogen, reaching an equilibrium state at high temperature. The lower curve shows the disc in a cold, low viscosity state. At point B ionization occurs, increasing the opacity of the disc, causing an increase in temperature. Figure from [Hellier \(2001\)](#).

to the orbital period (P_{orb}), with typical $P_{\text{spin}} \sim 1000$ sec for IPs and $P_{\text{spin}} \sim 50$ secs for the faster rotator DQ Her types.

- **Polars** or AM Her type stars. The accretion flow follows the magnetic lines of the WD, accreting onto the magnetic poles. In most polars P_{spin} is synchronized with P_{orb} .

Non-magnetic CVs The strength of the WD’s magnetic field is too low to affect the incoming material, thus the accretion stream forms an accretion disc around the WD. We distinguish the following types:

- **Dwarf novae (DNe)**. Eruptive variables showing periodic outbursts that typically last from 2 to 20 days, with recurrence times of 20 to 300 days reaching amplitudes in the range of 2 to 6 magnitudes. All of them have unstable discs with relatively low mass transfer rates. There are several DN sub-types depending on whether or not they have superoutbursts: (i) *U Gem*, presenting normal disc outbursts; (ii) *SU UMa*, DNe showing outbursts, superoutbursts and humps that do not match the orbital period, called superhumps. (iii) *Z Cam stars*, a small subgroup of DNe exhibiting irregular “standstills” seen to a constant value in magnitude in the light curve ([de Roy 1932](#)), and (iv) *WZ Sge stars*, those with very low mass-transfer and experiencing only superoutbursts, for which it takes decades to accumulate material for the next superoutburst. The absence of normal outbursts between superoutbursts could be

attributed to a disrupted accretion disc in the inner part by the WD magnetosphere (Lasota et al. 1999).

- **Nova-likes (NL)**. CVs with such high-mass transfer rates to keep the disc in an stable hot state, implying that they are in a continuous outburst state, occasionally declining into low states, possible a consequence of a (short-lived) decrease in the accretion rate. Most of them have orbital periods between 3 to 5 hrs just above the period gap (Catalogue of CVs, Ritter & Kolb 2003a).

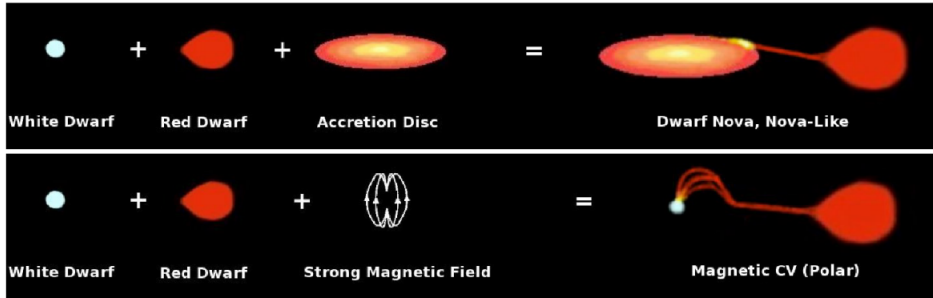


Figure 1.5: Schematic representation of the CV types. Top: Non-magnetic CVs. Bottom: Magnetic systems. Figure by Tappert (private communication).

1.5 CV evolution

1.5.1 Angular-momentum loss mechanisms in CVs

In order to maintain stable and continuous mass transfer from the secondary to the WD, angular momentum loss (AML) is required to keep the secondary in contact with its Roche Lobe. Theoretically, two mechanisms allow AML: Gravitational radiation (GR) and Magnetic braking (MB).

Two stars rotating around their common center-of-mass generate a periodic deformation of the space, according to the general relativity theory, creating gravitational waves known as **gravitational radiation**. The closer and more massive the two stars are, the higher the orbital velocity and consequently also the gravitational radiation. All binary stars lose angular momentum via GR, but for systems with short orbital period the GR effect becomes stronger, if the masses involved are similar.

On the other hand, at larger periods AML is predominantly carried out by the interaction between the stellar wind of the secondary with its surface magnetic field, which is generated by a dynamo effect produced by the circular motions of gas bubbles within the convective envelope (e.g. Schatzman 1962). The stellar rotation of the secondary is tied to the orbital motion due

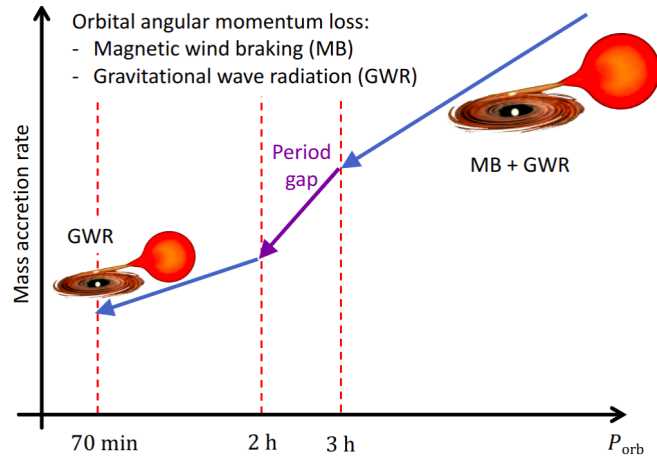


Figure 1.6: CV evolution in terms of the orbital period. CVs evolve from longer periods to shorter ones. Magnetic braking is the main AML mechanism for systems with longer periods. At shorter periods AML is driven by gravitational radiation. Figure from [Pala \(2019\)](#).

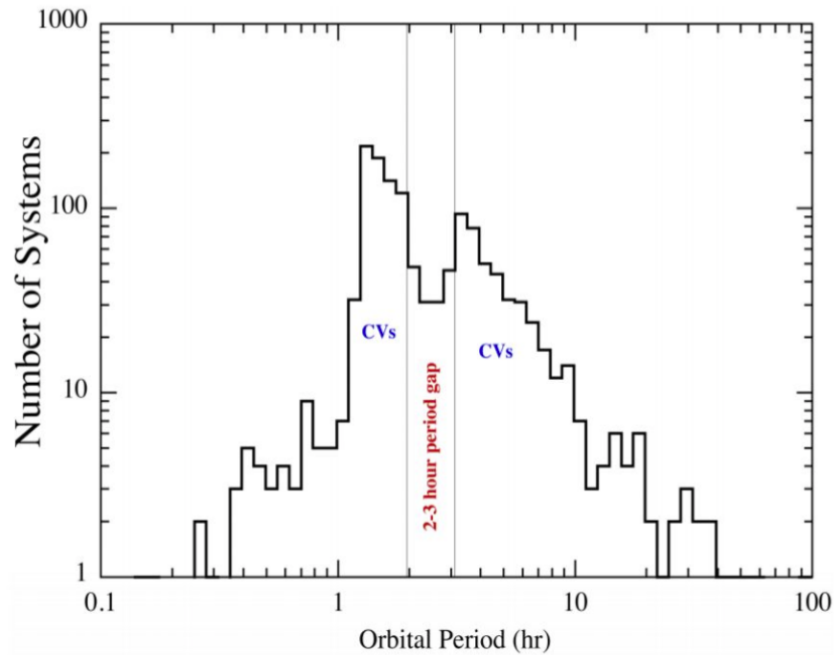


Figure 1.7: Orbital period distribution of non-magnetic CVs from [Ritter & Kolb \(2003a, version 7.11, black line\)](#).

to the tidal force, implying a faster rotation compared to isolated low-mass-main-sequence stars, which give rises to a stronger magnetic field compared to single stars. The particles of the stellar wind are forced to follow the magnetic field lines and then to co-rotate with the secondary. These outflowing particles are accelerated and released into space, carrying out a significant amount of angular momentum and as a consequence, braking the rotation of the secondary. This mechanism is known as **magnetic braking** (MB).

1.5.2 Other AML mechanisms

Additional AML mechanisms have been proposed in order to reproduce the observed CV orbital period distribution. An AML mechanism caused by the mass transfer process itself must be considered in the CV evolution, called consequential AML (CAML) (Webbink 1985; King & Kolb 1995). Different CAML origins have been proposed, the most developed model is the one that considers the effects of the interaction of the nova eruption with the secondary, which would enhance the mass-transfer rate driven by AML by magnetic braking (Schenker et al. 1998). Nevertheless, CAML models fail to reproduce the CV orbital period distribution. A new model has been proposed by Schreiber et al. (2016) considering the same scenario, but increasing CAML with decreasing WD mass. This model called empirical CAML (eCAML), has successfully reproduced both the observed CV orbital distribution, the WD distribution and space density of CVs. However, the insufficient theoretical and observational knowledge of the effects of the nova eruption in the CV evolution does not allow to conclude with certainty about the real origin of CAML and how it influences on the CV evolution.

1.5.3 The orbital period distribution of CVs

For non-magnetic CVs, the standard model of evolution indicates that they are supposed to evolve from long periods to short ones due to AML via GR and MB (see Fig. 1.6). At $P_{\text{orb}} \gtrsim 3$ h they are high mass transfer systems with AML mainly driven by MB and at $P_{\text{orb}} \lesssim 2$ h they have low mass transfer rates with AML regulated by GR (Rappaport et al. 1982; Knigge et al. 2011a).

The period gap. Between $2 \text{ h} \lesssim P_{\text{orb}} \lesssim 3 \text{ h}$ a drastic drop in numbers is observed in that range, the so-called period gap. According to the models, the mass transfer drives the secondary out of the thermal equilibrium due to the Kelvin-Helmholtz timescale being longer than the transfer timescale. The star becomes fully convective at $P_{\text{orb}} \approx 3$ h (Spruit & Ritter 1983) and as a result MB turns off or becomes less effective, allowing the mass transfer to decrease and therefore, the donor can relax to reduce its radius, losing contact with its Roche lobe and in consequence, the CV becomes a non-interacting detached system. In this state, AML is driven by GR and at $P_{\text{orb}} \approx 2$ h the mass transfer is restored, because the Roche lobe has shrunk sufficiently to re-establish contact with the secondary. This scenario was proposed by Rappaport et al. (1983a) and it is known as dis-

rupted magnetic braking (DMB), which is supported by strong observational evidence (Schreiber et al. 2010; Zorotovic et al. 2016a). The current edges of the gap (2.15 h and 3.18 h) were calculated by Knigge (2006).

Period minimum (P_{\min}). Each phase in the CV evolution is regulated by the mass loss from the secondary. When the sub-stellar mass limit is reached, the donor becomes partially degenerate. Because the donor is still transferring mass, but now as a degenerated star, when the thermal equilibrium is broken the donor responds by expanding instead decreasing. As a consequence, the binary orbit is expanded in order to adapt to the new size of the donor star, making the systems that have reached P_{\min} evolve now towards longer periods. CVs that evolve in this way are called **period bouncers**. The theoretical standard model predicts a period minimum at $P_{\min} \simeq 65$ min, however it is considerably shorter than the observed one. Knigge (2006) established $P_{\min} \simeq 75$ min based on the orbital period distribution of the available CV sample in 2006. Similarly, Gänsicke et al. (2009a) found an even greater value at $P_{\min} \simeq 82$ min based on the Sloan Digital Sky Survey (SDSS) CV sample. Given these discrepancies, the current period minimum is assumed to be $P_{\min} \simeq 80$ min.

The long-period cut off. For the steady mass-transfer the condition that the donor needs to be the less massive component implies that the secondary can not be more massive than the Chandrasekhar limit ($\sim 1.44M_{\odot}$) of the WD. As a consequence, assuming the maximum limit when $M_1 = M_2 = 1.44M_{\odot}$, calculations indicate that the maximum period should be ~ 12 h. Nevertheless, massive WD are not frequent, therefore the long-period cut off of CVs is established at $P_{\text{orb}} \simeq 6$ h (Hellier 2001). Longer-period CVs include an evolved secondary star, which is expanded enough to fill its Roche lobe. This star will continue to expand and the system will continue to evolve to longer periods. In this period range several interesting objects are found, such as the symbiotic novae, which are usually not in contact, but material is accreted via the stellar wind of the secondary.

Even though the standard CV evolution model fits well for the period minimum and the period gap theory, there are several observational disagreements related to the properties of the Galactic population in CVs. On the one hand, the predicted population below the gap is $\simeq 99$ per cent and above $\simeq 1$ per cent (e.g. Howell et al. 2001a), considering classical AML models. However, compared to the observational one, which is limited by magnitude (due to being biased towards brighter and long-period CVs), it is quite contradictory: $\simeq 77$ per cent below and $\simeq 23$ above the gap (Gänsicke et al. 2009a). Furthermore, the predicted period bouncers population fluctuates between $\simeq 40 - 70$ per cent of present-day Galactic CV population (Goliash & Nelson 2015). This is in contrast with the recent observational studies, which suggest that the fraction is very low ($\simeq 7$ per cent, Pala et al. 2020). Therefore, several disagreements point to the CV evolution still not

being completely understood.

1.5.4 The hibernation model

The standard model of CV evolution predicts that \dot{M} should essentially depend on the orbital period, however, CVs are found in a wide range of accretion rates at a particular orbital period. In this way, the nova event may be the cause of this non-uniform \dot{M} distribution for CVs. From an analysis of the nova population in which an apparent difference about two order of magnitudes was found between the expected nova spatial density from surveys in the Galactic neighborhood compared to the deduced density in the M31 galaxy, a model was proposed that would explain the effect of the nova on the CV evolution, the so-called “Hibernation scenario” (Shara et al. 1986). This model proposes that the spatial density of galactic novae is in fact higher than observed, but that novae would spend most of the time in a long hibernation stage between two successive eruptions. The mass loss during the eruption leads to an increase in the orbital separation, as a consequence of the conservation of the angular momentum after the eruption. The post-eruption heated WD irradiates the secondary, inducing an enhanced mass transfer rate that gradually decreases as the WD cools down. The mass transfer rate drops to the order of $10^{-10} - 10^{-12} M_{\odot}/\text{yr}$ to the point to lead to a detachment of the secondary star from its Roche lobe, thus stopping the transfer of material, and the system entering “hibernation”. The typical mass transfer rate $10^{-8} - 10^{-9} M_{\odot}/\text{yr}$ is expected to be recovered once either magnetic braking or gravitational radiation has decreased the separation between the binary components. As a consequence, all post-novae should appear as high \dot{M} CVs (so-called nova-likes) during the decades or centuries following an eruption, then undergo a gradual transition into a low- \dot{M} state and a dwarf-nova behaviour. As of yet, there is no clear evidence in favour of or against this scenario.

Shara et al. (2007, 2012a) has discovered nova shells around the dwarf novae Z Cam and AT Cnc, evidencing that some dwarf novae must have had nova eruptions a long time ago. The discovery of the former dwarf nova V1213 Cen appearing to transition to a brighter state with a stable, high-luminosity disc after the nova eruption is in good agreement with what is predicted by hibernation (Mróz et al. 2016). However, it should be noted that the last observations of that study, about seven years after the eruption, still show the system in decline from the eruption with a significant slope > 0.1 mag/yr, so it may well be that the object on a comparatively short time-scale returns to its dwarf-nova state. This would be similar to the case of V446 Her, that was found to show dwarf-nova-like variability already about 30 years after the nova eruption (Honeycutt et al. 2011b). In a study of pre and post-nova brightness of 30 novae, Collazzi et al. (2009) found that, while some objects present an increased luminosity after the eruption, most do not. Furthermore, Weight et al. (1994) found that \dot{M} did not decline for at least 140 yr after the eruption contrary to what the hibernation model predicts. A study of the long-term behaviour of post-novae (Vogt

et al. 2018) also concluded that any decrease in \dot{M} must be at much longer time scales than ~ 200 yr. Recently, Hillman et al. (2020) reported simulations of the multi-Gyr evolution of CVs, which demonstrated that the hibernation in fact occurs, but only for systems with a short orbital period, also reproducing the observed range of \dot{M} at a specific orbital period.

An alternative explanation for the luminous accretion discs in post novae was given by Schreiber et al. (2000). There, the ionized state of the disc is caused by the WD irradiating the accretion disc, and not by an increased \dot{M} from the secondary star. Depending on the size of the affected area in the disc, this would leave some outer parts in the disc in a non-ionized state, thus explaining the so-called stunted outbursts observed in some post-novae (e.g. Honeycutt et al. 1998). Tappert et al. (2013a) indeed found evidence for the presence of an optically thick inner disc in one such object. In the same line, Schreiber & Gänsicke (2001) concluded that the irradiated disc by the hot post-erupted WD plays a crucial role in the evolution of post-novae, with the decline in brightness being a direct consequence of the decrease of irradiation of the disc due to the cooling of the WD rather than an effect of a decrease in \dot{M} as was interpreted by Duerbeck (1992).

1.6 Optical properties of Novae

A nova is an eruption that occurs in CVs both in magnetic or non-magnetic systems. CVs in which a nova eruption has been observed are called classical novae (CN) or post-novae. The eruption is characterised as sudden increase in brightness reaching a typical amplitude range between 8 to 16 mag. The duration of the maximum brightness depends on the speed class, gradually fades to its normal magnitude in a span of months to years. An example of one light curve evidencing the rise to eruption is shown in Fig. 1.8. They are classified according to the brightness decay rate in the light curve. That classification will be explained in section 1.6.6.

1.6.1 The nova eruption: The Thermonuclear Runaway

The hydrogen-rich gas accumulated onto the WD gradually creates a layer which is compressed and heated by the strong gravitational field of the primary, to the point of turning into an electron-degenerated layer. The amount of accreted material necessary to trigger a thermonuclear runaway (TNR) has been calculated by multiple hydrodynamic simulations, which have shown that the required amount depends mainly on the WD size and mass, its luminosity and chemical composition, being of the order of $\sim 10^{-6} M_{\odot}$ to $10^{-4} M_{\odot}$ (Townesley & Bildsten 2004). On the other hand, the time to reach the TNR is conditioned if the accreted material is mixing with material from the core, which changes the opacity and metallicity. With more opacity, the heat is more efficiently trapped, thus the conditions for the TNR are reached more quickly, by accreting less material and consequently, ejecting less material in the eruption (Starrfield et al. 1998). In the pro-

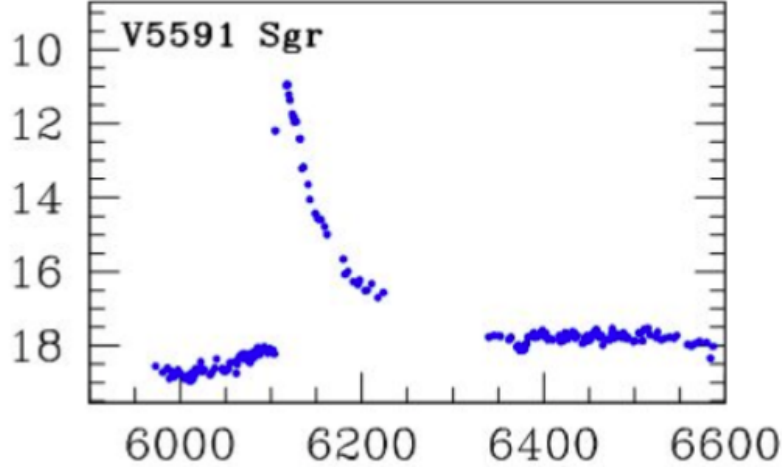


Figure 1.8: Light curve of V5591 Sgr (Nova Sgr 2012c) observed at the moment of the eruption. The x-axis corresponds to Heliocentric Julian day minus 2450000 and the y-axis is the I -band magnitude. Figure from Mróz et al. (2015).

cess of accretion, the closest layer to the WD reaches the temperature to start nuclear reactions of the proton-proton chain type, which becomes the main mechanism of energy production, with a T^4 dependence. Because this material is degenerate, the energy released by the nuclear reactions does not give rise to an expansion and cooling of the gas, but rather the increasing temperature raises the nuclear reaction rate, producing a runaway effect until the suitable temperature for the fusion of the CNO cycle is reached, that is $T \sim 2 \times 10^7$ K. This reaction rate is extremely dependent on the temperature, being proportional to T^{18} , speeding up the runaway effect. The deepest layer is supplied with a large amount of energy that drives convective fluctuations in the layer, transporting Carbon and other elements from the WD to the burning zone, improving the rate of energy production by the CNO cycle (Starrfield et al. 2000). The runaway effect continues until the temperature is high enough to give rise to the gas pressure exceeding the degenerate pressure, thus the degenerated condition is released and the layers start to expand discharging He and the radioactive nuclei created on the WD surface in the CNO phase. The expansion stage occurs on a short time scale ~ 1000 s with very high velocities ~ 3000 km/s. This stage is known as the "fireball" phase, in which the optical light curve rises and the expansion is accompanied by mass ejection. Additionally, the abundances of the ejecta can reveal whether the eruption occurred on a CO or O/Ne white dwarf (Gehrz et al. 1998).

1.6.2 The nova shell and the evolution of the spectrum after the eruption

The expelled material by the TNR is quickly mixing with the diffuse circumstellar gas in the interstellar medium (ISM). Considering that the observed rate of Galactic novae is 33 per year (Kemp et al. 2022) and the average of the processed material ejected is $\sim 2 \times 10^{-4} M_{\odot}$, then the

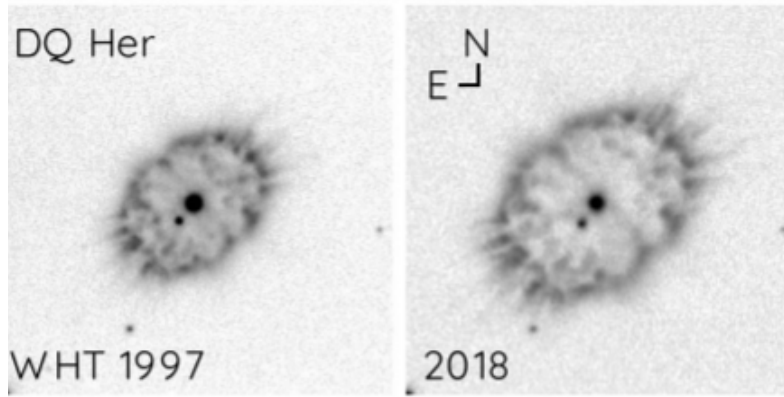


Figure 1.9: $H\alpha$ image for the nova shell surrounding to DQ Her as it was seen in 1997 and 2018. The central star is the nova host that erupted in 1934. Figure adapted from [Santamaría et al. \(2020\)](#).

nova eruptions are responsible for adding $\sim 7 \times 10^{-3} M_{\odot}/\text{yr}$, equivalent to $\sim 0.3\%$ of the total processed material to the ISM ([Gehrz et al. 1998](#)). Although this contribution could be regarded as not very significant, the nova explosion is considered as a crucial donor of ^{13}C , ^{15}N , ^{17}O , ^7Li and other radioactive elements into the ISM ([José & Hernanz 1998](#); [Gehrz et al. 1998](#)) as well as a source of the pre-solar grains found in meteoritic material ([Gehrz et al. 1998](#); [José et al. 2004](#); [Zinner 1998](#)). As such, novae are significant contributors to the Galactic chemical evolution.

The binary is covered by an expanding shell seen as a nebular structure surrounding the CV, which fades over time (see Fig 1.9). Its morphology depends on several factors, like the interaction of the ejected gas with the circumstellar material, but especially of the interaction with the binary companion and the WD rotation. The latter one can deliver angular momentum that can affect the asphericity and geometry of the nova shell ([Livio et al. 1990](#); [Porter et al. 1998](#)). The angular expansion rate allows to calculate the size of the shell knowing the time since the eruption and the expansion speed measured by the Doppler shifts in the spectrum. Comparing the calculated size with the apparent one measured in an $H\alpha$ image, it is possible to deduct the distance to the nova. This method is called the nebular parallax.

The properties of the spectrum throughout the expanding shell process are correlated with the behaviour of the luminosity decline (see 1.6.6) and were extensively described by [McLaughlin \(1960\)](#). Here they are detailed only with respect to the optical spectrum.

The principal spectrum. Around 0.5 mag after maximum, the spectrum is dominated by absorption lines in the initial stage, showing the characteristic outflow profile called P Cyg profile (see Fig 1.10) and the lines are displaced to negative velocities with respect to the pre-maximum. The CNO lines together with the relatively low ionization lines in the optical range are developed, such as Mg I, Mg II, Ca II, neutral iron Fe II and the strongest one, O I. As the brightness declines from the maximum, components of the initial stage start to fade, presenting only emission lines at

the end of the early decline. Forbidden lines [O I], [N II] and [O II] appear in this phase, showing very asymmetric profiles as a consequence of the non-uniform ejection of the material. When the brightness has descended about 2 mag after the maximum, a second stage is developed, called **the diffuse enhanced spectrum**. The absorption lines are very broad and blue-shifted with velocities about twice the value measured in the principal spectrum phase. This stage can last about 10 to 100 days depending on the speed class (Warner 1995; Bode & Evans 2008). When the brightness has decreased by about 2 to 4 mag (depending on the speed class), the next phase is a combination of the principal and the diffuse enhanced spectra, called **the Orion spectrum**, because it resembles the well defined absorption lines originated by stellar winds from OB stars, which present high blue-shift velocities about ~ -2000 km/s. The last phase in this transition stage is the **Nebular spectrum**. As the shell expands and adiabatically cools, the lines developed in the early stage with relatively low ionization as the auroral [O I] and [N II] lines, become stronger and others appear like [O III] and [N III], resembling the spectrum of a planetary nebula, i.e., a spectrum dominated by discrete strong and narrow emission lines emitted by ions and atoms as a consequence of the low density expanding environment where they are produced. If the ionizing radiation reaches $T > 10^6$ K, this phase ends with the presence of coronal lines, i.e forbidden lines of high ionization elements, such as [Fe X] 6347Å and [Fe XIV] 5303Å. The high excitation lines gradually vanish and the post-nova phase presents a spectrum again dominated by the accretion disc emission (see section 1.7).

The dispersion timescale of the nova shell into the ISM can be an important parameter to evaluate the connection between the nova eruption and the CV evolution, mainly described by the hibernation model (more information in section 1.5.4; Shara et al. 1986, 2017a). The timescale is depending on the morphology and the circumstellar density, being ultimately established in scales from decades to a few hundred years (Santamaría et al. 2020).

1.6.3 The recurrence scale of nova eruptions

The mass of the WD is the main factor that determines how much mass is accreted before the nova eruption. Less massive WDs have lower surface gravity, so they need more mass to cause enough pressure to trigger an eruption (Yaron et al. 2005). This parameter determines the speed of the nova, because more massive WDs cause a fast rate of decline after the eruptions and also short nova-cycle recurrence times. Considering the typical mass transfer rate of $\sim 10^{-9} M_{\odot} \text{ yr}^{-1}$, a CV with a $1.3 M_{\odot}$ WD would undergo a eruption every $\sim 10^4$ yr (Shara et al. 2012c; Schmidtobreick et al. 2015), while less massive ones may take about 5 million years. Thus, a nova eruption is a recurrent event on long time scales. Considering that the oldest photographic records of novae date back to the final quarter of the 19th century, the time scale of nova observations is very short compared to the time scale of the nova recurrence, so we have observed only a short range of the

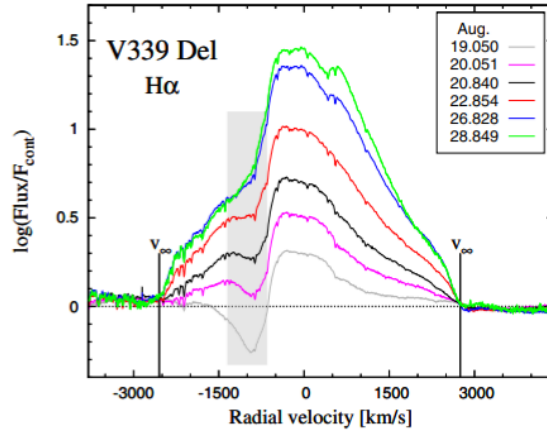


Figure 1.10: $H\alpha$ profile variations taken about one week after the nova eruption reported in 2013 for the nova V339 Del. The grey zone illustrates the position of the blue-shift absorption in the line, known as ‘P Cygni’ features, which are produced because the photons are scattered by the expansion in direction to the observer. The total line profile is a combination of the line emission and the blue-shifted absorption generated by the outflow. Figure from [Skopal et al. \(2014\)](#).

long-time scale of the nova cycle of CVs.

1.6.4 Recurrent novae

Systems that experience more than a nova eruption in a century are called recurrent novae (RNe). They are characterized by being composed of a massive WD and a high accretion rate. These factors determine that they have short recurrence times, on the order of decades to less than a century. Some of the RNe are not typical CVs, since the secondary is a giant or evolving into a giant star, so they have long orbital periods longer than 0.6 days (as in the case of RS Oph), although there are also RNe with short periods (T Pyx, with $P_{\text{orb}}=1.83$ hr, [Uthas et al. 2010](#)). To date, there are only 10 observed galactic RNe, however, it is believed that at least a quarter of the known classical novae must be RNe with short recurrence times. [Pagnotta & Schaefer \(2014\)](#) established a set of criteria to determine RN candidates, some of them are:

- (i) Novae with low-amplitude eruption, since half of the RNe are composed of an evolved secondary star and a massive WD, so in quiescence RNe are brighter than an average CV, thus the difference between magnitude at maximum and minimum is smaller than for novae. In addition, RNe decline faster, since the mass required to reach TNR is lower, so RNe would occupy a specific region in an A versus t_3 diagram.
- (ii) Novae with long orbital periods and infrared colour excess would be inescapable indicators that the secondary would be a sub-giant (like in the case of U Sco) or red giant (like in RS Oph) star.
- (iii) High expansion velocity, since RNe must have very massive WDs, and thus the escape velocities are much higher than for classical novae, considering that for explosive events the ejection

velocity could be comparable to the escape velocity.

From these criteria, a large number of novae are candidates for a RNe with short recurrence time. However, the fact that they meet some of these criteria does not guarantee that they are in fact these kind of objects, as is demonstrated by the case of GK Per, which although it has an evolved secondary, long P_{orb} and infrared colour excess, the WD is comparatively low-mass, with $M_{\text{WD}} = 1.15 M_{\odot}$ (Hachisu & Kato 2007), implying that it must have a very long recurrence timescale.

1.6.5 Spectral classification of novae

While the spectral classification described by McLaughlin (1960) is merely taxonomic because it lacks a physical interpretation associated with the eruption, Williams et al. (1991); Williams (1992) proposed a new spectral classification based on photoionization changes in the expanding nova shell attributed to the evolution of the radiation from the central source. Most spectra in the early stage exhibit two types of strong non-Balmer lines: Fe II and He II/N.

He II/N novae: Their early spectra exhibit permitted lines of He I, He II, N II and N III. They have high ionization level, rectangular and very broad line profiles due to high expansion velocities and fast decline time, displaying coronal lines, strong Neon lines and no forbidden lines over time. The origin of He II/N spectra is attributed to the ejected gas from the WD, which is abundant in helium and elements from the CNO cycle.

Fe II novae: They exhibit Fe II lines which are collisionally excited and numerous heavy element transitions with a low level of ionization, displaying rounded and narrow line profiles that present strong P Cyg absorption features, a typical signal of an optically thick expanding shell. They are characterized by a relatively slow decline time and the spectral features likely originate in an circumbinary envelope of gas with solar abundances coming from the secondary star (Williams 2012).

One third spectral class is found, called 'hybrids', which exhibits lines of both spectral classes.

1.6.6 Classification by light curve properties

In the 1930's, when sufficient data of the nova light curves were collected, several authors proposed to classify novae based on the behavior of their light curves after the eruption (e.g., Lundmark 1935; Gerasimovic 1936; McLaughlin 1939). The latter author was who introduced the term speed classes, which depends on the light-curves decay times. In general, the parameter t_n is used to denote the number of days that the nova decays n magnitudes from maximum. Thus, the speed

Table 1.1: Classification of nova light curves. The speed class, the time to decay 2 magnitudes from maximum and the rate of decline are given. Values taken from [Bode & Evans \(2008\)](#).

Speed class	t_2 (days)	dm_V/dt (mag/day)
Very fast	<10	> 0.20
Fast	11 – 25	0.18–0.8
Moderately fast	26 – 80	0.07–0.0025
Slow	81 – 150	0.024–0.013
Very Slow	151 – 250	0.013–0.008

classes are defined in relation with t_2 and t_3 , the times that the nova decays 2 and 3 magnitudes respectively. The speed classes were later classified based on t_2 -times by [Payne-Gaposchkin \(1964\)](#) and they are shown in Table 1.1. This classification is considered as the ‘official’ one, which is registered in the ‘Bible of CVs’, written by [Warner \(1995\)](#). On the other hand, it is worth mentioning that there is another type of speed class classification used by the General Catalogue of Variable stars (GCVS, [Samus’ et al. 2017](#)). They divided novae (N) into "fast" (NA), those with $t_3 < 100$ days, "slow" novae (NB) those with $t_3 > 150$ days, NAB, those with t_3 between 100–150 days and "very slow" (NC) those with t_3 greater than 10 years. However, this classification is not widely used outside the GCVS community.

From a compilation of well studied novae listed in his table 5.2, [Warner \(1995\)](#) derived the relation between t_2 and t_3 , finding:

$$t_3 \approx 2.75t_2^{0.88} \quad (1.10)$$

However, this approximation is calculated without considering the inhomogeneity of the passbands used in the light curve observations, because they were observed either using visual, blue or photographic plates¹. Similarly, using photometric data of novae collected from [Downes et al. \(2001\)](#), new values were calculated for this relation by [Bode & Evans \(2008\)](#), diving the sample according to the speed class defined by [Payne-Gaposchkin \(1964\)](#) into two groups: (i) very fast and fast novae and (ii) moderately fast, slow and very slow systems, yielding the conversion rules-of-thumb

$$t_3 = 2.10t_2, \quad \text{for group (i)} \quad \text{and} \quad t_3 = 1.75t_2, \quad \text{for group (ii)}. \quad (1.11)$$

¹The brightness of ancient novae observed in the early 19th century and before the advent of CCDs cameras was recorded on photographic plates that were more sensitive to blue than the red light. The photographic magnitude or m_p , was designated to star images on blue-sensitive black-and-white film, and the visual magnitude or m_v referred to how a star looked to the eye. The current apparent V magnitude coincides fairly closely with the old m_v . In this work the prescription $m_v - m_p \sim 0$ is assumed, except for highly reddened novae, as expressed by [Warner \(1986\)](#).

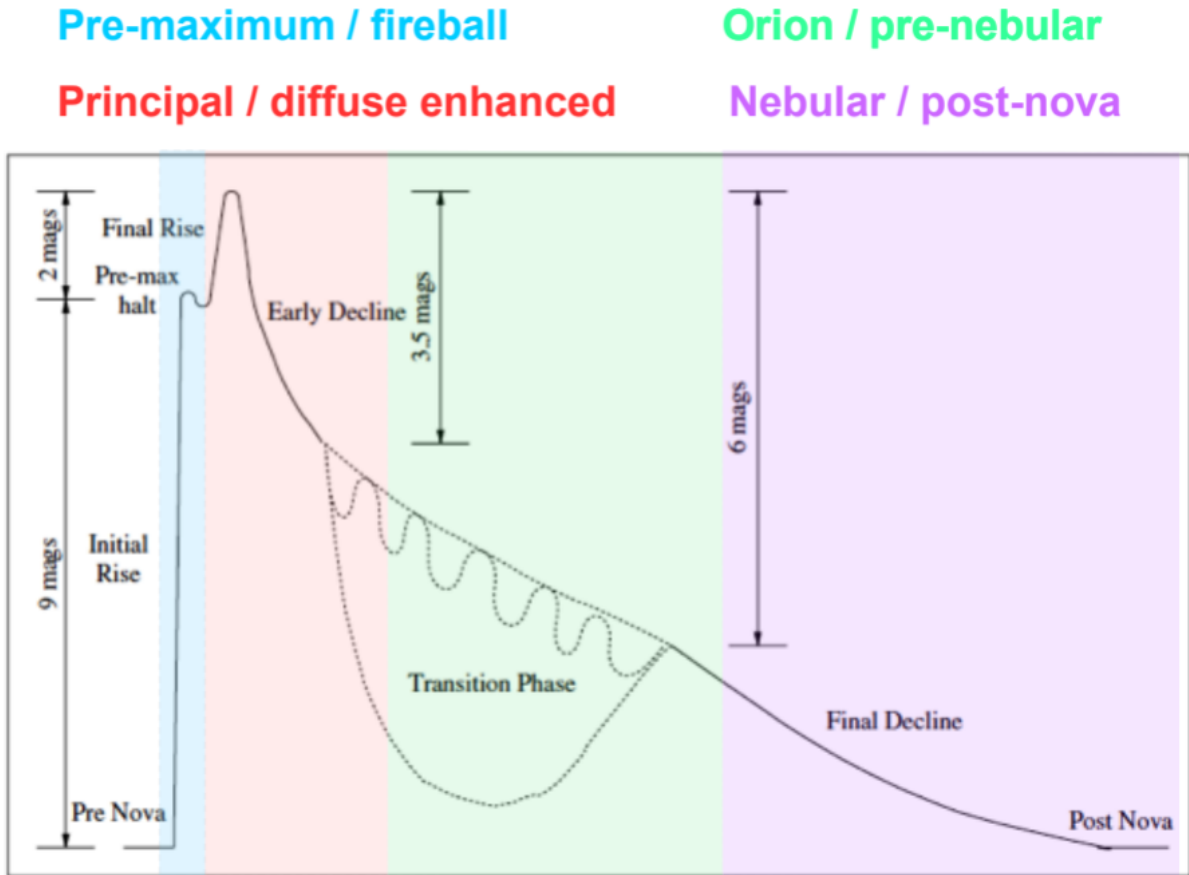


Figure 1.11: General structure of a nova light curve and its relation with the main spectroscopic phases. Figure from Della Valle & Izzo (2020).

Another essential point is the general behavior of the optical nova light curve, shown in Fig. 1.11. McLaughlin (1939, 1960) extracted the guidelines of the common behavior of the nova light curves comparing the similarities of them on particular time-scales, from the eruption to quiescence and contrasting them with their spectral evolution. The light curve is divided into the following phases:

- **Pre-maximum stage:** The initial rise has been caught just for a few novae, being constructed in most cases from different observation campaigns carried out by amateur astronomers (several good examples are found in the American Association of Variable stars observers, AAVSO web page²) or captured from surveys (as is the case with the Optical Gravitational Lensing Experiment, OGLE, Mróz et al. 2015, see Fig. 1.8), and thus the initial rise is observed discontinuously. However, it has been possible to establish that it takes about 3 days to reach the pre-maximum halt, even for the slowest novae. In many novae a plateau is observed 2 magnitudes before reaching the final rise, which lasts from a few hours for fast novae to a few days for slow novae. The final rise takes about two days for fast novae

²<https://www.aavso.org/LCGv2/>

and several weeks for slow novae. The maximum brightness is relatively short, lasting only hours for fast novae and only a few days for the slowest novae.

- **The early decline.** The decline from visual maximum is normally smooth except for slow novae, which have variations in amplitude up to 2 mag on time scales of 1–20 days.
- **The transition phase.** When the nova brightness falls to 3 to 4 mag below maximum three different behaviours have been observed: (i) about one-third of the fast or very fast novae continue to decline without major disruptions (e.g. CP Pup); (ii) some novae present large scale quasi-periodic oscillations with amplitudes between 1 to 1.5 mag in timescales of \sim 5–25 days; (iii) some systems decline into a minimum between 7 to 10 mag deep for months or even years and then the nova brightness follows the extrapolated early decline curve (e.g. DQ Her, LW Ser). The deep minimum is attributed to the formation of dust in the ejected material. Dust grains are formed from condensation of atoms of carbon and silicon, when the temperature in the expanding shell drops down to about 1000–2000 K. These dust particles block the radiation emitted by the nova, generating the appropriate conditions for more grains to condense. The radiation is absorbed by the grains and re-emitted at the infrared wavelengths, giving rise to an infrared excess when the optical luminosity declines in the transition phase.
- **The final decline.** Passing the transition phase, the nova luminosity declines with minor brightness variations apart from the characteristic orbital modulations until the brightness returns to quiescence, which is essentially, when the light curve becomes relatively flat in the post-nova phase. This stage is detailed in section 1.7.

While this description refers to the general behaviour of the nova light curves, a new classification for them was developed by [Strope et al. \(2010\)](#), based on a comprehensive analysis of 93 well-sampled nova visual light curves, covering the time from the eruption up to the post-nova phase and using data from the AAVSO. They classified them according to the shape and t_3 , defining seven categories (see Fig 1.12): S (smooth), F (flat-topped), C (cusps), J (jitters), P (plateau), O (oscillations) and D (dust dips), thereby, the classification is symbolized with one of this letter plus the t_3 value, so, for example, GK Per is D(100), RR Pic is (J150) and CP Pup is P(8).

Considering spectral and light curve classification, [Özdönmez et al. \(2018\)](#) found that about 80% of the Fe II novae are slow novae (72 of 87) with $t_3 \geq 20$ days and about 60% of the He II/N+hybrid class are fast novae (11 of 18), with $t_3 < 20$ days (for more information see their fig. 7).

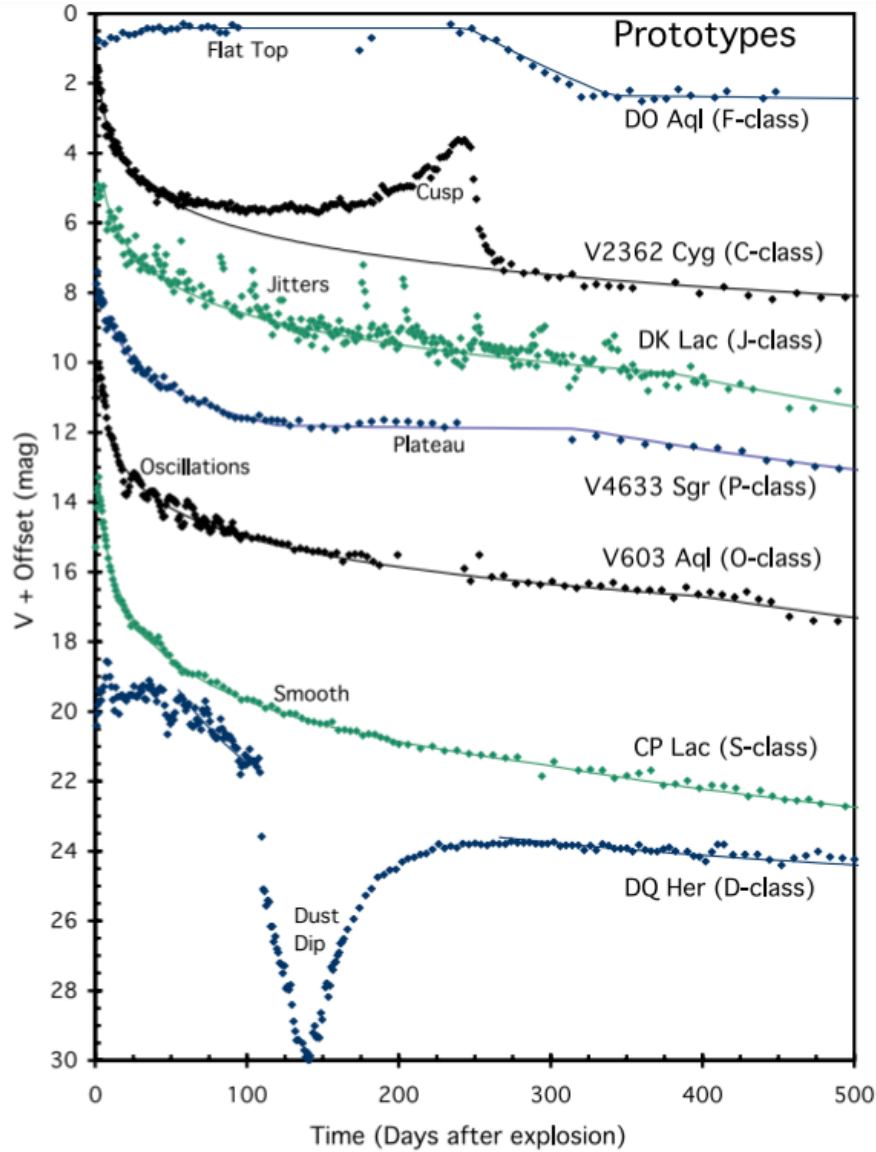


Figure 1.12: Classification system for nova light curves defined by [Strope et al. \(2010\)](#).

1.6.7 The colours of novae

In general, CVs appear with specific colours in a colour-colour diagram because their SED is a composition of three different components: a hot WD emitting mainly in the UV side, a MS-star contributing on the red range and a large and high temperature accretion disc dominating the optical range of the spectrum. This combination results in a peculiar colour expression for CVs in the colour-colour diagram (without considering reddening effects), appearing located between the main sequence and the white dwarf zone in the Hertzsprung-Russell diagram (H-R diagram). Particularly, novae are located on the blue and bright corner between the MS and the white dwarfs zone (Fig. 1.13, [Abril et al. 2020](#)).

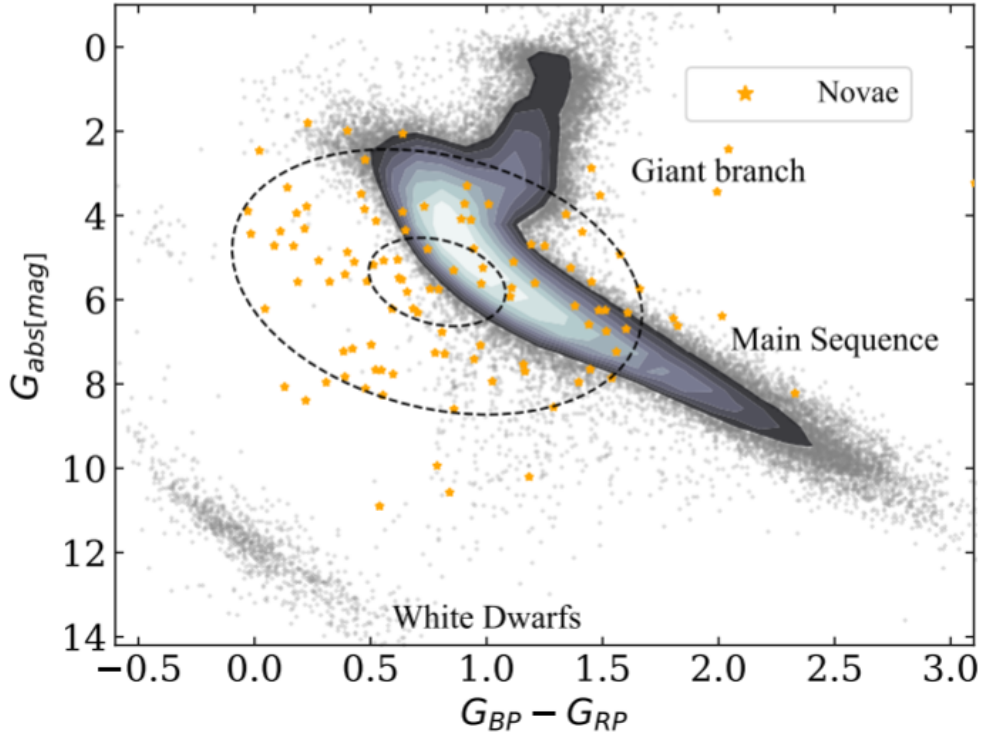


Figure 1.13: The distribution of novae in the HR-diagram derived from GAIA DR2. The sample is composed by the novae with known orbital periods from the [Ritter & Kolb's](#) catalogue. Figure from [Abril et al. \(2020\)](#).

1.6.8 Relationship for Maximum Magnitude vs Rate of Decline, t_3 and amplitude of eruption

An empirical relationship has been established between the absolute visual magnitude of novae at maximum, $M_{V_{\max}}$, and the rate of decline time, called the Maximum magnitude-rate of decline (MMRD), so that the brighter novae have shorter t_2 or t_3 . MMRD has been widely used in the past as a Galactic distance indicator when the reddening is known. This relation has been calculated using different samples by several authors (e.g. [McLaughlin 1945](#); [Cohen 1985](#); [della Valle & Livio 1995](#); [Downes & Duerbeck 2000a](#)), including extragalactic novae observed in M31 and from the Large Magellan Cloud (LMC), assuming a variety of galactic absorption values. Most of the authors have defined MMRD as a linear relation, but it also has been presented as a non-linear correlation as an S-curve ([della Valle & Livio 1995](#)). This S-shape function is supported by the theoretical relationship between $M_{V_{\max}}$ and the mass of the WD ([Livio 1992](#)). However, both derived MMRD relationships have a large scatter (e.g., ~ 3 mag for the MMRD derived by [Cohen 1985](#)), which is why its reliability as a distance indicator has been questioned. This scatter is mainly attributed to: (i) The absolute magnitudes derived by using the distance measured from the nebular parallax when a symmetric and spherical expansion is assumed, while they are commonly prolate ([Gill & O'Brien 2000](#); [Wade et al. 2000](#)), implying significant errors in the measurement of distances, especially for the most distant novae and, (ii) the great uncertainty associated to the visual extinction in

the direction of the nova, which mostly are located in the Galactic disc. In general, reddening is computed from empirical relations from the intensity of the interstellar lines, from comparison of observed and predicted emission lines ratios or from dust column densities measured from infrared surveys (e.g., [Schlafly & Finkbeiner 2011](#)).

In recent years, nova distances have been determined using the parallaxes delivered by GAIA data release 2 (DR2, [Gaia Collaboration et al. 2018](#)), providing precise parallax data to test the reliability of the distances measured by nebular parallaxes and by the MMRD. The results are being very controversially discussed, e.g, [Schaefer \(2018a\)](#), concluded that "the MMRD should not longer be used", while [Selvelli & Gilmozzi \(2019\)](#) found an improved MMRD to be still valid. Very recent work published by [Della Valle & Izzo \(2020\)](#) tested both results. Using data from both works and discarding the unreliable data, they derived the absolute calibration for the MMRD on Galactic novae:

$$M_V = -7.78(22) - 0.81 \times \arctan((1.32 - \log t_2)/0.23) \quad (1.12)$$

Comparing the distances measured from GAIA DR2 with the distances derived from MMRD, they found a consistent correlation between GAIA DR2 and MMRD distances. The deviating object (red point in Fig.1.15) is a recurrent nova, and an analysis of the residuals indicated that the MMRD distances are overestimated about 30% above ~ 2 kpc. In conclusion, their analysis is in total agreement with the [Selvelli & Gilmozzi \(2019\)](#) conclusions, in contrast to the [Schaefer \(2018a\)](#) results.

On the other hand, the relation between the amplitude of the eruption $A = m_{\min} - m_{\max}$ and the rate of decline has been considered one of the most direct indicators of the nova properties because it is independent of the distance and the reddening. [Vogt \(1990\)](#) analysed 97 nova light curves covering the time from pre-eruption to post-eruption phase, finding that the amplitude and the rate of decline are correlated in the sense that fast novae have larger amplitudes than slow ones, independently of the time interval chosen as selection criterion. The standard formulation for this relation is found by [Warner \(1995\)](#) using t_2 , where he also corrected the apparent amplitude by the inclination effects for those novae with known i , because A also can deliver information about i ([Warner 1986](#)). In fact, this dependence is shown in Fig. 1.14, in which the higher inclination novae appear with large amplitudes (points above the linear fit for $i = 82^\circ$), but they are not strongly correlated with t_2 . Additionally, [Vogt \(1990\)](#) also found a post-nova decline rate of 0.021(6) mag/year, but without considering corrections for the effect of inclination. Updated decline rates have been established just for bright individual post-novae (e.g. [Johnson et al. 2014](#)).

This diagram is also used as an indicator of recurrent nova candidates, since these systems are characterized by low amplitudes and faster declines (description in section 1.6.4), so they would be located in the lower left corner of the diagram ([Duerbeck 1987](#); [Pagnotta & Schaefer 2014](#)).

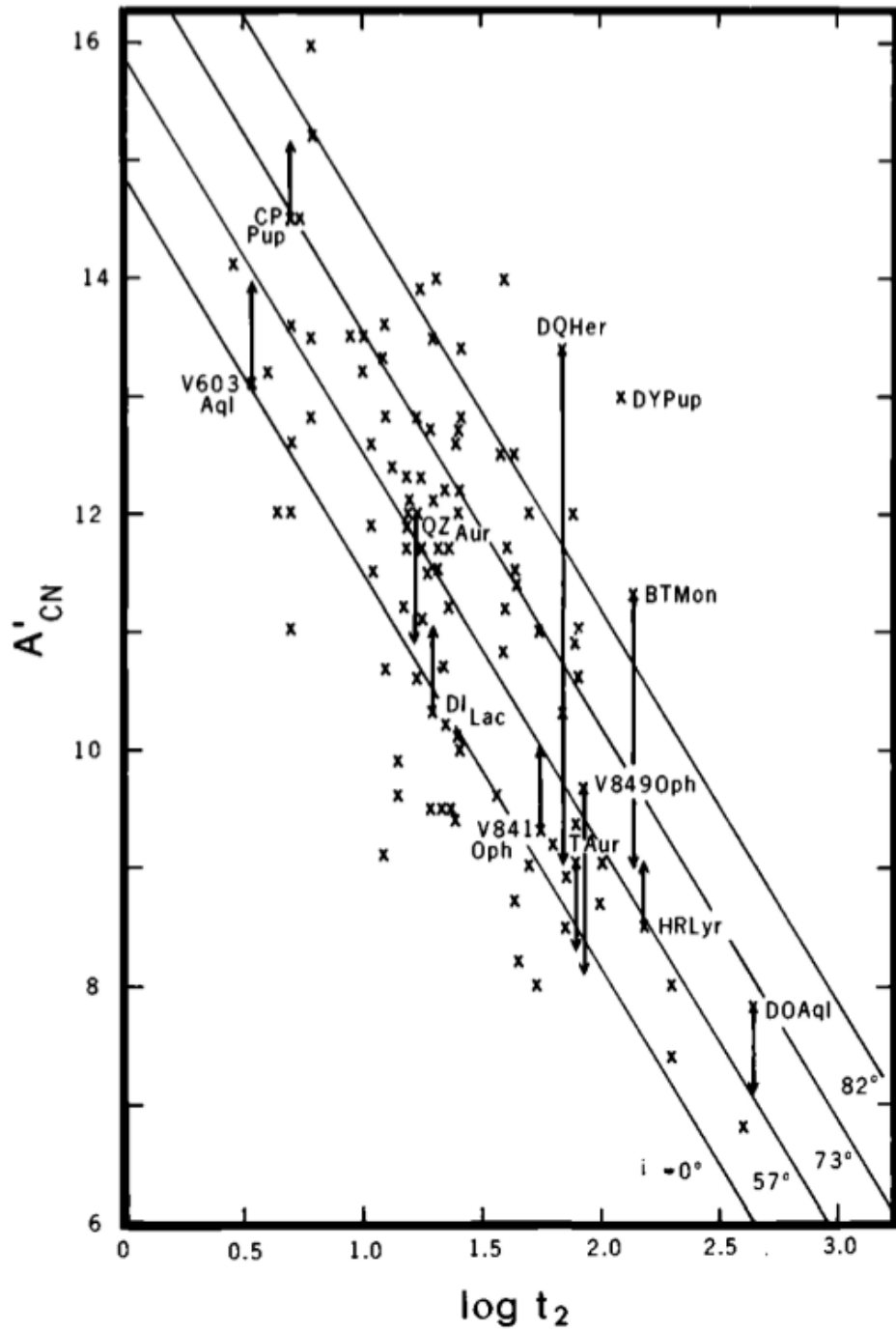


Figure 1.14: Amplitude of the eruption versus t_2 for novae. The diagonal lines represent three different fits for a linear relationship corrected for inclination effects. Figure from Warner (1995).

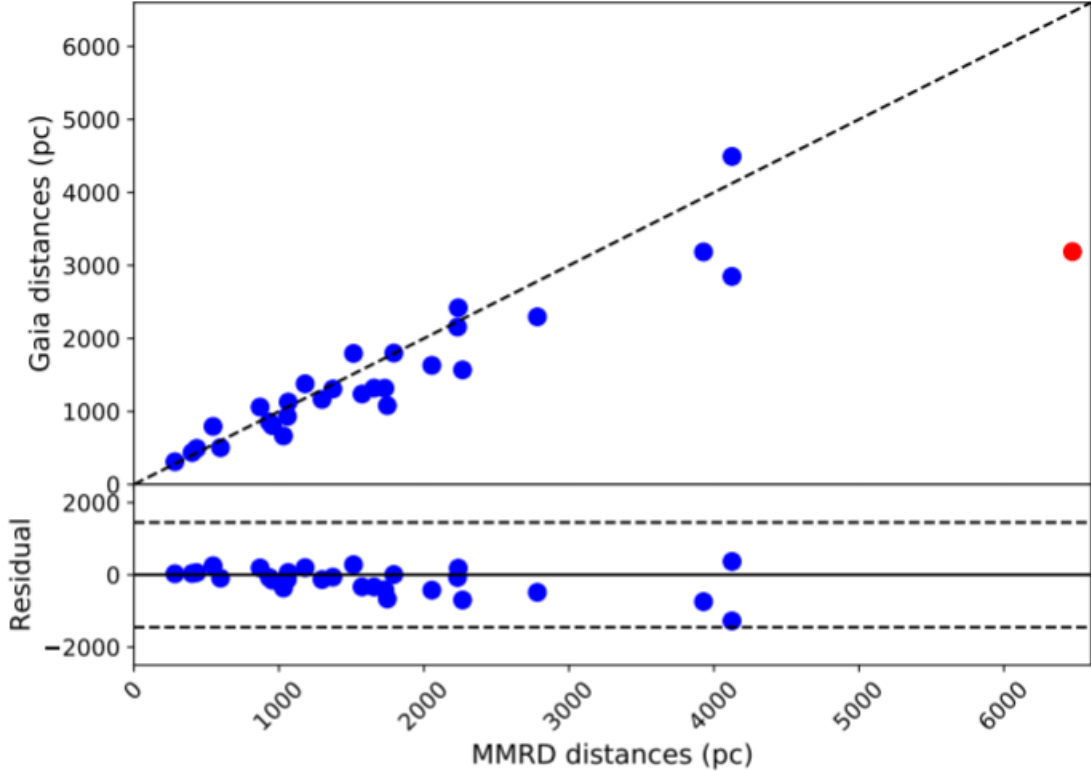


Figure 1.15: Computed distances from GAIA DR2 vs MMRD distances using data from [Schaefer \(2018a\)](#) and [Selvelli & Gilmozzi \(2019\)](#). The MMRD distances were calculated using the Equation 1.12. Figure from [Della Valle & Izzo \(2020\)](#).

1.7 The properties of post-novae

Some decades after the eruption the CVs return to quiescence with magnitudes very similar to those exhibited in the pre-nova stage ([Robinson 1975](#); [Collazzi et al. 2009](#)). Light curves in the post-nova stage are characterized by photometric variations at the quiescence magnitude or minimum magnitude (m_{\min}) with amplitudes of about $\sim 1\text{--}2$ mag, which have multiple origins, the most common being those related to the orbital period on time-scales of hours and/or to dwarf nova activity (Fig 1.17) on time-scales of days. In a study to look for stunted outbursts, i.e., dwarf nova-like mini-outbursts, in long-term post-nova light curves, [Vogt et al. \(2018\)](#) found such outbursts with amplitudes between 0.2–2.2 mag in cycles of about 9–32 days. Considering all post-novae with reported stunted outbursts (15 in total) they found a likely tendency for increasing outburst amplitudes from a nova age of 30 to 250 yr, at a rate of 0.52(23) mag/yr (Fig. 1.17), being based, however, on a small number of cases. Also they concluded that any decrease in \dot{M} must be at much longer time scales than predicted by the hibernation scenario, with time-scales larger than ~ 200 yr.

Spectra in quiescence are dominated by emission coming from the disc, mostly showing signa-

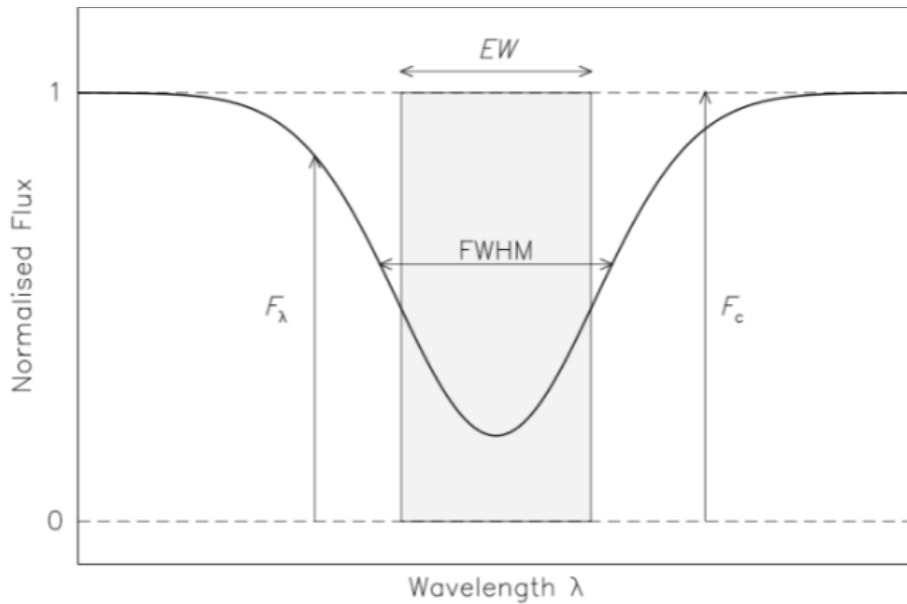


Figure 1.16: The equivalent width (W_λ) is defined as the width of a rectangle having the same area as the spectral line and is an indicator of the strength of the line. W_λ have positive values for absorption lines and negative ones for emission lines. However, for simplicity, in this thesis the definition is inverted, i.e. the W_λ of emission lines are defined as positive values. The full width at half maximum (FWHM) is defined as the width of a spectral line at half of its maximum amplitude. Figure adapted from [Carroll & Ostlie \(2006\)](#).

tures of a high mass transfer system with an optically thick disc, reflected as a blue continuum with broad Balmer emission lines, weak lines of the neutral helium series He I, the Bowen blend CIII/NIII 4650Å and He II 4686Å, the latter two probably the result of ionization by the ultraviolet radiation emitted by the eruption heated WD. Also, in a few post-novae the high ionized He II $\lambda 5412\text{Å}$ emission line is seen, which possibly can be related to the magnetic field of the WD (more details in section 2.5). The strength of the emission lines is directly related to the mass transfer rate but is also affected by the inclination. Low- \dot{M} systems produce discs with a relatively low density, giving rise to strong lines, while high- \dot{M} objects should present weak emission lines because they come from an optically-thick disc ([Patterson 1984](#)). The effect of the inclination on the equivalent width was expressed by [Warner \(1986\)](#) in his fig. 1. The two parameters are correlated in the sense that systems seen at high-inclination have large equivalent widths, while low-inclination ones have very weak lines and a strong continuum, because in face-on systems the full disc surface is visible and thus most of the continuum emission from the optically thick part of the disc, whilst in edge-on ones the contribution comes from the external part of the disc which has a lower density than the inner sections.

1.8 Life after eruption project

In order to obtain a significant sample of post-novae, [Tappert et al.](#) started a project to enlarge the post-novae sample since 2009. Their search criteria and the steps to recover them are described as follows:

- **The search for information in the literature of each individual nova.** This search begun in the catalogue of known or suspected CVs by [Downes et al. \(2005\)](#). The pre-1986 novae were selected, in order to minimize the probability that the contribution of the ejected shell is still dominant and thus does not allow for a proper analysis of the CV spectrum. The number of the such selected novae amounts to 232, of which 174 are visible from the Southern hemisphere. At the moment to start my participation in this project (2015), only 30% of the 232 pre-1986 novae had been correctly identified (equivalent to 67 systems; see [Fig. 1.19](#)). It is worth mentioning that this step was carried out before starting my thesis.
- **The search for the correct position in the field where the nova was reported.** At first, to identify post-nova candidates we have used *UBVR* photometry. A nova normally appears as an outlier in the colour-colour diagram, appearing as a blue object considerably above the main sequence. However also blue stars, WDs and quasars appear in that range of the diagram, and can be confused as the nova in the field. Also, because *U* and *B* observations require dark nights and long integration times, since the beginning of this PhD project, we proposed to replace *U* and *B* by an $H\alpha$ narrow band filter in the later proposals. Inasmuch as most novae are characterized by a blue continuum and generally weak emission lines, being $H\alpha$ the most significant one, the post-nova should be clearly separated in a colour-colour diagram from the other stars in the field using a $H\alpha$ filter. We used an $H\alpha$ narrow band and an $H\alpha$ off-band filter. For the latter, [SII] was used, to avoid possible contamination from [N II] nebular emission (see [Fig. 1.18](#) for a more comprehensive visualization of the wavelength ranges covered by the filters used in this work). In [section 2.2](#) the *UBVR*, *VH α [SII]*, *RH α [SII]* and *g'H α [SII]* photometries are detailed. In some cases, the [Downes et al.](#) catalog or the work by [Mróz et al. \(2015\)](#) provided candidates that were observed spectroscopically without first taking photometric data.
- **The confirmation and classification of post-nova candidates via spectral characteristics.** The nova can be unambiguously identified and characterized by the presence of characteristic emission lines. For example, strong Balmer lines together with the presence of He I lines can indicate a low mass-transfer system, while particularly strong He II $\lambda 4686\text{\AA}$ and the presence of He II $\lambda 5412\text{\AA}$ let suspect a magnetic CV. Broad lines point to a comparatively high inclination, thus indicating systems suited for photometric or spectroscopic time-series

follow-up observations to determine their orbital period (e.g. [Tappert et al. 2013a,b](#); [Fuentes-Morales et al. 2021](#)), which is the last step of the project. However this step is not always feasible, because faint novae require a large amount of observation time at large telescopes. This step will be described in more detail in chapter [3](#).

1.9 Thesis outline

This chapter [1](#) has presented a general overview of the optical properties of classical novae with emphasis on the post-nova phase, which is the focus of this work. Studies of post-novae are crucial to understand the role of the nova in CV evolution, however the known sample of post-novae is sparse, mainly due to the novae being only well studied during maximum brightness. [Tappert et al.](#) began a project to increase the sample of post-novae in 2009, making this thesis the direct continuation of their work, which is based on observations in the visual band both photometric and spectroscopically, using a variety of telescopes located in Chile. In chapter [2](#) the project is presented, detailing the steps to recover post-novae through colour-colour diagrams and to confirm their nature through the spectral characteristics, including a discussion about the general spectroscopic properties of post-novae. In chapter [3](#) an updated orbital period distribution of novae is presented and finally chapter [4](#) presents the thesis conclusions and the future work.

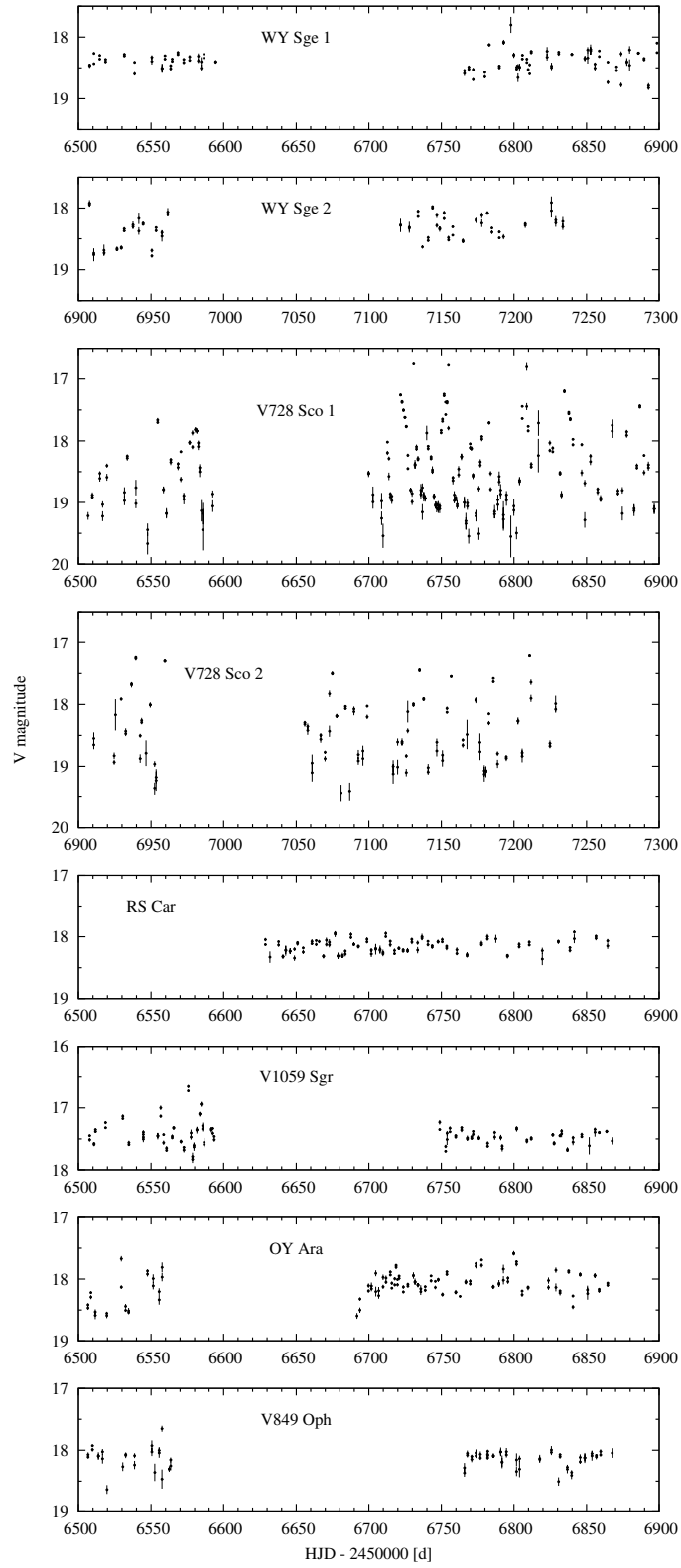


Figure 1.17: V-band light curves of post-novae showing brightness variations described in section 1.7. Figure from Vogt et al. (2018).

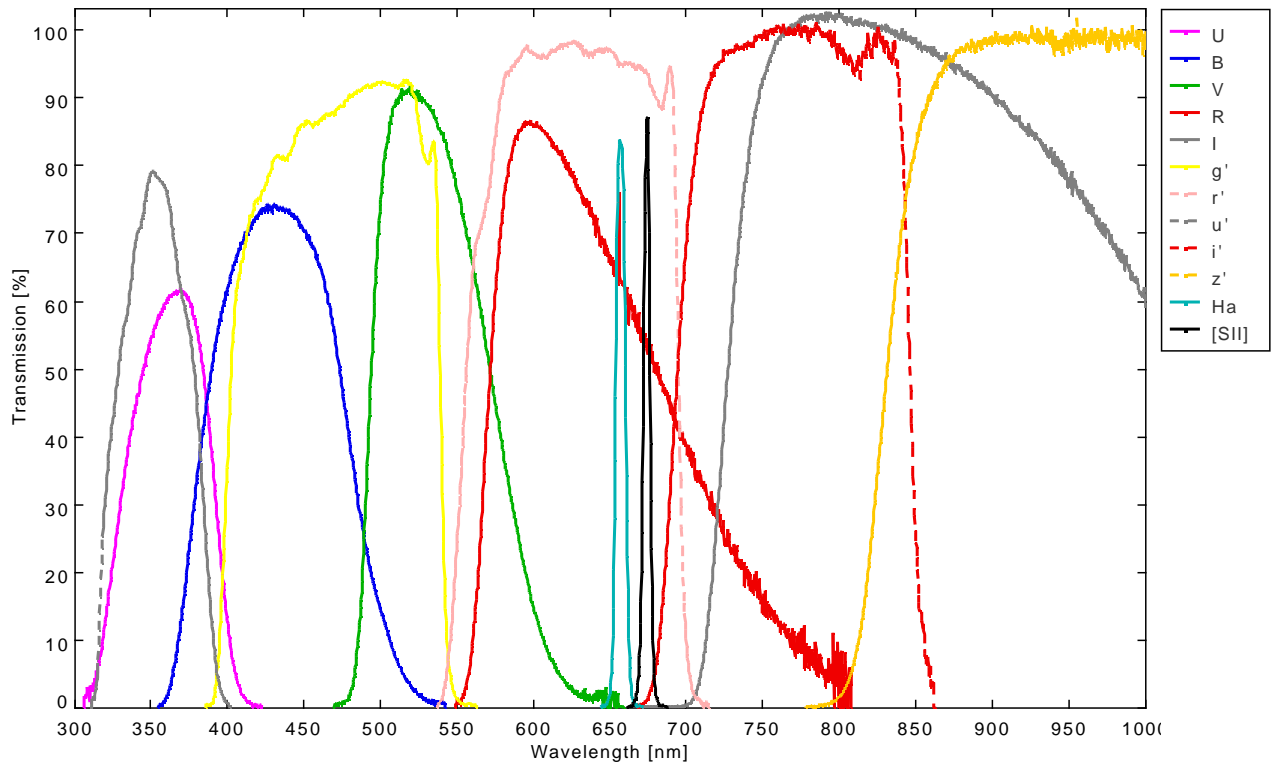


Figure 1.18: Transmission curves for Johnson-Cousins $UBVR_cI_c$, Sloan $griz$ broad-band filters together with $H\alpha$ and [SII] narrow-band filters. Diagram created with data from filters used at the Southern Astrophysical Research Telescope (SOAR).

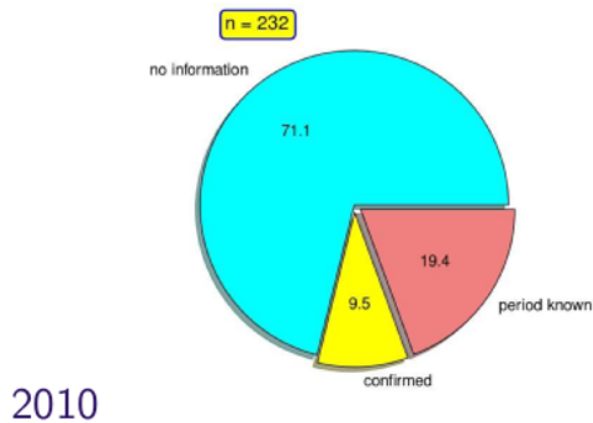


Figure 1.19: Sample of post-novae erupted before 1986 at the start of the project in 2009. The pie chart shows as a percentage of the total sample those old nova fields without identified post nova in cyan, spectroscopically confirmed post-novae in yellow and identified post-novae with orbital period known are shown in red. Figure by Tappert (private communication).

Chapter 2

Recovery of old Novae

Abstract

In this chapter the steps to recover old novae are shown. Colour-colour diagrams using a variety of filters are presented from which we extract post-nova candidates. Here we report the spectroscopic confirmation for eleven old novae: EL Aql, EY Aql, V606 Aql, V908 Oph, KT Mon, V726 Sgr, V1149 Sgr, V1583 sgr, V3964 Sgr, V4049 Sgr and V825 Sco. For the known post-novae V1370 Aql, V693 CrA, LW Ser and V4077 Sgr new spectra are presented. We also have discarded nine candidates proposed to be the post-nova counterparts presenting their true nature. They are: KY Sgr, V726 Sgr, V732 Sgr, V1012 Sgr, V1148 Sgr, V1174 Sgr, FS Sct, V719 Sco, and V902 Sco. In most cases they are confused with W Ursa Majoris binary stars. On the other hand, we discuss the efficiency of using $H\alpha$ photometry versus $UBVR$ photometry in order to recover the true position of old novae. Finally, using these new data we present an updated perspective of the post-nova population.

2.1 Introduction

A nova is a thermonuclear runaway triggered on the surface layer of a white dwarf as a consequence of the accreted material from the late-type MS star in a cataclysmic variable (CV). The eruption is seen as a sudden increase in brightness that can amount to up to ~ 16 magnitudes, making it possible to even see it with the naked eye if it is located close enough to Earth (e.g. RR Pic reached $V = 1.2$ mag at the maximum brightness, being located at $d = 388(88)$ pc, [Dawson 1926](#); [Ramsay et al. 2017](#)). Because the position of the old nova is usually reported when it is at maximum brightness, the recovery of the precise position after the eruption, when mostly post-novae turn into very faint objects, becomes a non-trivial task. This is due to several factors: (i) Most reported galactic novae are located in crowded fields in the Galactic disc (ii) The post-nova

Table 2.1: Proposals related to the project. The technique used is marked with \times .

Proposal ID	Year	Telescope	Instrument	Photometry	Spectroscopy
089.D-0505(A)	2012	VLT	FORS2	\times	
092.D-0225(A)	2013-2014	VLT	FORS2	\times	
CN2015A-2	2015	du Pont	Direct/SITe2K-1	\times	
GS-2015B-Q-54	2015	Gemini	GMOS-S		\times
098.D-0291	2016	VLT	FORS2		\times
GS-2016A-Q-1	2016	Gemini	GMOS-S		\times
GS-2016B-Q-27	2016	Gemini	GMOS-S		\times
CN2016A-25	2016	SOAR	Goodman HTS	\times	
GS-2017B-Q-4	2017	Gemini	GMOS-S		\times
0102.D-0488(A)	2018	VLT	FORS2		\times
CN2018A-80	2018	SOAR	Goodman HTS	\times	
CN2019A-17	2019	SOAR	Goodman HTS	\times	
GS-2019A-Q-225	2019	Gemini	GMOS-S		\times
GS-2019A-Q-226	2019	Gemini	GMOS-S		\times
GS-2020A-Q-107	2020	Gemini	GMOS-S	\times	

is easily to identify as one bright object at maximum brightness, and in that stage its PSF is extended, spanning a large area that can cover its immediate neighbours, while at minimum the post-nova is just one faint object amongst others within the same PSF area, (iii) old observations especially visual, but also photographic ones, have a lower spatial resolution, and thus the precision of the reported coordinates is rarely better than 10-20 arcsec, and can be even much worse (e.g. several arcmin).

The correct position of post-novae is recovered using colour-colour diagrams to identify candidates and to confirm them via low-resolution spectroscopy (a complete description of these steps is given in section 1.8). This method has proved to be very efficient (e.g., Tappert et al. 2012, 2014, 2015, 2016) In this chapter, we follow that method to recover post-novae. Table 2.1 summarizes the observing proposals relevant for this thesis project, which are the basis of the results shown here.

2.2 Photometric data

Colour-colour diagrams were created using both *UBVR* data and photometry based on the $H\alpha$ narrow-band filter. All *UBVR* data presented here were taken and analysed before starting this PhD project. The $H\alpha$ related data were acquired in the period of this thesis and those data are still unpublished.

The *UBVR* photometric data were collected in two service mode runs in 2012 and in 2014 at the Antu 8-m telescope that is part of the Very Large Telescope (VLT) of the European Southern

Observatory (ESO), at Cerro Paranal, Chile, using the FOcal Reducer/low dispersion Spectrograph (FORS2; Appenzeller et al. 1998) instrument with the high-throughput broad-band filters u_High , b_High , v_High and $R_Special$ in service mode. The field of view is 6.8×6.8 arcmin². Although FORS2 usually operates with a mosaic of two $2k \times 4k$ MIT CCDs, for the data obtained on 2012 August 18, exceptionally the blue-sensitive E2V CCDs were used.

$VRH\alpha$ photometry was collected in 2016, and $VH\alpha[SII]$ narrow-band photometry in 2018 and 2019 at the Southern Astrophysical Research Telescope (SOAR) located on Cerro Pachón, Chile, using the Goodman High Throughput Spectrograph (GHTS) instrument in imaging mode, with a 0.15 arcsec/pixel scale, 2×2 binning and a 7.2 arcmin diameter field of view. Furthermore, we collected $RH\alpha[SII]$ photometry in 2019 and $g'H\alpha[SII]$ in 2020 with the Gemini Multi-Object Spectrograph South (GMOS-S, Hook et al. 2004) in imaging mode, at the Gemini-South Telescope on Cerro Pachón, Chile, using part of the allocated time for spectroscopy to gather pre-imaging. Because the CCD detector array is composed of three 2048×4176 Hamamatsu chips arranged in a row, the separation between the detectors produces gaps about 4.9 arcsec wide in the image field. The field of view is 5.5 arcmin square and the effective pixel scale is 0.160 arcsec/pixel for 2×2 binning.

During the period of this thesis work, 27 fields were observed using the $H\alpha$ narrow-band filter, corresponding to 49% of the remaining sample. It is worth mentioning that almost 50% of the allocated total time was lost due to bad weather conditions and technical problems during the execution of all observing runs at SOAR. Details of the observed fields using the different filter combinations are shown in Table 2.3.

After combining the two mosaic CCD frames into one with the SFSMOSAIC routine from the FORS Instrument Mask Simulator package, the $UBVR$ data were further reduced using the CCDRED package of IRAF. The bias-subtracted and flat-fielded data were then corrected for the telescope offsets between them and averaged to a single frame per filter. A 3σ clipping algorithm was applied to exclude bad pixels and cosmic rays.

For photometry taken at SOAR the basic reduction was performed with the CCDPROC task of IRAF and the alignment of each field in the different bands was obtained with the ASTROIMAGEJ software (Collins et al. 2017).

The GMOS-S data were reduced and calibrated using the external GEMINI-GMOS IRAF package included in the GEMINICONDA environment, which is part of the ASTROCONDA channel, a collection of conda packages¹ provided by the Science Software Branch (SSB) of the Space Telescope Science Institute (STScI). Apart from the basic reduction, each field is presented as one image divided in three image extensions. They are joined using the GMOSAIC task, which takes into account the relative offsets and orientations of the each chip to generate a single image.

The $UBVR$ photometry was performed using IRAF's DAOPHOT package and the stand-alone

¹https://astroconda.readthedocs.io/en/latest/getting_started.html

DAOMATCH and DAOMASTER routines (Stetson 1992). For SOAR and GMOS-S fields the instrumental magnitudes were estimated with the SEXTRACTOR software using aperture photometry (Bertin & Arnouts 1996). For all configurations, the chosen aperture radius was slightly smaller than the full width at half-maximum (FWHM) of the point spread function (PSF) and the sky annulus radius to be twice the value of the aperture radius. The conversion to calibrated magnitudes was obtained using observations of standard fields (Landolt 1983, 1992; Stetson 2000) for the *UBVR* data. The *U* passband is not a part of ESO’s standard calibration plan, and in most nights, the standard field observations in this filter covered only a very limited range of airmasses that did not allow us to derive a value for the extinction from them. Thus, a standard value for the extinction was used that was taken from the La Silla observatory website. Comparison of the *UBVR* passbands for the few nights, where a sufficiently large airmass range was covered, showed identical values within the uncertainties.

On the other hand, conversion to *V* calibrated magnitude was made for photometry acquired at SOAR, and for those taken at GMOS-S the *R* and *g* magnitudes were calibrated, choosing stars with known magnitude in the field and comparing them with their tabulated magnitudes in the USNaval CCD Astrograph (UCAC4; Zacharias et al. 2013). The calibrated magnitudes in either *V* or *R* are calculated only for those fields where a candidate was found in the colour-colour diagram. They are shown in Table 2.2.

The calibrated magnitudes for the spectroscopic data on recovered novae were calculated in the same way as described above for the colour-colour diagrams and they are also displayed in Table 2.2.

The eruption amplitude *A* was directly calculated for those post-novae with *V* measured in quiescence state. For those with *R* magnitudes, *V* was calculated assuming as $V - R = 0.2(3)$ mag, the average value of those novae in the sample presented by Szkody (1994), which can be assumed a robust and statistically significant sample of novae (discarding the values for recurrent novae) with errors that do not affect the statistic evaluations of the amplitudes significantly. The values for *V* and *A* are displayed in Table 2.6 both for novae analysed in this chapter and for recompiled ones from the literature (more details in section 2.5).

2.3 Spectroscopic data

Long-slit spectroscopic data were obtained in 2015, 2016, 2017 and 2019 with GMOS-S at the Gemini-South Telescope in service mode. In all runs the configuration was the same: grating B600 with a central wavelength of 5600Å covering a wavelength range $\sim 4000 - 7000\text{Å}$, using a 1.5 arcsec slit which yields a spectral resolution $\sim 8\text{Å}$, and 2×4 (spatial \times spectral) binning. In order to minimise distortions by cosmic rays and the gaps between chips (which are seen in the wavelength range 5030 – 5080Å and 6100 – 6150Å using the settings described above), at least three spectra

Table 2.2: Log of observations.

Name	RA(J2000)	DEC(J2000)	date	Filter/Grism	t_{exp} (s)	mag
EY Aql	19:34:44.47	+15:01:51.17	2016 July 30	B600 (GMOS)	450×9	23.3R
EL Aql	18:56:01.87	-03:19:18.8	2012 July 18	<i>UBVR</i>	1576,420,160,120	20.9V
			2015 Apr 27	B600 (GMOS)	4760	19.9R
V606 Aql	19:20:24.29	-00:08:07.8	2012 June 24	<i>UBVR</i>	1576,420,160,120	20.4V
			2015 June 15	B600 (GMOS)	3600	20.1R
V1370 Aql	19:23:21.24	+02:29:26.20	2016 July 28	B600 (GMOS)	208×3	-
V693 CrA	18:41:58.02	-37:31:14.5	2015 Sept 4	B600 (GMOS)	825×4	-
KT Mon	06:25:18.652	+05:26:35.44	2013 Nov 27	<i>UBVR</i> (FORS2)	700×4,380×4,70×4,80×4	23.1V
			2016 Oct 06/ Nov 28-29	300V (FORS2)	685×9	-
V908 Oph	17:28:04.58	-27:43:04.4	2014 Apr 03	<i>UBVR</i>	1655,495,200,170	20.5V
			2015 Apr 28	B600 (GMOS)	3600	18.5R
LW Ser	17:51:50.90	-14:43:50.0	2017 Apr 4	B600 (GMOS)	305×9	20.2R
KY Sgr	18:01:25.20	-26:25:16.03	2019 Apr 2+10	B600 (GMOS)	240×2, 180×3	18.1R
			2018 may 15	$VH\alpha$ [SiI] (SOAR)	10,60,60	18.4V
V726 Sgr	18:19:33.73	-26:53:21.19	2019 June 6	$RH\alpha$ [SiI] (GMOS)	60,600,600	20.7R
			2019 July 5	B600 (GMOS)	900×4	20.9R
V1149 Sgr	18:18:29.85	-28:17:24.9	2012 Aug 15	<i>UBVR</i>	1576,420,160,120	18.4V
			2015 June 06	B600 (GMOS)	1350	18.1R
V1583 Sgr	18:15:26.53	-23:23:17.5	2012 July 24	<i>UBVR</i>	1576,420,160,120	20.5V
			2015 Apr 21	B600 (GMOS)	3600	19.5R
V3964 Sgr	17:49:42.42	-17:23:34.8	2015 Apr 26	B600 (GMOS)	3600	19.5R
V4049 Sgr	18:20:38.62	-27:56:24.39	2017 March 29	B600 (GMOS)	385×9	-
V4077 Sgr	18:34:39.46	-26:26:03.15	2015 Sept 03	B600 (GMOS)	825×4	19.5R
V825 Sco	17:49:53.78	-33:32:13.07	2016 Feb 11+17	B600 (GMOS)	480×6	19.0R

per target at three slightly different central wavelengths were taken.

Additionally, nine spectra in long-slit mode were collected for the faint old nova candidate KT Mon in 2016 using the FORS2 instrument. FORS2 offers a configuration with a higher efficiency at the cost of a slightly lower spectral resolution, and is thus better suited for the observation of very faint objects than GMOS-S. The grism used was 300V with a 1.3 arcsec slit providing a wavelength range of 3800 – 9000Å at a resolution of $\sim 15\text{\AA}$ and 2×2 binning.

The GMOS-S data were reduced and calibrated using the GEMINI-GMOS IRAF package. The reduction was performed as follows:

- Trim the overscan zone and averaged bias subtraction for flat-field, CuAr lamp, standard and science frames.
- Correction of the relative difference in quantum efficiency (QE) among the CCD detector array components for flat-field, science and standard exposures.
- The GMOS spectral response and the unequal illumination from the flat-field frame is removed fitting low-order cubic spline functions to each separated chip, that are afterwards concatenated to one frame. The science and standard frames are divided by the such obtained normalized flat field.
- Wavelength calibration was determined from a two-dimensional CuAr lamp spectrum and applied individually to each science spectrum with different central lambda.
- The sky-lines were removed by fitting a second order Chebyshev function to the background in the spatial direction.
- Combination of individual spectra in order to increase S/N, remove cosmic rays and minimize the distortions by the gaps.
- The instrumental response function was corrected through comparison with a standard star spectrum taken during the observing run. Because the data were acquired in non-photometric nights, the standard spectrum was not used to calibrate in flux.

The steps for FORS2-data reduction consisted in the subtraction of averaged bias, division by the normalized flat-field fitted with high-order Legendre function, combination of individual spectra to reject cosmic rays and increase S/N, sky-lines subtraction and extraction of the spectrum using the APALL task from IRAF and finally, flux calibration using spectrophotometric standard stars observed on October 06 and November 28.

The log of observations is shown in Table 2.2, where the equatorial coordinates were derived comparing the finding chart of each nova with the composed image provided by the Panoramic

Survey Telescope and Rapid Response System (Pan-STARRS, [Flewelling et al. 2016](#); [Chambers et al. 2016](#)) using the Aladin sky atlas².

The equivalent widths (W_λ) and FWHM of the main emission lines were measured with the IRAF routine SPLIT, which estimates the errors considering a Poisson statistics model of the data specified by the `sigma0` parameter, which is the RMS of the data measured in continuum regions and the inverse gain parameter (`invgain`). The error is calculated after running a number of Monte-Carlo simulations controlled by the parameter `nerrsamp`. In this work we established `nerrsamp=100`. The values are presented in Table 2.4.

Spectra from both sets were corrected for the average value of the galactic extinction $E(B - V)$ from NASA’s IPAC Infrared Science Archive (IRSA) web page³ adopting the calculations derived by [Schlafly & Finkbeiner \(2011\)](#) in a $2^\circ \times 2^\circ$ field, except for those novae with known distance, for which the reddening was derived from the Structuring by Inversion the Local Interstellar Medium (STILISM) web page⁴ ([Capitaniao et al. 2017](#)). This consists on a 3-D map of the galactic ISM constructed from diffuse interstellar bands (DIBs) measurements and the inversion of colour excess measurements for individual target stars or on statistical methods from stellar surveys. For those sources available in the Early Gaia Data Release 3 (EDR3, [Gaia Collaboration et al. 2016, 2018, 2021](#)), with non-negative parallax ($\bar{\omega}$) and uncertainty ($\sigma_{\bar{\omega}}$) that satisfy the fractional parallax error condition $f = \sigma_{\bar{\omega}} / \bar{\omega} \lesssim 20\%$ as defined by [Bailer-Jones \(2015a\)](#), the distances were calculated using the Bayesian inference method established by [Astraatmadja & Bailer-Jones \(2016\)](#), which assumes an exponentially decreasing space density prior depending on the length scale factor L , that characterizes the exponential decay. We assumed the same value considered by them, $L=1.35$ kpc.

Dereddening was applied using IRAF’s DEREDDEN task and considering as the value for the extinction ratio $R(V) = A(V)/E(B - V) = 3.1$. Both the original and the dereddened spectra were smoothed with a 5×5 box filter and are shown in Figs. 2.5 and 2.9, respectively. In order to get an approximation of the spectral energy distribution (SED) of the post-novae, the continuum of dereddened spectra in the wavelength range $4500 - 7000 \text{ \AA}$ was fitted with a power law $F = \lambda^{-\alpha}$ with the NFIT1D task, included in the Space Telescope Science Data Analysis System (STSDAS) IRAF package. The power-law exponents α are presented in Table 2.6.

²<https://aladin.u-strasbg.fr/aladin.gml>

³<https://irsa.ipac.caltech.edu/applications/DUST/>

⁴<https://stilism.obspm.fr>

Table 2.3: Fields with colour-colour diagrams in order to detect possible post-nova candidates. The set of filters used are shown in columns two to five and the field is marked with \checkmark whether it was observed using that configuration. Those indicated in parentheses were analysed before the start this PhD project. Column six indicated whether a candidate was detected and column seven whether the nova was confirmed spectroscopically. Those objects with ? will be spectroscopically observed during the semester 2022A.

Field	$UBVR$	$VH\alpha[SII]$	$r'H\alpha[SII]$	$g'H\alpha[SII]$	Candidate detected?	spectroscopically confirmed?
EL Aql	\checkmark	\times	\times	\times	\checkmark	\checkmark
V841 Aql	\times	\checkmark	\times	\times	\times	\times
V606 Aql	\checkmark	\times	\times	\times	\checkmark	\checkmark
T Boo	(\checkmark)	\checkmark	\times	\times	\times	\times
U Leo	(\checkmark)	\checkmark	\times	\times	\times	\times
KT Mon	\checkmark	\times	\times	\times	\checkmark	\checkmark
V341 Nor	\times	\checkmark	\times	\times	\times	\times
V906 Oph	(\checkmark)	\checkmark	\times	\times	\times	\times
V908 Oph	\checkmark	\times	\times	\times	\checkmark	\checkmark
AT Sgr	\times	\checkmark	\times	\times	\times	\times
FL Sgr	(\checkmark)	\times	\times	\checkmark	\times	\times
KY Sgr	\times	\checkmark	\times	\times	\checkmark	\checkmark
V441 Sgr	(\checkmark)	\times	\times	\checkmark	\times	\times
V726 Sgr	\times	\times	\checkmark	\times	\checkmark	\checkmark
V732 Sgr	(\checkmark)	\times	\times	\times	\times	\times
V990 Sgr	(\checkmark)	\checkmark	\times	\times	\times	\times
V1148 Sgr	(\checkmark)	\times	\times	\times	\times	\times
V1149 Sgr	\checkmark	\times	\times	\times	\checkmark	\checkmark
V1174 Sgr	\times	\times	\checkmark	\times	\times	\times
V1583 Sgr	\checkmark	\times	\times	\times	\checkmark	\checkmark
V3888 Sgr	\times	\checkmark	\times	\times	\checkmark	?
V4065 Sgr	\times	\times	\times	\checkmark	\times	\times
V4092 Sgr	\times	\checkmark	\times	\times	\times	\times
FS Sct	\times	\checkmark	\times	\times	\times	\times
KP Sco	(\checkmark)	\checkmark	\times	\checkmark	\checkmark	?
V707 Sco	(\checkmark)	\times	\times	\checkmark	\times	\times
V711 Sco	\times	\times	\times	\checkmark	\times	\times
V719 Sco	(\checkmark)	\checkmark	\checkmark	\times	\times	\times
V720 Sco	(\checkmark)	\times	\times	\checkmark	\times	\times
V721 Sco	\times	\checkmark	\times	\times	\times	?
V722 Sco	(\checkmark)	\times	\times	\checkmark	\times	\times
V723 Sco	\times	\times	\times	\checkmark	\times	\times
V825 Sco	\times	\times	\times	\times	\checkmark	\checkmark
V902 Sco	(\checkmark)	\times	\times	\times	\times	\times
V977 Sco	\times	\times	\times	\checkmark	\times	\times

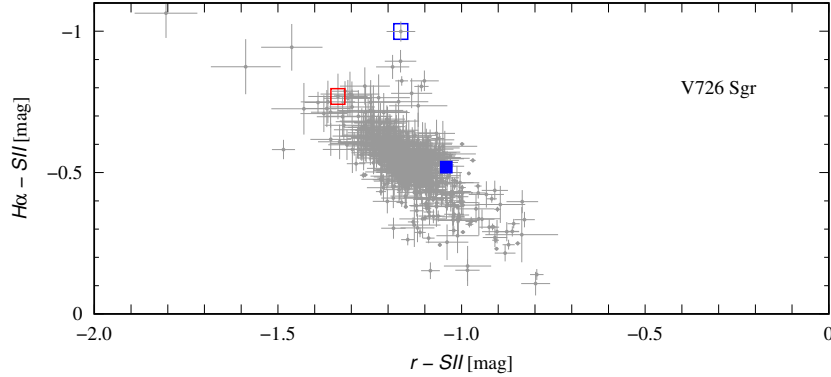


Figure 2.1: $H\alpha$ -[SII] v/s r -[SII] colour-colour diagram for V726 Sgr. The Mróz candidate is shown as the solid blue square, a rejected possible candidate appears as the open blue square while the recovered post-nova is shown as a red square.

2.4 Analysis and Results

2.4.1 Searching for post-novae in colour-colour diagrams

In the fields where the old nova counterpart position was still uncertain, colour-colour diagrams were created extending the search area for a nova to 3 arcmin^2 around the coordinates reported in the Downes et al. (2005) catalogue, allowing a higher probability of detecting the nova (e.g. the post-nova V728 Sco was recovered $\sim 2 \text{ arcmin}$ off its documented position; Tappert et al. 2013b). Here only diagrams based on $H\alpha$ photometry are presented for post-novae⁵ that were spectroscopically observed and the $UBVR$ data are presented for those fields where effectively the post-nova has been confirmed, which have been published in Tappert et al. (2016), except for KT Mon. For a summary on all fields with photometric observations see Table 2.3. The $H\alpha$ -[SII] v/s r -[SII], $U-B$ v/s $V-R$ and $H\alpha$ -[SII] v/s V -[SII] diagrams are shown in Figs. 2.1, 2.2 and 2.3 respectively. Observed, but rejected candidates, are marked with a blue square while the confirmed post-nova is marked with a red square. Further details are presented in the respective subsections of sections 2.4.2 and 2.4.4.

2.4.2 Recovered post-novae

The old novae recovered within this project are described in this section, that contains both results already published in Tappert et al. (2016) and yet unpublished ones, which are part of Fuentes-Morales et al. in prep. The published novae are: EL Aql, V606 Aql, V908 Oph, V1149 Sgr, V1583 Sgr and V3964 Sgr and the results from the paper are summarized here. Those unpublished are: EY Aql, V1370 Aql, V693 CrA, KT Mon, KY Sgr, V726 Sgr, V4049 Sgr and V825 Sco.

⁵V3888 Sgr, KP Sco and V721 Sco will be observed in semester 2022A.

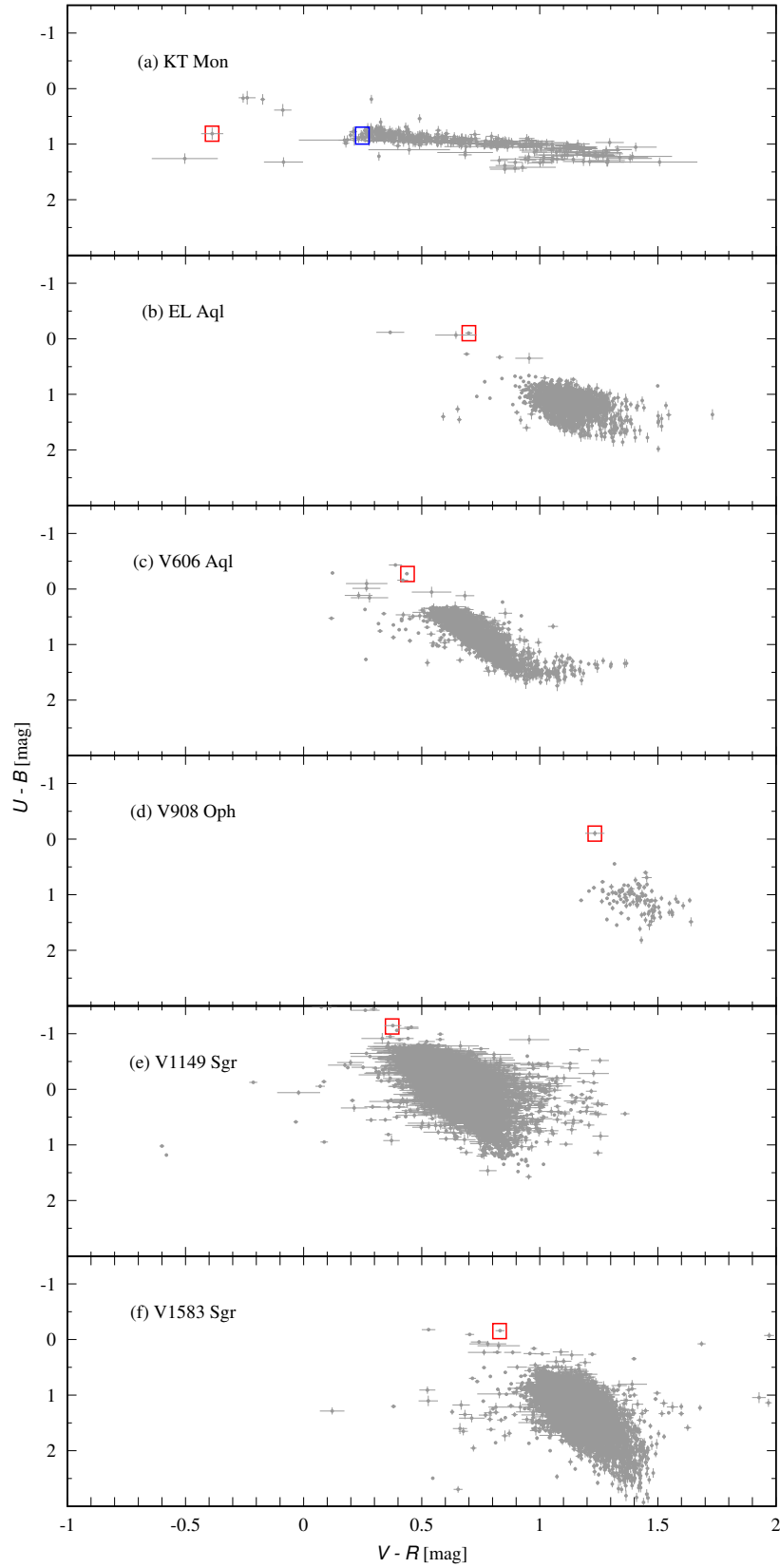


Figure 2.2: $U-B$ v/s $V-R$ colour-colour diagram for the recovered post-novae with respect to the fields stars. The confirmed post-novae are marked with a red square. For KT Mon also the candidate proposed by Kamath (2009) is shown, marked with a blue square (see more detail in section 2.4.2.5).

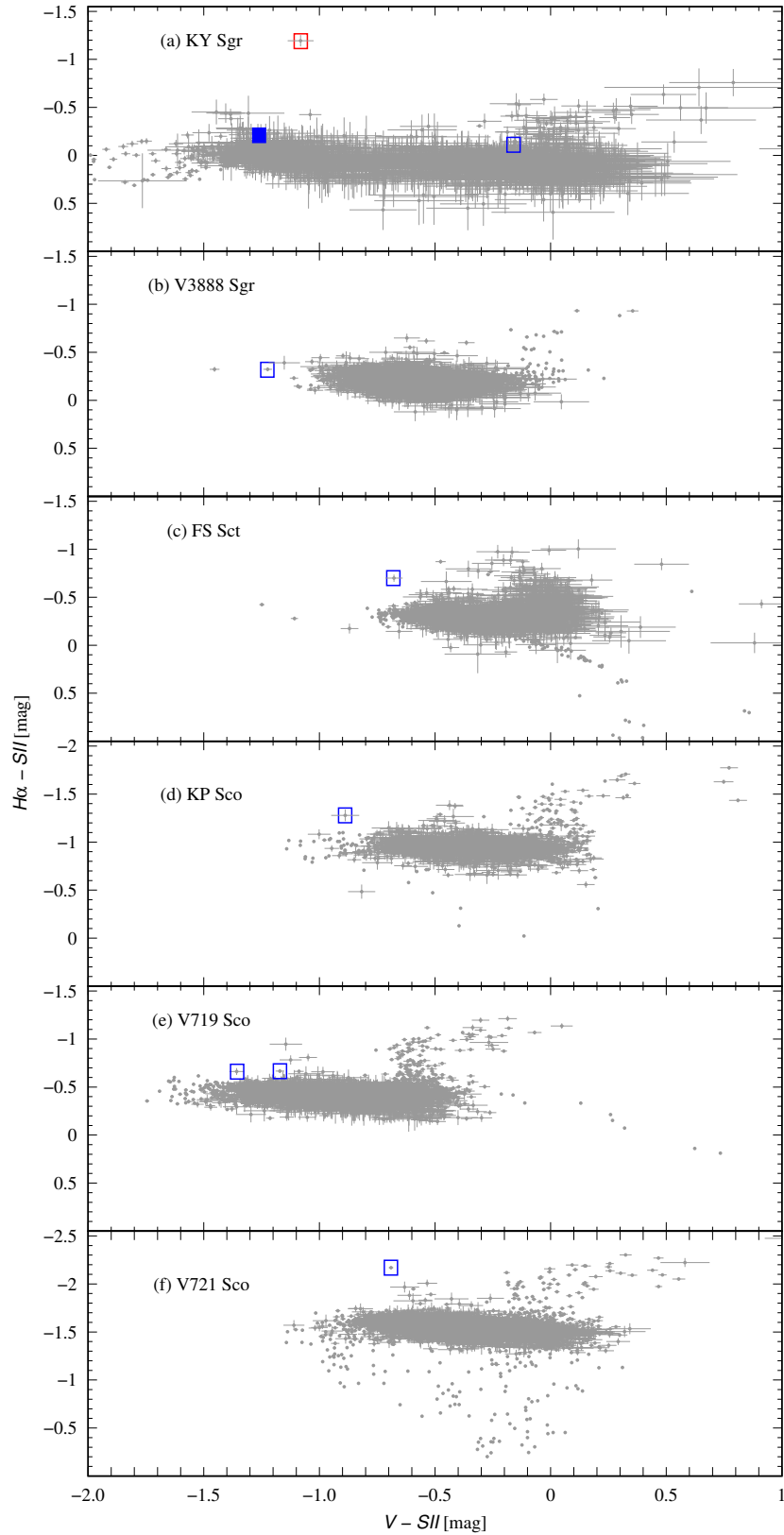


Figure 2.3: $H\alpha - [SII]$ v/s $V - [SII]$ colour-colour diagram for fields where post-nova candidates were detected. They are indicated with a blue square. For (c) and (e) they were spectroscopically observed but proved to be not the old nova counterpart. Candidates from (b), (d) and (f) will be observed in the course of the semester 2022A. For KY Sgr also our candidate, the Mróz one and the nova according to the coordinates from the [Downes et al.](#)' catalog are shown. They are marked with a red, filled and empty blue square respectively (for more detail see section 2.4.2.6).

2.4.2.1 EL Aql (1927)

The nova was discovered by [Wolf \(1927\)](#) as a star of photographic magnitude $m_p = 9$ mag on photographic plates taken on 1927 July 30 and 31. Examination of pre-discovery Harvard plates by [Cannon \(1927\)](#) revealed the object having reached its peak brightness before that date. The brightest recorded value is 6.4 mag on 1927 June 15. This nova was well covered during the decline phase both photometric and spectroscopically (e.g. [Wyse 1940](#)), however there is no information about its post-nova state.

A candidate for the post-nova was selected from our *UBVR* photometric data on the basis of its colours (Fig. 2.2, b) and its proximity (3 arcsec) to the coordinates reported in [Downes et al. \(2005\)](#). The spectrum of this object presents emission lines typical for a CV and we conclude that it is indeed the post-nova with $V = 20.9$ mag, considerably fainter than the magnitude derived by [Szkody \(1994\)](#), with a value of $V = 18.5$ mag for observations made in 1989. It is, in principle, possible that those observations above caught the post-nova in a bright state (or our data were taken in a low state). However, we consider this unlikely, because CVs in bright states are also expected to have bluer colours than in low states, and the object observed by [Szkody \(1994\)](#) is significantly redder in the visual range ($(B - V) = 1.34$ mag compared to our 0.62 mag, see Table 2.6). This led [Pagnotta & Schaefer \(2014\)](#) to suspect the nova to contain a giant secondary star. However, the spectral appearance of the post-nova (Fig. 2.4) and its position in the colour–colour diagram does not support this interpretation, and it thus again appears more likely that [Szkody \(1994\)](#) analysed a different object. We furthermore note that the resulting eruption amplitude $A=14.5$ mag basically excludes EL Aql as a recurrent nova candidate.

EL Aql presents a rich emission line spectrum (Fig. 2.4, Table 2.4). The Balmer lines are exceptionally strong for an old nova. The continuum has a slightly red slope, but as can be seen from the comparison of the colour–colour diagrams (Fig. 2.2), the field of EL Aql is significantly affected by interstellar reddening. From the IRSA website, we find $E(B - V) = 1.11(08)$ mag, and when corrected for that value, an inverse power law with an exponent $\alpha = 3.12(02)$ provides an excellent fit to the continuum slope.

The spectroscopic data on EL Aql consist of four individual spectra. In Fig. 2.7, the $H\alpha$ profile varies significantly over the course ~ 1 h of our observations. We find that the line as a whole shows a significant Doppler shift. Estimating the shift in radial velocity units by fitting a single Gaussian function to the line profiles yields a variation of $\Delta v_r \sim 100$ km/s over the observed time range, implying that this system can be seen at moderately or high inclination.

2.4.2.2 EY Aql (1926)

Nova EY Aql was discovered by [Albitzky \(1929\)](#) on five plates taken between 1926 September 8 and 30, at the Simeis Observatory in Ukraine. [Duerbeck \(1984\)](#) recompiled those photographic

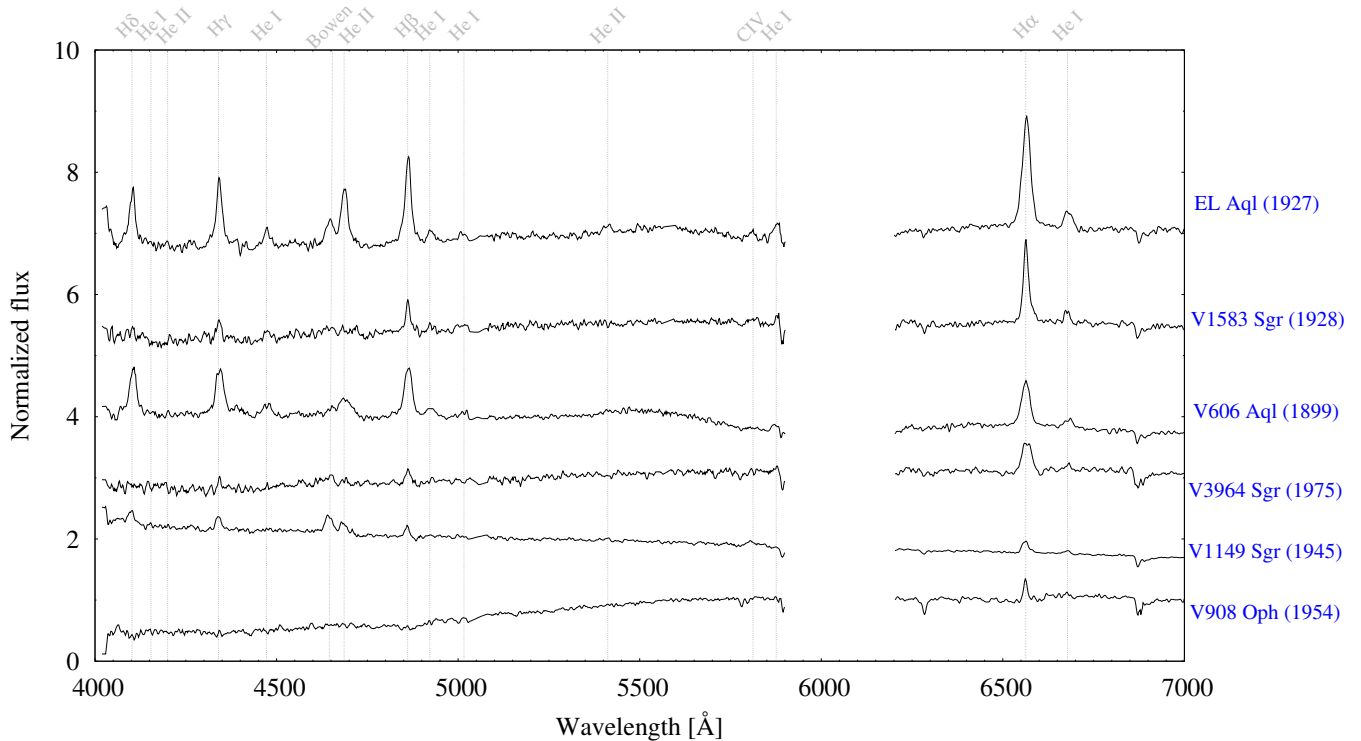


Figure 2.4: Spectra of recovered post-novae published in Tappert et al. (2016). The y-axis represents the normalized flux. Spectra are displaced in that direction for visualization purposes.

plates in order to improve the light curve of the outburst, concluding that the maximum was brighter than $m_p = 11$ mag, and that the decline was that of a moderately fast nova with a decline timescale $t_3 \sim 40$ d. Based on this information of the rate of decline and assuming an outburst amplitude $A \sim 9.5$ mag, Kato et al. (2001) catalogued it as a WZ Sge-Type dwarf nova candidate, i.e., a CV with very large disc brightness fluctuations, a strong presence of the primary in the optical spectrum and a short orbital period.

No spectroscopic confirmation is available in the literature for this nova. Our GMOS spectrum for the object at the Downes et al. catalog position reveals that the object is not the nova. Instead, the faint object ($R = 23.3$ mag) closest to the candidate position 2.07 arcsec away is identified as the nova. In total nine spectra were observed covering a time span of about 1 h. Because the original candidate is brighter, the exposure time for each frame is relatively low, so that the the individual spectra of the real nova have low S/N. For that reason, only the combined spectrum proved useful, and the individual spectra could not be used to examine them for time variations. Considering the average reddening calculated in IRSA, the field is substantially affected by interstellar extinction with $E(B - V) = 1.52(4)$, thus in our spectrum the blue section of the continuum is very noisy (Fig. 2.5). The corrected continuum is fitted with a power law index $\alpha = 2.61(7)$ (Table 2.6). In the spectrum, $H\beta$, the Bowen/He II blend, the He I series lines at $\lambda 5876\text{\AA}$, $\lambda 6678\text{\AA}$ and He II $\lambda 5412\text{\AA}$ emission lines are barely detected above the continuum. The spectrum exhibits a

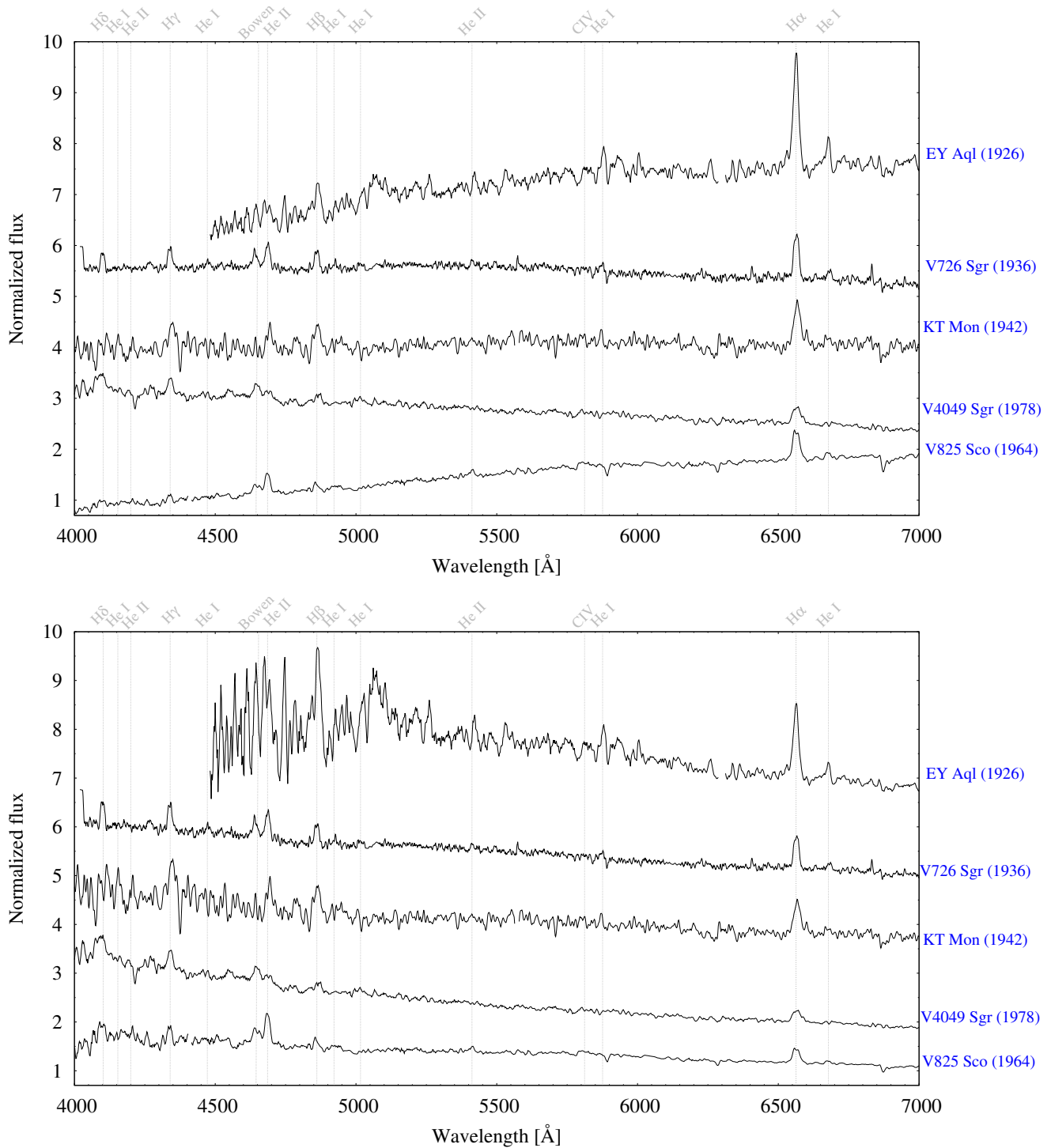


Figure 2.5: Top: Spectra of recovered post-novae in this work: EY Aql, KT Mon, V825 Sco, V726 Sgr, and V4049 Sgr. Bottom: The same spectra after reddening corrections considering as $E(B - V)$ those values presented in Table 2.6.

prominent $H\alpha$ line with an equivalent width value $W_\alpha = 30\text{\AA}$ (see Fig. 2.5 and Table 2.4). Finally, assuming a $V - R$ average value of 0.2 mag from Szkody (1994), $V = 23.5(5)$ mag in quiescence, yields $A > 12.5$ mag, which is much larger than that supposed by Kato et al. (2001).

2.4.2.3 V606 Aql (1899)

This nova was discovered by Fleming as an object of $m_p = 7$ mag on a photographic plate from 1899 April 21, as reported by Pickering & Fleming (1900). There is a ~ 200 d gap of observations prior to the discovery, and it is thus possible that the real maximum has been missed. Duerbeck (1987) estimates the peak brightness to 5.5 mag. The observed decline light curve as shown in Shapley (1933) covers ~ 160 d, and suggests a classification as type ‘P’ (Strope et al. 2010). In 1991, Ringwald et al. (1996) obtained spectroscopy of the suspected post-nova, but found a G7–K4 type spectrum for a $V = 16.3$ mag object.

The south-western component of an unresolved visual binary that was marked in Downes et al. (2005) as the possible post-nova showed promising colours (Fig. 2.2, Table 2.6). Subsequent spectroscopy of the $V = 20.4$ mag object confirmed the nova (Fig. 2.4). The spectrum presents comparatively strong Balmer emission lines, although not as strong as in EL Aql. The high excitation lines are even considerably weaker, and we do not detect $\text{He II } \lambda 5412\text{\AA}$. The spectrum presents a slightly blue continuum slope, and the colour–colour diagram shows that the field is only moderately affected by interstellar extinction (Fig. 2.2). After dereddening with a value $E(B - V) = 0.35(03)$ mag, it became apparent that the continuum was distorted by a number of large ‘bumps’. After examining the three individual spectra, we concluded that the bumpy structure is not intrinsic but an artefact. However, the presence of the bumps rendered large parts of the continuum unusable for fitting. We thus chose a number of small regions of continuum between the blue emission lines as well as a couple of regions around 6000\AA to determine an inverse power-law exponent of $\alpha = 2.02(02)$. When examining the $H\alpha$ line profile of the individual spectra, the changes are not as pronounced as in EL Aql, and the Doppler shift of the whole profile is not as large (Fig. 2.7). Still, the shape of the line profile is clearly variable, and the width of the emission lines is basically identical to those in EL Aql.

2.4.2.4 V908 Oph (1954)

Very few data are available for V908 Oph. Its discovery was reported by Blanco (1954) who detected O I emission in a near-infrared spectrum taken on 1954 July 2. He estimated the brightness in this spectral range to 9 mag, but suspected that the nova was observed about a week after its maximum brightness. The only other observations consist of two objective prism spectra taken on 1954 July 27 by Seyfert & Yoss (1954). Apart from strong $H\alpha$ emission, they could not distinguish

more detailed spectral features due to the object having declined to a blue magnitude ‘probably less than 14’. If the object was indeed observed several days after having reached its maximum brightness, and accounting for the colour differences between the two observations and for the strong interstellar reddening, the time t_3 is likely to be in the order of 30–40 d, which would classify the object as a moderately fast nova.

The coordinates of the nova had only been recorded with a precision in the order of arcmin, but fortunately, a candidate for the post-nova can be easily identified in the colour–colour diagram (Fig. 2.2). Its spectrum presents a few weak hydrogen emission lines, with those bluewards of $H\alpha$ being embedded in absorption troughs, and a red continuum slope (Fig. 2.4). From the *UBVR* photometry, it is clear that the field is strongly affected by interstellar reddening, and the respective catalogue yields an accordingly high $E(B - V) = 1.26(02)$ mag. Once corrected for this value, the SED corresponds to a steep blue power law with a negative exponent $\alpha = 3.38(02)$. Thus, the spectral characteristics are consistent with a high mass-transfer system. We also note that high excitation emission lines like the Bowen blend or He II are absent or, at least, very weak. This is in stark contrast to other likely high mass-transfer post-novae like GR Sgr (Tappert et al. 2015). Towards the red side of $H\alpha$ emission, there appears to be another peak that could be identified with the C II $\lambda\lambda 6578, 6583$ doublet. This line has been previously detected in a few old novae with sufficiently narrow $H\alpha$ emission lines (Tappert et al. 2013a), and the latter also applies to V908 Oph. However, the signal-to-noise ratio (S/N) in that part of the spectrum is low, and there are a number of similar large features close-by, which we were unable to identify and thus suspect to be artefacts. In consequence, the detection of C II in this object remains ambiguous.

We finally remark that we did not detect any significant positional variation of the $H\alpha$ line in the three individual spectra.

2.4.2.5 KT Mon (1942)

Nova Monocerotis 1942 (KT Mon) was discovered by A. N. Vyssotsky on a spectroscopic plate a few weeks after maximum brightness (Gaposchkin 1954). From later analysis of further photographic plates the observed maximum value results to 10.3 mag, but the shape of the light curve indicates that the real maximum must have been at 9.8 mag or brighter (Gaposchkin 1954), categorizing it as moderately fast nova with $t_3 = 40$ d (Duerbeck 1987).

The most extensive study of this nova was carried out by Kato & Yamaoka (2002). Based on the description of the spectral characteristics in above spectrum and the large distance estimated to the galactic center (Payne-Gaposchkin 1977), they suggest that KT Mon was not a classical nova. They explore several alternatives, namely that of a recurrent nova, a WZ Sge-type dwarf nova and an X-ray transient (mostly black hole candidates). Searching in the literature, just one attempt to identify the correct position has been reported. Kamath (2009) identified a possible candidate in the field based on its blue colour and $H\alpha$ brightness. However, no follow-up spectroscopic was

carried out in order to confirm its nature. Thus, the identification of the post-nova system remained ambiguous. From a colour-colour diagram based on *UBVR* photometric data taken with FORS2, we find a likely candidate for KT Mon at $V = 23.1$ mag and close to the reported position of the nova (at 4.45 arcsec to north-east away), while the candidate reported by Kamath (2009) does not present any exceptional colour (see blue square in Fig. 2.2, a).

Spectroscopy of our candidate confirmed its nature as a nova. The continuum is slightly affected by the reddening according to the value calculated in IRSA, exhibiting a slight slope towards the blue with a power law exponent $\alpha = 1.50(5)$ after reddening correction. The Balmer $H\alpha$ and $H\beta$ emission lines are broad and moderately strong with $W_{H\alpha} = 25\text{\AA}$ and $W_{H\beta} = 15\text{\AA}$. The He I series is barely present, while the Bowen blend is not detected and He II is almost stronger than $H\beta$ (see Fig. 2.5 and Table 2.4). On the other hand, like for EY Aql (Section 2.4.2.2), the S/N of the individual spectra is too low to examine time variations in the nine individual spectra, which were acquired over a time range of 1.7 h.

2.4.2.6 KY Sgr (1926)

Nova Sgr 1926 was discovered on plates taken in Arequipa with the Metcalf telescope by Woods (1928), who also indicates that the pre-nova brightness should have been fainter than 16.5 mag (the limit detection) because no star was reported in the position before June 11, 1926, date of the maximum light at $m_p = 10.6$ mag. The recorded position is very uncertain due to the low quality of the image on the plates. It was classified as a moderately fast nova with $t_3 = 60$ d (Duerbeck 1987).

No spectroscopic data are available in the literature and only studies based on photometry are found. Pagnotta & Schaefer (2014) listed the object at the position given in the Downes et al.’ catalog for KY Sgr as a likely recurrent nova with a red giant as secondary, according to its location in $J - H$ versus $H - K$ colour-colour diagram. Searching for old nova counterparts in the Optical Gravitational Lensing Experiment (OGLE) survey, Mróz et al. (2015) catalogued as a possible post-nova candidate the same object studied by Pagnotta & Schaefer (2014). However, Mróz via private communication sent us the coordinates and a finding chart of another object, an eclipsing one with an orbital period of 1.089652 d, which he also considered as a possible post-nova candidate. Our $H\alpha$ colour data analysis shows that both the Mróz candidate and the Downes et al. catalog object are placed within the field stars, while a different object 1.12 arcmin away from the original reported position was $H\alpha$ bright (see Fig. 2.3, a). Mróz (private communication) later confirmed that this object shows long-term irregular variability, without any significant stable periodicities in the light curve (in the range 0.04 – 1000 days). Spectroscopic data were obtained for his candidate and ours. The Mróz candidate is most likely a contact binary of the W UMa class. Our candidate presents a spectrum that resembles a symbiotic star rather than a classical nova (Fig. 2.6). Balmer emission lines are present, with $H\alpha$ as a very narrow and strong emission line. He I $\lambda\lambda 5876-$

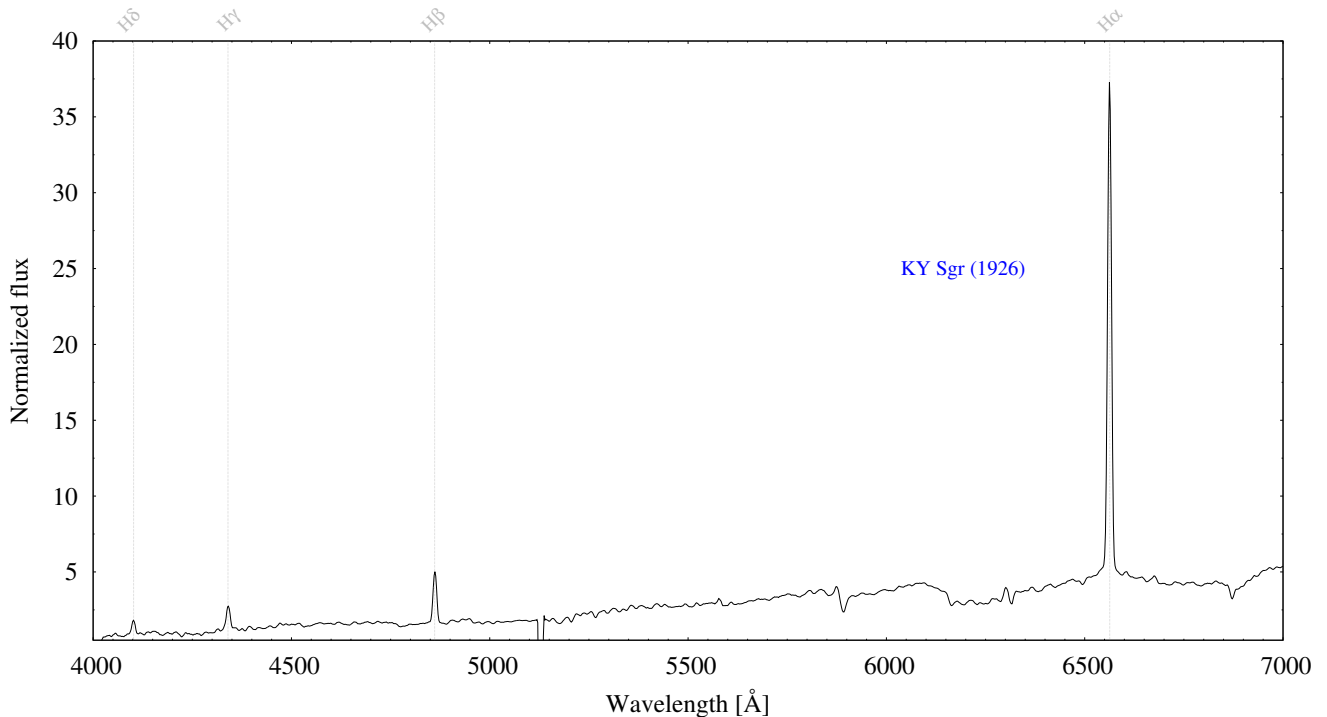


Figure 2.6: Dereddened spectrum of the likely recurrent nova KY Sgr. See section 2.4.2.6 for more details.

6678Å emission lines are also visible. Features from the secondary are clearly distinguishable, like Na I λ 5686Å, C IV λ 5805Å, O I λ 5577Å absorption lines, quite similar to the symbiotic recurrent nova RS Oph. The interstellar extinction was computed using the Stilism data, considering the calculated Gaia distance taking into account the considerations described in section 2.3, giving $d = 347(40)$ pc. This yields $E(B - V) = 0.125(62)$ which is in strong contrast to the large-scale value from IRSA ($E(B - V) = 3.35(8)$), emphasizing the uncertainty involved in averaging the reddening over a certain area instead of measuring it in the line-of-sight of an object. Hence, the continuum is not much affected by reddening, but is intrinsically red, with its slope being represented by a power law with exponent $\alpha = -3.29(7)$. Although we have insufficient data we consider it most likely that KY Sgr is a RN. With this, we ultimately agree with the conclusion of Pagnotta & Schaefer (2014), even though that one was based on a completely different object. The analysis for this object demonstrates the importance of using colours and spectroscopic confirmation instead of relying only on photometric variability.

2.4.2.7 V726 Sgr (1936b)

Nova Sgr 1936b was the second nova erupting in 1936. It was discovered by Luyten (1937) and separately by Mayall (1938), who published the light curve and also described its spectrum taken a few weeks after the eruption. According to the light curve, it was not visible until 1936 April 30, because it was fainter than the detection limit. The maximum brightness was possibly attained a

few days before May 13 at $m_p = 10.8$ mag, and with the decline timescales $t_2 = 45$ d and $t_3 = 95$ d it was classified as a moderately fast nova. The Harvard plate used by [Duerbeck \(1987\)](#) to derive the position of this nova did not allow a proper identification. [Mróz et al. \(2015\)](#) found an object very close to the reported position which shows ellipsoidal variability from OGLE photometric data, cataloguing it as the nova. From our H α photometry one object very close to the position reported by [Mróz et al. \(2015\)](#) is H α bright (blue square in Fig. 2.1). Because spectroscopy is the way to confirm the nova, we oriented the slit in such a way that both candidates were observed. However, neither of those objects turned out to be the nova, instead a faint object at $R=20.9$ mag located between both candidates, 1.68 arcsec away from Mróz’s position is the post-nova. Even though the nova was detected by our H α photometry, surprisingly that object is not H α bright (see Fig. 2.1 red square). The spectrum exhibits the Balmer series up to H δ , with a bluish continuum after the reddening correction, being fitted with a power law index $\alpha = 2.19(3)$. He I lines are barely above the continuum level, just as He II $\lambda 5412\text{\AA}$. The most remarkable features are the presence of C II $\lambda 4267\text{\AA}$ and the strength of the Bowen blend and He II $\lambda 4686\text{\AA}$, the latter one being even stronger than H β . A close-up of the four individual spectra taken over a time range of ~ 1 h, shows that the H α peak is displaced to the red, moving towards the center in the last spectrum (Fig. 2.10). On the other hand, the Mróz candidate shows pure absorption lines (see section 2.4.4 and Fig 2.16 for more details).

2.4.2.8 V1149 Sgr (1945)

The nova was discovered by [Mayall \(1949\)](#) on an objective prism plate at a photographic brightness of about 9 mag. Later research by Warren (1965) revealed the maximum brightness to 7.4 mag. The light curve is described as a ‘very steep increase in brightness [...] followed by a rapid initial decrease’, reaching a plateau by 1946 May 28. The nova was visible from 1945 May 16 to 1948 May 30, and afterwards faded below 14.7 mag. Large gaps in the observations prevent a more detailed analysis. From our *UBVR* photometry (Fig. 2.2) we selected two potential candidates for the post-nova based on their colours and coordinates. Spectroscopy showed one of those to present emission lines and a blue continuum, and we thus identify this object as the post-nova. It is located ~ 11 arcsec south-west of the previously reported position. We note that these coordinates do not coincide with the objects labelled as V1149 Sgr in [Saito et al. \(2013\)](#) and in [Mróz et al. \(2015\)](#). The spectrum shows a blue continuum, that becomes somewhat steeper ($\alpha = 2.41(01)$) when corrected for the catalogued interstellar reddening of $E(B - V) = 0.39(03)$ mag, and weak emission lines (Fig. 2.4). In contrast to V908 Oph (Section 2.4.2.4), V1149 Sgr counts with a strong Bowen blend and He II $\lambda 4686$ emission. The Balmer lines are comparatively narrow, and a bump on the red wing of H α could tentatively be identified with C II. The three individual spectra do not show any significant radial velocity variations.

2.4.2.9 V1583 Sgr (1928)

An examination of archival photographic plates by Dishong & Hoffleit (1955) led to the discovery of this nova almost 30 yr after its eruption. Still, in contrast to other novae, the maximum brightness of 8.9 mag on 1928 June 24 appears to be well established. The authors report that two days before that night, the nova was fainter than 15.6 mag and that it fell again below the plate detection limit 75 d after maximum brightness. The system is classified as a moderately fast nova with a decline time $t_3 = 37$ d (Duerbeck 1987). From its colours (Fig. 2.2, Table 2.6) and its position only 3.5 arcsec off the reported coordinates, we identified a candidate for the nova. Subsequent spectroscopy show a slightly reddish continuum (Fig. 2.4), which is likely the consequence of a comparatively strong interstellar reddening ($E(B - V) = 1.09(04)$ mag). Like for most of the other systems, the corrected SED presents a blue slope, with $\alpha = 3.27(02)$. Superposed are moderately strong emission lines (Table 2.4) of the Balmer and He I series. Similar to V908 Oph (Section 2.4.2.4), the Bowen blend and He II $\lambda 4686$ lines are weak and hardly detectable. The emission lines are also comparatively narrow, but still the line profile shows some clear asymmetric structure and marked differences between the individual exposures (Fig. 2.7). We especially notice that the line strength in the third spectrum of that series is significantly diminished, which indicates that the emission source is being obscured.

2.4.2.10 V3964 Sgr (1975)

Tappert et al. (2015) had observed a candidate for this nova that turned out to be a K1V star. However, examination of the 2D spectra showed the possibility of H α emission from a different star in the slit, and a likely source of this emission was identified. Here, we present further spectroscopic observations of that target. The spectrum in Fig. 2.4 clearly reveals it as the post-nova system, presenting the typical hydrogen and helium emission lines, as well as a weak Bowen blend. The continuum has a red slope, but like in the other objects, this is due to interstellar reddening. Still, even after the correction for $E(B - V) = 0.56(01)$ mag, the slope appears significantly flatter than in the other systems, being represented by an exponent $\alpha = 1.43(03)$. The emission lines are not particularly strong (Table 2.4), but broad, and even show, at times, a hint of a double-peaked disc profile (Fig. 2.7). Furthermore, like in V1583 Sgr (Section 2.4.2.9), the emission line in the third spectrum is significantly diminished compared to the other two spectra. On the other hand, a possible Doppler shift of the line is less clear.

2.4.2.11 V4049 Sgr (1978)

V4049 Sgr was spectroscopically discovered in the decline phase on a red-sensitive objective prism plate taken at Lund Observatory in Sweden, on 1978 March 8 (Stenholm & Lundstrom 1979). On March 9, it was detected at $m_p \sim 12$ mag. It was visible on Maria Mitchell plates in USA during

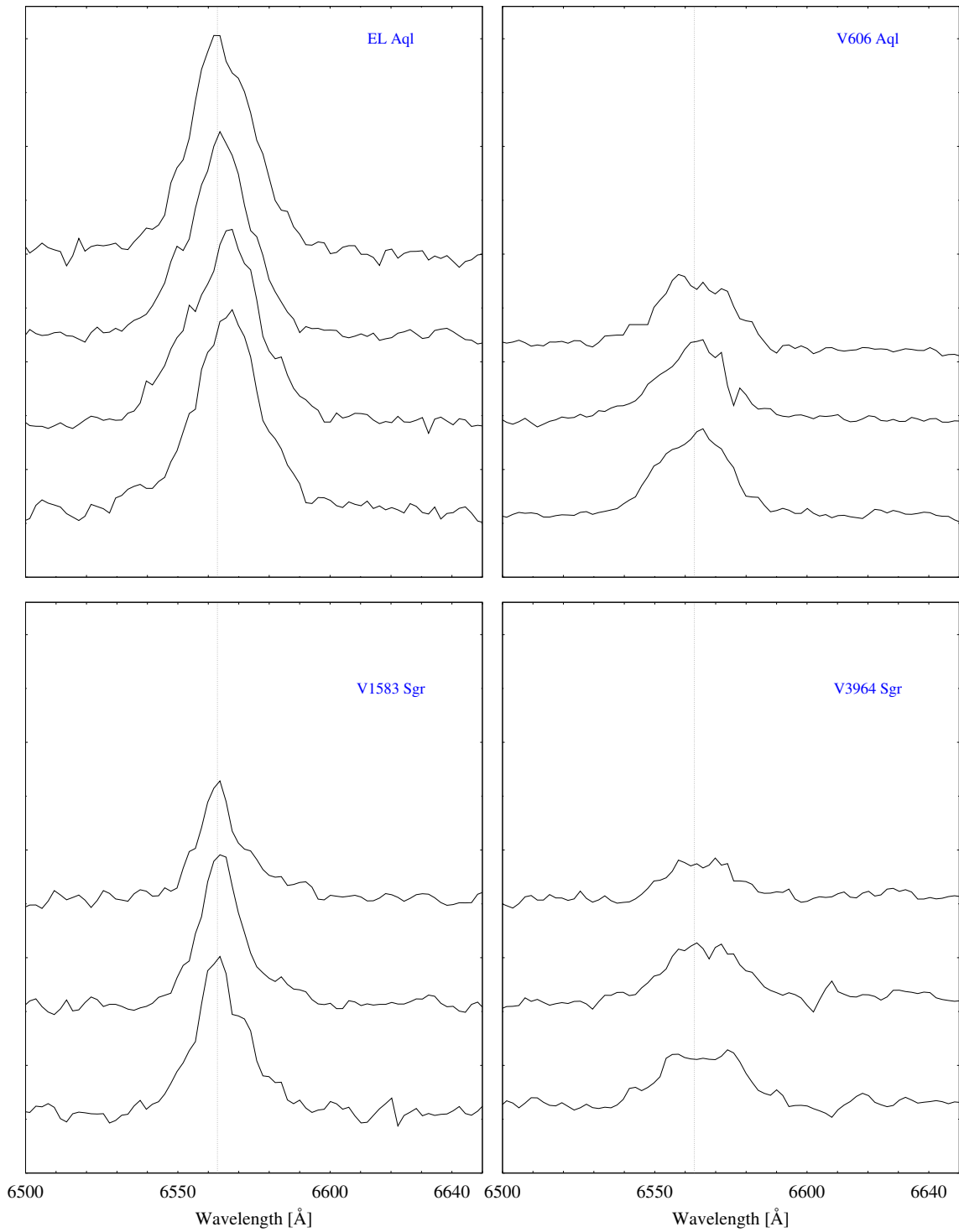


Figure 2.7: H α profiles for individual spectra of those novae showing short time variations. Those novae already published in [Tappert et al. \(2014\)](#) are EL Aql, V606 Aql V1583 Sgr and V3964 Sgr.

1978 June 30 to October 3 (Belsereine 1979a), but it could not be found in 1977 and 1979 due to it being fainter than the detection limit magnitude ($m_p \sim 15$). The light curve published by Belsereine (1979b) does not contain enough information to derive its speed class. On May 1979 the nova appeared fainter than the detection limit for the CTIO 4-m telescope, $m_p \sim 21$ mag, when optical spectroscopy revealed coronal lines, making it one of the few novae known with this type of lines (McCarthy et al. 1981). Despite its interesting behaviour no more spectroscopic follow-up was made.

Our spectroscopy reveals that the Downes et al. catalog coordinates are not correct. The true ones are those derived from the finding chart published by McCarthy et al. (1981). After reddening corrections (using the IRSA value $E(B - V) = 0.36(1)$), the spectrum shows a steep blue continuum fitted with a power law index $\alpha = 2.87(2)$, showing some artefacts (absorption at $\sim 4215\text{\AA}$ and emission at $\sim 4550\text{\AA}$) and weak and broad Balmer emission lines (Fig 2.5), with $H\gamma$ and $H\delta$ comparatively similar to $H\beta$ (see Table 2.4). The He I series is imperceptible while the Bowen blend is stronger than He II $\lambda 4686\text{\AA}$, with almost twice the equivalent width ($4.9(4)\text{\AA}$ vs $2.9(7)\text{\AA}$ respectively). No significant time variations in the $H\alpha$ profile are distinguished in the set of spectra taken.

2.4.2.12 V825 Sco (1964)

This nova was discovered several months after the maximum brightness as an object at $m_p = 12$ mag by A. Przybylski in 1964 May 19, at the Stromlo Observatory, Australia. The only spectra available for this object were taken by Wilde (1965) on June 14 and September 27, 1964, and they present strong [O III] and [Ne III] nebular emission lines. Assuming $t_3 = 80$ d, the typical time for a moderately slow nova, the author also estimated that the maximum should have occurred in December 1963 at $m_p \sim 8$ mag. However the light curve does not have enough data to accurately determine the speed class. There is no more information about this nova until Mróz et al. (2015), who detected deep eclipses for a faint object ($V = 19.54$ mag, $I = 18.23$ mag), 1.81 arcsec away from the Downes et al. catalog coordinates, with an orbital period $P_{\text{orb}} = 4.9$ h.

With the GMOS spectroscopy we confirm the Mróz candidate as the post-nova. It was observed during two epochs; on 2016 February 17 and March 11. For the first one the seeing was rather poor and the nova could not be resolved, whereas for the second one the conditions were much better. For this reason we considered only the three spectra of the latter run to produce an average spectrum (Fig. 2.5). The field is fairly affected by reddening considering the IRSA calculations, with $E(B - V) = 1.00(3)$ mag. The corrected continuum shows a gentle blue slope that can be fitted with a power law exponent $\alpha = 1.35(3)$. The spectrum presents moderately strong Balmer lines up to $H\delta$. C II $\lambda 4267\text{\AA}$ is also detected like in the case of V726 Sgr (Section 2.4.2.7). Both He II $\lambda 5412\text{\AA}$ and the Bowen/He II blend are present, with He II $\lambda 4686\text{\AA}$ being the strongest emission line with an equivalent width almost twice that for $H\beta$ (see Table 2.4). Another remarkable characteristic is the

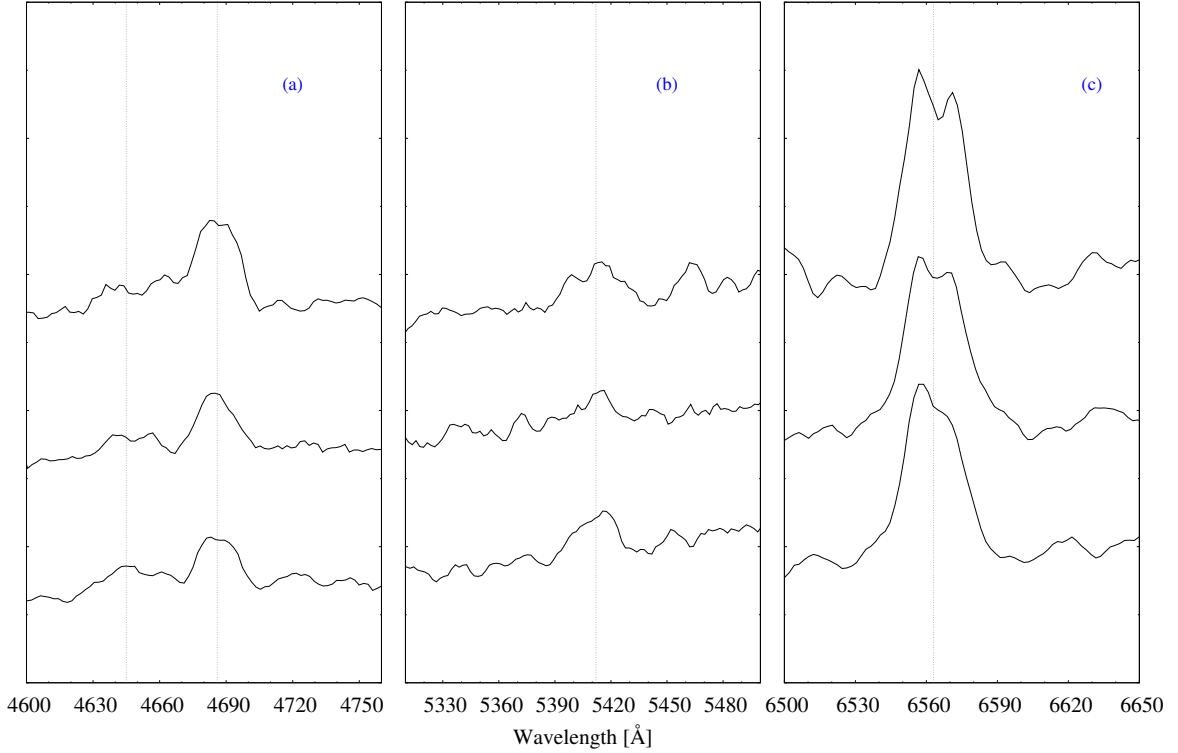


Figure 2.8: Close-up on selected wavelength ranges in the spectrum of the eclipsing post-nova V825 Sco. Individual spectra are shown in 15 min sequence from bottom to top. The vertical line indicates the rest wavelength of (a) Bowen/He II $\lambda 4686\text{\AA}$ (b) He II $\lambda 5412\text{\AA}$ and (c) for H α line profile.

absence of He I $\lambda 5876\text{\AA}$ and a strong Na I $\lambda 5892\text{\AA}$ absorption line. An analysis of the individual spectra show significant variability (Fig. 2.8), which is in good agreement with the eclipsing nature of this object. The H α line profile is showing the typical double-peaked profile and its shape points to it being captured in its blue-shifted phase, just after the mid-eclipse. No variations in H β can be detected due to the line being distorted by the gap between chips in the last spectrum. On the other hand, slight corresponding variations with respect to H α can be detected both in the Bowen/He II $\lambda 4686\text{\AA}$ and He II $\lambda 5412\text{\AA}$ lines, especially in the last spectrum, for which all lines appear to be double-peaked. Although this may be true for Bowen/He II $\lambda 4686\text{\AA}$, He II $\lambda 5412\text{\AA}$ is barely above the noise level, so that the observed variation could be strongly affected by the noise.

2.4.3 New spectra for known post-novae

2.4.3.1 V1370 Aql (1982)

This nova was discovered in Japan on 1982 January 27 at $V \sim 6 - 7$ mag (Kosai et al. 1982b). Only two years after the eruption it was observed at $V = 18.5$ mag and without any nebular contribution (Ringwald et al. 1996). An extensive summary on all available studies of this nova has been presented by Tappert et al. (2014). The spectrum analysed by them taken in 1993 exhibited a

Table 2.4: Equivalent width (top) and FWHM (bottom) of the emission lines present in the spectra of the old novae studied in this chapter. * refers to the Bowen/He II blend that could not be resolved. ** indicates emission cores in absorption troughs. Equivalent width for emission lines are defined as positive values for simplicity.

Object	H α	Balmer (\AA)		4472	4922	He I (\AA)			Bowen	He II (\AA)		C IV	OIII	
		H β	H γ			5016	5876	6678		4645	4686		5412	5805
EL Aql	47(1)	35(1)	26(1)	–	4(1)	3(1)	–	8(1)	–	45(2)*	3(1)	4(1)	–	–
EY Aql	33(1)	21(1)	–	–	–	–	4.2(8)	4.8(8)	–	–	4(1)	–	–	–
V606 Aql	26(1)	21(1)	18(1)	–	4(1)	2(1)	–	4(1)	–	16(1)*	–	–	–	–
V1370 Aql	34(2)	22(3)	17(1)	4(1)	1.5(4)	3.6(7)	8.9(8)	4(2)	9(2)	8.4(5)	–	–	–	–
V693 CrA	10(5)	–	–	–	–	–	–	–	–	–	–	–	–	–
KT Mon	24(3)	13.2(1.5)	–	–	–	–	3(1)	5(3)	–	14.5(2.5)	–	–	–	–
V908 Oph	3(1)	1(1)**	1(1)**	–	–	–	–	–	–	–	–	–	–	–
KY Sgr	81.6(3.1)	23.2(3.8)	17.1(3.1)	–	–	–	0.9(1)	1.5(2)	–	–	–	0.8(7)	–	–
V726 Sgr	24.9(3.6)	6(5)	6(4)	0.9(3)	–	–	–	4(2)	6(4)	9(5)	–	–	–	–
V1149 Sgr	6(1)	2(1)	3(1)	–	–	–	–	1(1)	5(1)	3(1)	1(1)	3(1)	–	–
V1583 Sgr	26(5)	9(1)	6(1)	–	3(1)	–	–	4(1)	5(1)	2(1)	–	–	–	–
V3964 Sgr	12(1)	5(1)	3(1)	–	1(1)	–	–	2(1)	3(1)	2(1)	–	–	–	–
V4049 Sgr	17(7)	4(2)	4.5(3)	–	–	–	–	–	4.9(4)	2.9(7)	–	–	–	–
V4077 Sgr	367(62)	52(2)	17.5(1.4)	2.2(3)	2.7(5)	–	20.7(2)	11.1(3)	18.1(3)	15.7(3)	–	5.0(5)	5.1(2)	23.6(2)
LW Ser	70(2)	12(2)	3(1)	3(1)	–	–	3.1(9)	2.5(1.2)	3.3(7)	1.8(7)	–	–	–	3.2(8)
V825 Sco	16(2)	4(0.5)**	6(1)	–	–	–	–	3(1)	6(1)	11(1)	3(0.5)	–	–	–
EL Aql	27	–	–	–	–	–	–	–	–	–	–	–	–	–
EY Aql	22(1)	19(1)	–	–	–	–	13(3)	13(3)	–	–	14(4)	–	–	–
V606 Aql	28	–	–	–	–	–	–	–	–	–	–	–	–	–
V1370 Aql	12.3(2)	23.3(7)	13.1(4)	14(2)	12(4)	24(6)	14(1)	11(3)	24(2)	19.5(1.5)	–	28(8)	–	–
V693 CrA	65(32)	–	–	–	–	–	–	–	–	–	–	–	–	–
KT Mon	28(2)	26(4)	–	–	–	–	11(4)	35(29)	–	27(4)	–	–	–	–
V908 Oph	12	–	–	–	–	–	–	–	–	–	–	–	–	–
KY Sgr	11.1(5)	10(2)	12(3)	–	–	–	10(8)	14(10)	–	–	–	12(11)	–	–
V726 Sgr	22(4)	17(14)	16(12)	8(7)	–	–	–	19(17)	20(17)	20(12)	–	–	–	–
V1149 Sgr	21	–	–	–	–	–	–	–	–	–	–	–	–	–
V1583 Sgr	17	–	–	–	–	–	–	–	–	–	–	–	–	–
V3964 Sgr	29	–	–	–	–	–	–	–	–	–	–	–	–	–
V4049 Sgr	35(17)	25(20)	18(14)	–	–	–	–	–	24(20)	33(30)	–	–	–	–
V4077 Sgr	23(1)	14(1)	14(1)	16(3)	20(3)	–	16(1)	20(1)	22(1)	24(1)	–	29(3)	11(1)	13(1)
LW Ser	31(1)	21(2)	10(3)	10(4)	–	–	14(5)	16(9)	10(3)	9(5)	–	–	–	11(3)
V825 Sco	31(1)	17(3)	26(5)	–	–	–	–	23(6)	26(5)	19(1)	23(5)	–	–	–

relatively flat continuum with strong and narrow Balmer emission lines, with $H\alpha$ showing probably an extra contributor as suggested by the flux ratio $H\alpha/H\beta$, a strong He I series and an outstanding Bowen/He II $\lambda 4686\text{\AA}$ blend. These characteristics were interpreted as indicators of V1370 Aql being an old nova with a comparatively low mass transfer rate seen likely at face-on.

Three spectra were acquired twenty three years after the one described above. The combined spectrum is quite similar in the sense of the Balmer lines being visible up to $H\delta$ with an almost flat continuum even after reddening correction, considering $E(B - V) = 0.41(2)$ mag from IRSA, giving a power law exponent $\alpha = 0.32(2)$ (it is worth mentioning that this parameter was not calculated by Tappert et al. (2014) because they did not correct for the instrumental response function and both the $H\beta$ and He I $\lambda 6678\text{\AA}$ line profiles are affected by artefacts in one of the spectra used in combining the spectra, for that reason the equivalent width and FWHM for both lines were calculated in the spectrum free of that distortion. The intensities of the He I, He II and Balmer lines are also similar within their error ranges, with the exception of He II $\lambda 4686\text{\AA}$, that has decreased to almost half its former intensity. Thus, the current state of the system definitively shows that those contributions seen in 1993 are diminished but not necessarily that the nova has already returned to its intrinsic quiescence state.

2.4.3.2 V693 CrA (1981)

V693 Corona Australis was a nova with maximum brightness at $V = 7$ mag reported by Honda in Japan, on 1981 April 2, who also informed that the object was not visible on observations taken in 1980 and one day before its discovery (Kozai et al. 1981). The optical light curve reveals a very fast speed class with $t_2 = 5.8$ d and $t_3 = 12$ d (Caldwell 1982). Despite being a bright object, this nova was not well studied at the optical wavelengths, but it was systematically monitored in the UV wavelength range by the International Ultraviolet Explorer satellite (IUE) for a period of seven months since April 10. Based on the chemical abundances it was concluded that the system is composed of a massive O-Ne-Mg white dwarf (Williams et al. 1985). Kato & Hachisu (2007) derived $M_{WD} = 1.3 M_{\odot}$ and a distance of 4.4 kpc from a light-curve model fitted to the UV 1455\AA light curve. Pagnotta & Schaefer (2014) catalogued it as a likely RN candidate based on the white dwarf mass criterion ($M_{WD} \geq 1.2M_{\odot}$) and a high FWHM attributed to a high expansion velocity. An optical spectrum taken twelve years after the outburst was presented by Tappert et al. (2014). They could not derive its magnitude because like with V1370 Aql, the spectra were not flux calibrated nor did they include any acquisition frames. The only information about the magnitude in quiescence has been recorded by Schmidtobreick et al. (2002) as $V = 21$ mag, implying a very large amplitude $A = 14$ mag. Despite the spectrum having a low S/N, a blue continuum with broad and weak emission Balmer lines can be distinguished. They concluded that the system has a high mass transfer rate and that the large FWHM is likely associated to a high inclination.

Our spectrum taken 22 years later exhibits a similar behaviour. Assuming the reddening value

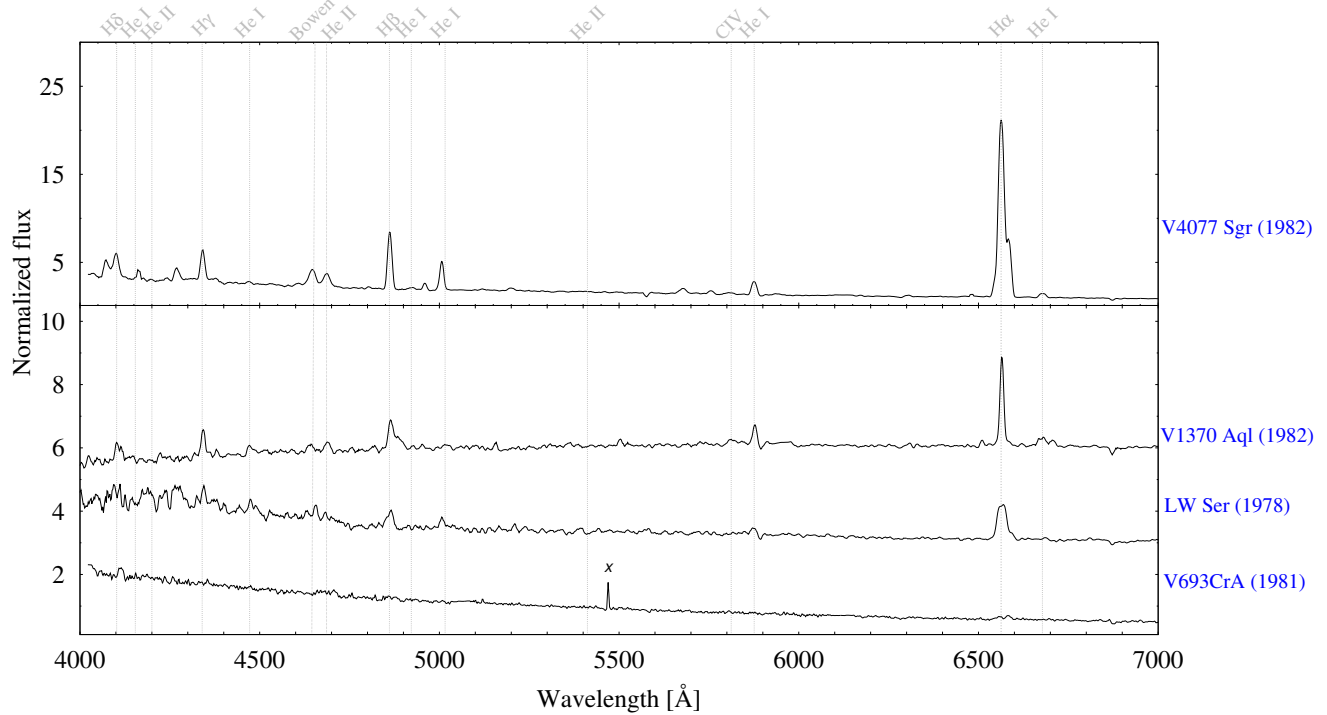
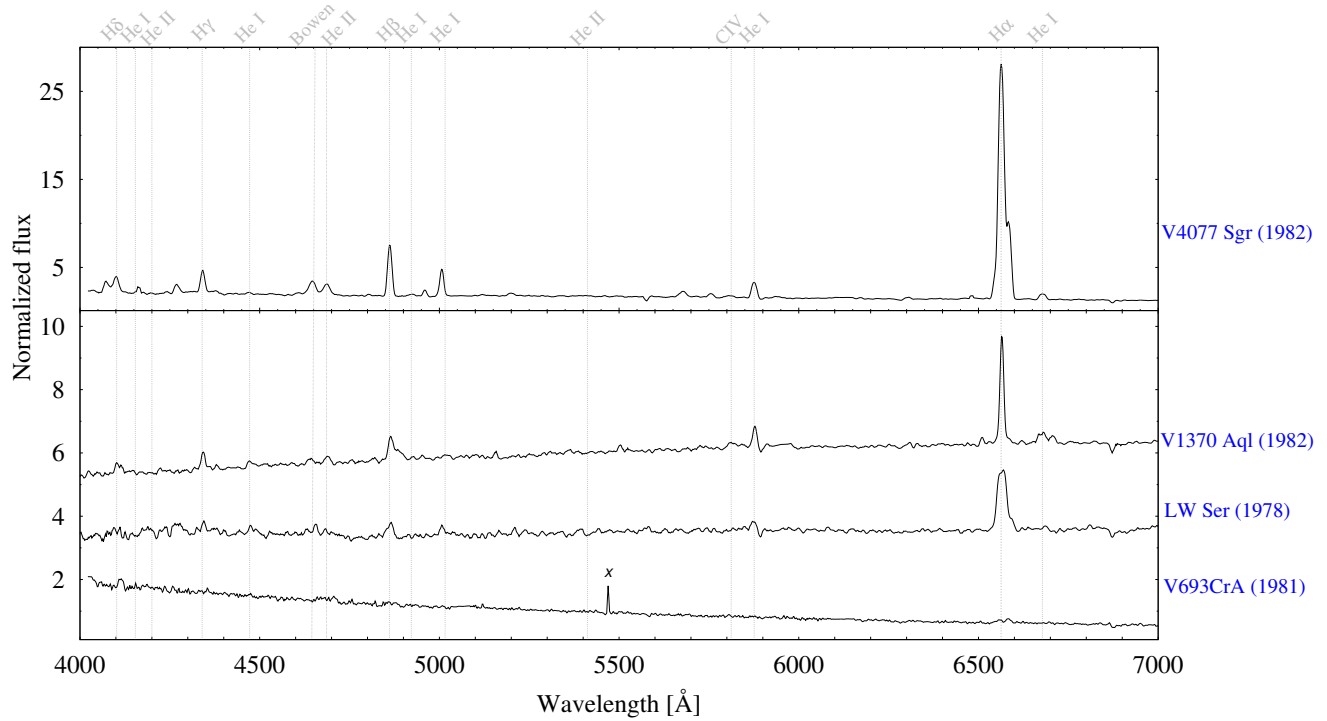


Figure 2.9: Top: Spectra of the previously known post-novae V1370 Aql, V693 CrA, LW Ser and V4077 Sgr, the latter is shown in a separated scale for purpose of a better view. Artefacts are marked with a \times . Bottom: the same spectra corrected by the $E(B - V)$ reddening values presented in Table 2.6.

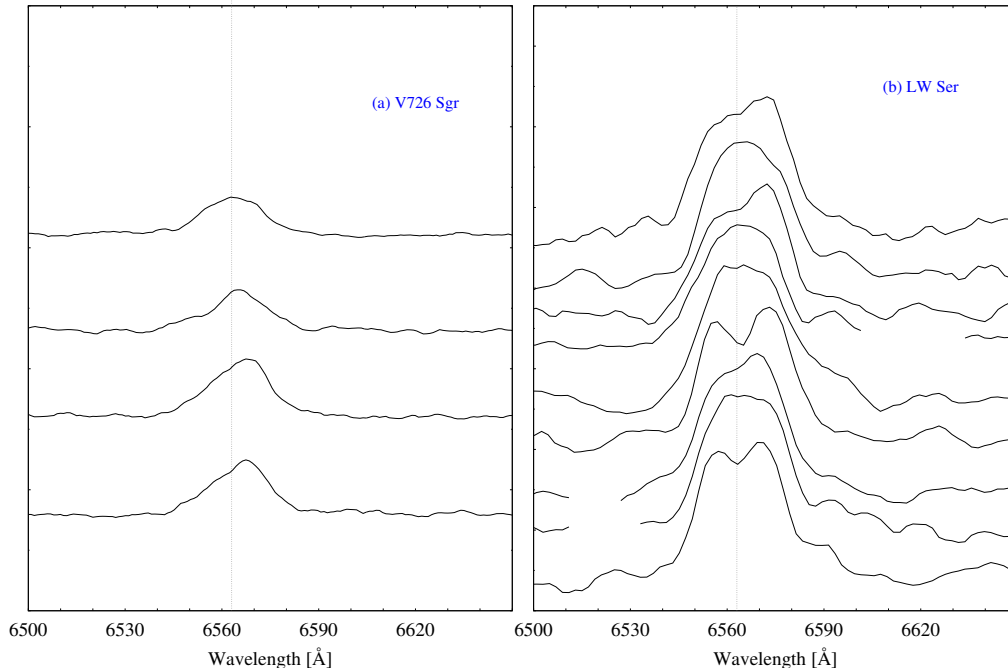


Figure 2.10: Close-up on the H α emission line for those novae seen apparently at high inclination: the individual spectra for V726 Sgr and LW Ser. The vertical line indicates the rest wavelength of H α . V726 Sgr and LW Ser are shown in a sequence with a step-size of 15 min and 5 min, respectively, from bottom to top.

$E(B - V) = 0.0985(6)$ mag given by IRSA, the continuum is fitted with a power-law index $\alpha = 2.52(2)$, which is an expected value for a high \dot{M} system. This means that the system is in a quiescence state with an optically thick disc. On the other hand, albeit V693 CrA has some characteristics of a RN according Pagnotta & Schaefer (2014), this post-nova is one of those with the highest amplitude (revise Table 2.6) while RNe typically have low eruption amplitudes. In consequence, we attribute the width of the lines to a high inclination instead to a high expansion velocity, and conclude that V693 CrA is at least not a very strong RN candidate.

2.4.3.3 LW Ser (1978)

Nova LW Serpentis is a well-studied nova. It was discovered by M. Honda in Japan, after the maximum brightness at $m_p = 8.3$ mag on 1978 March 4. It was first reported as a novalike star (Kozai et al. 1978a). Later, on March 8 it was seen at $V = 8.6$ mag and on March 7, a prism spectogram acquired at the Kiso station in Japan revealed its nature as a nova, showing Balmer emission lines with H β and H γ line profiles similar those of P Cygni, an indicator that the nova was just past its maximum state (Kozai et al. 1978b). This nova was extensively monitored by AAVSO observers after its discovery. The light curve presented by Mattei (1979) suggests a moderately fast nova speed class with $t_2 = 35$ d and $t_3 = 50$ d and dust formation, being also well-monitored after the eruption in the infrared band. Both because of the light curve shape and the optically thick

dust shell, it is considered very similar to the novae FH Ser (1970) and NQ Vul (1976) (Szkody et al. 1979; Gehrz et al. 1980). Based on optical spectroscopy for about one month after its early decline, Prabhu & Anupama (1987a,b) derived a kinematic model for the shell using the H α asymmetric line profile, which likely presented [N II] $\lambda 6548,6584\text{\AA}$ contribution. They calculated a distance $d = 4.2(4)$ kpc and suggested a structure composed of an equatorial disc and polar cones with the polar axis deviated $\sim 15^\circ$ from the line of sight. Expansion velocities were also measured by Cohen & Rosenthal (1983) from spectra taken in 1981 deriving $d = 2.34$ kpc. Using the reddening estimated by them Özdönmez et al. (2016) calculated the distance from the reddening-distance relation obtaining $d = 1.27(40)$ kpc.

Our captured spectrum forty years posterior to the eruption is still showing contribution from the shell. The spectra display significant variations over a span of 45 min, showing a broad and double peak profile at the H α line ($W_{H\alpha} = 70\text{\AA}$) and likely still contains contribution of [N II] $\lambda\lambda 6548,6584\text{\AA}$ (Fig 2.10, b). Other nebular lines also detected, such as [O I] $\lambda 5577\text{\AA}$, [O III] $\lambda 5007\text{\AA}$ and [N I] $\lambda 5199\text{\AA}$ (Fig.2.9). Considering an extinction value in the direction of LW Ser as $E(B - V) = 0.72(3)$ mag, the continuum becomes slightly inclined towards the blue and can be fitted with a power-law index $\alpha = 2.01(4)$. The He I series is barely above the continuum level and both Bowen blend and He II $\lambda 4686\text{\AA}$ are only weakly present compared to the other novae described in this work. In addition, we derived $R = 20.2$ mag from the acquisition frame, which is significantly fainter than that computed by Szkody (1994) in April 1989, $R = 18.6$ mag.

As we have seen, LW Serpentis is still being dominated by the contribution of the shell. Its short time variations together with the broadness of the lines are indicative of it being seen at a high inclination. This could explain the brightness difference between the observation made by Szkody (1994), since the acquisition frame possibly could have caught the system in eclipse. Another possibility is that the nova has declined by 2 mag in the past 25 years. With time-resolved photometry both this issue and the orbital period could be addressed.

2.4.3.4 V4077 Sgr (1982)

Nova Sgr 1982 was discovered by M. Honda at the Tokio Astronomical Observatory, Japan on 1982 October 4 at $V = 9$ mag and then seen on October 10 at $V = 8.72$ mag (Kosai et al. 1982a). The published optical light curve is composed of several IAU Circulars and AAVSO data observed over two months after its discovery. Its shape is characterized by gradual oscillations showing a pre-maximum phase one magnitude below the maximum, an early decline phase of about 10 d decreasing ~ 2.5 mag until a second maximum, which reached a similar magnitude as the first one, yielding $t_2 = 10$ d (Sowell & Cowley 1983; Iijima & Rosino 1983; Mazeh et al. 1985) and $t_3 = 100$ d from subsequent AAVSO data (Duerbeck 1987). Due to its early identification it was well covered over a wide wavelength range after the eruption, being spectroscopically monitored both in early decline, transitional and nebular phase, the latter seven months after the outburst (Drechsel et al.

1982; Sowell & Cowley 1983; Mazeh et al. 1985). An infrared band monitoring with the Infrared Astronomical Satellite (IRAS) in the early decline phase, suggested hot dust formation (Dinerstein 1986). From absorption features in the UV spectrum Mazeh et al. (1985) estimated the interstellar extinction $E(B - V) = 0.35(1)$ mag and the distance $d = 4.7$ kpc was calculated adopting as absolute magnitude $M_v = -6.35(5)$ mag, the characteristic value for type II light curves, according to Duerbeck (1981). Although V4077 Sgr is identified in the EDR3 (Gaia Collaboration et al. 2016, 2018, 2021) the distance can not be calculated due to the measured parallax not yielding a positive value.

The GMOS spectrum taken almost 30 years after the nova explosion is still showing strong flux contribution coming from the shell. $H\alpha$ is blended with [N II] $\lambda\lambda 6548, 6584\text{\AA}$, being the strongest line of all novae studied in this work as well as for the other Balmer lines up to $H\gamma$, which are also very narrow. In addition to the He I series and the Bowen/HeII fluorescence, a rich forest of recombination lines, ionized, non-ionized and forbidden species are visible: [SII] $\lambda 4076\text{\AA}$, [Fe II] $\lambda 4244\text{\AA}$, CII $\lambda 4267\text{\AA}$, N V $\lambda 4609\text{\AA}$, Fe II $\lambda 4924\text{\AA}$, [O III] $\lambda\lambda 4959\text{--}5007\text{\AA}$, [N I] $\lambda 5199\text{\AA}$, [O I] $\lambda 5577\text{\AA}$ in absorption, [O I] $\lambda 6300\text{\AA}$ in emission, [Fe VI] $\lambda 5677\text{\AA}$, [N II] $\lambda 5755\text{\AA}$, CIV $\lambda 5805\text{\AA}$, N II $\lambda\lambda 5939\text{--}6482\text{\AA}$ and [N II] $\lambda\lambda 6548\text{--}6584\text{\AA}$. In order to fit the continuum in our GMOS spectrum, a comparison between the reddening derived by Mazeh et al. (1985), $E(B - V) = 0.35(1)$ mag and the average reddening estimated with IRSA ($E(B - V) = 0.72(3)$ mag) is again demonstrating the large uncertain associated to the average reddening calculated over an entire field instead of estimating it directly over the line-of-sight of an object, as it was the case for KY Sgr. Considering the first value, the continuum is fitted with a power law index $\alpha = 2.48(1)$, a typical value for high \dot{M} discs. In view of the strong emission coming from the shell dominating in the spectrum, emission lines originating in the proper CV are hidden, hence it is not possible to derive intrinsic information on the CV.

2.4.4 Discarded post-nova candidates

As mentioned in section 2.1, post-nova candidates were selected either from $UBVR$, $H\alpha$ narrow-band photometry or because some of them were catalogued as possible old nova counterparts by Mróz et al. (2015). Spectra for some of the targets marked in blue in Figs. 2.1 and 2.3 were obtained in this work. The candidates were categorized according the criteria used to select them. Fig. 2.15 and 2.16 show those obtained from colour-colour diagrams and those considered as the post-novae according to Mróz et al. (2015) respectively. The spectra were not corrected by interstellar reddening. The object name, RA, DEC and colours of those objects are presented in Table 2.5. $UBVR$ candidates present strong absorption lines in general, being typically bluer than the narrow-band candidates. In the case of Mróz' candidates, he catalogued his candidates for V726 Sgr and V1174 Sgr as likely post-novae because they are showing ellipsoidal-like variability with I-band

Table 2.5: RA DEC coordinates, colours and date of the observation for those targets who are not the old nova counterpart.

Object	RA	DEC	$B - V$	$V - I$	Date	Ref.
KY Sgr	18:01:21.02	-26:24:40.0	–	4.151	April 02 2019	1,2
V726 Sgr 1	18:19:33.67	-26:53:19.7	–	1.141	March 13 2016	1,2
V726 Sgr 2	18:19:34.06	-26:53:25.46	–	–	March 13 2016	2
V732 Sgr 1	17:56:07.51	-27:22:17.1	1.24(1)	–	July 24 2015	1
V732 Sgr 1	17:56:06.742	-27:22:34.95	1.150(9)	–	July 24 2015	1
V1012 Sgr	18:06:14.10	-31:44:28.1	–	1.721	March 04 2017	1,2
V1148 Sgr	18:09:12.028	-25:58:03.04	–	–	March 13 2016	1
V1174 Sgr	18:01:37.03	-28:44:19.0	–	–	March 11 2016	1
FS Sct 1	18:58:16.90	-05:24:5.10	–	–	April 12 2019	1
FS Sct 2	18:58:15.96	-05:23:3.02	–	–	April 12 2019	1
V719 Sco 1	17:45:49.20	-34:00:54.05	–	–	April 13 2019	1
V719 Sco 2	17:45:54.20	-34:02:45.25	–	–	April 13 2019	1
V902 Sco 1	17:26:08.235	-39:03:44.9	–	–	March 25 2017	1
V902 Sco 2	17:26:08.364	-39:03:08.53	–	–	March 25 2017	1

References:

1. This work, 2. [Mróz et al. \(2015\)](#)

amplitudes at 0.3 mag and 0.8 mag and orbital periods ~ 0.82 and 0.31 days respectively. However our spectra in Fig. 2.16 show pure absorption lines with some artefacts. The V1174 Sgr candidate shows a moderately strong $H\alpha$ absorption line with an artefact redwards of it, and the most distinctive feature is a deep Na I $\lambda 5892\text{\AA}$ absorption line, whereas V726 Sgr is showing a more flat spectrum with weak $H\alpha$ and Na I absorption lines. Hence, the supposition made by [Mróz et al.](#) that V726 Sgr is composed of an evolved star according to its infrared colours and the location in colour-colour diagrams, seems to be unlikely. According to their light curves (see fig. 7 in [Mróz et al. 2015](#)) and their spectral characteristics seen here, in both cases they might be W Ursae Majoris binary stars, i.e., binaries sharing a common envelope where both stars have approximately the same spectral type with short orbital periods and photometric variability up to one magnitude in the light curve.

Finally, the candidates for KY Sgr and V1012 Sgr were classified as possible post-novae because they have photometric variability and they are close to the reported position of the eruption. Our spectra prove that they are not the post-nova, with the KY Sgr candidate being a very cold M-type star and V1012 Sgr likely a G-type star.

2.5 Discussion and conclusions

2.5.1 Remarks about spectroscopic characteristics of individual post-novae

As described in section 1.7 both the strength and the width of the lines have been considered indicators of the mass transfer rate process and the inclination of the system. The FWHM of the lines is also an indicator of the inclination because it is related to the projected velocities $v \sin i$ of the emission regions in the system. Given these points, the shape and the strength of the lines usually is the result of the combination of both scenarios.

Another essential point related to the nature of the components of the novae is the presence of the ionized He II emission lines⁶, which requires high excitation energy levels, and thus those lines are formed at high temperatures. He II $\lambda 4686\text{\AA}$ has been found in almost all novae, in all magnetic CVs and novalike CVs, but is rarely seen in dwarf novae (Kraft 1964). Based on its behaviour during an eclipse on three novae, Williams (1989) suggested that this line is not emitted in the disc (Ringwald et al. 1996). In the case of He II $\lambda 5412\text{\AA}$, this line is seen in a few novae but is not observed in novalikes nor dwarf novae (Warner 1995). Inasmuch as He II $\lambda 5412\text{\AA}$ is a transition involving higher energy than required for He II $\lambda 4686\text{\AA}$, the former is associated to more energetic events, like that produced by the the shock of the impact of material from the donor onto the WD as it follows the lines of its magnetic field. Consequently, this line can be considered as a signal of the presence of a magnetic WD, main spectroscopic indicators usually considered are the empirical criteria (i) $W_{H\beta} > 20\text{\AA}$ and (ii) He II $\lambda 4686\text{\AA} / H\beta$ ratio > 0.4 found by Silber (1992), because $\lambda 5412\text{\AA}$ is detected in only a few IP novae (e.g. DQ Her, CP Pup, V4743 Sgr among others, Zemko et al. 2016).

On the other hand, Carbon lines in novae could be interpreted as pointing to an evolved state of the donor star and/or the chemistry traits of the superficial layers of the secondary (Schmidtobreick et al. 2003a).

According to these indicators, we propose the following scenarios for the recovered post-novae in this chapter:

- The high strength of Balmer lines for EL Aql together with the large amplitude $A = 14.5$ mag and the large Balmer lines FWHM might be indicative of either a system seen at a moderately high inclination or a low mass-transfer rate. Assuming that it is quite affected by interstellar reddening according to IRSA calculations, α yields 3.12(02), above the expected value for a steady-state accretion disk, $\alpha = 2.33$ according to Lynden-Bell (1969). Nevertheless we note that the steepest continuum slopes are found for the systems with the largest interstellar

⁶an extensive discussion about He II $\lambda 4686\text{\AA}$ can be found in <https://asd.gsfc.nasa.gov/Koji.Mukai/iphome/issues/heii.html>

reddening. This appears suspicious and suggests a tendency to overcorrect for this effect. On the other hand, the strength of He II $\lambda 4686\text{\AA}$, the presence of He II $\lambda 5412\text{\AA}$, the large A and the fulfillment of Silber’s criteria, points to a magnetic system. However, since the former does not quite match the strength of $H\beta$, EL Aql is more likely to be an intermediate polar rather than a discless system seen at a moderately high inclination. In spite of its faintness, its orbital period might therefore be accessible with time series photometry. Nevertheless, our attempts to derive the orbital period have been unsuccessful using a medium telescope like the 2.5m du Pont telescope in Las Campanas Observatory during 2016, because long integration times were needed (~ 30 min per frame). The orbital period is only accessible via large telescopes.

- Almost one hundred years after the outburst the Balmer emission lines are very strong for EY Aql, with a similar equivalent width as EL Aql (see Table 2.4) and a continuum blueward with $\alpha = 2.61(7)$. This might be indicative for a low-mass transfer state, although we do not discard the possibility that it is affected by inclination effects according to its moderately high FWHM values. However, because we could not detect time variations we can not confirm this asseveration.

Kato et al. (2001) proposed that EY Aql is a WZ Sge-Type DN, however, we discard that supposition for these reasons: (i) the spectrum presents the characteristic nova features, such as strong Balmer emission lines, He I lines, the Bowen and He II $\lambda 4686\text{\AA}$ (although the latter appear very weak due to very low S/N in the blue), (ii) it has a larger amplitude $A > 12.5$ mag than the one assumed by them ($A \sim 9.5$ mag) and (iii) the main reason is that there is no presence of WD absorption lines in the Balmer lines.

- V606 Aql is the oldest nova in this sample. If we use the brightness at maximum estimated by Duerbeck (1981) to calculate the eruption amplitude $A = 14.5$ mag, then it becomes the largest amplitude of this sample together with EL Aql. Although the origin of the large A could be attributed to a discless system, both the relatively low strength of the He II $\lambda 4686\text{\AA}$ and the absence of He II $\lambda 5412\text{\AA}$ are strong evidence to discard a magnetic nature. Furthermore, significant time variations of the $H\alpha$ profile coupled with the fact that the lines are broad with high FWHM, are signs that the high A is a consequence of the high inclination of the system. This also fits well with the comparatively strong emission lines. According to its spectral characteristics we thus tentatively conclude that V606 Aql is a system seen at a moderately high inclination, which makes it a potential target for follow-up time series observations.
- The weak emission lines for V908 Oph, together with the very blue continuum fitted with a power law exponent $\alpha = 3.38(02)$ and the comparatively small A are consistent with an

optically thick disc and thus high- \dot{M} where the bluer hydrogen lines are even embedded in absorption troughs. The non-detection of any significant variations of the H α line in the three individual spectra and the narrowness of that line suggest that the system is seen at low inclination and as consequence, it is sure that the orbital period can not be easily established.

- The comparatively large $A = 13.3$ mag for KT Mon suggests at first glance a faint accretion disc, similarly to the cases of EL Aql and V606 Aql. Furthermore, since photometric colours are similar to two other, likely magnetic, post-novae, V909 Sgr and BS Sgr (Tappert et al. 2012, 2014), this could indicate the presence of a magnetic white dwarf. In addition, the absence of the Bowen blend and the strong presence of He II $\lambda 4686\text{\AA}$ may be enough indicators for a magnetic nova candidate, although Silber’s criterion is met only partially, because $W_{H\beta} < 20\text{\AA}$. On the other hand, because the lines are fairly broad with large FWHMs, a high inclination could be the explanation for the large amplitude of this old nova and the almost flat continuum fitted with $\alpha \sim 1.5$ would be consistent for a low- \dot{M} regime, but it would also be consistent with a disc seen at high inclination. We concluded that, KT Mon is very likely a high inclination system, for which under good meteorological conditions photometric time-series data at a telescope of the 4m-class could be obtained with a sufficiently short cadence (~ 10 min) to detect orbital variability.
- V726 Sgr is an old nova with a moderate amplitude, $A = 10.1$ mag and with some spectroscopic characteristics similar to KT Mon, like strong He II $\lambda 4686\text{\AA}$ emission, meeting the Silber criterion (ii) but non criterion (i), and unlike KT Mon, V726 Sgr is showing a strong Bowen blend. Even the H α equivalent width is similar for both cases, albeit the Balmer decrement is less steep than in KT Mon. The continuum with α below the average expected value for a steady-state accretion disk ($\alpha = 2.33$, Lynden-Bell 1969) would be indicative of a medium mass transfer rate. The presence of C II $\lambda 4267$ could be interpreted as a signature that the donor is not a MS star. Together with the strong time variations in the line profile and high FWHMs, we suggest that V726 Sgr is seen at medium-high inclination. In consequence, the orbital period is likely obtainable through time-series photometry.
- V1149 Sgr is a slow and old nova showing a blue continuum with weak Balmer lines but a Bowen blend that is stronger than He II $\lambda 4686\text{\AA}$. Based on the moderate amplitude, $A=11$ mag, the fact that only Silber’s criterion (ii) is met and that the He II $\lambda 5412\text{\AA}$ is not clearly identified, the system is not a strong candidate for a magnetic CV. In addition, the small A and weak lines are consistent with a high \dot{M} system, with the medium FWHM value and the non-detection of variability in the line profile suggesting that it is likely seen at a rather low inclination, similarly to the case of V908 Oph.

- V1583 Sgr is a nova presenting narrow and quite strong emission lines with time variations in the line profile, a moderate $A = 11.6$ mag, and without spectroscopic characteristics of magnetism. The FWHM value is quite low for that expected in a system showing variable time profiles. A possible explanation for this apparent discrepancy between narrow lines and an obscuration effect is that for V1583 Sgr the Doppler-broadened component of the line profile produced by the disc is weak and that the line profile is dominated by a narrow component that originates on the secondary star. Assuming that the narrow component is produced by irradiation, we would also expect that either the white dwarf in this system is still very hot or that the orbital period is comparatively short. Because of the ‘age’ of the post-nova ($\Delta t = 93$ yr), the former is less likely. In any case, the observed obscuration makes V1583 Sgr an attractive target for time series photometry.

- The old nova V3964 Sgr presents very similar characteristics to V1583 Sgr, in terms of A , magnetism and variable line profile, together with broad lines showing a possible obscuration effect in one spectrum. The broad lines then point to a system seen at high inclination. Although the continuum slope appears rather flat for the suspected high \dot{M} , but this again might just reflect a high system inclination. Thus, it should be feasible to determine the orbital period with time series photometry.

- V4049 Sgr is the youngest recovered nova in this sample ($\Delta t=43$ yr). Its slope indicates a hot continuum even before reddening corrections. In consequence the emission from the continuum dominates the optical spectrum, which is reflected in the broad but weak lines, typical features for a high mass transfer rate system. In the same way as V1149 Sgr, the Bowen blend is stronger than the He II $\lambda 4686$ emission. Although no significant time variations were detected in a time-span of 1 hr, the high FWHM values would indicate that the system is seen at high inclination and this object likely has a long period and/or was caught at an orbital phase where the line profile does not vary much. Time resolved observations on longer time scales should show the variability in the line profiles.

- V825 Sco is the only confirmed eclipsing object in this study with an orbital period ~ 4.6 h (Mróz et al. 2015). The strong He II $\lambda 4686\text{\AA}$ emission and the likely presence of He II $\lambda 5412\text{\AA}$ could be attributed to a magnetic nature. However, there is only one Silber’s criterion met, similarly to KT Mon and V726 Sgr, thus V825 Sco can not be considered a magnetic CV candidate with certainty. Finally, both power-law index and the low equivalent width can be seen as indicators of a moderate \dot{M} .

2.5.2 About the strategies to recover post-novae

The strategy to recover old novae was based on colour-colour diagrams or on photometric variability. Grouping them with respect to the different methods our results were:

1. nine fields observed with *UBVR* photometry, with the nova being recovered in six cases,
2. 14 fields in $VH\alpha$ [SII] photometry, out of which only in the field of KY Sgr a strong $H\alpha$ source was detected and even that is more likely to be a recurrent nova than a classical one,
3. two fields using $r H\alpha$ [SII] photometry, where both for V1174 Sgr and V726 Sgr the selected candidates proved not to be the nova. An especially interesting case is V726 Sgr, because the post-nova was recovered but is not $H\alpha$ bright in the diagram (see Fig. 2.1),
4. 10 fields using $g H\alpha$ [SII] data, for which no candidates were forthcoming,
5. six post-novae which were marked as candidates by Mróz et al. (2015) because they show photometric variability. Just one of those, V825 Sco, is effectively confirmed as the old nova counterpart.

In particular, the $H\alpha$ photometry non-results have been unexpected, considering that this idea has been deemed as a valid strategy to recover post-novae both by Ringwald et al. (1996) and by us. In none of the 26 fields with photometry that included the $H\alpha$ filter the post-nova was recovered up to now (there still are three fields with candidates that will be spectroscopically observed during the 2022A semester; KP Sco, V3888 Sgr and V721 Sco), although a RN candidate was recovered, which in fact underwent a nova eruption but in a system other than a CV. The non-detection of post-novae can be due to different factors such as, a) the reported eruption was not a nova event, b) the reported position inaccuracy is greater than the size of the field of view and thus the CCD images possibly did not include the post-nova, c) the post-nova is much fainter than presumed and thus below the detection limit of the observations, d) the proposed method is not capable of separating the nova from other objects.

According to the previous experience in recovering post-novae (see Tappert et al. 2012, 2014, 2015, 2016), we think it unlikely that the null detection can be attributed to a), b), c) and therefore it is probably associated to the strategy using $H\alpha$ photometry. Tests that involved applying the photometric narrow-band strategy to a couple of known novae with comparatively weak emission lines showed that the area in the respective colour-colour diagrams that is typically occupied by such post-novae is strongly affected by artefacts caused by close visual binaries (Tappert, private communication). Apparently, the combined light from two objects with different spectral manages to mimic a blue star with a weak emission line, especially when one of the stars is much brighter than its visual companion. Because novae are mostly located in the crowded fields of the Galactic

disc, this means that there is a considerable number of such artefacts, which makes this strategy (at least in its current form) not suitable to recover post-novae. Therefore, selection by, at least, our choice of narrow-band filters is not a feasible method for most post-nova fields. Under those circumstances, we suspect with this strategy it is only possible to catch those objects with strong $H\alpha$ emission, like novae in the nebular phase, novae with very low \dot{M} or recurrent novae, like in the case of KY Sgr.

Our results demonstrate that variability alone is not a sufficient criterion to identify post-novae, as demonstrated by the analysis of the Mróz candidates, because W UMa contact binaries or pulsating δ Scuti stars show periodic variability on very similar time-scales as CVs, but are much more frequent and the periodicity and amplitude of their variation is less dependent on geometric effects like the system inclination. Finally, the *UBVR* photometry has proved to be a much more efficient technique than those based on detecting $H\alpha$ emission or on variability even though it is the most expensive method of the three, since it requires dark nights and long exposure times even at large telescopes. Still, it emerges as the most suitable method to recover post-novae.

2.5.3 An updated perspective of the post-nova population

In Tables 2.6 and 2.7 we present both the most representative photometric and spectroscopic parameters for 61 post-novae collected⁷ from the literature, including those from the ‘Life after eruption’ project together with the new ones presented in this work. These data fill the lack of observed objects that erupted more than 60 years ago (in comparison with the samples analysed by Ringwald et al. 1996; Tomov et al. 2015).

2.5.3.1 Behavior of emission lines for post-novae

The following analysis is focused on the relation between equivalent widths, time Δt since the reported eruption (Fig. 2.11 and 2.12 (a) and (b)), as well as with respect to the amplitude ($A = m_{\min} - m_{\max}$), the latter being considered only for those post-novae erupted more than 50 years ago in order to ensure that they are observed in the quiescence state (Figs. 2.12 (c), (d) and 2.13). Not for all novae, all typical lines could be properly measured, so each plot can show a different amount of data (e.g., the Bowen blend and He II $\lambda 4686\text{\AA}$ could be not always resolved separately). In Figs. 2.11 and 2.12 red circles mark the objects presented in this work and black ones are from the literature.

In general $H\beta$ has been considered as a better indicator of the state of the system than $H\alpha$ because the latter likely contains contribution of the emission from both the disc and the nebular

⁷We have incorporated neither recurrent novae nor those data from Ringwald et al. (1996) because the comparison made by Tomov et al. (2015) with his data has demonstrated that they follow the same trend, and thus Tomov et al.’s data are considered adequately representative.

shell. In particular, the former was also used as a \dot{M} indicator according to [Patterson \(1984\)](#), however that relation did not consider the inclination effects. On the other hand, [Warner \(1986\)](#) found a strong dependence between $W_{H\alpha}$ and the inclination of the novae. He found that even those seen at the highest inclination are limited to have $W_{H\alpha} \sim 70\text{\AA}$. In our analysis (Fig. 2.11, plot a) we find a particular strong H α emission for the younger novae ($\Delta t < 50$ yr), which can be interpreted as the shell still being a significant contributor at that stage, as is the case for BY Cir, V812 Cen, V842 Cen, V868 Cen, LW Ser and V382 Vel. The strongest hydrogen emitter is V4077 Sgr (with $\Delta t = 40$ yr), with $W_{H\alpha} = 367(2)\text{\AA}$ (which is not displayed in the graph due to the scale used). The most remarkable exception is V888 Cen ($W_{H\alpha} = 8\text{\AA}$). Albeit it has erupted recently ($\Delta t = 26$ yr), there is no obvious contribution from the shell ([Downes & Duerbeck 2000b](#)). $W_{H\beta}$ shows approximately the same behavior as $W_{H\alpha}$ (plot b).

In general, post-novae with evident contribution from the shell with $W_{H\alpha} \geq 70\text{\AA}$ are located at an age below $\Delta t \sim 30 - 50$ yr, establishing, based on these criteria, the apparent end of the nebular phase. This asseveration could in principle be tested by comparison with nebular emission lines, like [O III], however, there are not enough data to correlate it. For older objects with $\Delta t > 60$ yr, there is no correlation on long-term scales between the H α equivalent width and Δt , in agreement with the results found by [Ringwald et al. \(1996\)](#) and [Tomov et al. \(2015\)](#).

In order to clarify the orbital inclination effects it is also helpful to analyse the equivalent width and FWHM as a function both of Δt and the amplitude. Fig. 2.12 plot (a) and (b) show on average, that both $\text{FWHM}_{H\alpha}$ and $\text{FWHM}_{H\beta}$ are a bit larger for the younger novae ($\Delta t < 50$ yr), but this trend can also be explained with the contribution from the expanding shell material. The FWHM as a function of A , on average, is larger for $A > 12$ mag, even considering that some objects have large uncertainties for m_{max} or m_{min} values, as can be seen in Fig. 2.12 (c), (d) and 2.13 (a) and (b). This means that the amplitude increases with the inclination. As an example, V908 Oph has $\text{FWHM}_{H\beta} \sim 549$ km/s pointing to be a moderately low inclination system, while V728 Sco with $\text{FWHM}_{H\beta} \sim 1850$ km/s is in fact an eclipsing old nova ([Tappert et al. 2013b](#)). Hence, equivalent width as a function of Δt is insufficient indicators for probing a possible decline of \dot{M} over time. W_{λ} and FWHM become strong inclination indicators when they are correlated with the amplitude (Fig. 2.13 a and b).

In the same way, analysing the behaviour of the more energetic lines, like the Bowen blend and He II $\lambda 4686\text{\AA}$ can be used to test the irradiation effects in the disc and the secondary as well as where they originate. The equivalent width for He II $\lambda 4686\text{\AA}$ seems not to be dependent on Δt as is displayed in Fig. 2.11 (c), in good agreement with [Tomov et al. \(2015\)](#), excluding the values for recurrent novae). Similarly, no obvious dependency is found as a function of the amplitude (Fig. 2.13 c). However, when He II $\lambda 4686\text{\AA}$ is compared with the intensity of the Bowen blend versus Δt (Fig. 2.11 d) we can see that, on average, the younger systems ($\Delta t < 50$ yr) have a slightly stronger Bowen blend than the older ones (considering $\Delta t > 90$ yr). Because the Bowen

blend is known to be a likely indicator of an irradiated cool secondary by a hot white dwarf (Ferguson et al. 1987) and He II $\lambda 4686\text{\AA}$ is a likely result of ionization by the strong radiation from the hot WD, one would actually expect that both lines become weaker with increasing Δt as the eruption-heated white dwarf cools down. Although He II does not show any such behaviour, the ratio between He II $\lambda 4686\text{\AA}$ and the Bowen blend reflects that the irradiation effectively decreases with the time after the eruption. He II $\lambda 4686\text{\AA}$ can be produced by a source other than radiation from the WD, such as a disc hot enough to produce ionization or by a magnetic field. In any case, this result is not conclusive, requiring more data of older systems ($\Delta t > 100$ yr) in order to test for a more significant trend.

Fig. 2.13 (c) and (d) can be used as indicators of magnetic systems, because A is influenced by the presence or absence of a disc. To test this, the post-nova sample is sub-divided according to the following conditions:

- (i) systems with He II $\lambda 5412\text{\AA}$ detection are shown as red circles,
- (ii) if Silber’s condition (i), $W_{H\beta} > 20\text{\AA}$ is met the post-nova is marked with a black circle
- (iii) if Silber’s condition (ii), equivalent width for He II $\lambda 4686\text{\AA}$ / $H\beta > 0.4$ is satisfied, they are marked with blue squares.

In both plots almost the entire sample fulfills the Silber (ii) criterion. Considering only the equivalent width for He II $\lambda 4686\text{\AA}$, neither the sub-samples (blue and red objects) nor the total one are correlated with the amplitude. Only one object satisfies the three conditions, BT Mon. This eclipsing nova seen at $i \approx 82^\circ$ is classified as an Intermediate polar (IP) candidate (Smith et al. 1998a). However, it is striking that CP Pup, the only confirmed IP in this sample does not meet the criterion (iii). This nova presents orbital modulations but no eclipses (Mason et al. 2013), implying that it seen at a lower inclination compared to BT Mon. In consequence, this fact is indicating that using criteria based on the presence of certain He II emission lines and/or the strength of W_β could not necessarily be reliable methods for indicating magnetic CVs, because W_λ is strongly affected by the inclination. In consequence, W_λ can not be used as a precise test of magnetism.

It is also important to realize that using only criterion (i) to establish magnetic candidates is not quite reliable, because there is a significant sample of IPs that do not exhibit He II $\lambda 5412\text{\AA}$, e.g. GI Mon, HZ Pup, V842 Cen, and V697 Sco (Woudt et al. 2009; Tomov et al. 2015; Tappert et al. 2014). Albeit it would be interesting to correlate the observed behaviour with other criteria for magnetic novae, like the detection of a spin period of the WD, there are not enough data available to investigate this topic at the moment, but it could be a possible future line of research.

2.5.3.2 Relationship between amplitude and speed class of post-novae

As described in section 1.6.8, the A/t_2 correlation has been considered as a tool to distinguish systems with certain characteristics, such as discriminating recurrent nova candidates (Pagnotta & Schaefer 2014), as well as to determine nova candidates that are probably seen at high inclination,

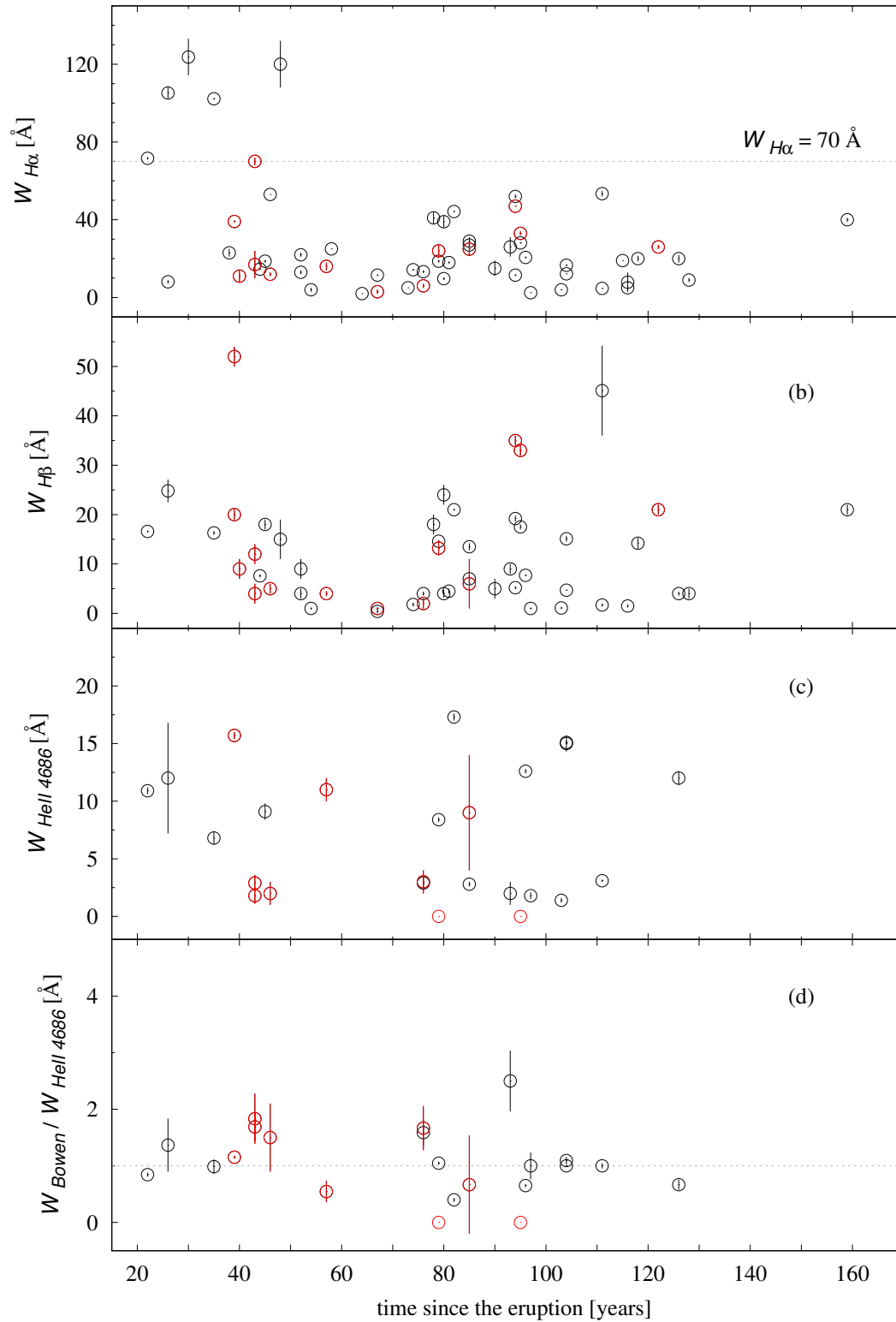


Figure 2.11: Equivalent width of the main emission lines seen in old novae versus time since the eruption. Black circles correspond to data found in the literature (see Table 2.7). Red circles are those old novae analysed in this chapter. Equivalent widths for $H\alpha$, $H\beta$, $He\ II\ \lambda 4686\text{\AA}$ and the Bowen blend / $He\ II\ \lambda 4686\text{\AA}$ ratio are shown in (a), (b), (c) and (d) respectively.

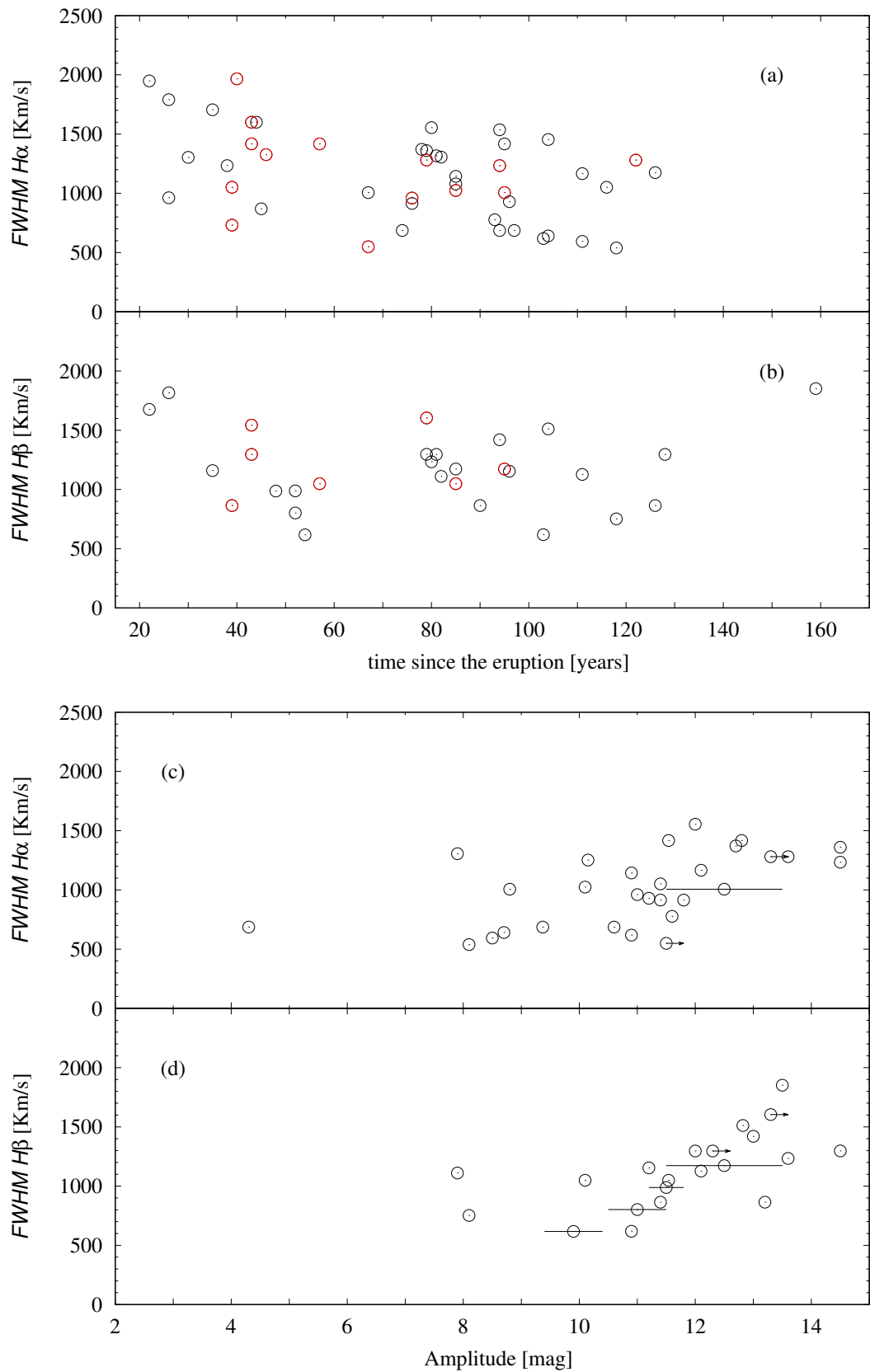


Figure 2.12: Top: FWHM for $H\alpha$ and $H\beta$ emission lines versus time since the eruption for old novae. Symbols are as in Fig. 2.11. Bottom: FWHM for $H\alpha$ and $H\beta$ emission lines versus Amplitude for old novae that erupted more than 50 years ago. Arrows indicate that A must be larger than the derived value. See section 2.5.3 for more details.

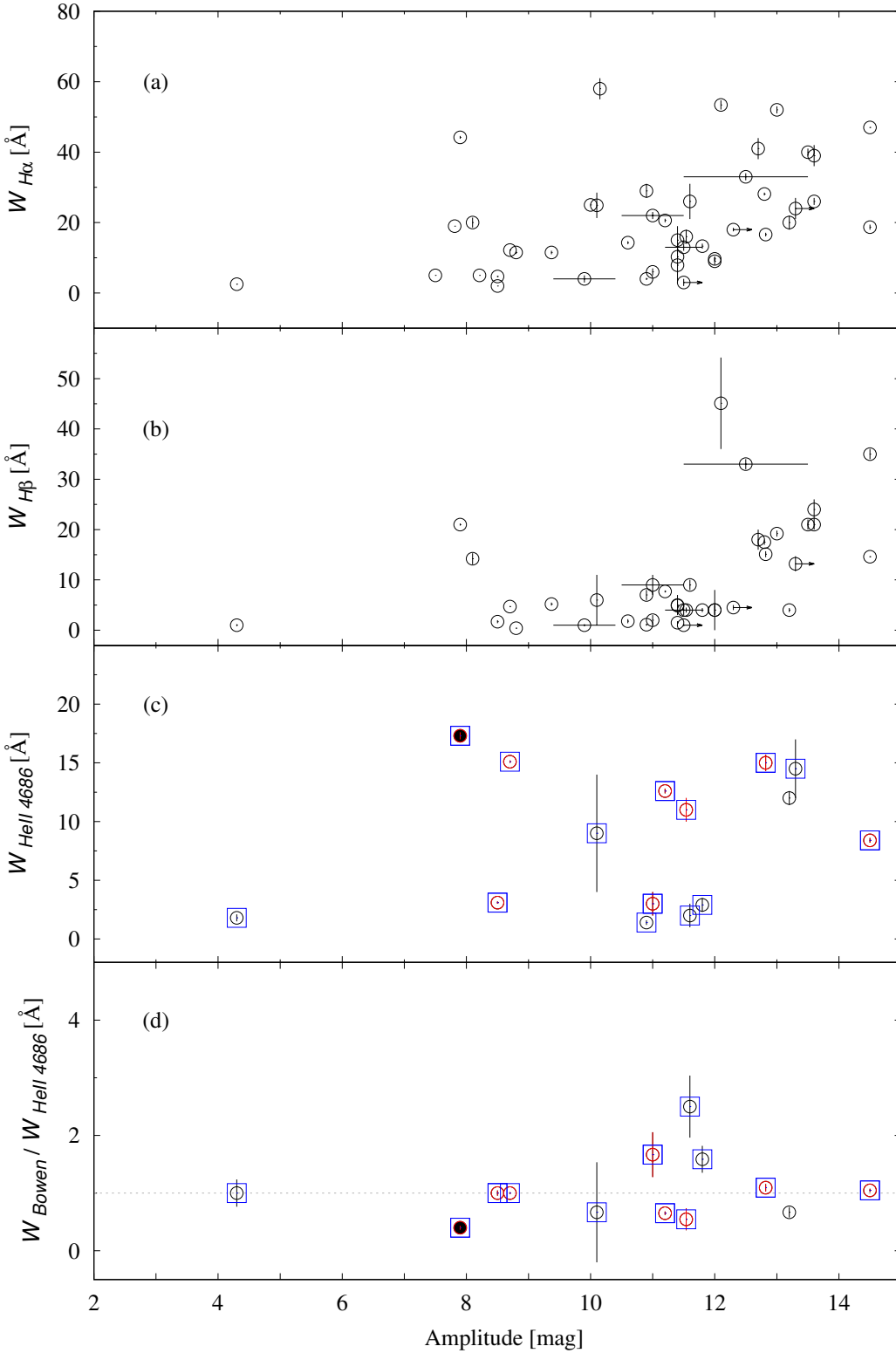


Figure 2.13: Equivalent width of the main emission lines seen in old novae versus the amplitude of the eruption. Equivalent widths for $H\alpha$, $H\beta$, $He\ II\ \lambda 4686\text{\AA}$ and the Bowen blend / $He\ II\ \lambda 4686\text{\AA}$ ratio are shown in (a), (b), (c) and (d) respectively. Red circles are systems showing also $He\ II\ \lambda 5412\text{\AA}$, blue squares are those that satisfy $W_{HeII\lambda 4686\text{\AA}} / W_{H\beta} > 0.4$ and the black filled circle if $W_{H\beta} > 20\text{\AA}$, the last two criteria established by Silber (1992). The meaning of the arrows is as in Fig. 2.12. More detail in section 2.5.3.

based on the standard formulation corrected for inclination effects found by Warner (1995, see Fig.1.14), for those novae with known i . In particular, his prediction that DY Pup should be a high inclination nova due to its position in his fig. 5.4, was corroborated in this work, since DY Pup turned out to be an eclipsing post-nova (see section 3.3.5).

An updated correlation for t_3 as a function of the amplitude for old novae with $\Delta t > 50$ yr from the data displayed in Table 2.6 is found in Fig. 2.14. The data are fitted with a least-squares fit given by

$$A = 15.77(83) - 2.53(44) \log t_3 \quad (2.1)$$

with a standard deviation of $\sigma = 1.37$ mag. This updated correlation is found to be similar to described previously within the errors (e.g, Vogt 1990, $A = 16.66(67) - 3.03(39) \log t_3$). There is a evident correlation in sense of fast novae reach large amplitude and slow ones have low amplitudes, but the huge dispersion allow a very broad interpretation.

2.6 Summary

In this work we have shown the steps to recover old novae. We have found the true position for eleven post-novae, new spectra for four old nova are presented and nine post-novae candidates have been discarded. The data presented here were included in a sample to discuss the post-novae properties based on their spectral characteristics. The main results are summarized here:

- V4077 Sgr and LW Ser still are in the nebular phase, presenting $W_{H\alpha} \geq 70\text{\AA}$ almost 30 and 40 years after the eruption respectively.
- The large A , strong Balmer lines and relatively high W_λ for EL Aql, EY Aql and KT Mon would be signatures for a low \dot{M} state, but they would be also affected by the inclination according to their high FWHM values. In consequence, we can not classify them properly.
- Based on the presence of He II emission lines, at least partial fulfillment of Silber’s conditions and their large A , we propose EL Aql, KT Mon and V825 Sco as IP nova candidates.
- Time variations in the $H\alpha$ emission line profile suggest that EL Aql, V606 Aql, V726 Sgr, V1583 Sgr, V3064 Sgr and LW Ser are good targets for follow-up time series observations in order to obtain the orbital period.
- The weak Balmer emission lines together with a blue continuum for V693 CrA, V908 Oph, V1149 Sgr and V4049 Sgr would indicate that they are high \dot{M} systems inhabiting an optically thick disc. The high FWHM for V693 CrA and V4049 Sgr would be signature of them being seen at high inclination, unlike V908 Oph and V1149 Sgr that would be seen at low inclination, making it difficult to detect the orbital period in the latter two novae.

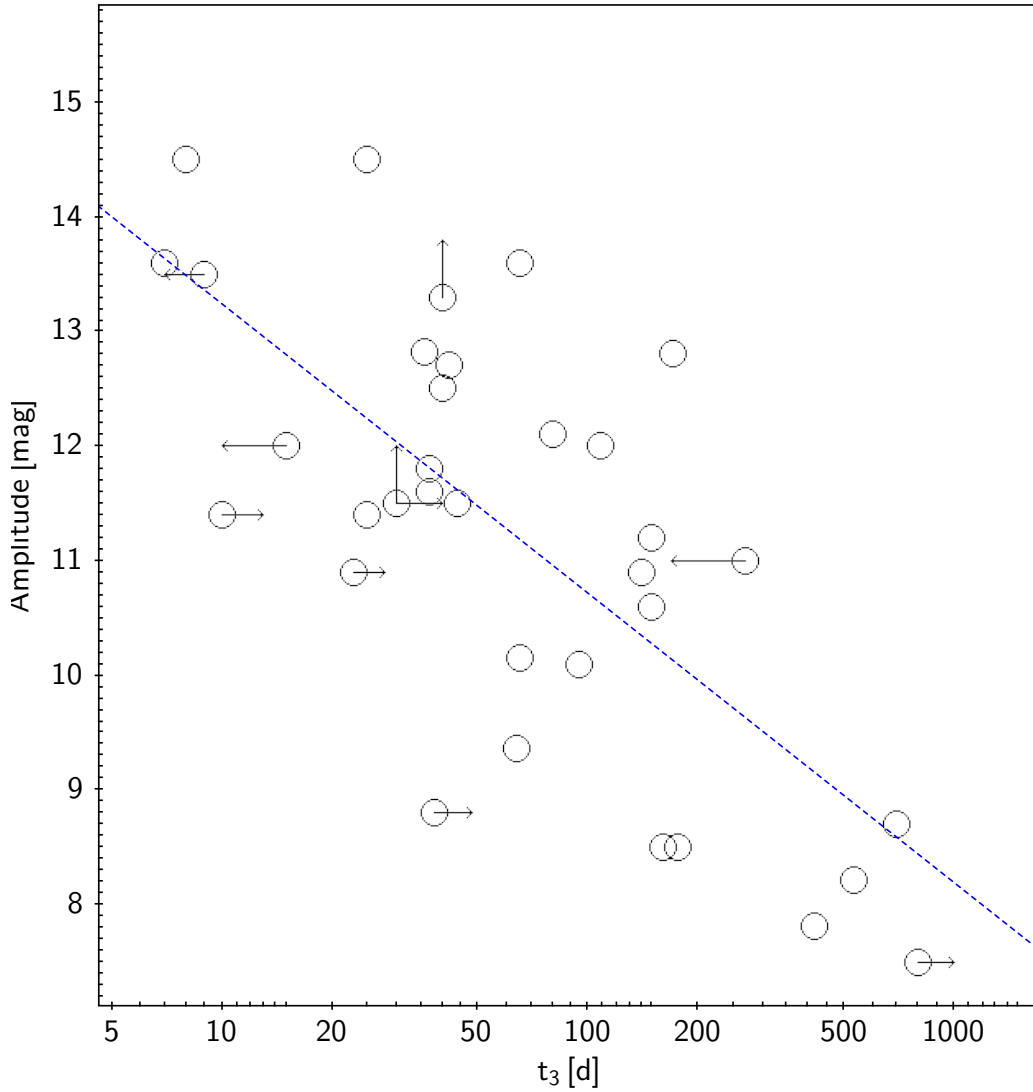


Figure 2.14: Amplitude versus t_3 . The arrows are shown for those systems where only upper or lower limits were established for both A and t_3 . The blue dashed line is a least-squares fit to the data.

- EY Aql is confirmed as a post-nova, discarding the assumption made by [Kato et al. \(2001\)](#) that it is a WZ Sge-type DN. The recovered binary in the KY Sgr field proves to be a symbiotic nova candidate rather than a classical nova. Furthermore, we rule out that V693 CrA is a recurrent nova candidate as was proposed by [Pagnotta & Schaefer \(2014\)](#), because its large A and the width of its lines are consistent with a high inclination rather than being attributed to a high expansion velocity.
- It is very likely that post-novae that erupted between 30 to 50 yr ago with $W_{H\alpha} \geq 70\text{\AA}$ are detected still in the nebular phase, as has been shown by previous studies ([Ringwald et al. 1996](#); [Tomov et al. 2015](#)).
- The mass transfer rate does not change significantly with time since the eruption, in good

agreement with previous studies.

- Because high equivalent widths are related to low \dot{M} but they also are indicators of inclination, we emphasize that studies of equivalent widths can only provide information on \dot{M} if FWHM is also analysed and there is information on the inclination. Establishing \dot{M} only as a function of W_λ is not recommended.
- In order to test the spectral indicators commonly used to define magnetic or IP nova candidates, we have investigated possible relations between the presence of He lines, the Silbers conditions and the amplitude. Our results do not show a correlation between them, therefore we consider that, so far, the most reliable criterion for determining magnetic or IP CVs is the detection of the period of the WD and not based on spectral characteristics.

Table 2.6: Selected photometric data for old novae from the literature including those obtained in this work.
More details in section 2.5.3.

Object	Eruption (year)	m_{\max}^a (mag)	V (mag)	R (mag)	A (mag)	t_3 (days)	t_2 (days)	$E(B-V)$ (mag)	$U-B$ (mag)	$B-V$ (mag)	$V-R$ (mag)	α_{prom}	Ref.
EY Aql	1926	<11p	23.5(5)	23.3	>12.5	40	–	1.52	–	–	–	2.61(7)	6
El Aql	1927	6.4p	20.9	–	14.5	25	–	1.11	-0.1(15)	0.62(8)	0.7(08)	3.12	5
V356 Aql	1936	7.1p	18.0	–	10.9	140	36	0.4	–	–	–	–	3
V500 Aql	1943	6.6p	19.3	–	12.7	42	19	0.15	–	–	–	–	3
V528 Aql	1945	6.9V	18.7	–	11.8	37	–	0.39	–	–	–	4.06(25)	4
V604 Aql	1905	8.2p	19.6	18.8	11.4	25	8	0.69	–	–	–	1.21(22)	3
V606 Aql	1899	<<6.8p	20.4	–	>13.6	65	–	0.35	-0.28(15)	0.4(07)	0.44(7)	2.02	5
V1370 Aql	1982	6.5v	18.5	–	>12	10	7	0.41	–	–	–	0.32(4)	3, 6
OY Ara	1910	6.0p	18.1	–	12.1	80	–	0.32	–	–	–	0.95(15)	7, 12
RS Car	1895	5.0p	18.2	–	13.2	–	~ 32	–	–	–	–	–	9, 12
V365 Car	1948	10.1p	18.31	17.65	8.21	530	–	–	–	–	–	–	2
MT Cen	1931	8.4p	19.8	–	11.4	~ 10	–	1.6	-0.04(3)	1.1(02)	0.47(2)	4.45(7)	1
V812 Cen	1973	11.0V	21.3	–	>10.3	–	–	0.5	-1.0(07)	0.57(6)	0.54(5)	1.75(11)	1
V842 Cen	1986	4.6v	–	–	–	48	–	0.55	–	–	–	2.9(1)	7
V868 Cen	1991	10.2V	19.9	–	9.7	–	–	1.75	–	–	–	3.54(19)	7
V888 Cen	1995	7.6V	16.4	–	8.8	12	–	0.4	–	–	–	2.04(8)	7
AR Cir	1906	10.5p	18.31	17.73	7.81	415	–	5.3	–	1.25	1.0	–	2
BY Cir	1995	7.2v	17.9	–	10.7	124	–	0.55	–	–	–	1.37(13)	7
X Cir	1926	6.5p	19.3	–	12.8	170	160	0.42	-0.45(2)	0.48(3)	0.45(4)	1.52(1)	3
V655 CrA	1967	8.0p	17.9(5)	17.7	9.9	–	–	0.12	–	–	–	1.44(2)	1
V693 CrA	1981	7.0V	21.0	–	14.0	12	5.8	0.10	–	–	–	2.52(1)	3, 6
BT Mon	1939	8.5p	16.4	–	7.9	–	–	0.24	–	–	–	1.27(2)	7, 13
GI Mon	1918	5.6p	16.5	–	10.9	~ 23	–	0.1	–	–	–	1.7(3)	7, 13
KT Mon	1942	9.8p	23.1	–	>13.3	40	–	0.46	-0.39(12)	0.51(1)	0.81(6)	1.5(5)	6
IL Nor	1893	7.0p	19.0	–	12.0	108	–	0.58	-0.69(1)	0.29(2)	0.34(2)	2.53(3)	1

Continued on next page

Table 2.6 – continued from previous page

Object	Eruption (year)	m_{\max}^a (mag)	V (mag)	R (mag)	A (mag)	t_3 (days)	t_2 (days)	$E(B - V)$ (mag)	$U - B$ (mag)	$B - V$ (mag)	$V - R$ (mag)	α_{prom}	Ref.
V840 Oph	1917	6.5p	19.32	–	12.82	36	–	0.4	-0.72(2)	-0.21(3)	0.4(03)	3.3	10
V908 Oph	1954	9.0r	20.5	–	>11.5	>30	–	1.26	-0.1(15)	1.02(15)	1.23(17)	3.38	5
V972 Oph	1957	8.0p	16.5	15.9	8.5	176	–	–	–	–	0.7	–	2
V2104 Oph	1976	8.8v	20.9	20.4	12.1	<29	6	0.15	-0.57(3)	0.5(02)	0.41(3)	-0.45(29)	3
V2109 Oph	1969	8.9b	19.9(5)	19.7	11.0	–	–	0.92	–	–	–	0.81(43)	1
RR Pic	1925	1.0v	12.2	–	11.2	150	–	0.0	–	–	–	2.61(2)	7
CP Pup	1942	0.5v	15.0	–	14.5	8	–	0.2	–	–	–	2.09(2)	7
HS Pup	1963	8.0p	18.0	17.6	10.0	65	–	–	–	–	0.39	–	2
HZ Pup	1963	7.7p	–	–	–	–	–	0.35	–	–	–	2.65(9)	7
V697 Sco	1941	8.0p	20.0	–	12.0	<15	8	0.43	–	–	–	–	3
V728 Sco	1862	5.0v	18.5	–	13.5	<9	–	0.37	-0.83(1)	0.42(1)	0.6(01)	1.85(3)	1
V825 Sco	1964	~8p	19.54	19	~11.54	–	–	1.0	–	–	–	1.35(3)	6
V373 Sct	1975	6.1V	18.4	–	12.3	79	–	–	–	–	0.3	–	2
LW Ser	1978	9.0p	20.4(8)	20.2	11.4	50	35	0.72	–	–	–	2.01(4)	6
Mu Ser	1983	7.7v	–	–	–	5	2.5	0.77	–	–	–	–	3
X Ser	1903	8.9p	17.0	–	8.1	–	–	0.25	–	–	–	1.46(9)	7, 11
HS Sge	1977	7.2v	20.0	–	12.8	21	–	1.2	-0.06(1)	0.88(1)	0.69(1)	3.12(16)	4
BS Sgr	1917	9.2p	17.9	–	8.7	700	–	0.33	0.21(1)	0.69(1)	0.62(1)	1.5(1)	4
GR Sgr	1924	11.4p	15.7	–	4.3	–	–	0.46	–	–	–	2.67(2)	4
V363 Sgr	1927	8.8p	18.17	19.2	9.37	64	22	0.103	-0.95(1)	0.16(1)	0.02(1)	2.43(1)	3, 12
V630 Sgr	1936	4.0v	–	–	–	6	–	–	–	–	–	1.88(2)	8
V726 Sgr	1936	10.8p	20.9	20.7	10.1	95	45	0.38	–	–	–	2.19(3)	6
V909 Sgr	1941	6.8p	20.4	–	13.6	7	–	0.11	–	–	–	1.41(4)	1
V928 Sgr	1947	8.9p	19.5	19.8	10.6	150	88	0.39	-0.55(1)	0.37(1)	0.22(2)	2.4(9)	3
V999 Sgr	1910	7.8p	16.3	–	8.5	160	–	1.7	–	–	–	6.65(2)	4
V1149 Sgr	1945	7.4p	18.4	–	11.0	<270	–	0.39	-1.44(15)	0.3(12)	0.3(07)	2.41	5
V1274 Sgr	1954	10.4p	19.2	18.9	8.8	>38	>20	0.52	-0.7(03)	0.42(3)	0.23(2)	2.88(1)	3
V1583 Sgr	1928	8.9p	20.5	–	11.6	37	–	1.09	-0.16(18)	0.96(9)	0.83(6)	3.27	5
V2572 Sgr	1969	6.5p	18.0(3)	17.8	11.5	44	–	0.15	-0.49(2)	0.32(2)	0.2(02)	2.19(2)	1

Continued on next page

Table 2.6 – continued from previous page

Object	Eruption (year)	m_{\max}^a (mag)	V (mag)	R (mag)	A (mag)	t_3 (days)	t_2 (days)	$E(B - V)$ (mag)	$U - B$ (mag)	$B - V$ (mag)	$V - R$ (mag)	α_{prom}	Ref.
V3964 Sgr	1975	8.5p	19.2(5)	19.0	>10.7	32	–	0.56	–	–	–	1.43	5
V4049 Sgr	1978	12.0p	–	–	–	–	–	0.36	–	–	–	2.87(2)	6
V4077 Sgr	1982	8.72V	19.7(8)	19.5	11	100	10	0.35	–	–	–	2.48(1)	6
XX Tau	1927	5.9p	18.9	–	>13.0	–	–	–	–	–	–	2.66(3)	8, 12
CN Vel	1905	10.2p	17.7	–	7.5	>800	–	–	–	–	0.16	–	2
CQ Vel	1940	9.0p	21.3	–	>12.3	–	–	–	–	–	–	–	8
V382 Vel	1999	2.3V	16.6	–	14.3	9	–	0.1	–	–	–	2.11(3)	7, 13

^a b: blue, p: photographic, r: red v: visual, V: Johnson V

References:

- (1) [Tappert et al. \(2012\)](#), (2) [Tappert et al. \(2013a\)](#), (3) [Tappert et al. \(2014\)](#),
- (4) [Tappert et al. \(2015\)](#), (5) [Tappert et al. \(2016\)](#), (6) This work,
- (7) [Tomov et al. \(2015\)](#), (8) [Schmidtobreick et al. \(2005\)](#), (9) [Bianchini et al. \(2001\)](#),
- (10) [Schmidtobreick et al. \(2003b\)](#), values from Feb 2003), (11) [Šimon \(2018\)](#),
- (12) [Vogt et al. \(2018\)](#), (13) VSX catalogue of AAVSO

Table 2.7: Equivalent width and FWHM data for the most representative emission lines seen in old novae gathered from the literature and including those obtained in this work. Note that the Bowen blend and He II $\lambda 4686\text{\AA}$ equivalent widths are shown only for those novae where they could be resolved. Values marked with * are considered uncertain. The error was designated as 20% for those values. More details in section 2.5.3.

Object	Outburst (year)	W_λ (\AA)			FWHM (Km/s)		W_{Hei} (\AA)		W_{Bowen} (\AA)	W_{Heii} (\AA)		W_{Civ} (\AA)	Ref.
		H α	H β	H γ	H α	H β	5876	6678	4645	4686	5412	5812	
EY Aql	1926	33(1)	33(1)	–	1006	1173	4.2(8)	4.8(8)	–	–	4(1)	–	6
El Aql	1927	47.0(1)	35(1)	26(1)	1234	–	–	8(1)	–	–	3(1)	4(1)	5
V356 Aql	1936	29(2)	7(1)	6(1)	1143	–	–	2.0(4)*	–	–	–	–	3
V500 Aql	1943	41(3)	18(2)	9(2)	1371	–	4(2)	4(2)	–	–	–	4(2)	3
V528 Aql	1945	13.3(7)	4.0(4)	1.8(3)	914	–	–	2.5(2)	4.6(5)	2.9(6)	–	–	4
V604 Aql	1905	8(5)	1.5(3)	–	1051	–	2.4(3)	0.6(2)	–	–	–	–	3
V606 Aql	1899	26(1)	21(1)	18(1)	1280	–	–	4(1)	–	–	–	–	5
V1370 Aql	1982	39.1(5)	20(1)	20(1)	731	–	7.1(5)	5.4(6)	–	–	–	–	3
OY Ara	1910	53.4(1.3)	45.1(9.1)*	34(3.6)	1166	1127	16.9(9)	–	–	–	–	–	7, 12
RS Car	1895	20(2)	4.0(4)	3.4	1175	864	–	–	8.0(6)	12.0(6)	–	–	9, 12
V365 Car	1948	5	–	–	–	–	–	–	–	–	–	–	2
MT Cen	1931	15(4)	5(2)	–	–	864	–	–	–	–	–	–	1
V812 Cen	1973	120(12)	15(4)	–	–	987	16(7)	6(3)	–	–	–	–	1
V842 Cen	1986	102.2(4)	16.3(4)	8.1(2)	1705	1160	4.1(4)	–	6.7(6)	6.8(6)	–	–	7
V868 Cen	1991	123.7(9.4)	–	–	1303	–	–	–	–	–	–	–	7
V888 Cen	1995	8.1(9)	–	–	962	–	–	–	–	–	–	–	7
AR Cir	1906	19	–	–	–	–	–	–	–	–	–	–	2
BY Cir	1995	105.2(3.1)	24.8(2.3)	–	1790	1816	–	–	16.4(4.0)	12.0(4.8)	–	–	7
X Cir	1926	28.1(4)	17.5(5)	11(2)	1417	–	2.5(5)	3.1(6)	–	–	0.8(3)	2.6(3)	3
V655 CrA	1967	4(1)	1.0(0.2)*	–	–	617	–	–	–	–	–	–	1

Continued on next page

Table 2.7 – continued from previous page

Object	Outburst (year)	W_λ (Å)			FWHM (Km/s)		W_{Hei} (Å)		W_{Bowen} (Å)	W_{Heii} (Å)		W_{Civ} (Å)	Ref.
		H α	H β	H γ	H α	H β	5876	6678	4645	4686	5412	5812	
V693 CrA	1981	11(3)	9(2)	5(1)	1966	–	–	–	–	–	–	–	3
BT Mon	1939	44.2(4)	21.0(2)	13.4(2)	1306	1111	6.9(2)	–	6.9(2)	17.3(3)	1.6(2)	1.3(2)	7, 13
GI Mon	1918	4.0(3)	1.1(2)	–	618	619	–	–	–	1.4(2)	–	–	7, 13
KT Mon	1942	24(3)	13.2(1.5)	–	1280	1604	3(1)	5(3)	–	14.5(2.5)	–	–	6
IL Nor	1893	9(1)	4(1)	3(1)	–	1296	1.0(2)*	–	–	–	–	–	1
V840 Oph	1917	16.6(5)	15.1(6)	15.8(6)	1454	1512	>12	2.7(1.0)	16.4(7)	15.0(7)	6.1(5)	9.6(3)	10
V908 Oph	1954	3(1)	1.0(0.2)*	1.0(2)*	549	–	–	–	–	–	–	–	5
V972 Oph	1957	2	–	–	–	–	–	–	–	–	–	–	2
V2104 Oph	1976	18.7(7)	18(1)	18(1)	869	–	4.9(5)	3.9(3)	–	9.1(7)	–	–	3
V2109 Oph	1969	22(1)	9(2)	14(3)	–	802	5(1)	3(1)	–	–	–	–	1
RR Pic	1925	20.6(5)	7.7(2)	3.4(1)	929	1154	–	–	8.2(2)	12.6(2)	3.0(2)	3.8(5)	7
CP Pup	1942	18.7(7)	14.6(1)	12.3(1)	1360	1297	2.4(3)	–	8.8(1)	8.4(2)	3.7(2)	2.5(1)	7
HS Pup	1963	25.0	–	–	–	–	–	–	–	–	–	–	2
HZ Pup	1963	59.9(1.2)	20.5(6)	14.1(5)	958	1074	9.7(9)	–	–	16.7(6)	–	–	7
V697 Sco	1941	9.7(7)	4.0(8)*	2.0(4)*	1554	–	–	2.1(8)	2.7(8)	–	–	–	3
V728 Sco	1862	40(1)	21(1)	16(1)	–	1852	5(1)	4(1)	–	–	–	–	1
V825 Sco	1964	16(2)	4.0(5)	6(1)	1417	1049	–	3(1)	6(1)	11(1)	3.0(5)	–	6
V373 Sct	1975	53	–	–	–	–	–	–	–	–	–	–	2
LW Ser	1978	70(2)	12(2)	3(1)	1417	1296	3.1(9)	2.5(1.2)	3.3(7)	1.8(7)	–	–	6
Mu Ser	1983	23(2)	–	18(2)	1234	–	–	4(1)	–	–	5(2)	7(2)	3
X Ser	1903	20(1.4)	14.2(1.1)	15.4(1.7)	538	752	–	–	–	–	–	–	7, 11
HS Sge	1977	14.6(3)	7.6(3)	6.0(6)	1600	–	–	2.5(2)	–	–	1.5(2)	–	4
BS Sgr	1917	12.2(1)	4.7(1)	3.5(2)	640	–	–	1.4(1)	15.1(2)	15.1(1)	2.8(1)	1.2(3)	4
GR Sgr	1924	2.5(1)	1.0(2)*	0.4(1)	686	–	–	0.8(1)	1.8(3)	1.8(3)	–	–	4
V363 Sgr	1927	11.5(5)	5.2(3)	4.1(5)	686	–	0.9(1)	2.0(5)	–	–	–	–	3, 12
V630 Sgr	1936	27.0(6)	13.5(7)	7.3(4)	1079	1173	–	–	–	2.8(2)	5.1(3)	–	8
V726 Sgr	1936	24.9(3.6)	6(5)	6(4)	1024	1049	–	4(2)	6(4)	9(5)	–	–	6
V909 Sgr	1941	39(3)	24(2)	16(2)	–	1234	2(1)	9(2)	–	–	10(2)	–	1

Continued on next page

Table 2.7 – continued from previous page

Object	Outburst (year)	W_λ (Å)			FWHM (Km/s)		W_{Hei} (Å)		W_{Bowen} (Å)	W_{Heii} (Å)		W_{Civ} (Å)	Ref.
		H α	H β	H γ	H α	H β	5876	6678	4645	4686	5412	5812	
V928 Sgr	1947	14.3(4)	1.8(4)*	–	686	–	–	0.6(5)	–	–	–	–	3
V999 Sgr	1910	4.7(2)	1.7(1.0)*	0.6(1)	594	–	–	1.1(1)	3.1(1)	3.1(1)	0.5(1)	0.8(2)	4
V1149 Sgr	1945	6(1)	2(1)	3(1)	960	–	–	1.0(2)*	5(1)	3(1)	1.0(2)*	3(1)	5
V1274 Sgr	1954	11.5(4)	0.40(8)*	–	1006	–	–	0.9(1)	–	–	–	0.9(2)	3
V1583 Sgr	1928	26(5)	9(1)	6(1)	777	–	–	4(1)	5(1)	2(1)	–	–	5
V2572 Sgr	1969	13(1)	4(1)	2.0(5)	–	988	1(5)	2(1)	–	–	–	–	1
V3964 Sgr	1975	12(1)	5(1)	3(1)	1326	–	–	2(1)	3(1)	2(1)	–	–	5
V4049 Sgr	1978	17(7)	4(2)	4.5(3)	1600	1543	–	–	4.9(4)	2.9(7)	–	–	6
V4077 Sgr	1982	367(62)	52(2)	17.5(1.4)	1051	864	20.7(2)	11.1(3)	18.1(3)	15.7(3)	–	5.0(5)	6
XX Tau	1927	52(1)	19.2(6)	13.6(3)	1536	1420	0.5(1)	0.39(10)	–	–	–	–	8, 12
CN Vel	1905	5.0	–	–	–	–	–	–	–	–	–	–	2
CQ Vel	1940	18.0(5)	4.5(5)	–	1317	1296	–	–	–	–	–	–	8
V382 Vel	1999	71.6(6)	16.6(2)	8.6(1)	1949	1677	5.6(2)	–	9.2(2)	10.9(3)	–	2.6(2)	7, 13

References:

- (1) Tappert et al. (2012), (2) Tappert et al. (2013a), (3) Tappert et al. (2014),
(4) Tappert et al. (2015), (5) Tappert et al. (2016), (6) This work,
(7) Tomov et al. (2015), (8) Schmidtobreick et al. (2005), (9) Bianchini et al. (2001),
(10) Schmidtobreick et al. (2003b, values from Feb 2003), (11) Šimon (2018),
(12) Vogt et al. (2018), (13) VSX catalogue of AAVSO

2.7 Appendix

Additional Figures are shown in this section.

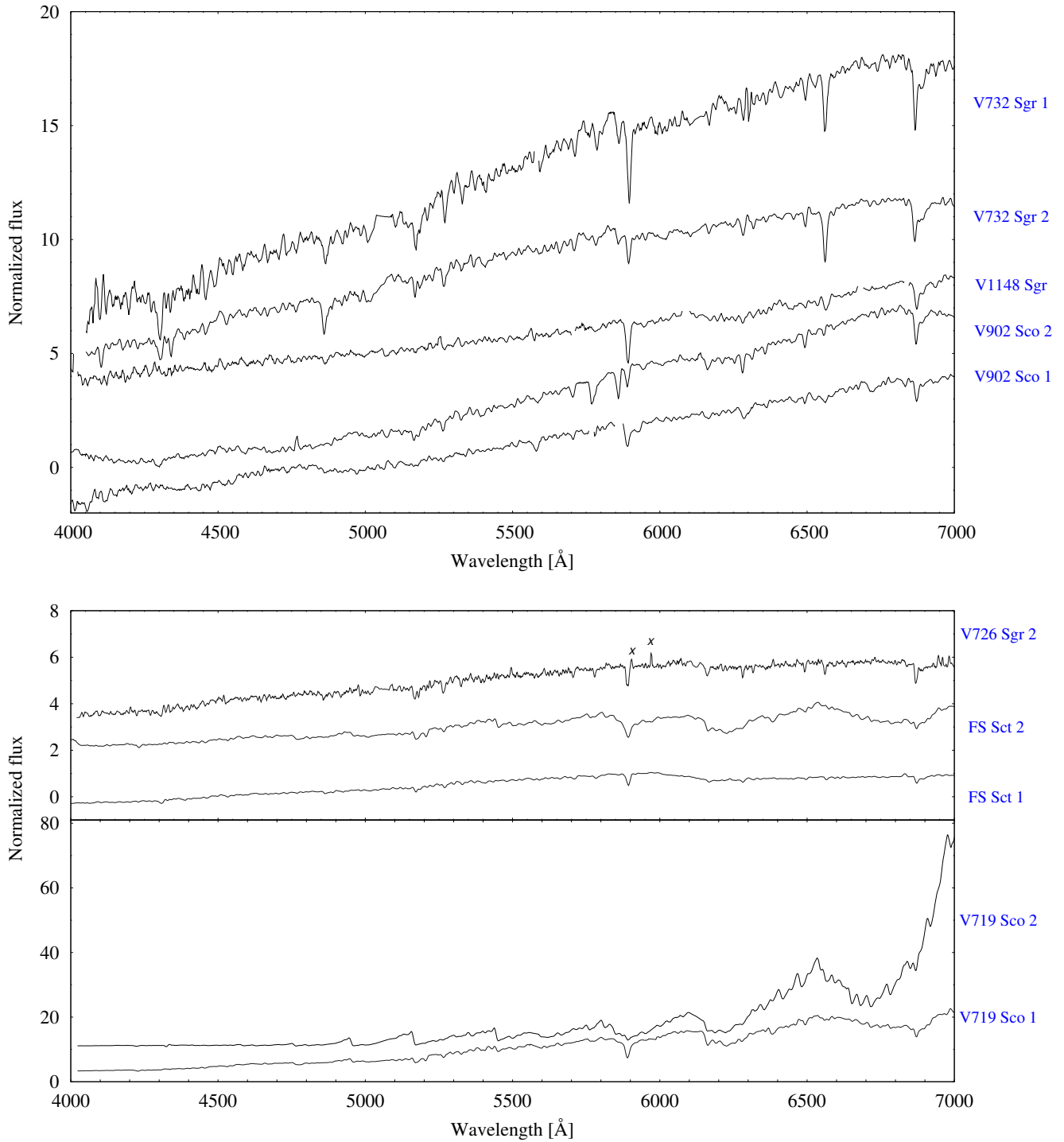


Figure 2.15: Spectra for those candidates found via colour-colour diagram which turned out to not be the post-novae. Top: Candidates from *UBVR* photometry. Bottom: Candidates from photometry based on *H α* off-band filter. Artefacts are marked with an \times . See section 2.4.4 for more details.

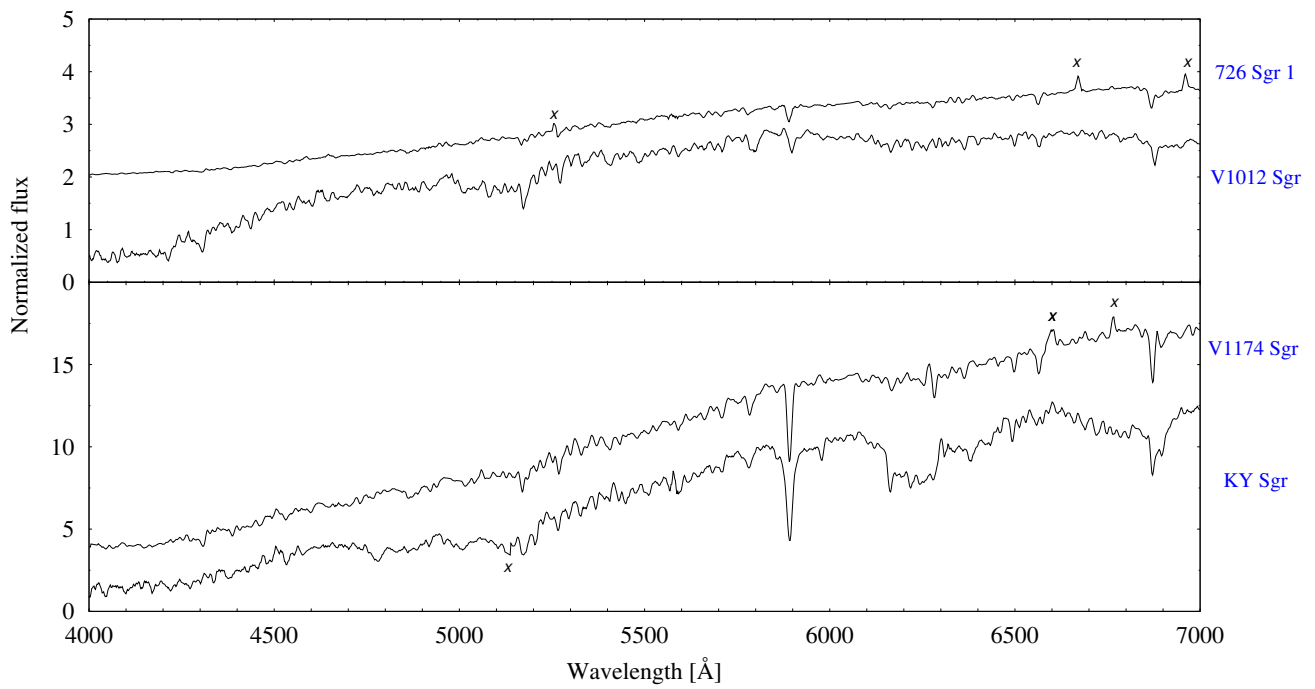


Figure 2.16: Spectra for selected candidates considered as the old nova counterpart by Mróz et al. (2015) which turned out to be misidentified. Artefacts are marked with an \times . More information in section 2.4.4.

Chapter 3

The orbital period distribution of novae

This chapter is published as

Life after eruption VIII: The orbital periods of novae

*I. Fuentes-Morales, C. Tappert, M. Zorotovic, N. Vogt, E. C. Puebla,
M. R. Schreiber, A. Ederoclite and L. Schmidtobreick*

Monthly Notices of the Royal Astronomical Society, 2020, Volume 501, Issue 4, p. 6083–6102

Abstract

The impact of nova eruptions on the long-term evolution of Cataclysmic Variables (CVs) is one of the least understood and intensively discussed topics in the field. A crucial ingredient to improve with this would be to establish a large sample of post-novae with known properties, starting with the most easily accessible one, the orbital period. Here we report new orbital periods for six faint novae: X Cir (3.71 h), IL Nor (1.62 h), DY Pup (3.35 h), V363 Sgr (3.03 h), V2572 Sgr (3.75 h) and CQ Vel (2.7 h). We furthermore revise the periods for the old novae OY Ara, RS Car, V365 Car, V849 Oph, V728 Sco, WY Sge, XX Tau and RW UMi. Using these new data and critically reviewing the trustworthiness of reported orbital periods of old novae in the literature, we establish an updated period distribution. We employ a binary-star evolution code to calculate a theoretical period distribution using both an empirical and the classical prescription for consequential angular momentum loss. In comparison with the observational data we find that both models especially fail to reproduce the peak in the 3 – 4 h range, suggesting that the angular momentum loss for CVs above the period gap is not totally understood.

3.1 Introduction

A nova eruption occurs in CVs, which are close interacting binary systems composed of a donor, usually similar to a late-type main-sequence star, that fills its Roche lobe, transferring material to the WD primary component. If the accumulated hydrogen onto low-luminosity WD reaches a critical value, a thermonuclear runaway (TNR) is triggered on the surface of the primary that ejects material into the interstellar medium. This process is known as a nova eruption and CVs that experienced such an event are called classical novae or post-novae. The binary is not destroyed by the nova eruption, allowing for the accretion process to start anew, which possibly occurs as early as within one or two years after the eruption (Retter & Leibowitz 1998). The typical length of this recurrence cycle is currently estimated to $\geq 10^4$ yr (Shara et al. 2012c; Schmidtobreick et al. 2015). This is thus not to be confused with the class of recurrent novae, which have much shorter recurrence cycles and stellar configurations that usually differ significantly from the main bulk of CVs.

It is still not clear whether the behaviour of the CV between two subsequent nova eruptions is largely defined by the eruption, e.g. with the latter causing the CV to switch between different states \dot{M} , or whether the CV is mainly unaffected by the eruption, e.g. a low \dot{M} pre-nova would emerge as a low \dot{M} post-nova, and likewise for high \dot{M} systems. In the latter case, it would be the intrinsic properties of the CV that determine the length of the nova cycle, without interaction with the nova eruption itself.

One widely used possibility is that the secondary star is irradiated by the hot post-eruption WD, enhancing \dot{M} (the so-called hibernation model; Shara et al. 1986), which could notably accelerate the CV evolution. Recently observational evidence appear to corroborate this hypothesis (Patterson et al. 2013; Mróz et al. 2016; Shara et al. 2017a), nevertheless, alternative scenarios exist (more details in section 1.5.4; King et al. 1995; Schreiber et al. 2000). One possibility to investigate the validity of above scenarios is to compare the physical parameters of the post-novae with those of the overall CV population. Of those, the orbital period (P_{orb}) is the most accessible one and also represents already a rough indicator of the state within the secular evolution of CVs (e.g., Knigge et al. 2011b). A number of theoretical orbital period distributions of novae have been published (Diaz & Bruch 1997; Nelson et al. 2004; Townsley & Bildsten 2005). However, for a proper comparison with the observed distribution, the latter needs to be made out of a sample of statistically significant size. The main problem related in general to the study of the post-nova population is that these are mostly very faint objects, requiring a significant amount of time on large telescopes to study them. Diaz & Bruch (1997) made the first observational period distribution of old novae from a sample of 28 novae with $P_{\text{orb}} < 10$ h. Analysing the influence of certain observational selection effects, they found that those parameters have a little effect on the shape of the period distribution. They also suggested a correlation between the nova explosion amplitude

and the orbital period. Warner (2002) analysed the period distribution using 50 orbital periods he qualified as reliable, indicating a concentration to 3.3 h, and noting a similarity to a pile-up of magnetic CVs near this value. Townsley & Bildsten (2005) used that period distribution to show that their simulations are consistent with the idea that CVs evolve across the period gap. Tappert et al. (2013a) compared the period distribution of all CVs (data from Ritter & Kolb 2003b, version 7.20, 2013) with 78 orbital periods of post-novae. They confirmed the concentration of novae at 3-5 h, in striking difference to the distribution of all CVs. This particular range is dominated by high mass-transfer systems (Rodríguez-Gil et al. 2007), in contrast to the general CV population, which is dominated by low-mass transfer and systems with orbital periods < 2 h (Pala et al. 2020). These differences were predicted by Townsley & Bildsten (2005) and likely reflect the shorter nova eruption recurrence times for high-mass transfer systems.

However, the period distribution of novae is both still undersampled in large parts of the period range, such that an addition of a comparatively low number of new periods has the potential to significantly change the shape of the distribution. Therefore, any comparison with the predicted distribution will suffer from large uncertainties. This is the more important, because, since the brightness of the post-nova is mainly determined by the brightness of the accretion disc, the observed period distribution is potentially biased towards bright, long-period systems with high mass-transfer rates and low nova eruption amplitudes. Thus, short-period low mass-transfer novae could still amount to a significant number, but are hidden, because they are intrinsically faint. The work by Gänsicke et al. (2009b) shows that observations of faint CVs are crucial for our understanding of CV evolution and the use of the period distribution as a diagnostic tool, and this likely is also the case for novae.

In this work we derive the orbital period for a number of faint post-novae, and to improve the precision of already established periods for mostly eclipsing systems that were included in Vogt et al. (2018). Furthermore, the theoretically predicted period distribution of novae based on a binary population model is calculated and compared to the observational data.

3.2 Observations and data reduction

3.2.1 Photometric data

We obtained time-series photometry in the V -band in 2013, 2014 and 2015 using direct CCD imaging with a field of view of 8.85 arcmin square, 0.259 arcsec pixel scale and a 2×2 binning at the 2.5-m du Pont telescope at Las Campanas Observatory, Chile. Alignment of the individual images for each field was performed by the ASTROIMAGEJ software (Collins et al. 2017). All fields were reduced by bias and flat field correction and instrumental magnitudes were calculated with aperture photometry using the DAOPHOT package from IRAF. The aperture radius in each frame

was adopted as the average of the full width at half maximum (FWHM) of the stellar point spread function (PSF) in a given frame. Differential magnitudes were calculated using comparison stars in the vicinity of the post-nova, within a radius of 400 pixels. In order to calibrate the instrumental magnitude, stars with known V magnitude were chosen to be compared with their tabulated V magnitudes either in the The Naval Observatory Merged Astrometric Dataset (NOMAD, [Zacharias et al. 2005](#)) or in the GSC (The HST Guide Star Catalogue, version 2.3.2) catalogue. The calculated V magnitudes are presented in the log of observations (Table 3.1).

Further V -band data were obtained between August 2013 and August 2015 with A novel Double-Imaging CAMera (ANDICAM) placed at the 1.3-m telescope operated by the Small and Moderate Aperture Research Telescope System (SMARTS) consortium, at the Cerro Tololo Inter-American Observatory (CTIO), located in La Serena, Chile. The field of view was six arcmin square and we used a 2×2 binning. These observations yielded differential photometry over a time range of two years with a time resolution of the order of 3 – 5 days. For more details concerning these data see [Vogt et al. \(2018, paper VII\)](#). Hereafter we refer to these observations as “CTIO set”.

3.2.2 Spectroscopic data

Time-series spectroscopic data were collected from the following observing runs: with the ESO Faint Object Spectrograph and Camera (EFOSC2, [Buzzoni et al. 1984](#)) at the ESO New Technology Telescope (NTT) in La Silla, Chile, we obtained data in June/July 2011, May 2012 and 2013. The grism used was #20 covering a wavelength range of 6040 – 7140 Å with a 1 arcsec slit, yielding a resolution of 3.7 Å. In December 2018 and January 2019, additional data on XX Tau were obtained at the Very Large Telescope (VLT) using the FOcal Reducer/low dispersion Spectrograph 2 (FOR2, [Appenzeller et al. 1998](#)) with the 1200R grism and a 0.7-arcsec slit, covering a wavelength range of 5750 – 7319 Å with a resolution of 2.14 Å. Acquisition frames were taken with the edge filter *GG435*, thus no broad-band photometric magnitudes are available for this run. The nova RW UMi was observed in June 2015 with the Gran Telescopio Canarias (GTC), installed in the Spanish Observatorio del Roque de los Muchachos of the Instituto de Astrofísica de Canarias, in the island of La Palma, using the Optical System for Imaging and low-Intermediate-Resolution Integrated Spectroscopy (OSIRIS, [Cepa 1998](#)). The R2500R volume-phased holographic grating was employed, covering a wavelength range of 5575 – 7685 Å. A 0.6 arcsec slit yielded a spectral resolution of 2.5 Å, measured as the FWHM of the night-sky spectral lines. No acquisition frames were available, thus no estimates can be given for the photometric brightness of the object at the time of the observations.

The reduction and calibration of the data was conducted with IRAF. Reduction of the spectra consisted in bias and overscan subtraction and division by a flat field that had been normalized by

fitting a cubic spline of high order. The cosmic rays removal was performed with the `LACOS_SPEC` task for IRAF (van Dokkum 2001). One-dimensional spectra were extracted with the `APALL` routine within the `ONEDSPEC` package. Wavelength calibration was determined with *He*, *Ar* and *Ne* lamp for datasets. The spectra were normalized with respect to the continuum and corrected to heliocentric velocity with the IRAF’s `RVCORRECT` task.

3.2.3 Periodicity search

While CVs are known for the presence of strong emission lines in their spectra, among whose $H\alpha$ is usually the most prominent one, most post novae actually show comparatively weak emission lines (e.g. Tappert et al. 2014, and references therein), indicative of an optically thick accretion disc and a high mass-transfer rate. Additionally, most spectroscopic targets of the present study proved to be rather faint ($V > 18.0$), and thus the best signal-to-noise values did not exceed 5 and 10 for the EFOSC2 and the FORS2 data, respectively. This, together with most lines being broad, asymmetric, and of variable shape, rendered the usual methods of fitting the line profile to measure its Doppler shift unsuccessful. Thus, the technique used by Tappert et al. (2013a) to measure the $H\alpha$ displacement was employed: First, each normalized spectrum was smoothed down to the effective spectral resolution of the instrument. Second, to account for potential imperfections related to the wavelength calibration, individual wavelength corrections were applied with respect to the $\lambda 6300.304 \text{ \AA}$ [O I] sky emission line. Subsequently, the average spectrum for each target was cross-correlated by eye to each individual spectrum by applying a positional shift and an intensity scale factor. The resulting displacement was recorded as the radial velocity shift.

The periodicity analysis in both light curves and radial velocities was performed with PERANSO (Paunzen & Vanmunster 2016), which allows to choose among different methods based on discrete Fourier transform algorithm. The Lomb-Scargle routine was used and the error was estimated as the frequency resolution in each campaign. i.e. $1/\Delta t$.

Radial velocities are fitted with a sinusoidal function as:

$$v_r(t) = \gamma + K \sin[2\pi (t - T_0)/P_{\text{orb}}] \quad (3.1)$$

Where: $v_r(t)$ is the measured radial velocity at time t , K corresponds to the semi amplitude, γ is the systemic velocity, T_0 is the chosen zero point and P_{orb} is the orbital period of the system.

Table 3.1: Log of observations. Above: time-series photometry. Bottom: time-series spectroscopy. N refers to the number of observations, t_{exp} is the exposure time in seconds, Δt is the time covered by observation in hours. Last column contains the magnitude value and the bandpass which it was measured. For the CTIO data, see [Vogt et al. \(2018\)](#).

Object	Date	N	t_{exp}	Δt	magnitude
X Cir	2015-05-19	209	60	7.93	18.77(32) <i>V</i>
	2015-05-20	80	60	2.89	18.76(38) <i>V</i>
	2015-05-21	56	60	1.99	18.82(33) <i>V</i>
	2015-05-23	37	60	1.48	18.81(37) <i>V</i>
	2015-07-10	66	90	3.33	19.04(23) <i>V</i>
IL Nor	2015-05-20	100	60	3.77	18.73(07) <i>V</i>
	2015-05-21	53	60	1.89	18.52(07) <i>V</i>
	2015-05-22	39	180	2.74	18.48(04) <i>V</i>
DY Pup	2015-05-23	42	60	1.66	18.24(07) <i>V</i>
	2013-12-31	139	90	5.11	19.16(07) <i>V</i>
V2572 Sgr	2014-01-01	47	60	1.66	19.14(07) <i>V</i>
	2012-05-16	142	40	3.15	17.92(08) <i>V</i>
V2572 Sgr	2015-05-20	79	60	2.88	17.65(14) <i>V</i>
	2015-05-21	121	60	4.36	17.77(10) <i>V</i>
	2015-05-22	167	60	6.15	17.73(19) <i>V</i>
	2015-05-24	90	60	3.34	17.68(08) <i>V</i>
	2015-07-11	52	60	2.78	17.81(10) <i>V</i>
XX Tau	2013-12-28	128	60	4.62	19.11(08) <i>V</i>
	2013-12-30	45	60	1.59	19.15(09) <i>V</i>
	2013-12-31	37	60	1.31	19.11(08) <i>V</i>
	2014-01-01	18	120	0.92	19.05(07) <i>V</i>
CQ Vel	2013-12-28	55	120	2.88	19.13(12) <i>V</i>
	2013-12-29	79	120	5.37	19.05(11) <i>V</i>
	2013-12-30	115	120	6.00	19.00(08) <i>V</i>
	2013-12-31	22	120	1.12	18.99(08) <i>V</i>
	2014-01-01	99	120	5.17	19.11(07) <i>V</i>
V2572 Sgr	2011-06-29	1	900	0.25	18.30(59) <i>R</i>
	2011-06-30	3	900	3.54	18.52(15) <i>R</i>
	2011-07-01	8	900	9.39	18.46(05) <i>R</i>
	2011-07-03	1	900	0.25	18.64(10) <i>R</i>
XX Tau	2018-12-30	8	600	0.90	–
	2018-12-31	6	600	1.17	–
	2019-01-01	20	600	3.72	–
	2019-02-10	4	600	0.91	–
	2019-02-12	4	600	0.91	–
RW UMi	2015-06-19	10	600	1.56	–
	2015-06-21	16	600	2.60	–
	2015-06-22	5	600	0.69	–
CQ Vel	2012-03-25	2	900	0.70	19.57(04) <i>R</i>
	2012-03-26	9	900	3.39	19.36(04) <i>R</i>
	2012-03-27	7	900	2.69	19.35(28) <i>R</i>

3.3 Results

3.3.1 RS Car (1895)

This nova flared up in 1895 being discovered by Mrs. Fleming on photographic plates taken at the Arequipa Station of the Observatory (Pickering 1895). The maximum light was reported at photographic magnitude $m_p = 7.2$ mag. It was categorized as a slow nova and it was spectroscopically recovered by Bianchini et al. (2001) 7 arcsec away from the published position. The spectrum exhibited a blue continuum and a SED typically of an optically thick disc indicating that the system is still in a high-mass transfer state. Woudt & Warner (2002) presented high-speed photometry in white light of this nova, exhibiting a light curve with several features resembling strong flickering. While they do not present a plot of the Fourier spectrum, they describe it as consisting of a strong signal corresponding to $P = 1.977$ h, i.e. 0.08238 d, and its harmonics. They ascribe this period to likely correspond to a superhump, based on RS Car showing the spectroscopic signatures of a high mass-transfer rate, which, at such short a period, is expected to produce an eccentric accretion disc, the latter being thought to be the physical reason behind the superhump signal (e.g., Wood et al. 2011). From our CTIO data, the periodogram presents two strong peaks at $f_1 = 11.13(01)$ and $f_2 = 12.13(01)$ c/d (Fig. 3.1, c). The frequency resolution of the data set, $1/\Delta t$, was used to estimate the associated uncertainty. We note that f_2 corresponds to a period that is very close to the signal detected by Woudt & Warner (2002), implying that it is stable in time. We thus choose this as the main signal, in spite of it being the slightly lower of the two main peaks. Unfortunately, from the lack of corresponding information in Warner (2002), we cannot examine the possible presence of f_1 in their data. Taking the maximum of the modulation according to f_2 as zero point, the ephemeris is

$$\text{HJD}(\text{max}) = 2\,456\,676.7876(09) + 0^{\text{d}}.082429(25) E, \quad (3.2)$$

and the alternative ephemeris to f_1 is

$$\text{HJD}(\text{max}) = 2\,456\,663.7723(16) + 0^{\text{d}}.089842(81) E. \quad (3.3)$$

The phased light curves using the ephemeris (3.2) are shown in Fig. 3.1 (a). We note that the light curve shows similar characteristics as the one from Woudt & Warner (2002), but the sequence of the humps has been inverted, with the large hump now following the minimum, and the small hump being the one preceding it. Other differences are that the minimum appears to be slightly broader (by about 0.1 phases) and that the total amplitude with ~ 0.3 mag is slightly larger.

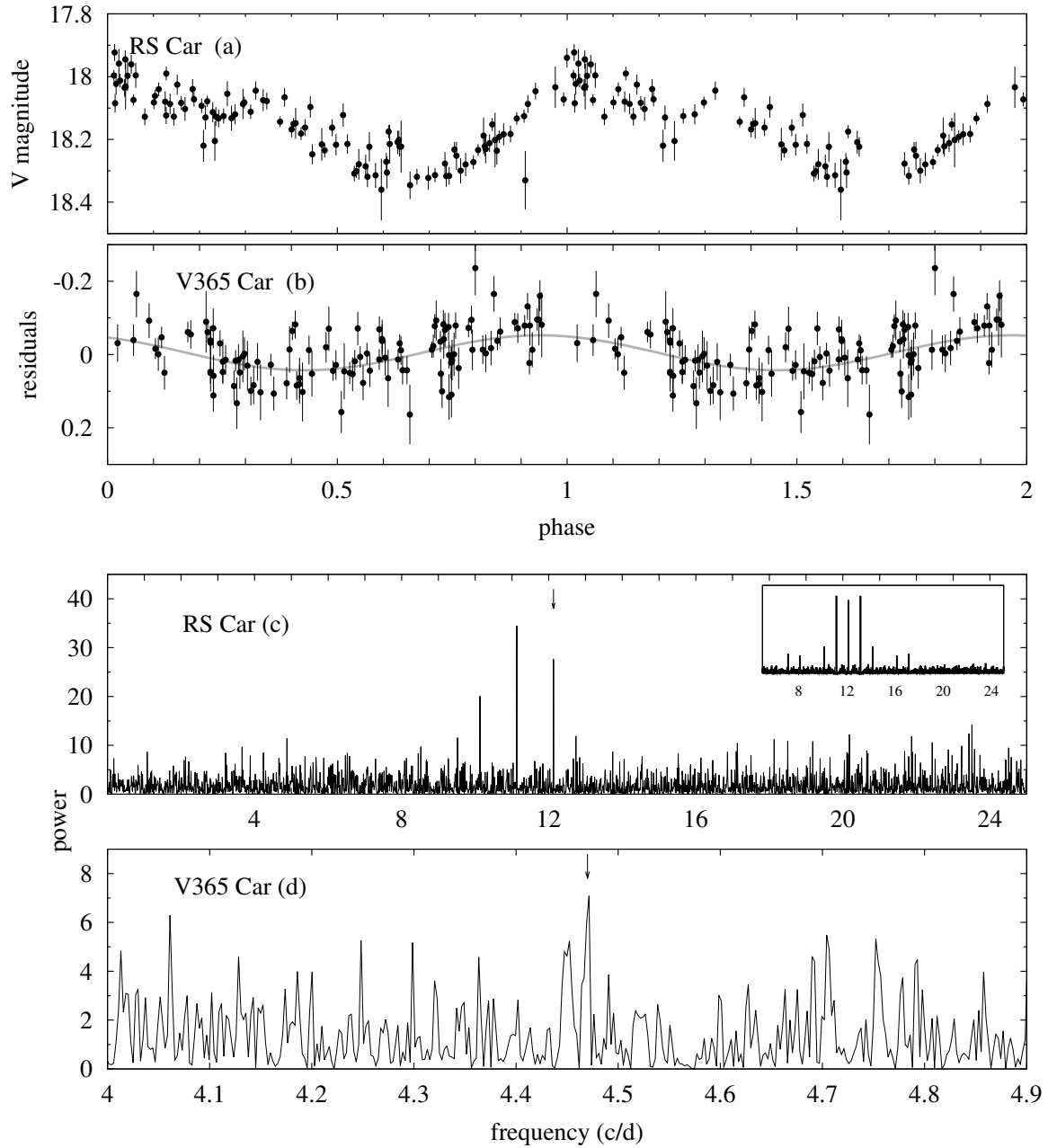


Figure 3.1: Phased light curves for (a) RS Car and (b) V365 Car according to ephemerides (3.2) and (3.4) respectively. (c) Scargle periodogram for RS Car and the spectral window centered at the frequency marked with an arrow. (d) the same for V365 Car in the range of the frequency found by Tappert et al. (2013a). The arrow marks the peak at $f = 4.47$ c/d.

3.3.2 V365 Car (1948)

This nova with an eruption in 1948, discovered by [Henize \(1967\)](#), has been largely described by [Tappert et al. \(2013a\)](#), who performed both radial velocities and R -band photometry. They found a periodicity to $P = 0.2247(40)$ d and their light curve present a sinusoid or hump shape with an amplitude of ~ 0.2 mag. The CTIO data on V365 Car showed a long-term decline in brightness (see [Vogt et al. 2018](#), for more details). After subtracting this trend, we performed a period search on the residuals. While the resulting periodogram does not present any obvious dominant signal, a closer look at the frequency range near the previously reported value of $f = 4.45$ c/d by [Tappert et al. \(2013a\)](#) shows a narrow feature at $f = 4.4704$ c/d that rises slightly above the background noise (see Fig. 3.1, d). Consequently, with the CTIO data was possible to refine the orbital period value. The improved ephemeris of the maxima is

$$\text{HJD}(\text{max}) = 2\,456\,628.845(78) + 0^{\text{d}}.22369(12) \text{ E.} \quad (3.4)$$

The folded light curve according to this period is shown in Fig. 3.1 (b). Its shape as a sinusoid is similar to the one presented by [Tappert et al. \(2013a\)](#), with an average amplitude of ~ 0.1 mag.

3.3.3 X Cir (1927)

X Cir underwent a nova eruption in 1927 ([Becker 1929](#)) and the position of the post-nova was recovered by [Tappert et al. \(2014\)](#). The spectrum indicated the presence of an accretion disc seen at high inclination, and the prominent Balmer emission lines along with a flat continuum point to low mass-transfer rate.

Special care was taken to perform the V -band photometry of this object, since a close visual companion is located at a distance of 0.8 arcsec southwestward. To assure a clean background subtraction and to account for the different seeing conditions, the aperture photometry was performed using a large annulus that covered both components of the visual binary. In good agreement with the conclusions drawn from the spectroscopic appearance, X Cir turned out to be an eclipsing CV with $P_{\text{orb}} = 3.71$ h. The light curves are shown in Fig. 3.2. A smooth variability is seen outside of the eclipse. The depth of the eclipse is slightly different in each cycle, varying from 1 mag to 1.5 over the seven observed cycles. At this stage it remains unclear whether these variations are intrinsic, or are caused by the presence of the companion in the aperture radius in combination with variable seeing.

X Cir was also part of the CTIO data set described in [Vogt et al. \(2018\)](#), although it is not included in that paper, for reasons stated below. The data consist of 96 frames with typically two subsequent exposures per night with integration times of 170 and 340 s. The set spans a time range of 168.7 d, from HJD 2 456 690.7934 to 2 456 859.5209. Basic reduction was performed as

for the other objects of the CTIO data. However, because of the close companion, in combination with very variable seeing conditions, it was necessary to perform the aperture photometry of this object without applying a centering algorithm. For this purpose, one image frame with good seeing conditions was selected, and the positions of X Cir and the other component of the visual binary (hereafter M2) were measured with respect to a number of reference stars. In all other frames, the positions of those two components were calculated corresponding to the average of the shift of those reference stars with respect to the initially selected frame. Aperture photometry was performed at the such defined positions, and additionally of one comparison star whose constant brightness had been previously established. Finally, the differential magnitudes of the post-nova were computed as the difference between the brightness measured at its position and the average of the values of the comparison star and M2. The resulting data are shown in Fig. 3.13 top. While it turned out that this light curve is still too strongly affected by the variable seeing to be used for a study of the intrinsic long-time behaviour of the post-nova, the fact that the data coverage includes a number of eclipses still made the set useful to refine above value of the orbital period obtained from the du Pont observations.

From the light curve, we identified 12 data points that could be unambiguously assigned to being part of an eclipse. Whenever there were two data points within the same night, we chose the fainter one as the time of eclipse, and in the cases where the two had identical brightness within the photometric uncertainty, we computed the average of those times. In order to calculate the correct cycles corresponding to each data point, we adjusted the orbital period iteratively. The value derived from the du Pont data was used to calculate the cycle corresponding to the second data point. A linear fit then yielded an improved period that was subsequently used to calculate the cycle corresponding to the third data point, and so forth. The fit to all six data points yielded $P_{\text{orb}} = 0.1544504(38)$ d, which served to bridge the cycle count gap between the du Pont and the CTIO data, and allowed for an unambiguous cycle count in the latter data set. The final fit to all eclipses gives the following ephemeris

$$\text{HJD}(\text{min}) = 2\,457\,166.5047(12) + 0^{\text{d}}.154\,459\,53(63) E , \quad (3.5)$$

where we chose the cycle number of the best defined of the most recent eclipse measurements as zero point. The cycles, the measured eclipse times and the fit residuals are given in Table 3.4, and the CTIO phased light curve folded with this ephemeris is shown in the bottom plot of Fig. 3.13. We ascribe the noisy eclipse shape and the light curve in general to the already mentioned different seeing conditions that caused a variable amount of the light of the close companion to be included in the aperture.

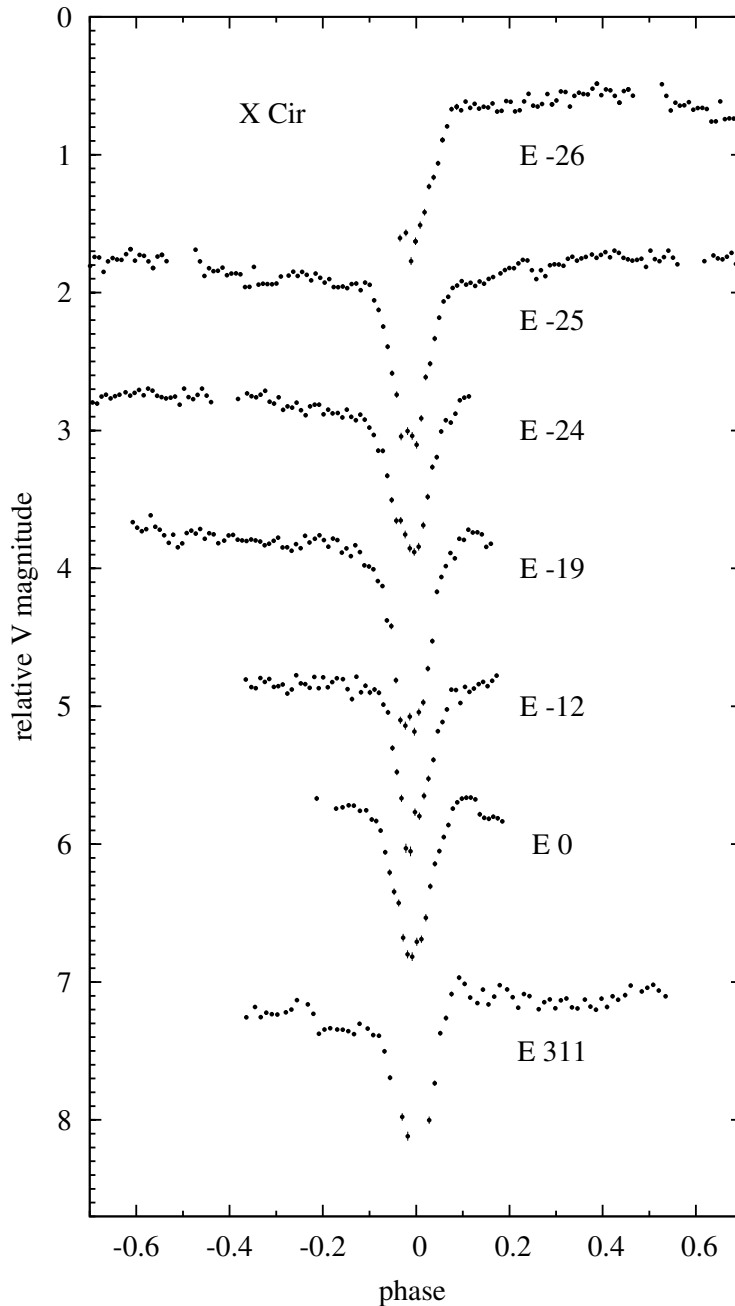


Figure 3.2: X Cir light curves from the du Pont telescope phased with the ephemeris (3.5). Each light curve was vertically shifted by 1.2 mag for the purpose of a clearer presentation.

3.3.4 IL Nor (1893)

This is the oldest nova in the sample of new orbital periods, with an eruption reported in 1893 by Fleming and published by Pickering (1893). It was identified by Woudt & Warner (2010) based on photometric variability and spectroscopically confirmed by Tappert et al. (2012). The spectrum is dominated by weak emission lines and a blue continuum, indicating equal to RS Car that, more than one hundred years after the eruption this object still is a high mass transfer rate system.

Photometry made by us (see Fig. 3.15) at du Pont revealed strong short-term variability with an average V magnitude of 18.5 mag. In order to perform a period analysis, the V magnitude was normalized with respect to the mean of each night. The periodogram (Fig. 3.3 bottom) shows a signal at $f_1 = 14.83$ c/d and strong aliases at $f_2 = 13.80$ c/d and $f_3 = 15.87$ c/d which, if attributed to orbital modulation, correspond to $P_{\text{orb1}} = 1.62(04)$ h, $P_{\text{orb2}} = 1.74(04)$ h and $P_{\text{orb3}} = 1.51(03)$ h respectively. Folding the data according to the alias frequencies does not present any significant differences with respect to the strongest peak. A comparison with the light curves of Woudt & Warner (2010) does not resolve this ambiguity either. However, from the spectral window (Fig. 3.3 bottom) it is evident that those peaks correspond to one cycle per day aliases. Considering the central peak in Fig. 3.3 at f_1 , the ephemeris is:

$$\text{HJD}(\text{max}) = 2\,457\,163.639(09) + 0^{\text{d}}.0674(15) \text{ E}, \quad (3.6)$$

and for f_2 and f_3 the ephemerides are

$$\text{HJD}(\text{max}) = 2\,457\,163.643(07) + 0^{\text{d}}.0724(15) \text{ E}. \quad (3.7)$$

$$\text{HJD}(\text{max}) = 2\,457\,163.642(05) + 0^{\text{d}}.0630(15) \text{ E}, \quad (3.8)$$

The phased light curve folded to ephemeris (3.6) together with its orbital phase averaged into 0.1 phase bins are shown in Fig. 3.3 (top) and could correspond to the orbital hump of IL Nor with a total amplitude ~ 0.1 mag. At least the two neighboring aliases mentioned above are also possible period solutions, requiring additional photometric and perhaps spectroscopic observations in order to decide which of the aliases is the valid one. In any case IL Nor turns out to be one of the very few classical novae below the period gap and is also the oldest confirmed nova among those short period systems.

3.3.5 DY Pup (1902)

The nova eruption was discovered in November 19, 1902 on Harvard plates, being reported by Shapley (1921), who established the photographic magnitude at maximum $m_p = 7$ mag. He also found that the pre-nova had $m_p > 10.3$ mag, and that must have been fainter than 16 mag in 1901, because a photograph made in 1901 showing stars fainter than 16 mag did not reveal any object at the nova position. DY Pup is catalogued as a slow nova considering the time it takes the brightness to decay by three magnitudes from maximum, i.e., $t_3 = 160$ d (Duerbeck 1987). The nova shell remnant is still visible and it was detected by Gill & O'Brien (1998) in 1995 as a ellipse-shaped remnant with a size of 7x5 arcsec. Despite its detection, the distance could not be estimated due to the lack of information on the expansion velocities. Comparison of the finding chart in Downes et al. (2005) and the images of the Panoramic Survey Telescope and Rapid Response System

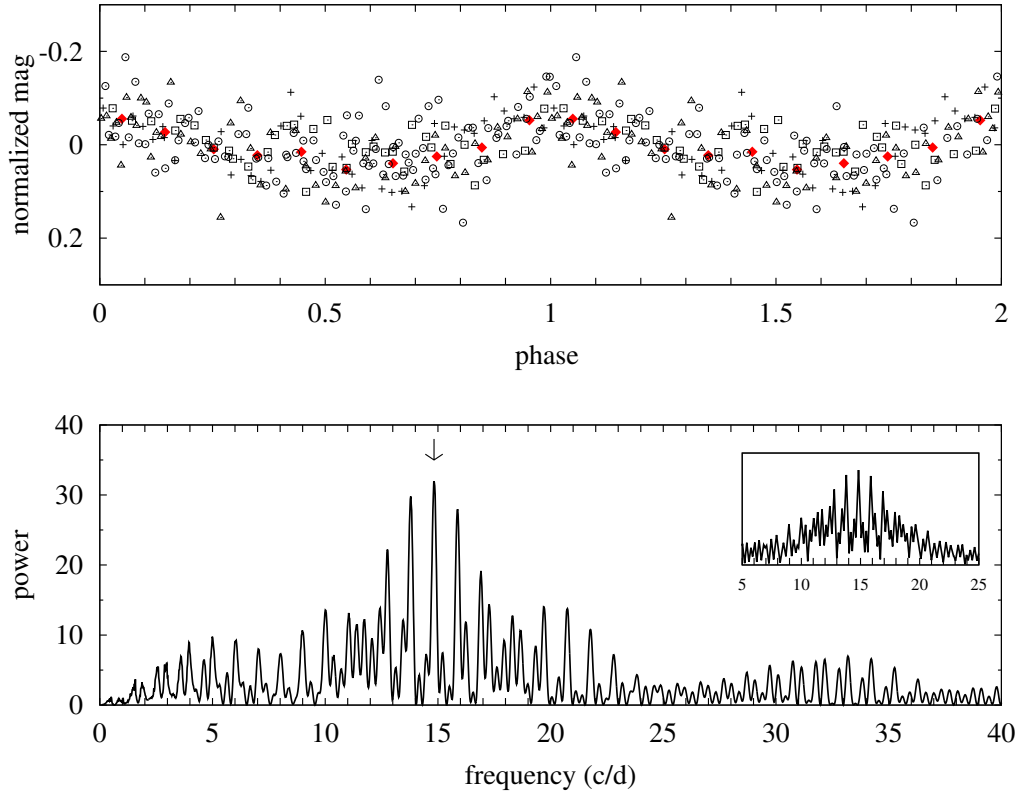


Figure 3.3: Top: Phased light curve for IL Nor according to ephemeris (3.6). The y axis corresponds to the normalized V magnitude and the x axis gives two orbital cycles in phase units. Different symbols indicate data from different nights. Red diamonds represent the average into 0.1 phase bins. Bottom: Periodogram of the photometric data. The arrow marks the highest peak, corresponding to $f = 14.83$ c/d. The inset shows the spectral window.

(Pan-STARRS, Chambers et al. 2016; Flewelling et al. 2016) unambiguously identifies DY Pup with a source in the Gaia Data Release 2 catalogue (Gaia Collaboration et al. 2018). However, the measured parallax is 0.26 ± 0.31 mas, and thus presents an uncertainty that is too large for a meaningful distance determination (Bailer-Jones 2015b; Schaefer 2018b; Tappert et al. 2020).

Only two spectral observations have been reported (Zwitter & Munari 1994; Tomov et al. 2015). Both spectra are dominated by a blue continuum and weak H α emission line. In a poster presentation, and in a later proceeding, Van Zyl reported that DY Pup is an eclipsing system with $P_{\text{orb}} = 3.35$ h (Downes et al. 2001; Warner 2003b), but the corresponding light curves were not published. Our V photometric observations confirm this information, detecting three eclipses during our two nights of observations (Fig. 3.4, Table 3.4). The corresponding ephemeris for the mid-eclipse timing results to

$$\text{HJD}(\text{min}) = 2\,456\,658.64779(74) + 0^{\text{d}}.13952(25) \text{ E.} \quad (3.9)$$

The eclipse is comparatively shallow, with a depth of ~ 0.3 mag. The very small amount of flickering in the light curve and the diminished pre-eclipse hump indicates that DY Pup is a high mass-transfer CV.

3.3.6 V363 Sgr (1927)

For a long time, the identification of this post-nova was ambiguous. Tappert et al. (2014) found, ~ 40 arcsec from the published position, a star with a blue continuum and narrow and weak emission lines. They suggest a low orbital inclination, but a rather high accretion rate. No orbital period of this star has been published. This nova was part of our CTIO data set, consisting of typically two subsequent data points per night every three nights over a range of 356 d. A period analysis of that data revealed an unambiguous signal at $f = 7.93$ c/d that corresponds to a periodic hump or sinusoidal variation with $P = 3.03$ h which we interpret as the orbital period (Fig. 3.5). The corresponding ephemeris for the maximum is

$$\text{HJD}(\text{max}) = 2\,456\,583.579(45) + 0^{\text{d}}.126066(95) \text{ E.} \quad (3.10)$$

This value places V363 Sgr inside the period gap of CVs as defined by Knigge (2006). The existence of the photometric modulation indicates a medium-high inclination, somewhat contradicting the conclusion by Tappert et al. (2014) based on the narrow emission lines. However, V363 Sgr could also be a permanent superhumper which allows for lower inclinations (Smak 2010). In this case the orbital period could be a few per cent different from the above value.

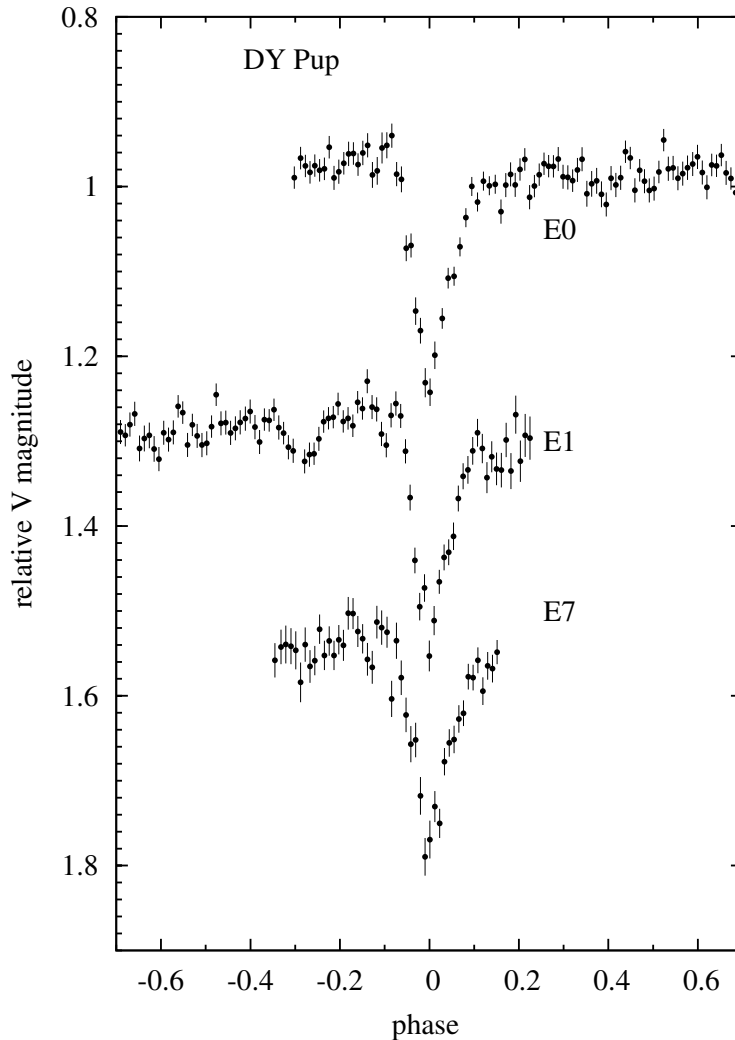


Figure 3.4: V magnitude vs phase using the ephemeris (3.9) for DY Pup.

3.3.7 V2572 Sgr (1969)

Tappert et al. (2012) give a brief description of the eruption light curve of this object and present a spectrum with comparatively weak Balmer emission lines, the He I series and Bowen/He II. They concluded that V2572 Sgr could be a high mass transfer system. In our attempts to determine its period, the periodogram of our radial velocities measured with EFOSC2 in 2011 showed a strong and broad peak at $f = 7.49(07)$ c/d corresponding to $P_{\text{orb}} = 3.20$ h and a broad and predominant alias at $f = 6.45(02)$ c/d (Fig. 3.6, f). One V -band light curve with 3.15 h time span, obtained with the same instrument in 2012 exhibited a hump structure with strong flickering (Fig. 3.16). If an orbital signature is present, the period should be larger than 3.15 h, because these data clearly do not cover a full orbit, thus frequencies > 7.6 c/d can be discarded. The V -band light curves taken at du Pont reveal a periodic hump with a variable amplitude, up to ~ 0.3 mag. The periodogram of this campaign (Fig. 3.6, e) shows a central peak at frequency 6.38(04) c/d and two aliases at

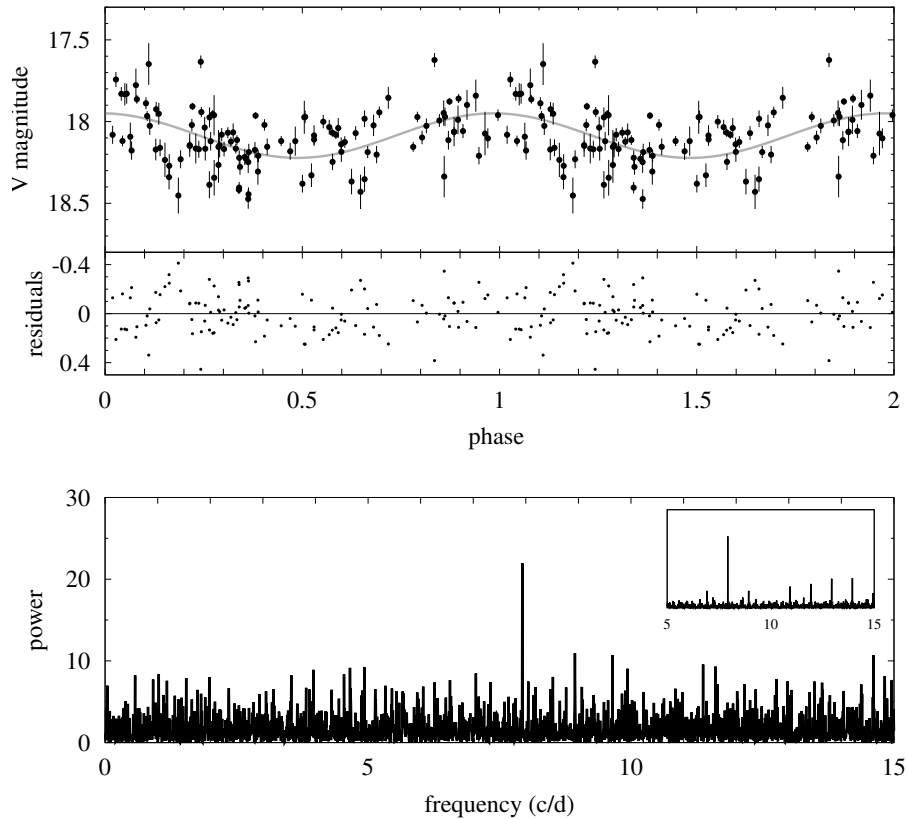


Figure 3.5: Top: Phased light curve for V363 Sgr according to ephemeris (3.10) together with a sine fit (grey line). Middle: Residuals of the fit. Bottom: Periodogram showing the highest peak corresponding to $f = 7.93$ c/d. As inset plot the spectral window centered at this frequency is shown.

5.35(08) and 7.41(08) c/d of similar height as the central one, being these values comparable to those found in the radial velocities periodogram. Folding the radial velocities and the du Pont photometry according to these frequencies yielded reasonable light and radial velocity curves for the frequencies 6.38 and 7.41, but systematically offsets for individual data sets from the general behaviour for $f = 5.38$ c/d, so that it was discarded.

V2572 Sgr was also included in the CTIO data set, in two seasons, implying a total coverage of nearly one year (see Fig. 3.14). The search for periodicities was performed independently in each of the two data sets as well as combining all the data to a single set. Its periodograms present large noise level due to the high cadence (only two points per night), however a narrow and outstanding frequency at $f_1 = 6.40(01)$ c/d in each of the single sets and in the combined one is present, together with several frequencies of similar height (Fig. 3.6, d). The frequencies at 6.47(01) and 6.66(01) c/d were discarded because the light curves from du Pont are not fitted properly with these periods. Comparing with the results from the du Pont data, this leaves only two viable frequencies $f_1 = 6.40(01)$ and $f_2 = 7.41(01)$ c/d. Accordingly, we assumed that the orbital frequency could be equivalent to $P_1 = 0.156211(29)$ d or $P_2 = 0.135125(22)$. For both, the

rather accurate period allowed to bridge the CTIO data to those of du Pont enabling to derive a unique cycle number difference between their epochs and, consequently, also to that of the early EFOSC2 run.

For the final ephemerides we used not only the hump maxima, but also the minima which happen to appear always very near to phase 0.5 in all time-resolved data. Those epochs correspond to the extremes of a polynomial function of degree two fitted for both EFOSC2 and du Pont HJD data. For CTIO data those epochs were derived from the phase data plot. We identified the HJD of the points located close to zero phase and those close to phase 0.5. Making sure that a slight variation of the orbital period did not have a markedly effect on their position in phase space they were then counted as maxima and minima, i.e. the respective HJDs were assigned to full and half cycles, respectively. It should be mentioned that a high uncertainty is associated to this calculation, since those two points per night can correspond to any part of the wide hump. Table 3.2 gives the resulting cycle numbers E and HJD epochs considering both periods; integer numbers E refer to observed maxima, the remaining ones to minima. A least square fit through the data E_1 in Table 3.2 yields the ephemeris for the hump maximum

$$\text{HJD}(\text{max}) = 2\,456\,507.6959(66) + 0^{\text{d}}.1562146(19) E, \quad (3.11)$$

with a standard deviation of $\sigma = 0.018$ d and for f_2

$$\text{HJD}(\text{max}) = 2\,456\,507.6563(66) + 0^{\text{d}}.1351221(16) E, \quad (3.12)$$

with a standard deviation of $\sigma = 0.018$ d. Phased light curves considering the ephemeris (3.11), for all photometric data sets are shown in the upper part of Fig. 3.6. The sinusoidal parameters for the radial velocities listed in Table 3.8 according to P_1 are $\gamma = 44(7)$ km/s and $K = 19(8)$ km/s and for P_2 are $\gamma = 47(5)$ km/s and $K = 26(8)$ km/s.

3.3.8 XX Tau (1927)

The history of this nova that erupted in 1927 has been extensively described by [Schmidtobreick et al. \(2005\)](#) who also present an optical spectrum dominated by strong Balmer and HeI emission lines resembling more a dwarf nova than an old nova. However, the CTIO data did not present any clear evidence for outburst behaviour in roughly 1.5 yr spanning monitoring.

[Rodríguez-Gil & Torres \(2005\)](#) found a number of periodicities in time-series photometric data at periods of 23.69(03) min, 3.26(05) h and 5 d. While the shortest value was considered as very uncertain, the middle one was attributed to an orbital or superhump modulation, and the longest period was interpreted as evidence of an eccentric/tilted accretion disc.

Our light curves taken in a five nights spanning observing run at the 2.5-m du Pont are dom-

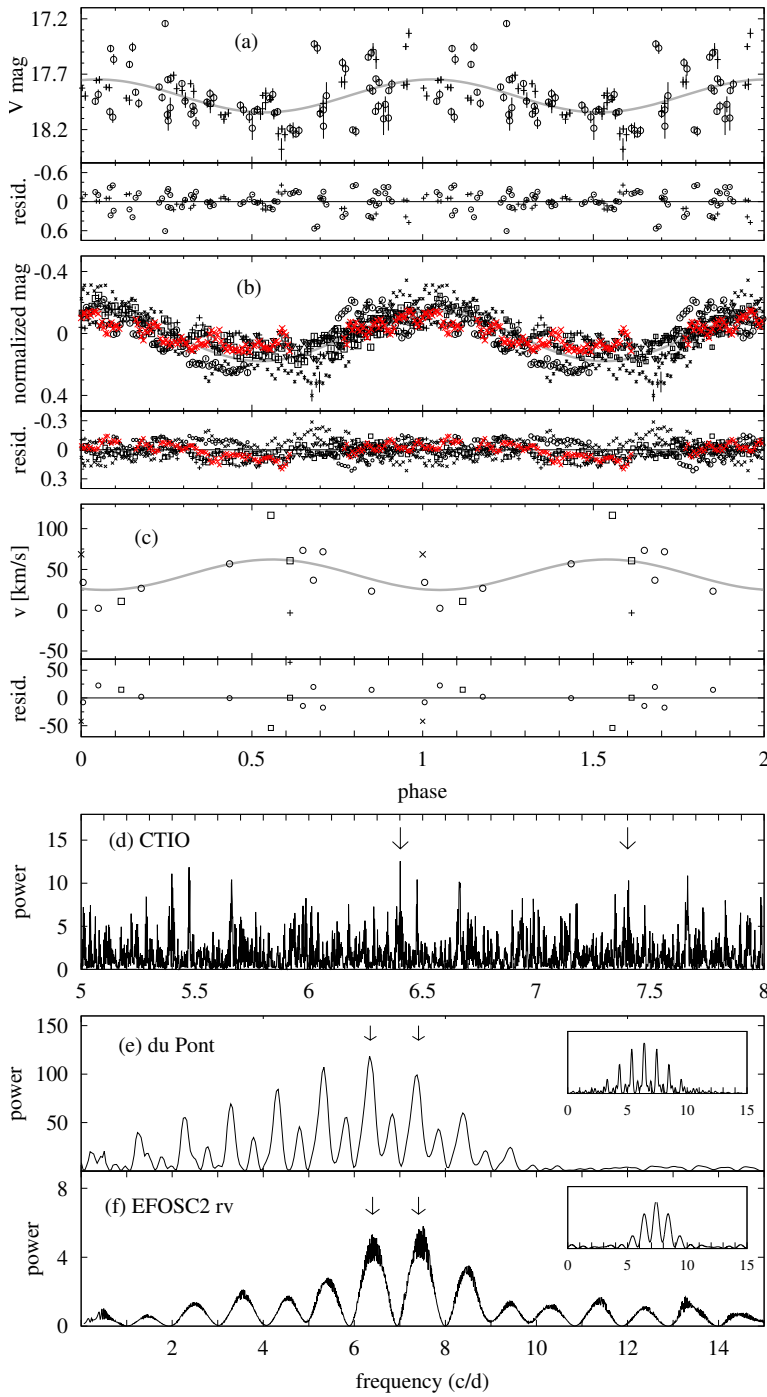


Figure 3.6: (a): Phase light curves of V2572 Sgr folded with the ephemeris (3.11) for CTIO data. set 1 and 2 are shown with crosses and circles respectively. (b) The same for EFOSC2/NTT’s light curve (red crosses) and du Pont observations (different black symbols represent different nights). (c) Radial velocity fitted with the ephemeris (3.11). A sine curve fitted to the data as a grey line and residuals are also shown. Scargle Periodogram for (d) CTIO data in the range of $f = 5 - 8$ c/d. (e) du Pont photometric data (f) radial velocity data. As inset plot is shown the spectral window centered at the dominant frequency. The arrows point to $f = 6.40$ c/d and $f = 7.41$ c/d (see text for details).

Table 3.2: Epochs of humps observed in the time-resolved data for V2572 Sgr. The E_1 , $(O - C)_1$ and E_2 , $(O - C)_2$ values refer to Eq. (3.11) and to Eq. (3.12) respectively.

HJD -2 450 000 d	E_1	E_2	$(O - C)_1$	$(O - C)_2$
EFOSC2				
6063.759(06)	-2842	-3285	0.023	-0.021
6063.829(70)	2841.5	-3284.5	0.015	-0.019
CTIO				
6507.684(25)	0	0	-0.014	0.028
6510.732(36)	19.5	22.5	-0.013	0.035
6792.907(50)	1826	2111	-0.039	0.008
6838.770(30)	2119.5	2450.5	-0.025	-0.003
du Pont				
7162.853(08)	4194	4849	-0.009	-0.010
7163.810(02)	4200	4856	0.010	0.001
7163.890(08)	4200.5	4856.5	0.012	0.013
7164.748(01)	4206	4863	0.011	-0.007
7164.822(01)	4206.5	4863.5	0.007	-0.001
7164.903(07)	4207	4864	0.010	0.013
7166.765(03)	4219	4878	-0.003	-0.017
7214.662(08)	4525.5	5232.5	0.015	-0.021

inated by strong irregular flickering. The periodogram does not show any sign of the suspected orbital or superhump modulation (Fig. 3.7, c). Instead, its highest peak is at $f = 4.82(06)$ c/d, equivalent to $P = 4.98$ h. However, this signal is clearly not stable (Fig. 3.17), and thus probably is simply caused by flickering mimicking a periodicity within our comparatively short time-series.

Radial velocities measured from time-series spectroscopic data taken at FORS2/VLT in five nights spanning two weeks in total show a periodogram with a central peak and a number of significant broader one-day aliases, each one composed of a number of narrow peaks as can be seen in bottom panel of Fig 3.7. The broad central peak is at $f_1 = 6.38(01)$ c/d (equivalent to 3.76 h), the second most significant at $f_2 = 5.38(06)$ c/d (4.46 h), the third at $f_3 = 7.36(01)$ c/d (3.26 h) and others at $f_4 = 4.31(06)$ c/d (5.57 h), $f_5 = 8.29(06)$ c/d (2.90 h) and $f_6 = 9.29(01)$ c/d (2.58 h). We noted that f_3 agrees well with the period favoured by Rodríguez-Gil & Torres (2005). However, the periodogram presented in that article (their fig. 14) shows a number of similarly strong aliases that are not properly discussed by the authors. A comparison with the periodogram for our data shows that all our significant frequencies coincide with the peaks in their periodogram. Thus, we find that, from the periodograms, we have six valid frequencies. However, folding our data with each of the corresponding periods for frequencies f_2 , f_4 , f_5 and f_6 showed systematic deviations from the fit (e.g. in the sense that a data set from one specific night presented a systematic offset), while for f_1 and f_3 the distribution of all data was consistent with random noise. As mentioned above, each broad peak in our periodogram is formed by a series of narrow peaks, and thus each

Table 3.3: Values of the possible orbital frequencies and its respective orbital period for XX Tau within one FWHM of the broad peaks centered at $f_1 = 6.38$ c/d and $f_3 = 7.36$ c/d in the periodogram shown in Fig. 3.7 (d).

f c/d	P days	f c/d	P days
f_1		6.48(02)	0.15432(45)
6.14(01)	0.16289(30)	6.51(02)	0.15364(45)
6.16(01)	0.16223(30)	f_3	
6.19(01)	0.16158(30)	7.19(01)	0.13908(22)
6.21(01)	0.16093(29)	7.21(01)	0.13863(22)
6.24(01)	0.16033(29)	7.24(01)	0.13816(22)
6.26(01)	0.15971(29)	7.26(01)	0.13768(22)
6.29(01)	0.15904(29)	7.29(01)	0.13724(21)
6.31(01)	0.15848(29)	7.31(01)	0.13678(21)
6.34(01)	0.15782(28)	7.34(01)	0.13632(21)
6.36(01)	0.15724(28)	7.38(01)	0.13544(21)
6.41(01)	0.15609(28)	7.41(01)	0.13499(21)
6.43(01)	0.15546(28)	7.43(01)	0.13452(21)
6.46(01)	0.15485(27)	7.46(01)	0.13408(20)

of the broad peaks for f_1 and f_3 contains several valid frequencies, which are displayed in Table 3.3. We thus here give the respective strongest ones of those as fiducial frequencies, but have to keep in mind that more valid possibilities within $3\sigma \sim 0.2$ c/d exist. Defining T_0 as the red-to-blue crossing time in the radial velocities sinusoidal fit, the ephemeris for f_1 then is

$$\text{HJD} = 2\,458\,484.620(23) + 0^{\text{d}}.0.15664(28) \text{ E}, \quad (3.13)$$

and for f_3 is

$$\text{HJD} = 2\,458\,484.632(45) + 0^{\text{d}}.13588(21) \text{ E}. \quad (3.14)$$

As example, in Fig. 3.7 we show the light curve and the radial velocities folded with the period from Eq.3.14, since this is the value favoured by Rodríguez-Gil & Torres (2005). The sinusoidal fit corresponding to this period exposes a wide semi-amplitude $K = 167(12)$ km/s and the systemic velocity $\gamma = -22(10)$ km/s is slightly blueshifted. In the case for f_1 the fit parameters are $K = 160(16)$ km/s and $\gamma = -10(8)$ km/s. The photometric data (Fig. 3.7 top) does not show any modulation for either period.

One possibility for the modulation found (Rodríguez-Gil & Torres 2005) not being present in our photometric data is that strong flickering on larger time-scales than in the LCO data mimicked a periodic signal in their data. However, this flickering would then to have maintained these same properties over a time span of six nights, which appears unlikely. Furthermore, the proximity

to the spectroscopic signal is suspicious. A different possibility is that the system was caught in two different brightness states. In that case, the data from [Rodríguez-Gil & Torres \(2005\)](#) could correspond to a state with a fainter accretion disc, where the bright spot would be more dominant and thus could produce an orbital hump in the light curve. In brighter, optically thick, accretion discs, on the other hand, the bright spot is typically much diminished or even not visible at all ([Warner 2003a](#)). Still, the long-term light curve from [Vogt et al. \(2018\)](#), if noisy, is consistent with a constant brightness over a range of about 1.5 yr. However, comparing our spectroscopic data with that of [Schmidtobreick et al. \(2005\)](#), we find that the equivalent width of the H α line in our data with 28 Å amounts to only roughly half the value that they found in their data (52 Å). This points to a difference in the disc brightness, with a stronger line indicating a fainter disc. Unfortunately, we do not have any calibrated photometric information for either the [Schmidtobreick et al. \(2005\)](#) nor the [Rodríguez-Gil & Torres \(2005\)](#) data. However, reviewing above evidence and sorting the dates, we find that XX Tau likely inhabited a fainter disc in late October and early November 2002 ([Rodríguez-Gil & Torres 2005](#)), and in January 2003 ([Schmidtobreick et al. 2005](#)), but a brighter disc in December 2013 and January 2014 (our photometric data) and in December 2018 and January 2019 (the spectroscopic data). The long-term CTIO data covers the range from November 2013 to April 2015. This timeline is thus consistent with the possibility that XX Tau at some point between January 2003 and November 2013 (at least once) underwent a change from a low mass-transfer state with a faint disc to a higher mass-transfer state with a brighter one.

3.3.9 CQ Vel (1940)

This nova reached its maximum brightness, $m_p = 9$ mag in April 19, 1940, being discovered on Franklin-Adams plates by C. J. Van Houten ([Hoffleit 1950](#)). It was categorized as a moderately fast nova with $t_3 = 53$ d ([Duerbeck 1981](#)) and a large amplitude ($A_v > 13.1$ mag). The nova was recovered by [Woudt & Warner \(2001\)](#), who performed high speed photometry in the field of a candidate for the nova proposed by [Duerbeck \(1987\)](#). A strong flickering activity in a single, 4.07 h long, light curve was detected in an object 9 arcsec from the suspected position. Spectroscopic observations made by [Schmidtobreick et al. \(2005\)](#) using those coordinates confirmed the post-nova. They reported an equivalent width of H α line as 18 Å, while from our new EFOSC2 spectra the value is 14.5 Å.

Our light curves (Fig. 3.18) show strong flickering activity as was seen by [Woudt & Warner \(2001\)](#). The periodogram of the photometry (Fig. 3.8) shows two dominant frequencies at $f_1 = 8.87$ and $f_2 = 9.86$ c/d. Using both frequencies we found the following ephemerides for the photometric minima

$$\text{HJD}(\text{min}) = 2\,456\,655.786(03) + 0^{\text{d}}.11272(12) E, \quad (3.15)$$

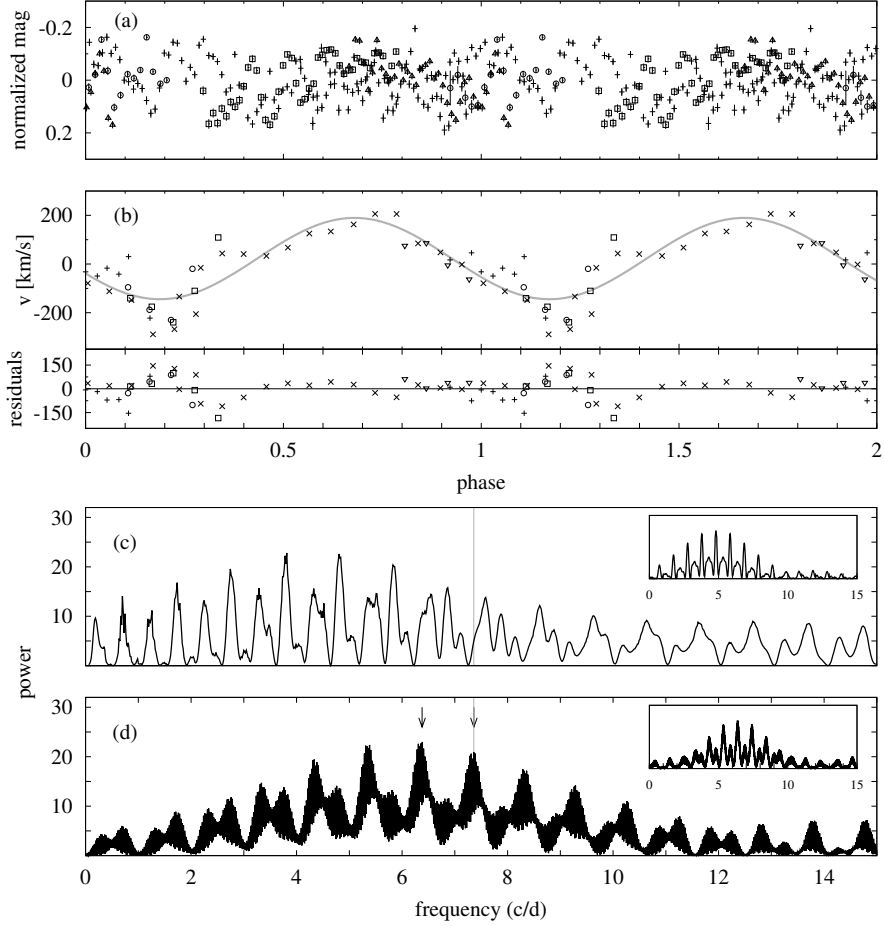


Figure 3.7: (a) Photometric phased light curve for XX Tau according to ephemeris (3.14). (b) Radial velocity, the sine fit and the residuals. Different nights are shown as different symbols. Phases very likely do not coincide because two data sets have different T_0 . (c) Periodogram of the photometric data together with the spectral window centered at the main frequency. Vertical grey line indicates the position of the detection made by Rodríguez-Gil & Torres (2005). (d) Periodogram of the radial velocities. The arrows point to the frequencies f_1 and f_3 (see text for details).

for f_1 and the alternative:

$$\text{HJD}(\text{min}) = 2\,456\,655.782(06) + 0^{\text{d}}.0.10138(24) \text{ E}. \quad (3.16)$$

The RMS scatter of the observed minima around ephemeris (3.15) is 0.0039 d and for (3.16) is 0.0088 d. Both the radial velocity and the photometric data were folded with these ephemeris, however no significant differences were found. In the same way, the average semi amplitude (K) for the photometric phased data are practically identical within the errors, $K = 0.0966(32)$ mag and $K = 0.0932(34)$ mag respectively.

We also note that, while a photometric sinusoidal signal could in principle be explained as the result of ellipsoidal modulation with orbital period twice the observed period, the radial velocities from our EFOSC2 spectra rule this out. The sine fit according to Eq. (3.15) yields a systemic

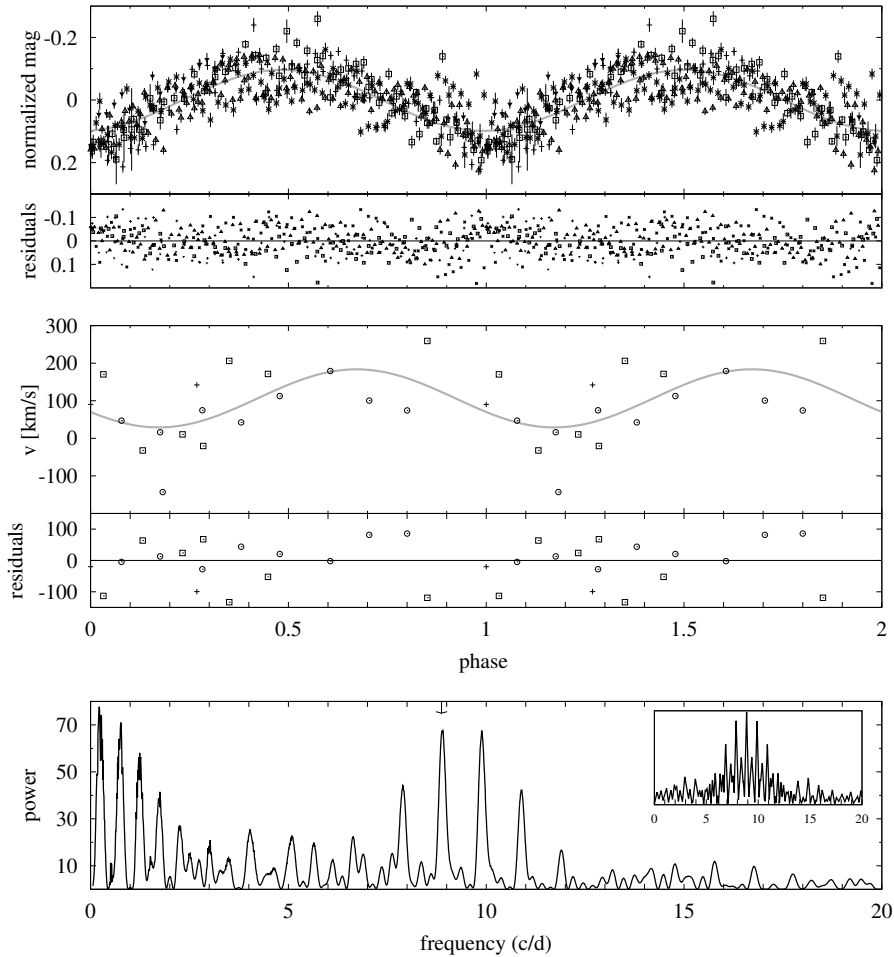


Figure 3.8: Top: Phased light curve for CQ Vel according to ephemeris (3.15), the sinus fit to the orbital modulation (grey line) and the residuals of the sine fit are shown. Middle: Radial velocity, the sinus fit and the residuals. Bottom: Periodogram of the photometric data including its spectral window centered to frequency pointed with the arrow.

velocity $\gamma = -106(15)$ km/s and a semi-amplitude $K = 77(20)$ km/s. The radial velocities are displayed in Table 3.8.

Under those circumstances, a decision which of the alternatives is the correct one must await more data. In any case, both of these periods place CQ Vel within the period gap.

3.3.10 RW UMi (1956)

In the Ritter & Kolb (2003a) catalogue, RW UMi is listed as the nova with the shortest orbital period that is not marked as “uncertain”. The value of $P = 0.05912(15)$ d is based on photometric data taken in 14 nights over a total time range spanning almost four months (Retter & Lipkin 2001). The period corresponds to a sinusoidal variation in the light curve with an amplitude of 0.05mag in white light. Later photometric studies by Bianchini et al. (2003) and Tamburini et al. (2007) found a number of other periodicities with larger amplitudes, suggesting that RW UMi is

Table 3.4: Epochs for the eclipsing systems.

Object	E	HJD −2 450 000 d	O − C d
X Cir	−3041	6696.7977	0.0044
	−3028	6698.8051	0.0038
	−2931	6713.7858	0.0020
	−2879	6721.8137	−0.0020
	−2782	6736.7933	−0.0050
	−2058	6848.6214	−0.0056
	−26	7162.4907	0.0020
	−25	7162.6453	0.0021
	−24	7162.8000	0.0023
	−19	7163.5690	−0.0010
	−12	7164.6497	−0.0015
	0	7166.5036	−0.0011
	311	7214.5411	−0.0005
DY Pup	0	6658.6478	0.0001
	1	6658.7873	−0.0001
	7	6659.6245	0.0001

an intermediate polar showing quasi-periodic oscillations. They also found that the brightness of the nova is still declining at an approximate rate of 0.03 mag/yr as measured from the year 1988 to 2006. The existence of multiple photometric periods lets the identification of the reported value with an orbital modulation appear ambiguous, thus motivating the present spectroscopic study.

Compared to other post-novae, the emission lines in RW UMi are relatively strong, with $H\alpha$ presenting an equivalent width of -17 \AA . However, the line profile is complex and non-Gaussian, with a broad base and a more narrow main component, with likely more than one source contributing to the latter, as evidenced by its markedly variable shape (Fig. 3.12). Additionally, we were unfortunate in that the longest data set counted with the worst weather conditions of the three nights, resulting in significantly diminished S/N. Finally, obtaining a conclusive radial velocity curve is further complicated by the line presenting a comparatively small Doppler shift. In view of these difficulties, we employed a number of methods to determine the radial velocities, measuring different parts of the line or using the manual cross-correlation mentioned above. However, we found that in the end the clearest curve was produced by fitting a single Gaussian function to the full line profile. The corresponding Scargle periodogram is presented in Fig. 3.9. The strongest peak corresponds to a frequency $f = 16.80(10) \text{ c/d}$, with the uncertainty being estimated by assuming a normal distribution. This translates to a period $P = 0.0595(4) \text{ d}$, which, within one sigma, is identical to the photometric period of [Retter & Lipkin \(2001\)](#). Our periodogram shows

several aliases that are close in strength to the main peak, and, taken on its own, it does not represent sufficient evidence to assign the orbital period. However, the good agreement with the photometric period strongly suggests that this indeed reflects the orbital motion of the system.

A sine fit to the radial velocity data according to Eq. (3.1) yields the aforementioned small semi-amplitude $K = 13(1)$ km/s and a markedly blueshifted systemic velocity $\gamma = -145(1)$ km/s (lower plot in Fig. 3.9). Choosing the red-to-blue crossing of the radial velocities as the zero point of the phase-folded curve and using the more precise photometric period yields a formal ephemeris of

$$\text{HJD} = 2\,457\,196.4397(10) + 0^{\text{d}}.059\,12(15) \text{ E} , \quad (3.17)$$

although, considering the complex nature of the line profile, it is unlikely to correspond to the superior conjunction of the white dwarf.

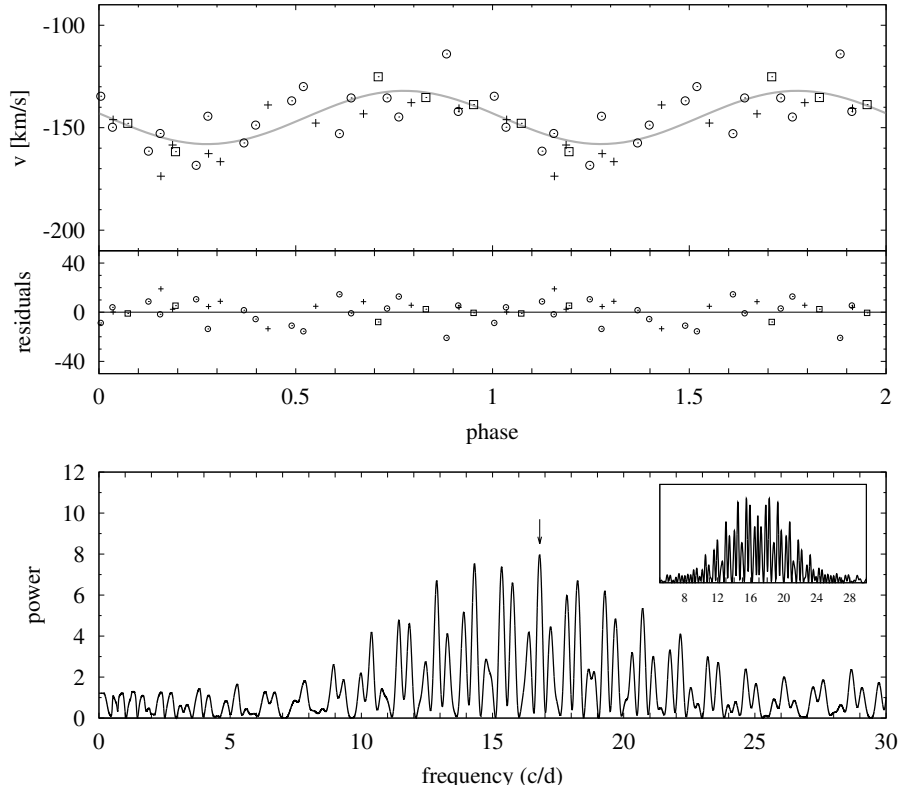


Figure 3.9: Top: Phase-folded radial velocities of RW UMi, the corresponding sine fit according to Eq. (3.17) and the residuals. Different symbols indicate data from different nights. Bottom: Scargle periodogram of the radial velocity data. The arrow marks the highest peak at $f = 16.80(10)$ c/d. As inset plot is shown the spectral window centered at this frequency.

3.3.11 Improved ephemerides of eclipsing novae with previously known orbital periods

We present refined orbital periods of WY Sge, V728 Sco, OY Ara and V849 Oph from CTIO data, which, by chance, have occasionally been caught during eclipse phases, showing fainter brightness than normally. The resulting ephemerides are listed in Table 3.5. Their epochs and O-C values, together with previously available literature and their references are listed in Table 3.7. Because the CTIO data consist of only two data points in any given night, they do not necessarily correspond to the central part of an eclipse, and thus the corresponding O-C deviations are larger in average than those from published photometry. Despite this, due to the larger time intervals covered now the new periods are more accurate.

We also have performed searches for periodicity in the other novae included in the CTIO data, V500 Aql, HS Pup, V1059 Sgr and V373 Sct, without finding any significant photometric periodicity.

3.4 The Orbital period distribution of novae

The current sample analysed here contains 92 orbital periods. From the sample listed by Tappert et al. (2013a), we selected those periods that satisfied the criteria defined below, giving a total of 74 periods, to which six new periods presented here were added, together with those new periods listed by Ritter & Kolb 2003a (version 7.24, 2016) since 2013. It is worth mentioning that 13 new periods were recently published (Schaefer 2021), however they are not considered in this distribution because the data have not yet been published. Via private communication, Schaefer announced us that he will publish an extensive collection of new orbital periods in the first half of 2022.

Here we present an analysis of the observed orbital period distribution of novae and compare it to simulated distributions both from the literature and with a newly established one that takes into account consequential angular momentum loss.

Table 3.5: Ephemerides for the eclipsing systems whose orbital periods could be confirmed by the CTIO observations (Vogt et al. 2018). T_0 refers to minima of eclipses.

Name	T_0 HJD - 2 400 000	P_{orb} d
OY Ara	56516.5722(10)	0.155390(30)
V849 Oph	48799.7412(18)	0.17275611(06)
WY Sge	47059.8678(04)	0.153634547(10)
V728 Sco	56015.8066(09)	0.13833866(18)

3.4.1 Observed period distribution

We used the catalogue of [Ritter & Kolb 2003b](#) (version 7.24, 2016) to gather the period information on the novae included here. We excluded objects from the sample if their tabulated periods: (a) were not sufficiently coherent and might be attributed to QPOs; (b) might be caused by ellipsoidal variations at twice the orbital period; and (c) were based on data that has never been published. In addition, we (d) excluded objects for which the CV classification is not confirmed, with the data allowing for alternatives (e.g., in the case of light curves showing comparatively smooth sinusoidal variations that could also originate in pulsating stars). Table 3.6 presents the 24 novae that were excluded from the sample, based on above criteria. To the such established distribution we added our own results presented in the previous section. We have also included the novae RS Car, IL Nor, V2572 Sgr, XX Tau and CQ Vel, in spite of the fact that in those systems we cannot distinguish between more than one possible values for the orbital period. However, the periods are sufficiently close to correspond to the same period bin in the histogram, so that the overall distribution is identical for either of the alternatives. These novae are marked as “provisionals” in the Table used (3.9) for resulting distribution presented in Fig. 3.10.

Comparing the current distribution with the one published by [Tappert et al. 2013a](#) (in Fig. 3.10 are shown as a solid black line and grey blocks respectively) and using their same criteria to analyse the sample, i.e., considering the period gap as the range between 2.15 to 3.18 h ([Knigge 2006](#)), it is evident that both follow the same trend, with a strong maximum in the range of 3 – 4 hr. In the new distribution most of the periods are above the period gap, corresponding to 79 per cent (equivalent to 72 objects), out of which 45 systems have $P_{\text{orb}} > 4$ h, equivalent to $\sim 50\%$ of the total sample. The peak in the 3 – 4 hr period range becomes more pronounced, concentrating 34 percent of the total sample (equivalent to 31 novae). On the other hand, eight per cent of the post-novae, corresponding to seven systems, are below the period gap and 14 per cent are in the period gap (corresponding to 13 systems).

3.4.2 Simulation

We generated an initial main-sequence plus main-sequence (MS+MS) binary population of 10^9 systems with the following assumptions: initial-mass function of [Kroupa et al. \(1993\)](#) for the mass of the primary star; flat initial mass-ratio distribution for the mass of the secondary star ([Sana et al. 2009](#)); distribution of initial orbital separations (a) flat in $\log a$ ranging from $a = 3$ to $10^4 R_{\odot}$ ([Popova et al. 1982](#); [Kouwenhoven et al. 2009](#)); constant star formation rate within the age of the Galaxy (13.5×10^9 yr, [Pasquini et al. 2004](#)); solar metallicity; and no eccentricity.

The binary-star evolution code (BSE) from [Hurley et al. \(2002\)](#) was used to evolve the systems until the end of the common-envelope phase, i.e. until the close but detached WD+MS binaries (which are the direct progenitors of CVs) are formed. A common-envelope efficiency of $\alpha_{\text{CE}} = 0.25$

Table 3.6: Novae with uncertain published P_{orb} . The last column indicates the exclusion criterion as defined in the text.

Name	P_{orb} (hr)	Outburst	Ref.	Cause
V705 Cas	5.47	1993	(1)	(c)
V842 Cen	3.94	1986	(2)	(a)
V2274 Cyg	7.2	2001	(3)	(c)
V2362 Cyg	1.58	2006	(4)	(c)
V2491 Cyg	17	2008	(5)	(a)
DM Gem	2.95	1903	(7)	(a)
DI Lac	13.05	1910	(8)	(c)
DK Lac	3.11	1950	(9)	(a)
U Leo	3.21	1855	(10)	(d)
GI Mon	>4.8	1918	(6), (7)	(a)
LZ Mus	4.06	1998	(11)	(c)
V400 Per	3.84	1974	(7)	(a)
V445 Pup	15.62	2000	(12)	(a)
V574 Pup	1.13	2004	(13)	(b)
V1186 Sco	1.39	2004	(3)	(c)
V1324 Sco	3.8	2012	(14)	(c)
V726 Sgr	19.75	1936	(15)	(d)
V999 Sgr	3.64	1910	(15)	(b)
V1174 Sgr	7.42	1952	(15)	(d)
V4077 Sgr	3.84	1982	(16)	(c)
V5582 Sgr	3.76	2009	(15)	(b)
V5980 Sgr	30.34	2010	(15)	(b)
V382 Vel	3.79	1999	(17), (18), (19)	(a)
PW Vul	5.13	1984	(20)	(c)

References:

- (1) [Retter & Leibowitz 1995](#), (2) [Woudt et al. 2009](#), (3) [Ritter & Kolb 2003b](#) (4) [Balman et al. 2009](#), (5) [Zemko et al. 2018](#) (6) [Woudt et al. 2004](#), (7) [Rodríguez-Gil & Torres 2005](#), (8) [Goransky et al. 1997](#), (9) [Katysheva & Shugarov 2007](#), [Honeycutt et al. 2011a](#), (10) [Downes & Szkody 1989](#), (11) [Retter et al. 1999b](#), (12) [Goranskij et al. 2010](#), (13) [Walter et al. 2012](#), (14) [Finzell et al. 2018](#), (15) [Mróz et al. 2015](#), (16) [Diaz & Bruch 1997](#), (17) [Woudt et al. 2005](#), (18) [Balman et al. 2006](#), (19) [Egan et al. 2014](#), (20) [Hacke 1987](#)

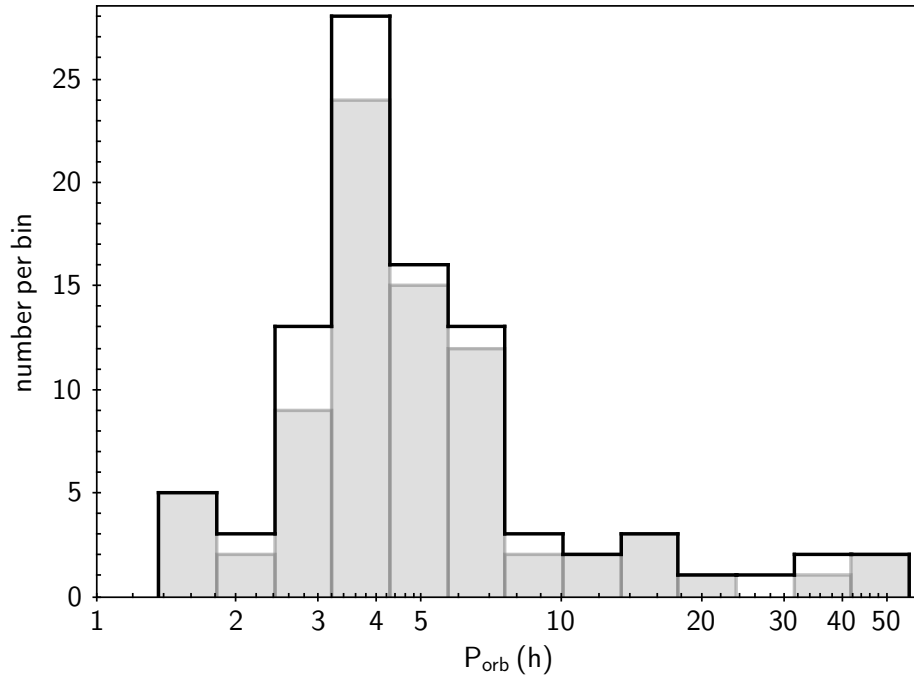


Figure 3.10: The current orbital period distribution of the novae on logarithmic scale (solid black line) in comparison with the distribution published previously by Tappert et al. (2013a, grey blocks).

was assumed (Zorotovic et al. 2010) and the binding energy parameter λ was computed assuming that the recombination energy stored in the envelope does not contribute to the ejection process (Zorotovic et al. 2014). After this phase, the WD+MS systems were evolved using the CV evolution code developed by us and described in Schreiber et al. (2016) and Zorotovic et al. (2016b). It is based on the disrupted magnetic braking model for systemic angular momentum loss (AML), i.e., AML that is present even in the absence of mass transfer, due to gravitational radiation and magnetic wind braking (the latter only for CVs above the period gap). Inflation of the radius of the secondary star as a consequence of mass transfer is incorporated by using the observed mass-radius relation and the scaling factors for systemic AML from Knigge et al. (2011c). This code also takes into account the consequential AML produced by mass transfer and nova eruptions after the CV phase begins. Two models for consequential AML due to nova eruptions were included: the classical non-conservative model from King & Kolb (1995) and the empirical model from Schreiber et al. (2016). The latter predicts a smaller number of CVs, mainly because systems with low-mass WDs are driven into a dynamically unstable mass transfer regime and merge. As shown in Schreiber et al. (2016), this has an effect not only on the WD mass distribution but also on the distribution of orbital periods. Here we want to test if there is also an effect on the predicted orbital period distribution of post-nova systems.

Once the simulated populations of CVs have been generated, the probability of observing a nova eruption was computed for each system. This probability is inversely proportional to the

nova recurrence time P_{rec} , which can be written as:

$$P_{\text{rec}} = m_{\text{acc}}/\dot{M}, \quad (3.18)$$

where \dot{M} is the mass transfer rate and m_{acc} is the accreted mass needed to produce a nova outburst. For each system we derived the value for m_{acc} , which depends on the WD mass, the mass transfer rate, and the core temperature, based on [Yaron et al. \(2005\)](#), interpolating their table 2), who presented models for different fixed core temperatures. [Townsend & Bildsten \(2004\)](#) found that the equilibrium core temperatures of WDs are below 10^7 K in typical CVs, and [Chen et al. \(2016\)](#) compared the observational data of novae in the M31 galaxy with the models from [Yaron et al. \(2005\)](#) and preferred the low temperature models. We have therefore chosen the values of m_{acc} listed by [Yaron et al. \(2005\)](#) for their models with the minimum core temperature (10^7 K).

We also defined systems that experience more than a nova eruption in a century as recurrent novae (e.g. [Shara et al. 2018](#)). This means that if the computed recurrence period of a system in our simulation is less than 100 years, more than one nova eruption could be observed during that period of time. Therefore, we set an upper limit for the detection probability $\mathcal{P}_{\text{det}} = (P_{\text{rec}}[\text{yr}])^{-1}$ of 0.01, which corresponds to a recurrence period of 100 years, to avoid counting recurrent novae more than once in the simulated period distribution.

Systems in which the mass of the donor star falls below $0.05M_{\odot}$ were eliminated from our simulated sample, because their mass-radius relation is not well constrained (e.g. [Knigge et al. 2011c](#)). This has virtually no effect on the simulated distribution of orbital periods, because CVs with low-mass donors (below the brown-dwarf mass limit) have very low mass transfer rates which translate into very long recurrence periods, i.e. extremely low probabilities of being detected as post-nova systems. We also excluded CVs that experienced a thermal time-scale mass transfer phase, i.e. systems with initially massive donors ($M_2 \gtrsim 1.5M_{\odot}$), because the evolution during this phase is not well understood (e.g., [Nomoto et al. 1979](#); [Hachisu et al. 1996](#)), and it is especially not clear how the mass of the WD could be affected. However, these systems should make up a small percentage of the current CV population ($\sim 5\%$; [Pala et al. 2020](#)).

3.4.3 Comparison

The predicted orbital period distributions were constructed using the same bins as for the observed distribution, adding the detection probabilities for all the simulated systems within that period range, and normalizing to the observed number of systems. The results are shown in [Fig. 3.11](#). The two models of AML predict broadly similar distributions, and both show the majority of systems above the gap, in keeping with the observed distribution (top panel). The classical non-conservative model from [King & Kolb \(1995\)](#), bottom panel) predicts that $\sim 18\%$ of novae should be observed below the orbital period gap, $\sim 2 - 3\%$ in the gap, and $\sim 79 - 80\%$ above it. For

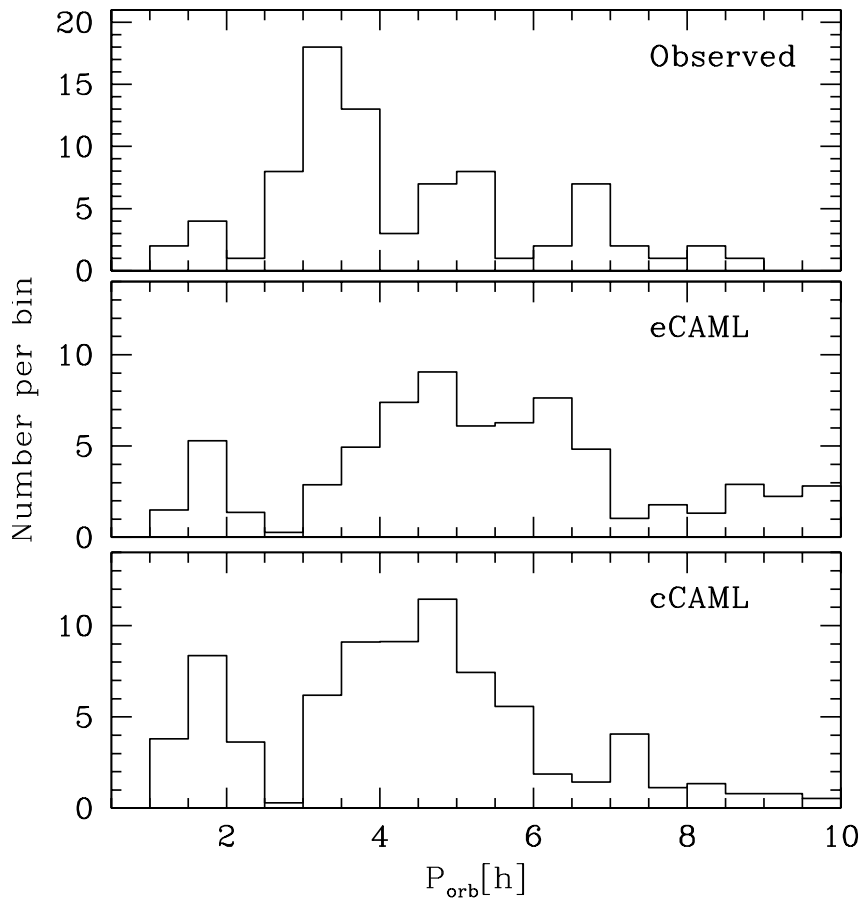


Figure 3.11: Orbital period distribution of post-nova systems. From top to bottom: observed systems (this work), simulation assuming the empirical consequential AML model from [Schreiber et al. \(2016\)](#) and simulation assuming the classical consequential AML model from [King & Kolb \(1995\)](#).

the simulations that assume the empirical model from [Schreiber et al. \(2016, middle panel\)](#), the expected fractions are $\sim 9 - 10\%$ below the gap, only $\sim 1\%$ in, and $\sim 89 - 90\%$ above. The empirical model is therefore in better agreement with the observations, regarding the fraction of systems that we expect to observe below the orbital period gap. However, this conclusion should be taken with caution because we are dealing with low-number statistics and our poor knowledge of CV evolution.

The over-prediction of systems below the gap in the two simulations with respect to the observed distribution might be explained by poorly constrained aspects of CV evolution. A key parameter that might affect the simulated distribution is the assumed core temperature. As explained before, we used a constant core-temperature for the calculations of the accreted mass needed to produce a nova outburst (m_{acc}). As calculated by [Yaron et al. \(2005\)](#), colder WDs should need to accrete more mass before triggering the eruption of a nova. Given that the evolution of a CV towards shorter periods is mainly driven by systemic AML, the lifetime of a system is much shorter above the gap than below it due to the efficiency of magnetic braking. This implies that CVs below the

gap are, on average, older than CVs above the gap. Therefore, the core temperature of the WDs in CVs below the gap should be lower, on average, because they have had more time to cool. Also, it is not clear whether the accretion process can affect the temperature of the core of the WD (e.g., [Cumming 2002](#); [Townesley & Bildsten 2004](#); [Townesley & Gänsicke 2009](#)). If the core temperature can increase as a result of mass accretion, this increase should be larger for CVs above the gap, in which the accretion rate is higher. Combining these two effects implies that by assuming a constant WD core temperature for all the systems we are probably underestimating the value of m_{acc} needed to trigger a nova eruption for CVs below the gap, which means that their contribution to the predicted post-nova population is overestimated. A more accurate derivation of m_{acc} that depends on the core temperature for each WD is beyond the scope of this paper, but the effect of such an improvement on the models would probably be to reduce the fraction of novae predicted below the gap, for both models.

Another discrepancy with the observations is that our simulations predict an extremely low fraction of novae in the orbital period range that corresponds to the period gap, for both models of consequential AML (below 3%, while observationally it is $\sim 14\%$). This is a direct consequence of assuming efficient magnetic braking for all CVs above the period gap. However, magnetic braking can become very inefficient for CVs containing WDs with strong magnetic fields. According to [Belloni et al. \(2020\)](#), the WD magnetic field in strongly magnetized CVs can trap part of the wind from the donor reducing the loss of angular momentum through this wind. This implies that magnetic CVs above the gap have lower mass transfer rates than their non-magnetic counterparts, and have therefore less bloated donors. This translates into a shift of the upper edge of the gap towards shorter periods, or even a complete absence of the detached phase for CVs with the strongest WD magnetic fields. In other words, magnetic CVs can cross, or at least enter, the orbital period gap. Indeed, the gap seems to be much less pronounced in the observed period distribution of magnetic CVs than in that of non-magnetic CVs (e.g., [Ferrario et al. 2015](#), their Fig. 17). The fraction of magnetic WDs in CVs is known to be high (e.g., $\sim 33 \pm 7$ per cent in the first volume-limited sample of CVs, recently published by [Pala et al. 2020](#)). Therefore, including a fraction of magnetic CVs in our simulation, with reduced magnetic braking model like the one described by [Belloni et al. \(2020\)](#), could help reconcile the fraction of novae observed in the gap.

Regardless of the model, the main difference between our simulations and the observed period distribution is the presence of a peak in the number of observed systems with periods between 3 and 4 hours that our models do not reproduce. Above the period gap, the mass transfer rate depends mainly on the formalism assumed for magnetic braking. Here we assumed the [Rappaport et al. \(1983b\)](#) prescription for $\gamma = 3$, with the normalization factor derived by [Knigge et al. \(2011c\)](#). As can be seen in [Knigge et al. \(2011c\)](#), their figure 2), this formulation predicts a reduction in AML when approaching the period gap from larger periods. The simulated mass transfer rates are therefore lower for systems in the period range of 3 – 4 h compared to systems with larger

periods, making their recurrence periods longer. [Knigge et al. \(2011c\)](#) also showed that assuming a smaller value for γ in the [Rappaport et al. \(1983b\)](#) prescription for magnetic braking, or the formulation developed by [Kawaler \(1988\)](#), which is the same as the [Andronov et al. \(2003\)](#) model in the unsaturated limit), would all predict an increase of AML towards shorter periods, which would transfer into larger mass transfer rates and smaller recurrence periods that could reconcile the predictions with the observations.

The existence of a peak in the period distribution of post-nova system at 3–4 h, in addition to observational evidence of higher mass transfer rates for CVs in the same period range ([Townesley & Gänsicke 2009](#); [Pala et al. 2017](#)), seems to indicate that the [Rappaport et al. \(1983b\)](#) prescription with $\gamma = 3$ might not be the best approximation for magnetic braking in non-magnetic CVs. A similar conclusion is drawn in [Belloni et al. \(2020\)](#), where the simulated mass transfer rates for non-magnetic CVs above the gap drastically disagree from observations (when assuming also $\gamma = 3$ in the [Rappaport et al. \(1983b\)](#) prescription for magnetic braking), suggesting that AML caused by magnetic braking is not well understood. An interesting future work would be to derive the normalization factors, similar to what was done in [Knigge et al. \(2011c\)](#), but for magnetic braking prescriptions that predict an increase of AML while approaching the gap from larger periods. This would allow us to test whether the peak in the observed period distribution can be reproduced by changing the formulation for magnetic braking only.

Comparing with the literature, the only theoretical orbital period distribution of novae previously published is that of [Townesley & Bildsten \(2005\)](#). They predict a strong peak in the range of $P_{\text{orb}}=3-4$ h, but their cumulative distributions do not fit well for periods larger than 4 hours, which corresponds to $\sim 50\%$ of the observed sample. As the same authors mentioned, they use a very simple CV population model, where the number of CVs at each period interval was taken from [Howell et al. \(2001b\)](#) with a fixed WD mass, instead of evolving the systems from a binary population synthesis model. In order to obtain the mass transfer rate, they used the same prescription as we did for magnetic braking (i.e., [Rappaport et al. 1983b](#) prescription with $\gamma = 3$), but with a different mass-radius relation for the donor stars above the gap (also from [Howell et al. 2001b](#)). The accreted mass needed to produce a nova outburst was based on [Townesley & Bildsten \(2004\)](#) instead of [Yaron et al. \(2005\)](#). It is therefore impossible to make a more detailed comparison between their models and ours, although the need to include magnetic CVs with reduced magnetic braking in order to reproduce the fraction of novae observed in the period gap is a common conclusion of both studies.

3.5 Summary and conclusions

We have presented six new orbital periods and have reviewed and/or improved the periods for eight old novae, and discussed the resulting distribution of observed orbital periods with respect

to theoretical predictions based on a binary population synthesis model. In the following we summarize the most noteworthy results and conclusions.

- With X Cir, we report one new eclipsing nova, and with DY Pup, we confirm another one that was previously reported, but lacked the data to sustain such claim. Both have orbital periods in the 3 – 4 h range, corresponding to the period regime that is dominated by high \dot{M} objects. Comparing those systems, we find that the eclipses in DY Pup with a depth of ~ 0.3 mag are considerably more shallow than those of X Cir that show an average depth of 1 mag, which could indicate that the latter object is seen at a somewhat higher inclination than the former. X Cir’s high inclination could also possibly account for the spectral appearance that was interpreted by (Tappert et al. 2014) as a signature of a low \dot{M} system (Warner 1986).
- For RS Car, IL Nor, V2572 Sgr, XX Tau and CQ Vel, there is still some ambiguity concerning the orbital period, with more than one possible values existing for both objects. Still, we can already conclude that CQ Vel, together with V363 Sgr are situated in the period gap, while IL Nor is placed below it, making it the oldest nova in that short-period regime. The detection of an orbital modulation in the light curve of V363 Sgr indicates that it is seen at a somewhat higher inclination than suspected by Tappert et al. (2014).
- For three targets (V2572 Sgr, CQ Vel and RW UMi) the orbital period was determined or confirmed by time-resolved radial velocity observations. For the confirmation of the orbital period for XX Tau we suggest trying by this technique, observing with a baseline larger than four hours.
- In addition to short-term time-resolved photometric observations, we also used the CTIO data set, with a typical time resolution of 3 – 4 days, a by-product of a search for stunted dwarf nova-like outbursts in classical novae (Vogt et al. 2018). Our new period of V363 Sgr is entirely based on these data; they also enabled to derive a long-term orbital ephemeris of V2572 Sgr, and to improve the periods of other six novae (four with eclipses and two with orbital humps).
- We also present a statistic of all currently known orbital periods of novae, which are distributed in the following way: 79 per cent are located above the gap, equivalent to 72 objects, ~ 50 per cent of them (= 45 objects) have $P_{\text{orb}} > 4$ h. Only seven systems are located below the period gap, corresponding to eight per cent of the sample, meanwhile 13 systems (14 per cent) were found within the period gap. It is worth mentioning here again that this distribution differs significantly from the one of all CVs, with the main differences being the low number of objects below the gap, the majority of the novae having period

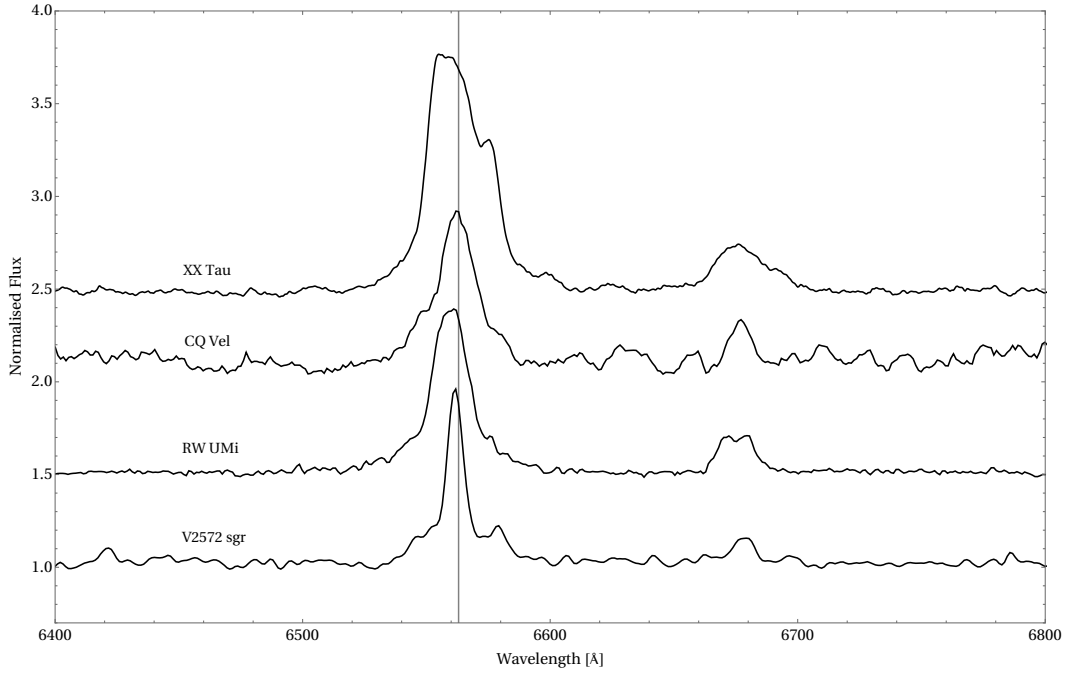


Figure 3.12: Normalised average spectrum for V2572 Sgr, RW UMi, CQ Vel and XX Tau for which radial velocities were measured from the H α emission line. The gray line marks the central lambda of H α . The $\lambda 6678$ Å He I emission line is also present in all spectra.

above the gap, and especially the peak located above the gap at 3 – 4 h that with the new data has become even more pronounced.

- There are striking differences between the theoretically predicted period distribution of novae and the observed one. Population model calculations are in accordance with the observed number ratios of novae below, within and above the period gap, but they are not able to reproduce the rather narrow peak observed at 3 – 4 h. Instead, they predict a more flat distribution in the range $3 \text{ h} \leq P_{\text{orb}} \leq 6 - 8 \text{ h}$. This implies that the prescription usually used for AML due to magnetic braking in CVs above the period gap might not be correct.

3.6 Appendix

Individual light curves and spectra for the analysed novae are shown as extra material. The epochs for the eclipses and the radial velocity measurements are also presented in the follow tables.

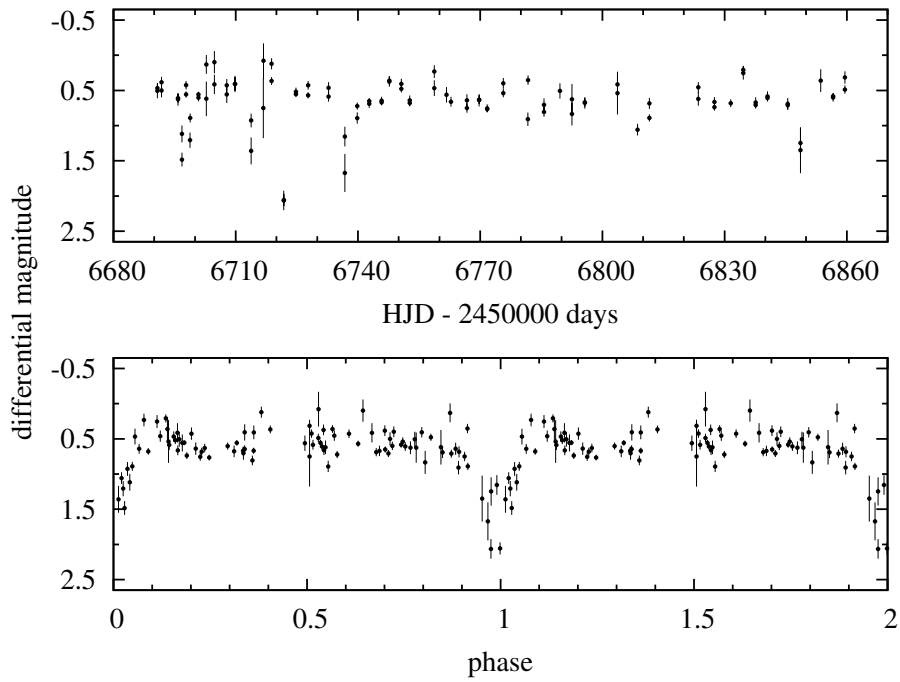


Figure 3.13: Top: The CTIO light curve of X Cir. Bottom: Phase light curve of this data according to ephemeris (3.5) described in section 3.3.3.

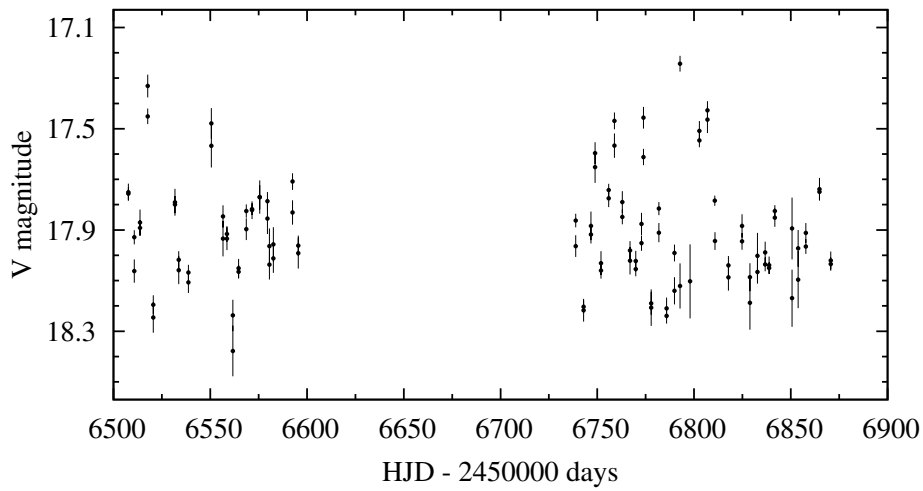


Figure 3.14: The CTIO light curves of V2572 Sgr described in section 3.3.7.

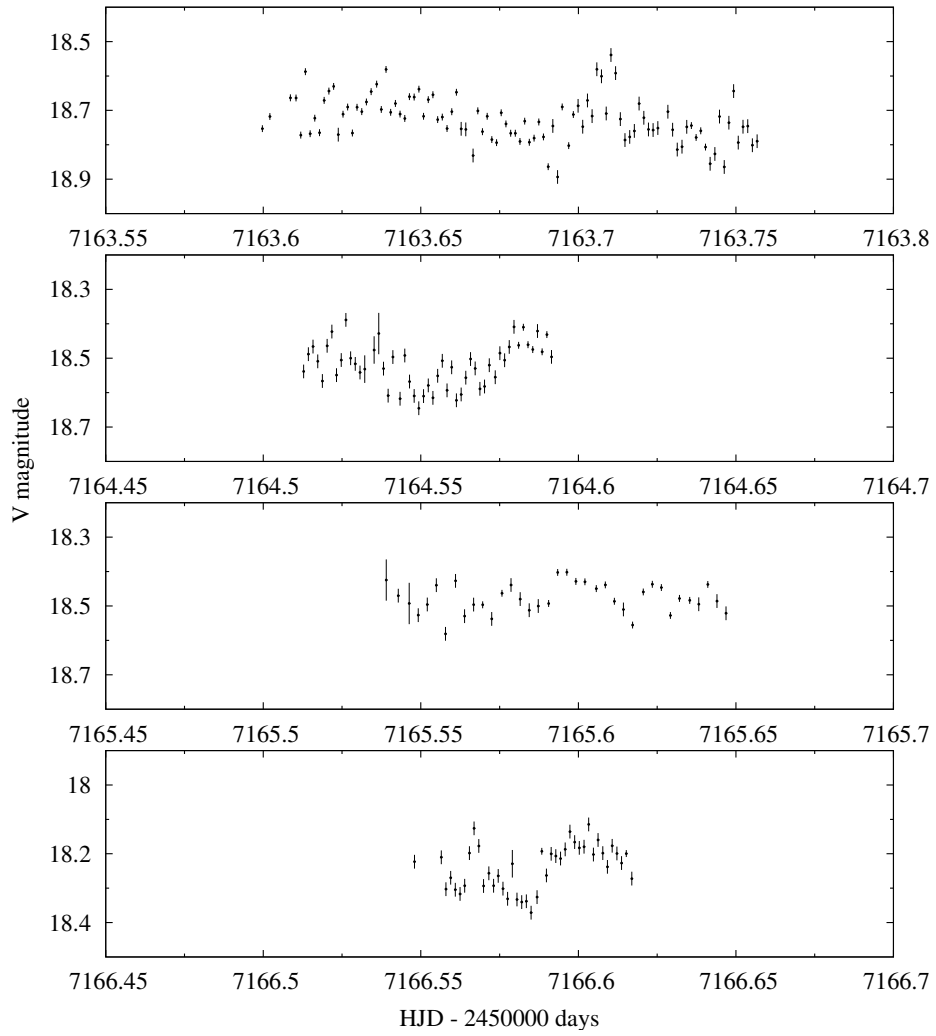


Figure 3.15: V-band light curves of IL Nor taken in 2015 at du Pont telescope.

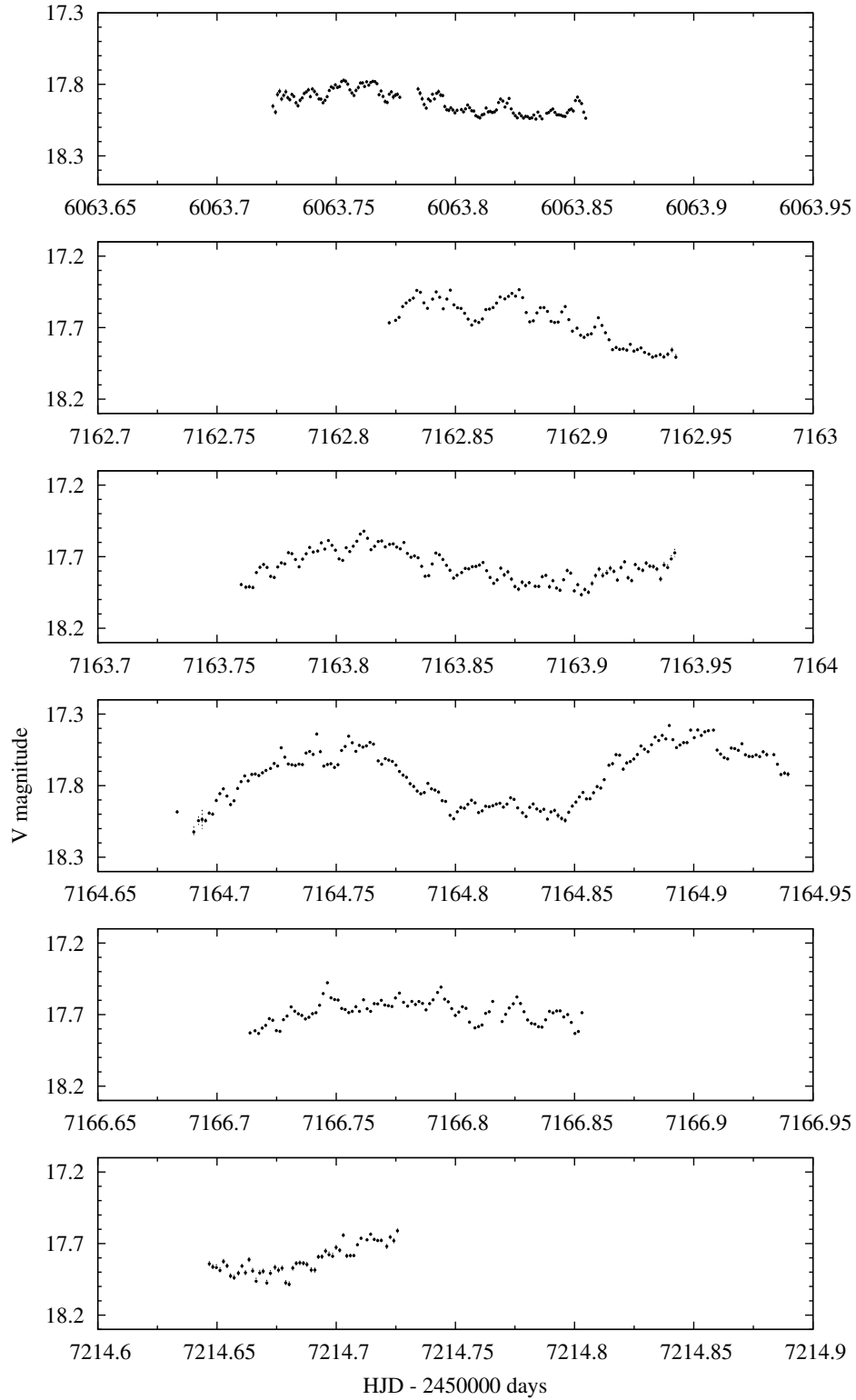


Figure 3.16: V-band Light curves of V2572 Sgr. The first one was observed with EFOSC2/NTT in May 2012 and the other ones with du Pont telescope in May-July 2015.

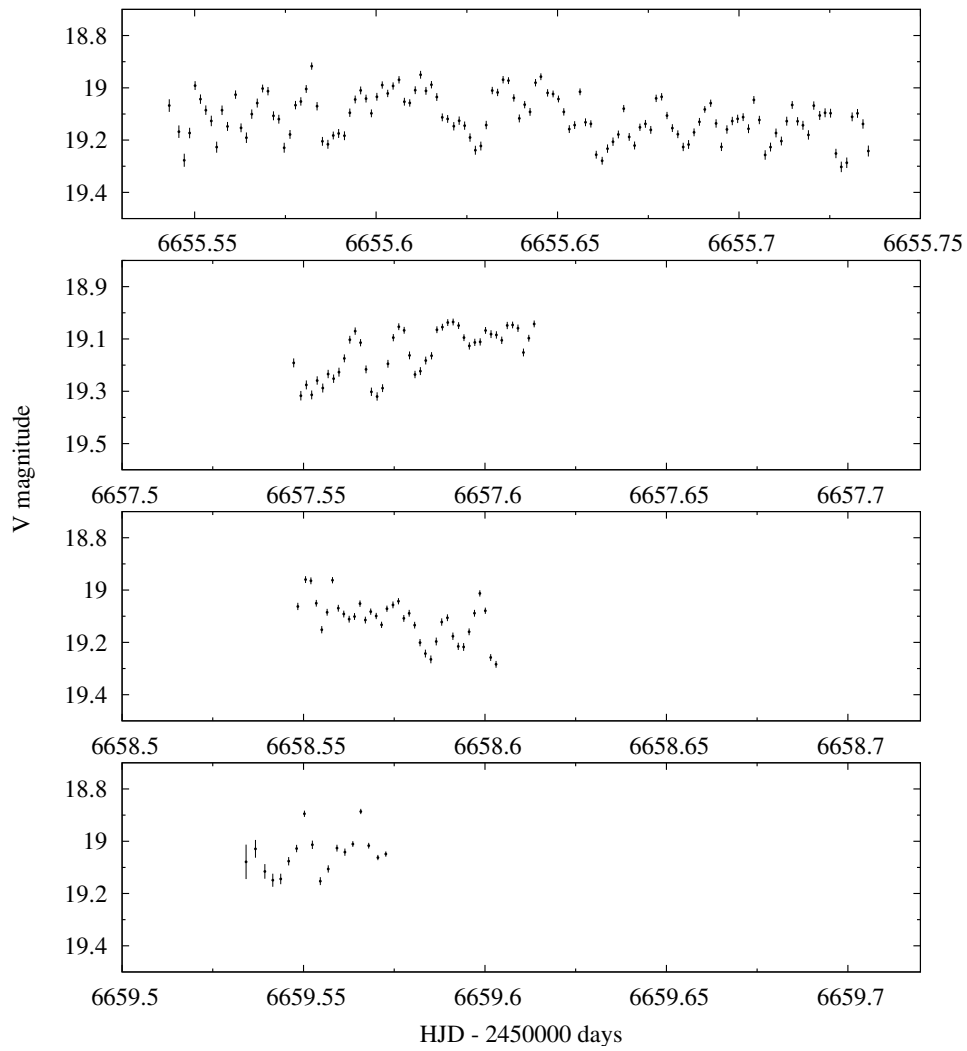


Figure 3.17: Light curves of XX Tau taken at du Pont telescope.

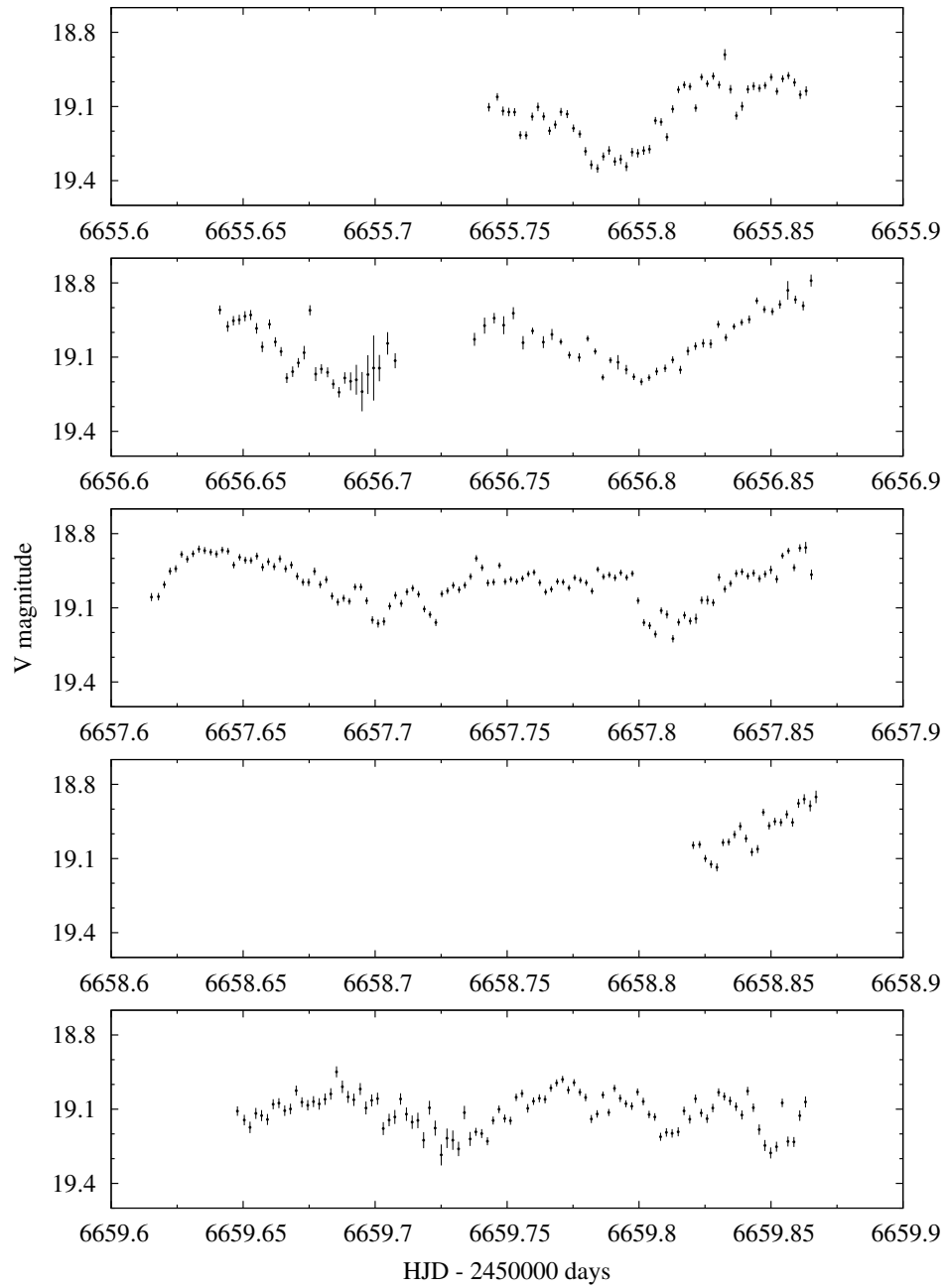


Figure 3.18: V-band Light curves of CQ Vel taken at du Pont telescope.

Table 3.7: Eclipse epochs of the four eclipsing novae from the literature and from CTIO observation data. The O-C values refer to the ephemerides given in Table 3.5.

Object	E	HJD −2 400 000 d	O − C d	Ref.
WY Sge	-14178	44881.639	0.0018	(1)
	-14171	44882.711	-0.0017	(1)
	-14003	44908.524	0.0007	(1)
	-12510	45137.8998	0.0001	(1)
	-12498	45139.7434	0.0001	(1)
	11564	48836.4976	-0.0001	(2)
	11571	48837.5726	-0.0006	(2)
	14151	49233.9498	-0.0005	(2)
	14157	49234.8722	0.0001	(2)
	14170	49236.869	-0.0004	(2)
	14176	49237.791	-0.0002	(2)
	14177	49237.945	0.0002	(2)
	63241	56775.8667	-0.0035	(3)
	63306	56785.8580	0.0015	(3)
	63618	56833.7893	-0.0012	(3)
	63637	56836.7094	-0.0001	(3)
	63696	56845.7720	-0.0020	(3)
63884	56874.6585	0.0013	(3)	
63942	56883.5697	0.0017	(3)	
65552	57130.9224	0.0028	(3)	
V728 Sco	-14	56013.8704	0.0002	(4)
	-7	56014.8379	-0.0007	(4)
	0	56015.8073	0.0004	(4)
	29	56019.8182	-0.0005	(4)
	346	56063.6729	0.0008	(4)
	353	56064.6404	-0.0001	(4)
	354	56064.7750	-0.0010	(4)
	4988	56705.8401	0.0003	(3)
	5082	56718.8412	-0.0025	(3)
	5147	56727.8347	-0.0010	(3)

Continued on next page

Table 3.7 – continued from previous page

Object	E	HJD –2 400 000 d	O – C d	Ref.
	5169	56730.8801	0.0010	(3)
	5234	56739.8729	0.0017	(3)
	5558	56784.6921	-0.0007	(3)
	6244	56879.5948	0.0017	(3)
	6446	56907.5382	0.0007	(3)
	6800	56956.5117	0.0023	(3)
	6865	56965.5034	0.0020	(3)
	7569	57062.8920	0.0002	(3)
	8154	57143.8197	-0.0001	(3)
	8709	57220.5947	-0.0031	(3)
	8804	57233.7386	-0.0014	(3)
OY Ara	-42829	49862.822	0.0001	(5)
	0	56516.5710	-0.0012	(3)
	283	56560.5463	-0.0009	(3)
	1160	56696.8211	-0.0022	(3)
	1289	56716.8686	0.0002	(3)
	1366	56728.8375	0.0041	(3)
V849 Oph	0	48799.7412	0.0000	(6)
	1	48799.9149	0.0009	(6)
	186	48831.8736	-0.0003	(6)
	191	48832.7384	0.0008	(6)
	29884	53962.3846	-0.0003	(7)
	29890	53963.4197	-0.0017	(7)
	29895	53964.2840	-0.0012	(7)
	44687	56519.6881	-0.0056	(3)
	46487	56830.6621	0.0074	(3)

References:

- (1) [Shara et al. \(1984\)](#), (2) [Somers et al. \(1996\)](#),
(3) this work, (4) [Tappert et al. \(2013a\)](#),
(5) [Zhao & McClintock \(1997\)](#), (6) [Shafter et al. \(1993\)](#),
(7) [Zengin Çamurdan et al. \(2010\)](#)

Table 3.8: Spectroscopic measurements. The name of the nova, the radial velocities parameters defined in Eq. (3.1), the equivalent width for $H\alpha$ emission line and the radial velocity measures from that line together with its HJD are given.

HJD -2 450 000 d	v_r (km/s)	HJD -2 450 000 d	v_r (km/s)	HJD -2 450 000 d	v_r (km/s)
V2572 Sgr					
5242.9278	68.52	8484.6188	84.78	7195.6736	-161.44
5243.6482	60.60	8484.6265	47.56	7195.6809	-168.36
5243.7272	10.86	8484.6339	-1.74	7195.6881	-157.43
5243.7956	116.31	8484.6412	-79.13	7195.6953	-136.91
5244.5174	26.86	8484.6486	-112.06	7195.7025	-152.90
5244.6005	71.65	8484.6562	-148.03	7195.7097	-135.46
5244.6470	34.06	8484.6636	-289.09	7196.4224	-125.13
5244.7140	56.87	8484.6710	-267.78	7196.4296	-135.27
5244.7475	73.38	8484.6784	-205.82	7196.4368	-138.73
5244.7789	23.29	8524.5969	-95.74	7196.4440	-147.87
5244.8102	42.36	8524.6042	-187.88	7196.4512	-161.69
5244.9086	36.79	8524.6116	-229.88	CQ Vel	
5246.9286	-3.30	8524.6190	-19.75	6012.5655	90.20
XX Tau					
		8526.5939	75.46	6012.5958	142.19
8482.6026	-31.96	8526.6013	86.15	6013.4878	-143.14
8482.6100	-16.86	8526.6086	-4.80	6013.4991	74.73
8482.6174	30.55	8526.6160	-62.70	6013.5101	42.50
8482.6247	222.31	RW UMi		6013.5212	112.31
8482.7278	16.99	7193.5948	-158.45	6013.5356	179.21
8482.7352	45.82	7193.6020	-166.56	6013.5466	100.48
8482.7425	-49.28	7193.6092	-138.88	6013.5574	74.32
8482.7499	-41.51	7193.6164	-147.71	6013.5888	46.92
8483.5690	-140.80	7193.6237	-143.23	6013.5998	16.15
8483.5764	-175.68	7193.6309	-137.75	6014.4854	170.30
8483.5837	-239.57	7193.6381	-140.61	6014.4966	-32.18
8483.5911	-110.32	7193.6453	-146.05	6014.5079	10.55
8483.5992	109.02	7193.6525	-173.64	6014.5212	206.04
8484.5368	-133.65	7193.6597	-162.63	6014.5323	171.34
8484.5441	-15.55	7195.6015	-142.06	6014.5777	259.17
8484.5515	43.39	7195.6087	-149.77	6014.6266	-20.27
8484.5589	40.82	7195.6159	-152.83	6015.4856	181.25
8484.5667	33.30	7195.6231	-144.41		
8484.5741	67.47	7195.6303	-148.72		
8484.5815	125.17	7195.6376	-129.93		
8484.5888	133.73	7195.6448	-135.47		
8484.5967	162.77	7195.6520	-144.77		
8484.6040	206.05	7195.6592	-114.02		
8484.6114	205.86	7195.6664	-134.63		

Table 3.9: The orbital periods of old novae considered to create the distribution shown in Fig. 3.10. The name, P_{orb} , the method used to derived it and the references are presented (OM: photometric orbital modulation, RV: Radial velocity, E: eclipse and SH: superhump). Those novae with daily alias ambiguities are categorized as “provisional” and they are marked with *. The choice for the orbital period value presented here is discussed in section 3.5.

Name	$P_{\text{orb}}(\text{d})$	method	reference	Name	$P_{\text{orb}}(\text{d})$	method	reference
RW UMi	0.05912	OM-RV	(1), (2), This paper	V2467 Cyg	0.1596	OM	(34)
GQ Mus	0.059365	OM-RV	(3), (4)	DO Aql	0.167762	E	(35)
CP Pup	0.061264	OM-RV-SH	(5), (6)	V849 Oph	0.17275611	E	(35), This paper
IL Nor*	0.06709	OM	This paper	V697 Sco	0.187	OM	(36)
V458 Vul	0.068126	RV	(7)	V825 Sco	0.19165877	E	(16)
V1974 Cyg	0.08126	OM-SH	(8)	DQ Her	0.193621	E-RV	(37)
RS Car*	0.082429	OM-SH?	(9), This paper	CT Ser	0.195	RV	(38)
DD Cir	0.09746	E	(10)	AT Cnc	0.201634	RV-OM	(39), (40), (41)
V Per	0.107123	E-RV	(11)	T Aur	0.204378	E	(42)
V597 Pup	0.11119	E	(12)	V446 Her	0.207	RV	(29)
QU Vul	0.111765	E	(13)	V4745 Sgr	0.20782	OM	(43)
CQ Vel*	0.11272	OM-RV	This paper	HZ Pup	0.212	RV	(44)
V2214 Oph	0.117515	OM	(14)	AP Cru	0.213	OM	(9)
V630 Sgr	0.11793	E-SH	(15), (16)	AR Cir	0.214	OM-RV	(22)
V351 Pup	0.1182	OM	(15)	HR Del	0.214165	RV	(45)

Continued on next page

Table 3.9 – continued from previous page

Name	$P_{\text{orb}}(\text{d})$	method	reference	Name	$P_{\text{orb}}(\text{d})$	method	reference
V5116 Sgr	0.1238	E	(16)	V5588 Sgr	0.214321	OM	(16)
V4633 Sgr	0.1255667	OM-SH	(16), (17)	NR TrA	0.219	E-RV	(46)
V363 Sgr	0.126066	OM	This paper	CN Vel	0.2202	RV	(22)
DN Gem	0.127844	RV	(18), (19)	V365 Car	0.223692	OM-RV	(22), This paper
V339 Del	0.1314	OM	(20)	V1039 Cen	0.247	OM	(47)
V4742 Sgr	0.1336159	E	(16)	V1425 Aql	0.2558	OM	(48)
V1494 Aql	0.134614	E	(21)	HS Pup	0.2671	RV	(22)
V5585 Sgr	0.137526	E	(16)	V2615 Oph	0.272339	OM	(16)
V603 Aql	0.138201	OM-RV-SH	(18)	V4743 Sgr	0.2799	OM	(49)
V728 Sco	0.13833866	E-RV	(22), This paper	V972 Oph	0.281	RV	(22)
V1668 Cyg	0.1384	E	(23)	BY Cir	0.2816	E	(10)
XX Tau*	0.13588	RV	This paper	V2540 Oph	0.284781	OM	(50)
DY Pup	0.13952	E	This paper	V1059 Sgr	0.2861	RV	(51)
V1500 Cyg	0.139613	OM	(24)	Z Cam	0.289841	RV	(52), (53)
RR Cha	0.1401	E-SH	(9)	V959 Mon	0.29585	OM	(54)
V909 Sgr	0.14286	OM-RV	(22)	V838 Her	0.297635	E	(55)
RR Pic	0.145025959	OM-SH	(25), (26)	V2275 Cyg	0.3145	OM	(56)
CP Lac	0.145143	RV	(18)	BT Mon	0.333814	E-RV	(57)
V500 Aql	0.1452	OM-RV	(27), (11)	V2677 Oph	0.3443	OM	(16)
V2468 Cyg	0.14525	OM	(28)	QZ Aur	0.357496	E-RV	(58), (59)
V533 Her	0.147	RV	(29)	Q Cyg	0.42036	RV	(16)
V2574 Oph	0.1477	OM-SH	(30)	J17014 4306	0.5340257	E	(60)
V5113 Sgr	0.150015	OM	(16)	V841 Oph	0.601304	RV	(18)
V4579 Sgr	0.15356146	E	(16)	V368 Aql	0.690509	E	(61)

Continued on next page

Table 3.9 – continued from previous page

Name	$P_{\text{orb}}(\text{d})$	method	reference	Name	$P_{\text{orb}}(\text{d})$	method	reference
V992 Sco	0.15358	OM	(10)	V723 Cas	0.693277	OM	(62)
V373 Sct	0.1536	RV	(22)	CP Cru	0.944	E	(10)
WY Sge	0.153634547	E	(31), This paper	V2674 Oph	1.30207	E	(16)
X Cir	0.15445953	E	This paper	X Ser	1.48	RV	(29)
OY Ara	0.155390	E-RV	(32), This paper	V5589 Sgr	1.5923	E	(16)
V1493 Aql	0.156	OM	(33)	HV Cet	1.772	OM	(63)
V2572 Sgr*	0.156215	OM-RV	This paper	GK Per	1.996803	RV	(64)

References:

- (1) Retter & Lipkin (2001), (2) Bianchini et al. (2003), (3) Diaz & Steiner (1994), (4) Narloch et al. (2014),
- (5) Mason et al. (2013), (6) Bianchini et al. (2012), (7) Rodríguez-Gil et al. (2010), (8) Olech (2002),
- (9) Woudt & Warner (2002), (10) Woudt & Warner (2003), (11) Haefner & Fiedler (2007),
- (12) Warner & Woudt (2009), (13) Shafter et al. (1995), (14) Baptista et al. (1993), (15) Woudt & Warner (2001),
- (16) Mróz et al. (2015), (17) Lipkin & Leibowitz (2008), (18) Peters & Thorstensen (2006), (19) Retter et al. (1999a),
- (20) Chochol et al. (2014), (21) Kato et al. (2004), (22) Tappert et al. (2013a), (23) Kaluzny (1990),
- (24) Pavlenko et al. (2018), (25) Vogt et al. (2017), (26) Fuentes-Morales et al. (2018), (27) Haefner (1999),
- (28) Chochol et al. (2013), (29) Thorstensen & Taylor (2000), (30) Kang et al. (2006a), (31) Somers et al. (1996),
- (32) Zhao & McClintock (1997), (33) Dobrotka et al. (2006a), (34) Swierczynski et al. (2010), (35) Shafter et al. (1993),
- (36) Warner & Woudt (2002), (37) Dai & Qian (2009), (38) Ringwald et al. (2005), (39) Nogami et al. (1999),
- (40) Shara et al. (2012b), (41) Bruch et al. (2019), (42) Dai & Qian (2010), (43) Dobrotka et al. (2006b),
- (44) Thorstensen et al. (2017), (45) Kuerster & Barwig (1988), (46) Walter (2015), (47) Woudt et al. (2005),
- (48) Retter et al. (1998), (49) Kang et al. (2006b), (50) Ak et al. (2005), (51) Thorstensen et al. (2010),
- (52) Thorstensen & Ringwald (1995), (53) Shara et al. (2007), (54) Munari et al. (2013), (55) Ingram et al. (1992),
- (56) Balman et al. (2005), (57) Smith et al. (1998b), (58) Szkody & Ingram (1994), (59) Campbell & Shafter (1995),
- (60) Shara et al. (2017b), (61) Marin & Shafter (2009), (62) Ochner et al. (2015), (63) Beardmore et al. (2012),
- (64) Morales-Rueda et al. (2002)

Chapter 4

Concluding summary and future prospects

The study of the behavior of novae after eruption has proven to be a cornerstone for testing current models of CV evolution. This work has mainly focused on increasing the sample of post-novae and removing unconfirmed ones, in order to analyze a significant and reliable sample, and to update some perspectives on their main features, such as the orbital period distribution and the spectral characteristics in the post-nova stage.

The “Life after eruption” project has notably contributed to increase the total sample of post-novae. Since the beginning of this PhD project in 2015, six new orbital periods were added to the current sample, eleven post-novae were spectroscopically confirmed and nine post-novae candidates were discarded. In comparison with the recovered sample between 2010 – 2015 (eight new orbital periods, 18 post-novae recovered and 10 post-nova candidates discarded, see Fig. 4.1), the increment from this thesis is somewhat smaller, mainly because the search strategy for post-nova candidates was not as effective as expected and also because most of the “easy” cases were already discovered. 26 fields were observed using $H\alpha$ photometry in order to search for post-nova candidates, but only one binary system was found that turned out to be a source with strong $H\alpha$ emission but is not a CV. Thus the search for post-nova based on $H\alpha$ emission does not appear as a suitable method. However, it can be useful to search for comparatively young novae in the nebular phase or to detect symbiotic novae of the RS Oph type. $UBVR$ photometry, despite being the most expensive method, - since it requires dark nights and long exposure times even at large telescopes-, has proved to be the most effective method in that search.

In chapter 2 we have presented an updated spectral study with data filling the lack of studied post-novae that erupted more than 60 years ago, in comparison with previous studies. The most outstanding results are detailed as follows:

1. with a sample of post novae comparatively older than earlier samples, our results are in agreement with the previous ones that post-novae that erupted between 30 to 50 yr ago with equivalent width greater than 70\AA are most likely still in the nebular phase stage.

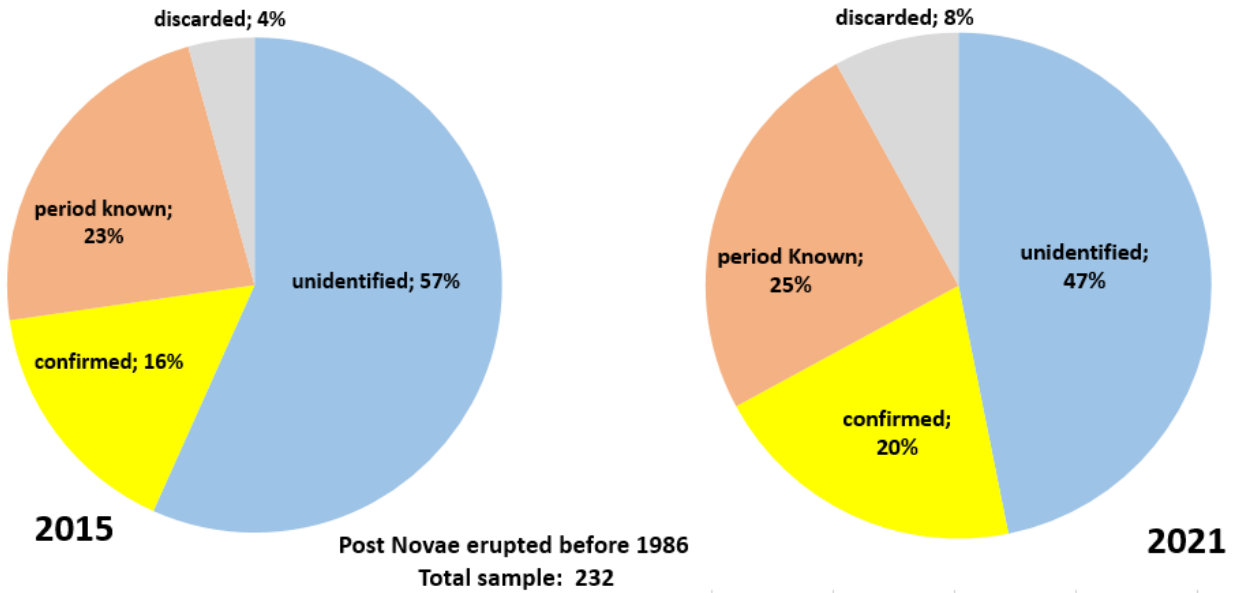


Figure 4.1: Sample of post-novae erupted before 1986 at the begin of this thesis in 2015 (left) compared to the current state (right). The pie charts show as a percentage of the total sample those old nova fields without identified post nova in blue, spectroscopically confirmed post-novae in yellow, identified post-novae with known orbital period are shown in orange and wrongly reported novae in grey.

2. No correlation has been found between mass transfer rate and time since eruption, in good agreement with previous studies. The equivalent widths can be indicative of the state of \dot{M} , but also is an indicator of the inclination, and thus it is a mixture that can only can be resolved taken also the FWHM into account. If the mass transfer rate drops after the eruption due to the decrease in irradiation effects proposed by the hibernation model, this does not occur on a time scale of decades but on a time scale longer than a century, which is the baseline of the recorded data. These results are in agreement with the results presented by [Vogt et al. \(2018\)](#) regarding the long-term photometric behavior of post-novae.
3. No significant correlation was found between amplitude and Silber’s empirical criterion that a CV is magnetic. This criterion can be useful to analyse CVs, but it may not be effective for novae, since He II lines may be formed by the effects of the hot-WD after the eruption. So far, the most reliable criterion for determining magnetic or IP CVs is the detection of the period of the WD and not based on spectral characteristics. At the moment, there are not enough data available to investigate this topic, but it could be a possible future line of research.

The currently observed orbital period distribution of 92 novae analysed in chapter 3, places 80% of the novae above the period gap, 14% in the gap and only 8% is below the gap, suggesting that very few novae exit below the gap, making it difficult to define a “gap” for the nova population. The fact that most novae have periods between 3 and 4 hrs where the highest values for \dot{M} are found, is likely due to the recurrence time being related to \dot{M} , i.e. those systems have a shorter recurrence

time, and that is the reason why we see more novae in that period range. For the same reason, we probably do not find many novae with $P_{\text{orb}} < 3$ hrs because due to their low \dot{M} , they have much longer recurrence times than the novae in the 3 – 4 hr period range.

While we do not have any definite evidence, because there are still too many novae that are not yet recovered, so that perhaps a significant number of low \dot{M} systems may be among them, from the current sample it looks as if the most significant parameter that defines the period distribution is the (average) mass-transfer rate of CVs.

The orbital period distribution is evidently different from the observed distribution for all CVs, which is dominated by systems with $P_{\text{orb}} < 2$ hr, i.e., by low-mass transfer objects.

Regarding the comparison of the observed versus theoretical distribution, assuming both consequential AML affected by mass transfer and nova eruption, neither the classical non-conservative (cCAML) model nor the empirical (eCAML) accurately reproduce the observed distribution in general. Below the gap cCAML predicts a higher number than observed ($\sim 18\%$), while the eCAML prediction is more precise ($\sim 10\%$). An effect of the initial assumption of a constant core temperature for the simulated CV evolution can be the main factor for this discrepancy below the gap. Alternatively, it may also be true, that an observational bias is responsible for the disagreement between simulated and observed P_{orb} in this range. In the gap, both models predict a very low population of novae ($\sim 3\%$ by cCAML and $\sim 1\%$ by eCAML), which can be a consequence of the fact that the simulated systems correspond to non-magnetic CVs, meaning that novae in the gap likely contain a WD with a strong magnetic field, which do not experience significant AML by magnetic braking, which is the predicted AML pathway in this orbital period range. In addition, neither model reproduces the observed peak at 3 – 4 hr. This seems to indicate that the prescription for magnetic braking commonly used in CV evolution above the period gap is not the best approximation. Although eCAML has proven to successfully reproduce the orbital distribution of CVs, it is not sufficiently adequate in reproducing the orbital period distribution of novae.

Future work

This work has shown that there is still a long way to go in understanding the impact of the nova eruption on the CV evolution. Although this is a project that has been running for several years, there is still a long list of post-novae to be confirmed, and this is the most pressing task that we will continue to develop on an ongoing basis. With the new data from the recovered novae to date together with an updated orbital period distribution, we will update the list of post-novae based on the database published by [Özdönmez et al. \(2018\)](#), which has incorporated reliable GAIA distances and reddening data.

Using the table of discarded periods (Table 3.6), we will aim the observing proposals to detect the orbital periods of those brightest southern novae that can be observed by medium telescopes.

Finally, we would like to mention that a new generation of terrestrial survey telescopes will soon become into operation, for instance the Vera C. Rubin Observatory (previously referred to as the Large Synoptic Survey Telescope, LSST), which will observe photometrically the southern hemisphere sky every ~ 3 days (a similar cadence as the CTIO set used in chapter 3), revealing crucial information on the behavior of many not yet observed, or even not yet identified old novae. This way, we will finally obtain better statistics on the orbital period distribution and other unsolved questions addressed here.

Furthermore, the binary star community will begin a new stage of discoveries once the optical spectroscopic mapping project of 77.000 southern hemisphere binary stars begins in 2024, using the 4-meter Multi Object Spectroscopy Telescope consortium (4MOST), which is being installed at the Visible and Infrared Survey Telescope for Astronomy (VISTA) in Cerro Paranal. Our understanding on CV evolution and in particular on post-novae will advance significantly already within the next few years.

Publication list of Irma Fuentes-Morales

Publications in refereed journals

1. **Fuentes-Morales, I.**, Tappert, C., Zorotovic, M., Vogt, N., Puebla, E. C., Schreiber, M. R., Ederoclite, A. & Schmidtobreick, L. (2021). Life after eruption VIII: The orbital periods of Novae. *Monthly Notices of the Royal Astronomy Society*, 501, 6083.
<https://doi.org/10.1093/mnras/staa3482>
2. **Fuentes-Morales, I.**, Vogt, N., Tappert, C., Schmidtobreick, L., Hamsch, F. -J., Vučković, M. (2018). Photometric long-term variations and superhump occurrence in the Classical Nova RR Pictoris. *Monthly Notices of the Royal Astronomy Society*, 474, 2493.
<https://doi.org/10.1093/mnras/stx2838>
3. Vogt, N., Tappert, C., Puebla, E. C., **Fuentes-Morales, I.**, Ederoclite, A. & Schmidtobreick, L. (2018). Life after eruption - VII. A search for stunted outbursts in 13 post-novae. *Monthly Notices of the Royal Astronomy Society*, 478, 5427.
<https://doi.org/10.1093/mnras/sty1445>
4. Vogt, N.; Schreiber, M. R.; Hamsch, F.-J., Retamales, G., Tappert, C., Schmidtobreick, L., **Fuentes-Morales, I.**, (2017). The orbital ephemeris of the classical nova RR Pictoris: presence of a third body?. *Publications of the Astronomical Society of the Pacific*, 129, 01420.
<https://doi.org/10.1088/1538-3873/129/971/014201>
5. Shara, M. M; Ilkiewicz, K.; Mikolajewska, J.; Pagnotta, A., Bode, M. F., Crause, L. A., Drozd, K., Faherty, J., **Fuentes-Morales, I.**, Grindlay, J. E., Moffat, A. F. J., Pretorius, M. L., Schmidtobreick, L., Stephenson, F. R., Tappert, C. & Zurek, D. (2017). Nova Scorpius 1437 A.D. is now a dwarf nova, age-dated by its proper motion. *Nature*, 548, 558.
<https://doi.org/10.1038/nature23644>
6. Tappert, C., Barria, D., **Fuentes-Morales, I.**, Vogt, N., Ederoclite, A. & Schmidtobreick, L., (2016). Life after eruption - VI. Recovery of the old novae EL Aql, V606 Aql, V908 Oph,

V1149 Sgr, V1583 Sgr and V3964 Sgr. Monthly Notices of the Royal Astronomy Society, 462, 1371-1381.

<https://doi.org/10.1093/mnras/stw1748>

7. Vogt, N., Contreras-Quijada, A., **Fuentes-Morales, I.**, Vogt-Geisse, S., Arcos, C., Abarca, C., Agurto-Gangas, C., Caviedes, M., DaSilva, H., Flores, J., Gotta, V., Peñaloza, F., Rojas, K. & Villaseñor, J. I., (2016). Determination of Pulsation Periods and Other Parameters of 2875 Stars Classified as MIRA in the All Sky Automated Survey (ASAS). The Astrophysical Journal Supplement Series, 227, 6.

<https://doi.org/10.3847/0067-0049/227/1/6>

8. **Fuentes-Morales, I.** & Vogt, N. (2014). Multiperiodic semiregular variable stars in the ASAS data base: A pilot study. Astronomische Nachrichten, 335, 1072-1077.

<https://doi.org/10.1002/asna.201412117>

Publication in books

1. **Fuentes-Morales, I.** (2021). Innovación evaluativa en educación en astronomía, en Antonio González Grez (Ed.), Innovación Digital en espacios educativos (I ed., Vol 1 pp 24 – 32). ISBN: 123-456-7899-12-0. <https://bit.ly/3KGwlaT>

Bibliography

- Abril, J., Schmidtbreick, L., Ederoclite, A., & López-Sanjuan, C. 2020, MNRAS, 492, L40
- Ak, T., Retter, A., & Liu, A. 2005, Publ. Astron. Soc. Aust., 22, 298
- Albitzky, V. 1929, Astronomische Nachrichten, 235, 317
- Andronov, N., Pinsonneault, M., & Sills, A. 2003, ApJ, 582, 358
- Appenzeller, I., Fricke, K., Fürtig, W., et al. 1998, The Messenger, 94, 1
- Astraatmadja, T. L. & Bailer-Jones, C. A. L. 2016, ApJ, 832, 137
- Bailer-Jones, C. A. L. 2015a, PASP, 127, 994
- Bailer-Jones, C. A. L. 2015b, PASP, 127, 994
- Balman, S., Nasiroglu, I., & Akyuz, A. 2009, The Astronomer's Telegram, 2137
- Balman, Ş., Retter, A., & Bos, M. 2006, AJ, 131, 2628
- Balman, Ş., Yılmaz, A., Retter, A., Saygac, T., & Esenoglu, H. 2005, MNRAS, 356, 773
- Baptista, R., Jablonski, F. J., Cieslinski, D., & Steiner, J. E. 1993, APJ, 406, L67
- Beardmore, A. P., Osborne, J. P., Page, K. L., et al. 2012, A&A, 545, A116
- Becker, F. 1929, Astronomische Nachrichten, 237, 71
- Belloni, D., Schreiber, M. R., Pala, A. F., et al. 2020, MNRAS, 491, 5717
- Belserene, E. P. 1979a, IAU, 3414, 2
- Belserene, E. P. 1979b, Information Bulletin on Variable Stars, 1706, 1
- Bertin, E. & Arnouts, S. 1996, A&AS, 117, 393
- Bianchini, A., Alford, B., Canterna, R., & Della Valle, M. 2001, MNRAS, 321, 625
- Bianchini, A., Saygac, T., Orío, M., Della Valle, M., & Williams, R. 2012, A&A, 539, A94
- Bianchini, A., Tappert, C., Canterna, R., et al. 2003, PASP, 115, 811
- Bode, M. F. & Evans, A. 2008, Classical Novae, Vol. 43
- Bruch, A., Boardman, J., Cook, L. M., et al. 2019, New A, 67, 22

Buzzoni, B., Delabre, B., Dekker, H., et al. 1984, *The Messenger*, 38, 9

Caldwell, J. A. R. 1982, *Information Bulletin on Variable Stars*, 2147, 1

Campbell, R. D. & Shafter, A. W. 1995, *ApJ*, 440, 336

Cannizzo, J. K. & Kaitchuck, R. H. 1992, *Scientific American*, 266, 42

Cannon, A. J. 1927, *Harvard College Observatory Bulletin*, 851, 7

Capitanio, L., Lallement, R., Vergely, J. L., Elyajouri, M., & Monreal-Ibero, A. 2017, *A&A*, 606, A65

Carroll, B. W. & Ostlie, D. A. 2006, *An introduction to modern astrophysics and cosmology* (Institute for Mathematics and Its Applications)

Cepa, J. 1998, *Ap&SS*, 263, 369

Chambers, K. C., Magnier, E. A., Metcalfe, N., et al. 2016, arXiv e-prints, arXiv:1612.05560

Chandrasekhar, S. 1931, *ApJ*, 74, 81

Chen, H.-L., Woods, T. E., Yungelson, L. R., Gilfanov, M., & Han, Z. 2016, *MNRAS*, 458, 2916

Chochol, D., Shugarov, S., Pribulla, T., & Volkov, I. 2014, *Contributions of the Astronomical Observatory Skalnaté Pleso*, 43, 330

Chochol, D., Shugarov, S. Y., Volkov, I. M., et al. 2013, *Information Bulletin on Variable Stars*, 6045

Cohen, J. G. 1985, *ApJ*, 292, 90

Cohen, J. G. & Rosenthal, A. J. 1983, *ApJ*, 268, 689

Collazzi, A. C., Schaefer, B. E., Xiao, L., et al. 2009, *AJ*, 138, 1846

Collins, K. A., Kielkopf, J. F., Stassun, K. G., & Hessman, F. V. 2017, *AJ*, 153, 77

Cumming, A. 2002, *MNRAS*, 333, 589

Dai, Z. & Qian, S. 2010, *New A*, 15, 380

Dai, Z. B. & Qian, S. B. 2009, *A&A*, 503, 883

Dawson, B. H. 1926, *AJ*, 36, 148

de Roy, F. 1932, *Gazette Astronomique*, 19, 1

- Della Valle, M. & Izzo, L. 2020, *A&ARv*, 28, 3
- della Valle, M. & Livio, M. 1995, *ApJ*, 452, 704
- Diaz, M. P. & Bruch, A. 1997, *A&A*, 322, 807
- Diaz, M. P. & Steiner, J. E. 1994, *ApJ*, 425, 252
- Dinerstein, H. L. 1986, *AJ*, 92, 1381
- Dishong, J. & Hoffleit, D. 1955, *AJ*, 60, 259
- Dobrotka, A., Friedjung, M., Retter, A., Hric, L., & Novak, R. 2006a, *A&A*, 448, 1107
- Dobrotka, A., Retter, A., & Liu, A. 2006b, *MNRAS*, 371, 459
- Downes, R. A. & Duerbeck, H. W. 2000a, *AJ*, 120, 2007
- Downes, R. A. & Duerbeck, H. W. 2000b, *AJ*, 120, 2007
- Downes, R. A., Duerbeck, H. W., & Delahodde, C. E. 2001, *Journal of Astronomical Data*, 7, 6
- Downes, R. A. & Szkody, P. 1989, *AJ*, 97, 1729
- Downes, R. A., Webbink, R. F., Shara, M. M., et al. 2005, *Journal of Astronomical Data*, 11, 2
- Drechsel, H., Rahe, J., Wargau, W., et al. 1982, *IAU*, 3736, 1
- Duerbeck, H. W. 1981, *PASP*, 93, 165
- Duerbeck, H. W. 1984, *Information Bulletin on Variable Stars*, 2490, 1
- Duerbeck, H. W. 1987, *Space Sci. Rev.*, 45, 1
- Duerbeck, H. W. 1992, *MNRAS*, 258, 629
- Egan, J. M., Woudt, P. A., Warner, B., et al. 2014, in *Astronomical Society of the Pacific Conference Series*, Vol. 490, *Stellar Novae: Past and Future Decades*, ed. P. A. Woudt & V. A. R. M. Ribeiro, 67
- Ferguson, D. H., Liebert, J., Cutri, R., et al. 1987, *ApJ*, 316, 399
- Ferrario, L., de Martino, D., & Gänsicke, B. T. 2015, *Space Sci. Rev.*, 191, 111
- Finzell, T., Chomiuk, L., Metzger, B. D., et al. 2018, *ApJ*, 852, 108
- Flewelling, H. A., Magnier, E. A., Chambers, K. C., et al. 2016, *arXiv e-prints*, arXiv:1612.05243

Frank, J., King, A., & Raine, D. 1992, *Accretion power in astrophysics* (Cambridge Astrophysics Series, Vol. 21)

Fuentes-Morales, I., Tappert, C., Zorotovic, M., et al. 2021, *MNRAS*, 501, 6083

Fuentes-Morales, I., Vogt, N., Tappert, C., et al. 2018, *MNRAS*, 474, 2493

Gaia Collaboration, Brown, A. G. A., Vallenari, A., et al. 2018, *A&A*, 616, A1

Gaia Collaboration, Brown, A. G. A., Vallenari, A., et al. 2021, *A&A*, 649, A1

Gaia Collaboration, Brown, A. G. A., Vallenari, A., et al. 2016, *A&A*, 595, A2

Gänsicke, B. T., Dillon, M., Southworth, J., et al. 2009a, *MNRAS*, 397, 2170

Gänsicke, B. T., Dillon, M., Southworth, J., et al. 2009b, *MNRAS*, 397, 2170

Gaposchkin, S. 1954, *AJ*, 59, 199

Gardner, J. P., Mather, J. C., Clampin, M., et al. 2006, *Space Sci. Rev.*, 123, 485

Gehrz, R. D., Grasdalen, G. L., Hackwell, J. A., & Ney, E. P. 1980, *ApJ*, 237, 855

Gehrz, R. D., Truran, J. W., Williams, R. E., & Starrfield, S. 1998, *PASP*, 110, 3

Gerasimovic, B. P. 1936, *Popular Astronomy*, 44, 78

Gill, C. D. & O'Brien, T. J. 1998, *MNRAS*, 300, 221

Gill, C. D. & O'Brien, T. J. 2000, *MNRAS*, 314, 175

Goliasch, J. & Nelson, L. 2015, *ApJ*, 809, 80

Goranskij, V., Shugarov, S., Zharova, A., Kroll, P., & Barsukova, E. A. 2010, *Peremennye Zvezdy*, 30

Goransky, V. P., Shugarov, S. Y., Dmitrienko, E. S., & Pavlenko, E. P. 1997, in *Astrophysics and Space Science Library*, Vol. 218, *Astronomical Time Series*, ed. D. Maoz, A. Sternberg, & E. M. Leibowitz, 219–222

Hachisu, I. & Kato, M. 2007, *ApJ*, 662, 552

Hachisu, I., Kato, M., & Nomoto, K. 1996, *APJ*, 470, L97

Hacke, G. 1987, *Information Bulletin on Variable Stars*, 2979

Haefner, R. 1999, *Information Bulletin on Variable Stars*, 4706

- Haefner, R. & Fiedler, A. 2007, *Information Bulletin on Variable Stars*, 5751
- Hellier, C. 2001, *Cataclysmic Variable Stars*, (Springer)
- Henize, K. G. 1967, *ApJS*, 14, 125
- Hillman, Y., Shara, M. M., Prialnik, D., & Kovetz, A. 2020, *Nature Astronomy*, 4, 886
- Hoffleit, D. 1950, *AJ*, 55, 149
- Honeycutt, R. K., Kafka, S., Jacobson, H., et al. 2011a, *AJ*, 141, 122
- Honeycutt, R. K., Robertson, J. W., & Kafka, S. 2011b, *AJ*, 141, 121
- Honeycutt, R. K., Robertson, J. W., & Turner, G. W. 1998, *AJ*, 115, 2527
- Hook, I. M., Jørgensen, I., Allington-Smith, J. R., et al. 2004, *PASP*, 116, 425
- Horne, K. & Marsh, T. R. 1986, *MNRAS*, 218, 761
- Hoshi, R. 1979, *Progress of Theoretical Physics*, 61, 1307
- Howell, S. B., Nelson, L. A., & Rappaport, S. 2001a, *ApJ*, 550, 897
- Howell, S. B., Nelson, L. A., & Rappaport, S. 2001b, *ApJ*, 550, 897
- Hurley, J. R., Tout, C. A., & Pols, O. R. 2002, *MNRAS*, 329, 897
- Iijima, T. & Rosino, L. 1983, *PASP*, 95, 506
- Ingram, D., Garnavich, P., Green, P., & Szkody, P. 1992, *PASP*, 104, 402
- Johnson, C. B., Schaefer, B. E., Kroll, P., & Henden, A. A. 2014, *APJ*, 780, L25
- José, J. & Hernanz, M. 1998, *ApJ*, 494, 680
- José, J., Hernanz, M., Amari, S., Lodders, K., & Zinner, E. 2004, *ApJ*, 612, 414
- Kaluzny, J. 1990, *MNRAS*, 245, 547
- Kamath, U. S. 2009, in *Astronomical Society of the Pacific Conference Series*, Vol. 404, *The Eighth Pacific Rim Conference on Stellar Astrophysics: A Tribute to Kam-Ching Leung*, ed. S. J. Murphy & M. S. Bessell, 93
- Kang, T. W., Retter, A., Liu, A., & Richards, M. 2006a, *AJ*, 131, 1687
- Kang, T. W., Retter, A., Liu, A., & Richards, M. 2006b, *AJ*, 132, 608

- Kato, M. & Hachisu, I. 2007, *ApJ*, 657, 1004
- Kato, T., Ishioka, R., Uemura, M., Starkey, D. R., & Krajci, T. 2004, *PASJ*, 56, S125
- Kato, T., Sekine, Y., & Hirata, R. 2001, *PASJ*, 53, 1191
- Kato, T. & Yamaoka, H. 2002, *A&A*, 396, 629
- Katysheva, N. A. & Shugarov, S. Y. 2007, in *Astronomical Society of the Pacific Conference Series*, Vol. 372, 15th European Workshop on White Dwarfs, ed. R. Napiwotzki & M. R. Burleigh, 523
- Kawaler, S. D. 1988, *ApJ*, 333, 236
- Kemp, A. J., Karakas, A. I., Casey, A. R., Kobayashi, C., & Izzard, R. G. 2022, *MNRAS*, 509, 1175
- King, A. R., Frank, J., Kolb, U., & Ritter, H. 1995, *APJ*, 444, L37
- King, A. R. & Kolb, U. 1995, *ApJ*, 439, 330
- Knigge, C. 2006, *MNRAS*, 373, 484
- Knigge, C., Baraffe, I., & Patterson, J. 2011a, *ApJS*, 194, 28
- Knigge, C., Baraffe, I., & Patterson, J. 2011b, *ApJS*, 194, 28
- Knigge, C., Baraffe, I., & Patterson, J. 2011c, *ApJS*, 194, 28
- Kosai, H., Honda, M., Mack, P., & Cousins, A. W. J. 1982a, *IAU*, 3733, 1
- Kosai, H., Honda, M., Nishimura, S., et al. 1982b, *IAU*, 3661, 1
- Kouwenhoven, M. B. N., Brown, A. G. A., Goodwin, S. P., Portegies Zwart, S. F., & Kaper, L. 2009, *A&A*, 493, 979
- Kozai, Y., Honda, M., & Kosai, H. 1978a, *IAU*, 3186, 1
- Kozai, Y., Kosai, H., Hamajima, K., Schmidt, T., & Annal, R. 1978b, *IAU*, 3188, 1
- Kozai, Y., Kosai, H., Honda, M., & Cragg, T. 1981, *IAU*, 3590, 1
- Kraft, R. P. 1962, *ApJ*, 135, 408
- Kraft, R. P. 1964, *ApJ*, 139, 457
- Kroupa, P., Tout, C. A., & Gilmore, G. 1993, *MNRAS*, 262, 545

Kuerster, M. & Barwig, H. 1988, A&A, 199, 201

Landolt, A. U. 1983, AJ, 88, 439

Landolt, A. U. 1992, AJ, 104, 340

Lasota, J.-P. 2001, , 45, 449

Lasota, J.-P., Kuulkers, E., & Charles, P. 1999, MNRAS, 305, 473

Lipkin, Y. M. & Leibowitz, E. M. 2008, MNRAS, 387, 289

Livio, M. 1992, ApJ, 393, 516

Livio, M., Shankar, A., Burkert, A., & Truran, J. W. 1990, ApJ, 356, 250

Lundmark, K. 1935, Meddelanden fran Lunds Astronomiska Observatorium Serie II, 74, 1

Luyten, W. J. 1937, Astronomische Nachrichten, 264, 63

Lynden-Bell, D. 1969, Nature, 223, 690

Marin, E. & Shafter, A. W. 2009, PASP, 121, 1090

Mason, E., Orio, M., Mukai, K., et al. 2013, MNRAS, 436, 212

Mattei, J. A. 1979, , 73, 50

Mayall, M. W. 1938, Harvard College Observatory Bulletin, 907, 28

Mayall, M. W. 1949, AJ, 54, R191

Mazeh, T., Netzer, H., Shaviv, G., et al. 1985, A&A, 149, 83

McCarthy, M. F., Lasker, B. M., & Kinman, T. D. 1981, PASP, 93, 470

McLaughlin, D. B. 1939, Popular Astronomy, 47, 410

Mclaughlin, D. B. 1945, PASP, 57, 69

McLaughlin, D. B. 1960, in Stellar atmospheres. Edited by Jesse Leonard Greenstein. Supported in part by the National Science Foundation. Published by the University of Chicago Press, 585

Meyer, F. & Meyer-Hofmeister, E. 1981, A&A, 104, L10

Morales-Rueda, L., Still, M. D., Roche, P., Wood, J. H., & Lockley, J. J. 2002, MNRAS, 329, 597

Mróz, P., Udalski, A., Pietrukowicz, P., et al. 2016, Nature, 537, 649

Mróz, P., Udalski, A., Poleski, R., et al. 2015, *ApJS*, 219, 26

Munari, U., Dallaporta, S., Castellani, F., et al. 2013, *MNRAS*, 435, 771

Narloch, W., Kaluzny, J., Krzeminski, W., et al. 2014, *Baltic Astronomy*, 23, 1

Nelson, L. A., MacCannell, K. A., & Dubeau, E. 2004, *ApJ*, 602, 938

Nogami, D., Masuda, S., Kato, T., & Hirata, R. 1999, *PASJ*, 51, 115

Nomoto, K., Nariai, K., & Sugimoto, D. 1979, *PASJ*, 31, 287

Ochner, P., Moschini, F., Munari, U., & Frigo, A. 2015, *MNRAS*, 454, 123

Olech, A. 2002, *Acta Astron*, 52, 273

Osaki, Y. 1974, *PASJ*, 26, 429

Osaki, Y. 1996, *PASP*, 108, 39

Özdönmez, A., Ege, E., Güver, T., & Ak, T. 2018, *MNRAS*, 476, 4162

Özdönmez, A., Güver, T., Cabrera-Lavers, A., & Ak, T. 2016, *MNRAS*, 461, 1177

Pagnotta, A. & Schaefer, B. E. 2014, *ApJ*, 788, 164

Pala, A. F. 2019, in *Compact White Dwarf Binaries*, ed. G. H. Tovmassian & B. T. Gansicke, 2

Pala, A. F., Gänsicke, B. T., Breedt, E., et al. 2020, *MNRAS*, 494, 3799

Pala, A. F., Gänsicke, B. T., Townsley, D., et al. 2017, *MNRAS*, 466, 2855

Pasquini, L., Bonifacio, P., Randich, S., Galli, D., & Gratton, R. G. 2004, *A&A*, 426, 651

Patterson, J. 1984, *ApJS*, 54, 443

Patterson, J., Uthas, H., Kemp, J., et al. 2013, *MNRAS*, 434, 1902

Paunzen, E. & Vanmunster, T. 2016, *Astronomische Nachrichten*, 337, 239

Pavlenko, E. P., Mason, P. A., Sosnovskij, A. A., et al. 2018, *MNRAS*, 479, 341

Payne-Gaposchkin, C. 1964, *The galactic novae*

Payne-Gaposchkin, C. 1977, *Past and Future Novae*, ed. M. Friedjung, Vol. 65, 3

Peters, C. S. & Thorstensen, J. R. 2006, *PASP*, 118, 687

Pickering, E. C. 1893, *Astronomische Nachrichten*, 134, 181

Pickering, E. C. 1895, *Astronomische Nachrichten*, 139, 119

Pickering, E. C. & Fleming, W. P. 1900, *ApJ*, 12, 52

Popova, E. I., Tutukov, A. V., & Yungelson, L. R. 1982, *Ap&SS*, 88, 55

Porter, J. M., O'Brien, T. J., & Bode, M. F. 1998, *MNRAS*, 296, 943

Prabhu, T. P. & Anupama, G. C. 1987a, *Journal of Astrophysics and Astronomy*, 8, 369

Prabhu, T. P. & Anupama, G. C. 1987b, *Ap&SS*, 131, 479

Ramsay, G., Schreiber, M. R., Gänsicke, B. T., & Wheatley, P. J. 2017, *A&A*, 604, A107

Rappaport, S., Joss, P. C., & Webbink, R. F. 1982, *ApJ*, 254, 616

Rappaport, S., Verbunt, F., & Joss, P. C. 1983a, *ApJ*, 275, 713

Rappaport, S., Verbunt, F., & Joss, P. C. 1983b, *ApJ*, 275, 713

Retter, A. & Leibowitz, E. M. 1995, *IAU*, 6234

Retter, A. & Leibowitz, E. M. 1998, *MNRAS*, 296, L37

Retter, A., Leibowitz, E. M., & Kovo-Kariti, O. 1998, *MNRAS*, 293, 145

Retter, A., Leibowitz, E. M., & Naylor, T. 1999a, *MNRAS*, 308, 140

Retter, A., Liller, W., & Garradd, G. 1999b, *IAU*, 7124

Retter, A. & Lipkin, Y. 2001, *Astronomy and Astrophysics*, 365, 508

Ringwald, F. A., Chase, D. W., & Reynolds, D. S. 2005, *PASP*, 117, 1223

Ringwald, F. A., Naylor, T., & Mukai, K. 1996, *MNRAS*, 281, 192

Ritter, H. & Kolb, U. 2003a, *A&A*, 404, 301

Ritter, H. & Kolb, U. 2003b, *A&A*, 404, 301

Robinson, E. L. 1975, *AJ*, 80, 515

Rodríguez-Gil, P., Gänsicke, B. T., Hagen, H.-J., et al. 2007, *MNRAS*, 377, 1747

Rodríguez-Gil, P., Santander-García, M., Knigge, C., et al. 2010, *MNRAS*, 407, L21

Rodríguez-Gil, P. & Torres, M. A. P. 2005, *A&A*, 431, 289

Saito, R. K., Minniti, D., Angeloni, R., et al. 2013, *A&A*, 554, A123

Samus', N. N., Kazarovets, E. V., Durlevich, O. V., Kireeva, N. N., & Pastukhova, E. N. 2017, *Astronomy Reports*, 61, 80

Sana, H., Gosset, E., & Evans, C. J. 2009, *MNRAS*, 400, 1479

Santamaría, E., Guerrero, M. A., Ramos-Larios, G., et al. 2020, *ApJ*, 892, 60

Schaefer, B. E. 2018a, *MNRAS*, 481, 3033

Schaefer, B. E. 2018b, *MNRAS*, 481, 3033

Schaefer, B. E. 2021, *Research Notes of the American Astronomical Society*, 5, 150

Schatzman, E. 1962, *Annales d'Astrophysique*, 25, 18

Schenker, K., Kolb, U., & Ritter, H. 1998, *MNRAS*, 297, 633

Schlafly, E. F. & Finkbeiner, D. P. 2011, *ApJ*, 737, 103

Schmidtobreick, L., Shara, M., Tappert, C., Bayo, A., & Ederoclite, A. 2015, *MNRAS*, 449, 2215

Schmidtobreick, L., Tappert, C., Bianchini, A., & Mennickent, R. 2002, in *American Institute of Physics Conference Series*, Vol. 637, *Classical Nova Explosions*, ed. M. Hernanz & J. José, 527–531

Schmidtobreick, L., Tappert, C., Bianchini, A., & Mennickent, R. E. 2003a, *A&A*, 410, 943

Schmidtobreick, L., Tappert, C., Bianchini, A., & Mennickent, R. E. 2005, *A&A*, 432, 199

Schmidtobreick, L., Tappert, C., & Saviane, I. 2003b, *MNRAS*, 342, 145

Schreiber, M. R. & Gänsicke, B. T. 2001, *A&A*, 375, 937

Schreiber, M. R., Gänsicke, B. T., & Cannizzo, J. K. 2000, *A&A*, 362, 268

Schreiber, M. R., Gänsicke, B. T., Rebassa-Mansergas, A., et al. 2010, *A&A*, 513, L7

Schreiber, M. R., Zorotovic, M., & Wijnen, T. P. G. 2016, *MNRAS*, 455, L16

Selvelli, P. & Gilmozzi, R. 2019, *A&A*, 622, A186

Shafter, A. W., Misselt, K. A., Szkody, P., & Politano, M. 1995, *APJ*, 448, L33

Shafter, A. W., Misselt, K. A., & Veal, J. M. 1993, *PASP*, 105, 853

Shakura, N. I. & Sunyaev, R. A. 1973, *A&A*, 24, 337

Shapley, H. 1921, *Harvard College Observatory Bulletin*, 760, 1

Shapley, H. 1933, *Annals of Harvard College Observatory*, 84, 121

Shara, M. M., Drissen, L., Martin, T., Alarie, A., & Stephenson, F. R. 2017a, *MNRAS*, 465, 739

Shara, M. M., Ikkiewicz, K., Mikołajewska, J., et al. 2017b, *Nature*, 548, 558

Shara, M. M., Livio, M., Moffat, A. F. J., & Orio, M. 1986, *ApJ*, 311, 163

Shara, M. M., Martin, C. D., Seibert, M., et al. 2007, *Nature*, 446, 159

Shara, M. M., Mizusawa, T., Wehinger, P., et al. 2012a, *ApJ*, 758, 121

Shara, M. M., Mizusawa, T., Wehinger, P., et al. 2012b, *ApJ*, 758, 121

Shara, M. M., Mizusawa, T., Zurek, D., et al. 2012c, *ApJ*, 756, 107

Shara, M. M., Moffat, A. F. J., McGraw, J. T., et al. 1984, *ApJ*, 282, 763

Shara, M. M., Prialnik, D., Hillman, Y., & Kovetz, A. 2018, *ApJ*, 860, 110

Silber, A. D. 1992, PhD thesis, MASSACHUSETTS INSTITUTE OF TECHNOLOGY.

Skopal, A., Drechsel, H., Tarasova, T., et al. 2014, *A&A*, 569, A112

Smak, J. 2010, *Acta Astron*, 60, 357

Smith, D. A., Dhillon, V. S., & Marsh, T. R. 1998a, *MNRAS*, 296, 465

Smith, D. A., Dhillon, V. S., & Marsh, T. R. 1998b, *MNRAS*, 296, 465

Somers, M. W., Mukai, K., & Naylor, T. 1996, *MNRAS*, 278, 845

Sowell, J. R. & Cowley, A. P. 1983, *Information Bulletin on Variable Stars*, 2283, 1

Spruit, H. C. & Ritter, H. 1983, *A&A*, 124, 267

Starrfield, S., Sparks, W. M., Truran, J. W., & Wiescher, M. C. 2000, *ApJS*, 127, 485

Starrfield, S., Truran, J. W., Wiescher, M. C., & Sparks, W. M. 1998, *MNRAS*, 296, 502

Stenholm, B. & Lundstrom, I. 1979, *IAU*, 3411, 2

- Stetson, P. B. 1992, in *Astronomical Society of the Pacific Conference Series*, Vol. 25, *Astronomical Data Analysis Software and Systems I*, ed. D. M. Worrall, C. Biemesderfer, & J. Barnes, 297
- Stetson, P. B. 2000, *PASP*, 112, 925
- Strope, R. J., Schaefer, B. E., & Henden, A. A. 2010, *AJ*, 140, 34
- Swierczynski, E., Mikolajewski, M., Tomov, T., et al. 2010, in *Astronomical Society of the Pacific Conference Series*, Vol. 435, *Binaries - Key to Comprehension of the Universe*, ed. A. Prša & M. Zejda, 297
- Szkody, P. 1994, *AJ*, 108, 639
- Szkody, P., Dyck, H. M., Capps, R. W., Becklin, E. E., & Cruikshank, D. P. 1979, *AJ*, 84, 1359
- Szkody, P. & Ingram, D. 1994, *ApJ*, 420, 830
- Tamburini, F., di Mille, F., Bianchini, A., & Johnson, P. 2007, *A&A*, 464, 697
- Tappert, C., Barria, D., Fuentes Morales, I., et al. 2016, *MNRAS*, 462, 1371
- Tappert, C., Ederoclite, A., Mennickent, R. E., Schmidtbreick, L., & Vogt, N. 2012, *MNRAS*, 423, 2476
- Tappert, C., Schmidtbreick, L., Vogt, N., & Ederoclite, A. 2013a, *MNRAS*, 436, 2412
- Tappert, C., Vogt, N., Della Valle, M., Schmidtbreick, L., & Ederoclite, A. 2014, *MNRAS*, 442, 565
- Tappert, C., Vogt, N., Ederoclite, A., et al. 2020, arXiv e-prints, arXiv:2007.10940
- Tappert, C., Vogt, N., Schmidtbreick, L., & Ederoclite, A. 2015, *MNRAS*, 450, 943
- Tappert, C., Vogt, N., Schmidtbreick, L., Ederoclite, A., & Vanderbeke, J. 2013b, *MNRAS*, 431, 92
- Thorstensen, J. R., Peters, C. S., & Skinner, J. N. 2010, *PASP*, 122, 1285
- Thorstensen, J. R. & Ringwald, F. A. 1995, *Information Bulletin on Variable Stars*, 4249
- Thorstensen, J. R., Ringwald, F. A., Taylor, C. J., et al. 2017, *Research Notes of the American Astronomical Society*, 1, 29
- Thorstensen, J. R. & Taylor, C. J. 2000, *MNRAS*, 312, 629
- Tomov, T., Swierczynski, E., Mikolajewski, M., & Ilkiewicz, K. 2015, *A&A*, 576, A119

Townsley, D. M. & Bildsten, L. 2004, *ApJ*, 600, 390

Townsley, D. M. & Bildsten, L. 2005, *ApJ*, 628, 395

Townsley, D. M. & Gänsicke, B. T. 2009, *ApJ*, 693, 1007

Uthas, H., Knigge, C., & Steeghs, D. 2010, *MNRAS*, 409, 237

van Dokkum, P. G. 2001, *PASP*, 113, 1420

Vogt, N. 1990, *ApJ*, 356, 609

Vogt, N., Schreiber, M. R., Hamsch, F.-J., et al. 2017, *PASP*, 129, 014201

Vogt, N., Tappert, C., Puebla, E. C., et al. 2018, *MNRAS*, 478, 5427

Šimon, V. 2018, *A&A*, 614, A141

Wade, R. A., Harlow, J. J. B., & Ciardullo, R. 2000, *PASP*, 112, 614

Walter, F. M. 2015, in *Astronomical Society of the Pacific Conference Series*, Vol. 493, 19th European Workshop on White Dwarfs, ed. P. Dufour, P. Bergeron, & G. Fontaine, 507

Walter, F. M., Battisti, A., Towers, S. E., Bond, H. E., & Stringfellow, G. S. 2012, *PASP*, 124, 1057

Warner, B. 1986, *MNRAS*, 222, 11

Warner, B. 1995, *Cataclysmic variable stars* (Cambridge Astrophysics Series, Vol. 28)

Warner, B. 2002, in *American Institute of Physics Conference Series*, Vol. 637, *Classical Nova Explosions*, ed. M. Hernanz & J. José, 3–15

Warner, B. 2003a, *Cataclysmic Variable Stars*

Warner, B. 2003b, *Monthly Notes of the Astronomical Society of South Africa*, 62, 74

Warner, B. & Woudt, P. A. 2002, *PASP*, 114, 1222

Warner, B. & Woudt, P. A. 2009, *MNRAS*, 397, 979

Webbink, R. F. 1985, in *Interacting Binary Stars*, ed. J. E. Pringle & R. A. Wade, 39

Weight, A., Evans, A., Naylor, T., Wood, J. H., & Bode, M. F. 1994, *MNRAS*, 266, 761

Wilde, K. 1965, *PASP*, 77, 208

Williams, R. 2012, AJ, 144, 98

Williams, R. E. 1989, AJ, 97, 1752

Williams, R. E. 1992, AJ, 104, 725

Williams, R. E., Hamuy, M., Phillips, M. M., et al. 1991, ApJ, 376, 721

Williams, R. E., Ney, E. P., Sparks, W. M., et al. 1985, MNRAS, 212, 753

Wolf, M. 1927, Astronomische Nachrichten, 230, 421

Wood, M. A., Still, M. D., Howell, S. B., Cannizzo, J. K., & Smale, A. P. 2011, ApJ, 741, 105

Woods, I. E. 1928, Harvard College Observatory Bulletin, 861, 5

Woudt, P. A. & Warner, B. 2001, MNRAS, 328, 159

Woudt, P. A. & Warner, B. 2002, MNRAS, 335, 44

Woudt, P. A. & Warner, B. 2003, MNRAS, 340, 1011

Woudt, P. A. & Warner, B. 2010, MNRAS, 403, 398

Woudt, P. A., Warner, B., Osborne, J., & Page, K. 2009, MNRAS, 395, 2177

Woudt, P. A., Warner, B., & Pretorius, M. L. 2004, MNRAS, 351, 1015

Woudt, P. A., Warner, B., & Spark, M. 2005, MNRAS, 364, 107

Wyse, A. B. 1940, Publications of Lick Observatory, 14, 217

Yaron, O., Prialnik, D., Shara, M. M., & Kovetz, A. 2005, ApJ, 623, 398

Zacharias, N., Finch, C. T., Girard, T. M., et al. 2013, AJ, 145, 44

Zacharias, N., Monet, D. G., Levine, S. E., et al. 2005, VizieR Online Data Catalog, 1297

Zemko, P., Ciroi, S., Orio, M., et al. 2018, MNRAS, 480, 4489

Zemko, P., Orio, M., Mukai, K., et al. 2016, MNRAS, 460, 2744

Zengin Çamurdan, D., İbanoğlu, C., & Çamurdan, C. M. 2010, New A, 15, 476

Zhao, P. & McClintock, J. E. 1997, ApJ, 483, 899

Zinner, E. 1998, Annual Review of Earth and Planetary Sciences, 26, 147

Zorotovic, M., Schreiber, M. R., & Gänsicke, B. T. 2011, *A&A*, 536, A42

Zorotovic, M., Schreiber, M. R., Gänsicke, B. T., & Nebot Gómez-Morán, A. 2010, *A&A*, 520, A86

Zorotovic, M., Schreiber, M. R., & Parsons, S. G. 2014, *A&A*, 568, L9

Zorotovic, M., Schreiber, M. R., Parsons, S. G., et al. 2016a, *MNRAS*, 457, 3867

Zorotovic, M., Schreiber, M. R., Parsons, S. G., et al. 2016b, *MNRAS*, 457, 3867

Zwitter, T. & Munari, U. 1994, *A&AS*, 107

